Waste Management 32 (2012) 1459–1467

Contents lists available at SciVerse ScienceDirect

Waste Management

journal homepage: www.elsevier.com/locate/wasman

Leaching of heavy metals from solidified waste using Portland cement and zeolite as a binder

Chuwit Napia[a], Theerawat Sinsiri[a,*], Chai Jaturapitakkul[b], Prinya Chindaprasirt[c]

[a] School of Civil Engineering, Institute of Engineering, Suranaree University of Technology, Nakorn Ratchasima 30000, Thailand
[b] Department of Civil Engineering, Faculty of Engineering, King Mongkut's University of Technology Thonburi, Bangkok 10140, Thailand
[c] Sustainable Infrastructure Research and Development Center, Department of Civil Engineering, Faculty of Engineering, Khon Kaen University, Khon Kaen 40002, Thailand

ARTICLE INFO

Article history:
Received 1 July 2011
Accepted 27 February 2012
Available online 31 March 2012

Keywords:
Leaching
Heavy metal
Solidified waste
Zeolite

ABSTRACT

This study investigated the properties of solidified waste using ordinary Portland cement (OPC) containing synthesized zeolite (SZ) and natural zeolite (NZ) as a binder. Natural and synthesized zeolites were used to partially replace the OPC at rates of 0%, 20%, and 40% by weight of the binder. Plating sludge was used as contaminated waste to replace the binder at rates of 40%, 50% and 60% by weight. A water to binder (*w*/*b*) ratio of 0.40 was used for all of the mixtures. The setting time and compressive strength of the solidified waste were investigated, while the leachability of the heavy metals was determined by TCLP. Additionally, XRD, XRF, and SEM were performed to investigate the fracture surface, while the pore size distribution was analyzed with MIP.

The results indicated that the setting time of the binders marginally increased as the amount of SZ and NZ increased in the mix. The compressive strengths of the pastes containing 20 and 40 wt.% of NZ were higher than those containing SZ. The compressive strengths at 28 days of the SZ solidified waste mixes were 1.2–31.1 MPa and those of NZ solidified waste mixes were 26.0–62.4 MPa as compared to 72.9 MPa of the control mix at the same age. The quality of the solidified waste containing zeolites was better than that with OPC alone in terms of the effectiveness in reducing the leachability. The concentrations of heavy metals in the leachates were within the limits specified by the US EPA. SEM and MIP revealed that the replacement of Portland cement by zeolites increased the total porosity but decreased the average pore size and resulted in the better containment of heavy ions from the solidified waste.

1. Introduction

Currently, over 80% of the hazardous wastes are from industrial processes. The sludge, heavy metals, oils and infectious waste are the most abundant hazardous wastes. The amount of industrial waste and hazardous waste from industrial plants increases every year. The toxic wastes containing heavy metals are, therefore, causing serious environmental problems in the contamination of water, air and soil. It is an issue that deserves attention to find ways to properly and appropriately capture the waste.

The hazardous waste water from industries is released from industrial facilities and is also causing critical environmental problems. The treatment processes could reduce the concentrations of the toxic waste depending on the condition of the sediment's dry residue. However, the final disposal of the waste sediment is still not safe in terms of storage and transportation because some heavy metals remain unstable and may leak into the environment. To solve the problem, the method of reducing or storing hazardous toxic waste is required to stop the leaching of toxic substances to the environment.

Solidification is a process used to treat hazardous waste from industrial plants, particularly hazardous substances or inorganic substances contaminated by heavy metals. The hazardous substances are stored in the structure by chemical bonding which neutralizes them and reduces the chance of spreading. The placeholder used in this process is normally Portland cement blended with pozzolanic materials such as fly ash, rice husk ash and silica fume. Solidification eases the safe transport of the solid cast mass and allows disposal in a landfill.

Zeolites are framework silicates consisting of interlocking tetrahedrons of SiO_4 and AlO_4. The alumino-silicate structure is negatively charged and attracts the positive ions that reside within the zeolites. This results in large vacant spaces or cages in their structures that allow space for large cations such as sodium, potassium, barium, calcium and even relatively large molecules as well as cation groups of water, ammonia, carbonate ions and nitrate ions (Feng et al., 2000). The spaces are interconnected and form long and wide channels of various sizes depending on the minerals. These channels allow easy movement of the resident ions and molecules into and

---

* Corresponding author. Tel.: +66 4422 4420; fax: +66 4422 4607.
E-mail address: sinsiri@sut.ac.th (T. Sinsiri).

0956-053X/$ - see front matter © 2012 Elsevier Ltd. All rights reserved.
http://dx.doi.org/10.1016/j.wasman.2012.02.011

Table 1
Sample mix proportions (by weight).

Binder			S (%)	*w*/*b*	Symbol
OPC (%)	SZ (%)	NZ (%)			
100	–	–	–	0.4	OPC100
			40	0.4	OPC40S
			50	0.4	OPC50S
			60	0.4	OPC60S
80	20	–	–	0.4	OPC20SZ
			40	0.4	OPC20SZ40S
			50	0.4	OPC20SZ50S
			60	0.4	OPC20SZ60S
60	40	–	–	0.4	OPC40SZ
			40	0.4	OPC40SZ40S
			50	0.4	OPC40SZ50S
			60	0.4	OPC40SZ60S
80	–	20	–	0.4	OPC20NZ
			40	0.4	OPC20NZ40S
			50	0.4	OPC20NZ50S
			60	0.4	OPC20NZ60S
60	–	40	–	0.4	OPC40NZ
			40	0.4	OPC40NZ40S
			50	0.4	OPC40NZ50S
			60	0.4	OPC40NZ60S

out of the structure. The zeolites are thus characterized by their ability to lose and absorb water without damaging their crystal structures (Quanlin and Naiqian, 2005).

Clinoptilolite is a naturally occurring zeolite that forms through the devitrification (the conversion of glassy material to crystalline material) of volcanic ash in lake and marine waters. It is the most studied of all zeolites and is widely regarded as the most useful. Clinoptilolite has a particularly high cation exchange capacity which provides many useful properties (Poon et al., 2000). Clinoptilolite is used in many applications such as chemical sieves, gas absorbers, feed additives, food additives, odor control agents and water filters for municipality, residential drinking water and aquariums (Feng and Peng, 2005). Clinoptilolite is well suited for these applications because of its large amount of pore space, high resistance to extreme temperatures and chemically neutral basic structure.

Sludge produced by the metal plating industry is generally considered to be "hazardous waste" because of its toxic heavy metal content. Solidification techniques applied prior to the deposition of this waste in landfills provide good results allowing the safe disposal of inorganic sludge. The use of materials such as zeolite with its pozzolanic property and the ability to bind metal ions generally gives a good performance. The solidification can store a large amount of sludge and help protecting the environment. This study, therefore, aims to investigate an effective solidification technique for sludge from a metal plating factory using both natural and synthesized zeolites in corporation with Portland cement.

2. Experimental investigation

2.1. Materials

The materials used were ordinary Portland cement (OPC) per ASTM C150, sodium aluminum silicate ($Na_{96}Al_{96}Si_{96}O_{384}$) as synthesized zeolite (SZ), clinoptilolite ($(Na,K,Ca)_6(Si{\cdot}Al)_{36}O_{72}20H_2O$) as natural zeolite (NZ), sludge (S) from the treatment of wastewater from a nickel plating plant and tap water. The S contained 35% water and 65% solid. It was dried and then sieved through a No. 100 sieve.

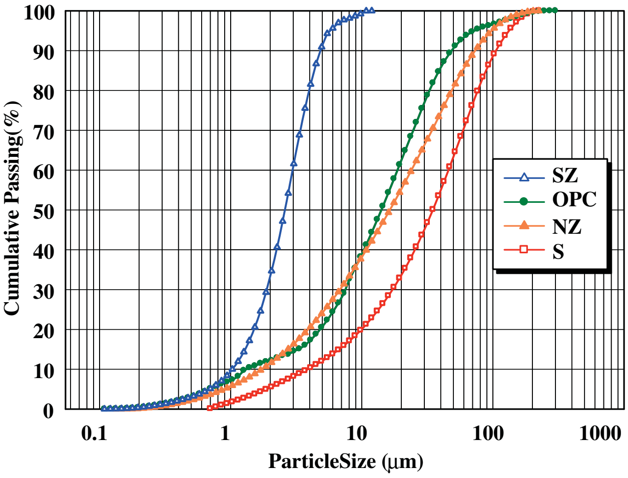

Fig. 1. Particle size distribution of OPC, SZ, NZ and S.

2.2. Mixture proportions

The sludge waste was solidified using OPC containing SZ and NZ as a binder. Zeolites were used to partially replace OPC at rates of 0%, 20%, and 40% by weight of the binder. The plating sludge was used to replace the binders at the rates of 40%, 50% and 60% by weight. A constant water to binder (*w*/*b*) ratio of 0.40 was used. The pastes were mixed in a mechanical mixer, and the specimens were cast in 50-mm cube molds. The fresh samples were covered with a plastic sheet to prevent water evaporation. After casting for 24 h, the samples were removed from the molds and cured in saturated lime water (Table 1).

3. Test programs

3.1. Specific gravity and particle size

The specific gravity of OPC, SZ, NZ and S was measured in accordance with ASTM C188, and their particle sizes were measured using laser particle size analysis.

3.2. Normal consistency

The normal consistency of the pastes was measured in accordance with ASTM C187 using Vicat apparatus.

3.3. Compressive strength

The compressive strength of the solidified waste was tested in accordance with ASTM C109 at ages of 7, 28, and 90 days. Five samples were tested for each age group.

Table 2
Specific gravity, median particle size and surface area of OPC, SZ, NZ and S.

Sample	Specific gravity	Mean particle size d_{50} (μm)	Surface area[a] (cm^2/g)
OPC	3.15	14.12	2600
SZ	1.87	2.51	32,500
NZ	2.09	16.17	5400
S	2.14	34.81	1900

[a] BET analysis.

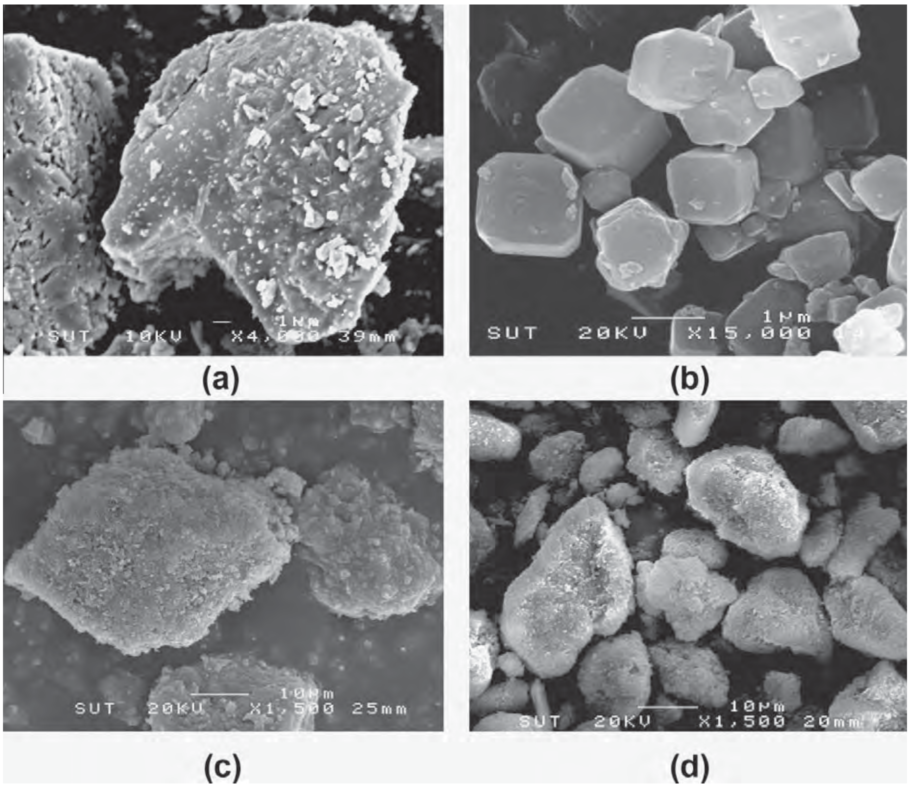

Fig. 2. SEM micrographs of (a) OPC at 4000 time, (b) SZ at 15,000 time, (c) NZ at 1500 time and (d) S at 1500 times.

Table 3
Chemical composition of materials.

Chemical composition (%)	OPC	SZ	NZ	S
SiO_2	19.85	65.3	75.32	5.53
Al_2O_3	4.49	26.18	10.28	3.78
Fe_2O_3	3.56	0.03	2.66	–
CaO	66.96	0.12	3.95	25.32
MgO	1.36	0.08	1.2	–
K_2O	0.34	2.64	4.29	–
Na_2O	–	1.87	0.89	–
NiO	–	–	–	40.88
CuO	–	–	–	13.08
ZnO	–	–	–	10.33
CrO	–	–	–	0.64
LOI	0.98	5.65	2.3	0.44

3.4. Scanning electron microscopy (SEM)

A JEOL scanning electron microscope (model JSM6400) was used to examine the phase development and microstructure of the solidified plating waste. The paste cubes at the ages of 7 and 28 days were broken and the fractions in the middle part of the specimens were used for the analyses. The solid was placed on a brass stub sample holder with double stick carbon tape. Then, the sample was dried using infrared light for 5 min. Subsequently, the sample was coated with a layer of gold approximately 20–25 Å thick using a blazer sputtering coater. Micrographs were recorded at 12 kV and 500–10,000× magnifications (Chindaprasirt et al., 2005).

3.5. X-ray diffractometer (XRD) and X-ray fluorescence (XRF) analyses

The XRD scans were performed for $2\theta°$ between 10° and 70°, with an increment of 0.03°/step and a scan speed of 0.5 s/step. XRD analysis using Bruker's TOPAS software and using wavelength dispersive XRF (WDXRF). The positions of the diffraction peaks were identified by comparison to reference database compounds (Chindaprasirt et al., 2005).

3.6. Mercury intrusion porosimetry procedure (MIP)

The pore diameter distribution in the hardened cement pastes was measured by mercury intrusion porosimetry (MIP) at a pressure capacity of 228 MPa. After curing for 7, 28 and 90 days, the samples were split from the middle portion of the hardened blended cement paste. To stop the hydration reaction, the samples were submerged directly into liquid nitrogen for 5 min and were then evacuated at a pressure of 0.5 Pa at −40 °C for 48 h. This method has been used previously to stop the hydration reaction of cement paste (Chindaprasirt et al., 2007).

3.7. Toxicity characteristic leaching procedure (TCLP)

The metal leaching from the solidified plating waste cured for 7, 28 and 90 days and was assessed using the TCLP as defined by the US EPA (Li et al., 2001). The samples were crushed to reduce the particle size to less than 9.5 mm. The crushed sample was extracted using an acetic acid solution (pH 2.88) in a volume with a weight equal to 20 times the weight of the sample. The extraction vessels were rotated in an end-over-end manner at 30 rpm for 18 h. The leachate was filtered through a 0.45-μm membrane filter to remove suspended solids and was then divided into two portions. One portion was used for a pH measurement, and the other was used for the determination of the metals present in the leachate by ICP-AES. Each extraction was performed in triplicate, and the average value was reported to ensure the reproducibility of the data (Asavapisit et al., 2005).

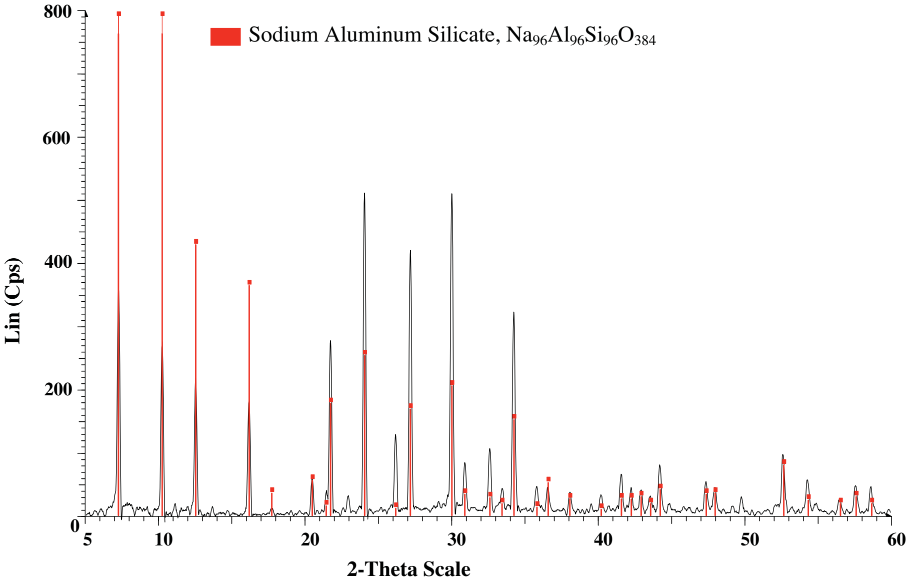

(a) synthesized zeolite

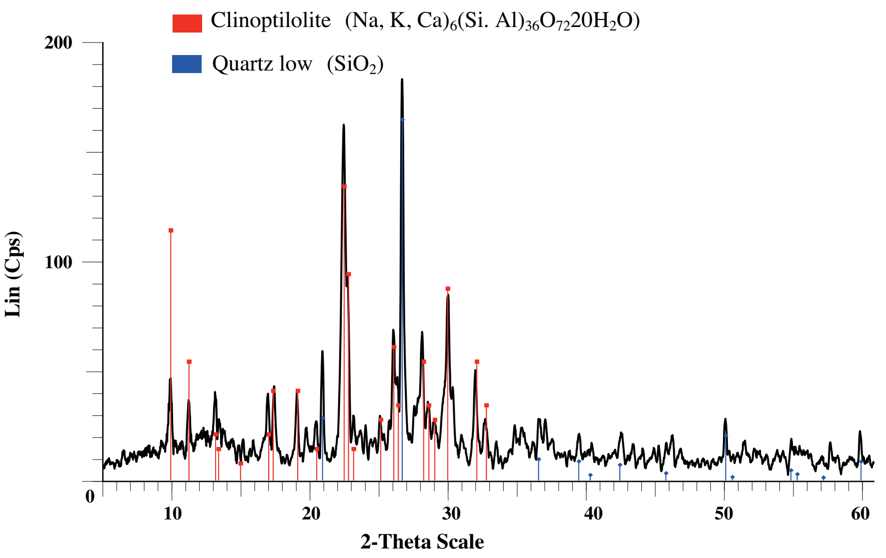

(b) natural zeolite

Fig. 3. XRD patterns of synthesized zeolite and natural zeolites.

4. Results and discussion

4.1. Properties of materials

4.1.1. Physical results for OPC, SZ, NZ and S

The specific gravity and median particle size (d_{50}) of the OPC, SZ, NZ and S are shown in Table 2. The median particle size (d_{50}) of the OPC was approximately 14.1 µm, while those of SZ, NZ and S were 2.5, 16.2 and 34.8 µm, respectively. The surface areas of the OPC, SZ, NZ and S were 2600, 32,500, 5400 and 1900 cm^2/g, respectively. The particle size distribution for the OPC, SZ, NZ and S was measured with a Mastersizer and is graphically shown in Fig. 1. For the OPC, NZ and S, the particle shape was solid and angular, whereas the surface of the SZ was smooth and exhibited a hexagonal character (Fig. 2).

4.1.2. Chemical composition and material patterns

Table 3 shows the chemical composition of the OPC, SZ, NZ and S, which was analyzed by XRF. SZ and NZ were found to be mainly SiO_2 and Al_2O_3. As can be seen, these two components were 90% for SZ and 85% for NZ. Additionally, the main elements of S were NiO (40.88%), CaO (25.32%), CuO (13.08%) and ZnO (10.33%).

Fig. 3 shows the XRD patterns for the SZ and NZ. The figure indicates that the intensity peak of sodium aluminum silicate ($Na_{96}Al_{96}Si_{96}O_{384}$) and $(Na,K,Ca)_6(Si{\cdot}Al)_{36}O_{72}20H_2O$ appeared at 0–60° (2θ).

4.2. Properties of pastes

4.2.1. Normal consistency of pastes

The normal consistency of OPC100 was found to be 25.5%. Higher replacement of SZ and NZ resulted in a higher normal consistency. For example, the normal consistencies of pastes OPC20SZ, OPC40SZ, OPC20NZ and OPC40NZ were 32.4%, 34.4%, 31.2% and 32.0%, respectively. The normal consistency of pastes containing SZ and NZ, which have a higher fine content, was higher than those containing coarser zeolites. This occurs because the particles of SZ and NZ have a higher fine content and a higher porosity; thus, they absorb more water, which results in greater water consumption.

Table 4
Setting time and compressive strength of the solidified wastes.

Sample	Time (min)		Compressive Strength (MPa)		
	Initial setting time	Final setting time	7-day	28-day	90-day
OPC100	132	181	53.8	72.9	79.4
OPC40S	148	192	0.9	1.3	1.5
OPC50S	151	195	0.6	1.0	1.2
OPC60S	154	197	0.5	0.8	1.1
OPC20SZ	141	185	21.6	31.1	38.2
OPC20SZ40S	149	186	2.1	13.5	16.1
OPC20SZ50S	152	186	1.3	4.9	10.7
OPC20SZ60S	156	185	0.8	1.4	2.0
OPC40SZ	143	187	10.2	23.4	26.9
OPC40SZ40S	149	188	0.3	6.0	17.4
OPC40SZ50S	151	189	0.3	4.2	13.6
OPC40SZ60S	152	190	0.1	1.2	3.2
OPC20NZ	133	183	52.0	62.4	71.1
OPC20NZ40S	135	184	43.4	57.3	65.2
OPC20NZ50S	135	185	35.7	49.1	58.4
OPC20NZ60S	136	186	30.5	41.3	50.3
OPC40NZ	134	184	40.5	50.7	61.3
OPC40NZ40S	135	184	19.5	36.2	43.4
OPC40NZ50S	136	185	15.2	31.5	39.3
OPC40NZ60S	136	187	12.1	26.0	33.8

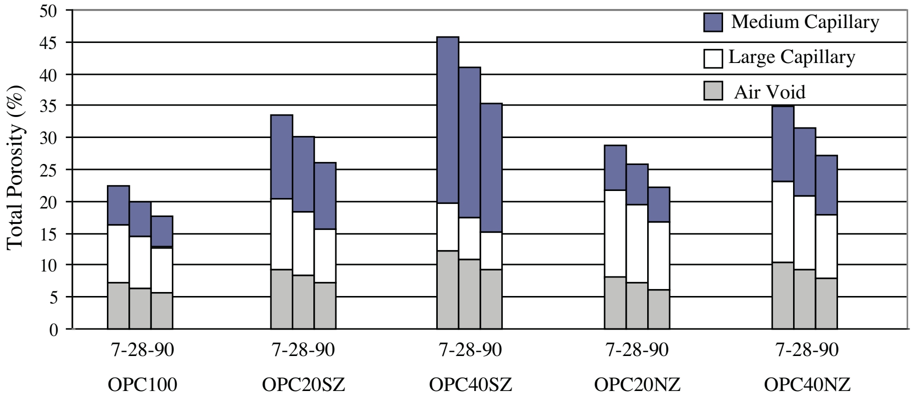

Fig. 4. Total porosity of cement paste and blended cement pastes at 7, 28 and 90 days.

4.2.2. Setting time of blended cement pastes and pastes containing solidified plating waste

The setting times of the blended cement pastes containing SZ and NZ were similar to those of the Portland cement paste. For example, the final setting times of OPC paste, was 181 min. The initial setting time of mixes with SZ was 185 and 187 min and those with NZ were 183 and 184 min. For the incorporation of S, the initial setting time was increased to 148–154 min and the final setting times to 191–192 min. The similar or slightly increase in the setting time were probably due to the pastes mixed with zeolites have higher water contents at normal consistency than Portland cement paste. Moreover, the use of zeolite to replace Portland cement resulted in a smaller amount of cement and thus caused a longer setting time to be observed. For the use of S, the reductions in the amount of cement and pozzolan resulted in an even smaller amount of cementing material and hence the setting times increased.

4.2.3. Compressive strength of the blended cement pastes

Table 4 shows the development of compressive strength in the cement paste in relation to the cement replacement level for the case of synthesized zeolites and natural zeolites. Concerning the use of SZ and NZ, replacement of 20% and 40% zeolites led to lower compressive strengths at all ages. It was observed that the compressive strengths of the cement pastes containing NZ were higher than those with SZ for the same replacement conditions and age, because more silica dioxide (the main component of nat-

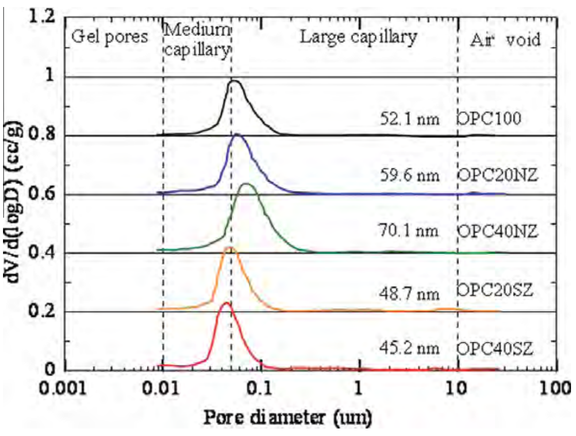

Fig. 5. Relationship between pore diameter and volume intruded of the blended cement pastes at 28 days.

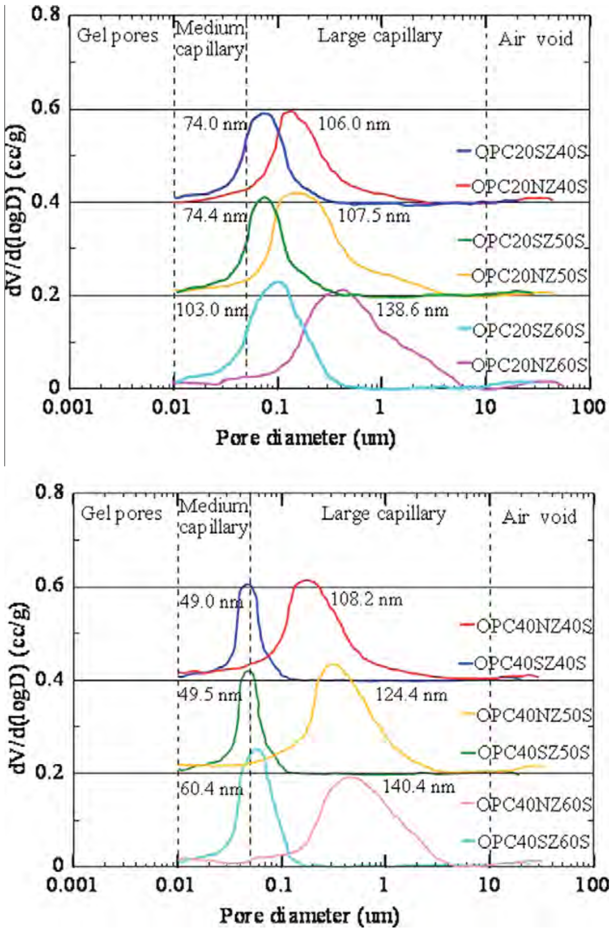

Fig. 6. Relationship between pore diameter and volume intruded of the solidified plating wastes using OPC, NZ and SZ as binders at 28 days.

ural zeolite) is contained than in the synthesized zeolites and cement. The pozzolanic activity of zeolite normally depends on the amount of the active amorphous phases of silica and alumina. As indicated in the XRD patterns in Fig. 3, the amount of the active amorphous phases of NZ is higher than that of SZ. The results of the compressive strengths of pastes OPC20SZ, OPC40SZ, OPC20NZ and OPC40NZ at 28 days of 31.1, 23.4, 62.4 and 50.7 MPa, respectively confirms the observation.

4.2.4. Compressive strength of pastes containing solidified plating waste

The experimental results showed that the rates of strength development in the solidified waste using SZ and NZ as solidification binders were higher than that with OPC. The composition of OPC hydration product is dominated by calcium silicate hydrate (C–S–H) which typically comprises 70–80% of the product (Deja, 2002). The metals may react with calcium hydroxide to produce insoluble compounds as a form of metal hydroxide; this mechanism inhibited the hydration and decreased the strength of the wastes, especially when the concentration of metal in the solidified waste was more than 0.3% by weight (Li et al., 2001; Asavapisit et al., 2001; Qin et al., 2003). The strength of these solidified wastes could be very low due to the inhibition of the cement reactions by the metal ions in the waste. Additionally, the strength of the solidified waste decreased when the amount of waste increased. For example, the strengths of pastes OPC20NZ40S, OPC20NZ50S, and OPC20NZ60S at 28 days were 57.3, 49.1 and 41.3 MPa, respectively. The results indicated that the plating sludge can be loaded in a proportion as high as 60 wt.% of the cement blended with 40 wt.% SZ and NZ at a 28-day compressive strength that meets the minimum requirement for disposal in a secure landfill (0.34 MPa).

4.2.5. Porosity and average pore diameter of blended cement pastes

The total porosity, capillary porosity and average pore diameter of the pastes at 7, 28 and 90 days are shown in Fig. 4. The incorporation of SZ and NZ increased the total porosity of the blended cement pastes as compared with the OPC paste at all ages. The total porosity increased with an increase in replacement by SZ and NZ. The increase in total porosity as a result of the utilization of zeolite was mainly due to the decrease in capillary porosity. Note that the compressive strength decreased, while the porosity of the blended cement paste increased (Poon et al., 2000; Isaia et al., 2003). The capillary porosity of the cement paste blended with NZ at all replacement levels decreased in comparison to that with SZ.

Fig. 4 shows the effect of the percent replacement of SZ and NZ on the average pore size in the cement pastes at age 7, 28 and 90 days. It can be observed that the average pore size of the additives decreased at the respective period of hydration because of the gradual filling of large pores by hydration products of cementitious materials; however, the extent of the decrease was variable. A greater decrease was observed for replacement by SZ, whereas the decrease was comparatively less for replacement by NZ. The average pore size tends to decrease as the percent replacement increases. The relationship between the pore diameter and incremental pore volume of the blended cement paste at 28 days is shown in Fig. 5. The critical pores sizes of the OPC100, OPC20NZ and OPC40NZ pastes were 52.1, 59.6 and 70.1 nm, respectively, and the pores were distributed as large capillary pores. The critical pores sizes of the OPC20SZ and OPC40SZ pastes were 48.7 and 45.2 nm, respectively, and these were distributed as medium capillary pores. These values were lower than that of the OPC100 paste. This suggests that the greater fineness of the zeolite was more effective in reducing the pore diameter of the paste. The results also showed that the blended cement paste containing zeolite presented a smaller pore size than the Portland cement paste. The pore size decreased with an increase in zeolite replacement. Similar results have also been reported in other studies (Poon et al., 1997, 1999a,b).

The relationship between the pore diameter and incremental pore volume of the solidified waste using OPC, SZ and NZ as binders at 28 days is shown in Fig. 6. The critical pore sizes of OPC20SZ40S, OPC20SZ50S and OPC20SZ60S were 74.0, 74.4 and 103.0 nm, respectively, and these pores were distributed as large capillary pores. Additionally, the critical pore sizes of the OPC40SZ40S, OPC40SZ50S and OPC40SZ60S pastes were 49.0, 49.5 and 60.4 nm, respectively. These results suggested that the increase in the amount of the plating waste resulted in increase in pore diameter of the paste. In contrast, the increase in the amount of SZ resulted in the decrease in the pore diameter of the paste.

As shown in Fig. 6, the critical pore sizes of OPC20NZ40S, OPC20NZ50S, OPC20NZ60S, OPC40NZ40S, OPC40NZ50S and OPC40NZ60S were 106.0, 107.5, 138.6, 108.2, 124.4 and 140.4 nm, respectively. These results suggested that as the amount of plating sludge increased, the pore diameter of the paste increased.

4.2.6. Fracture surface analysis byscanning electron microscopy (SEM)

The microstructure morphology of the fractured surface was determined by SEM for OPC100, OPC20SZ, OPC40SZ, OPC20NZ and OPC40NZ pastes at 28 days (see Fig. 7). The microstructure of OPC100 was porous and exhibited many voids, while OPC20SZ, OPC40SZ, OPC20NZ and OPC40NZ showed uniform and dense pastes. The incorporation of zeolites resulted in the increased hydration and pozzolanic reaction and thus reduced the pore sizes.

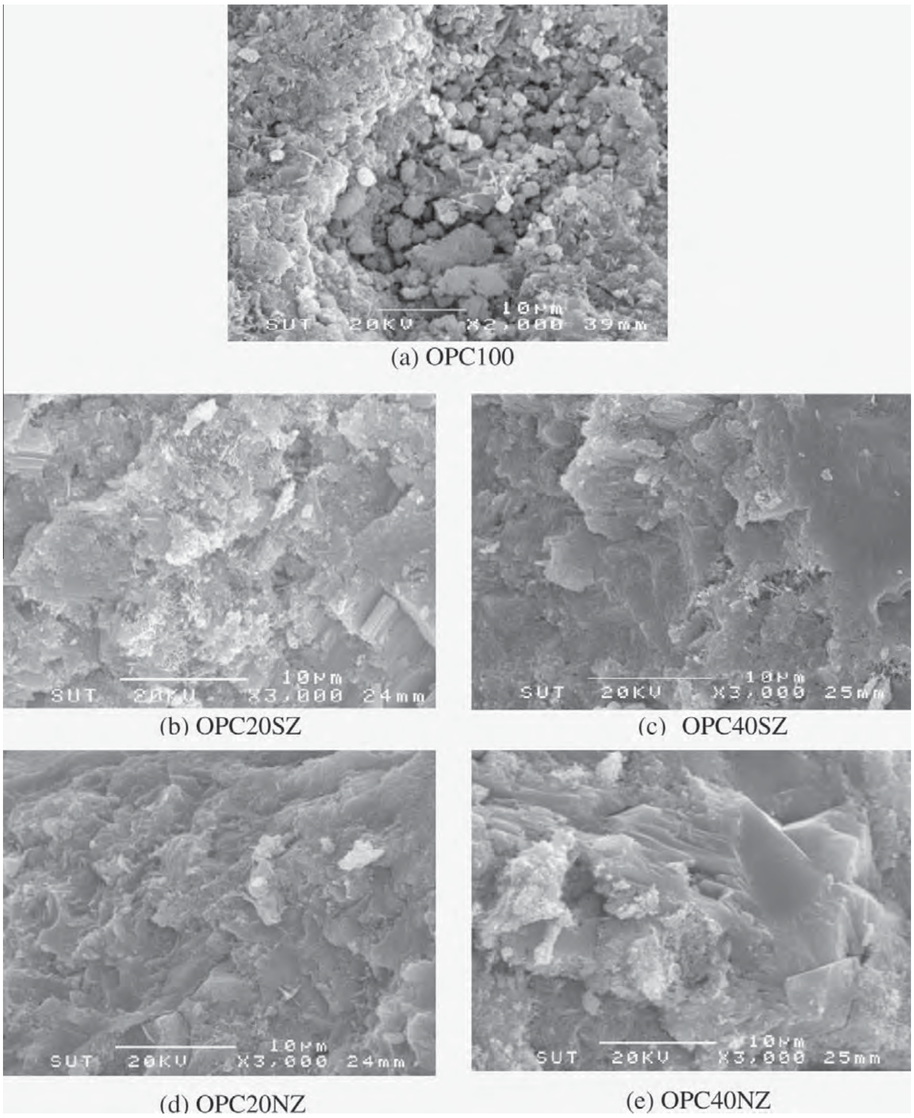

(a) OPC100

(b) OPC20SZ

(c) OPC40SZ

(d) OPC20NZ

(e) OPC40NZ

Fig. 7. Fracture surface of the blended cement pastes at 28 days.

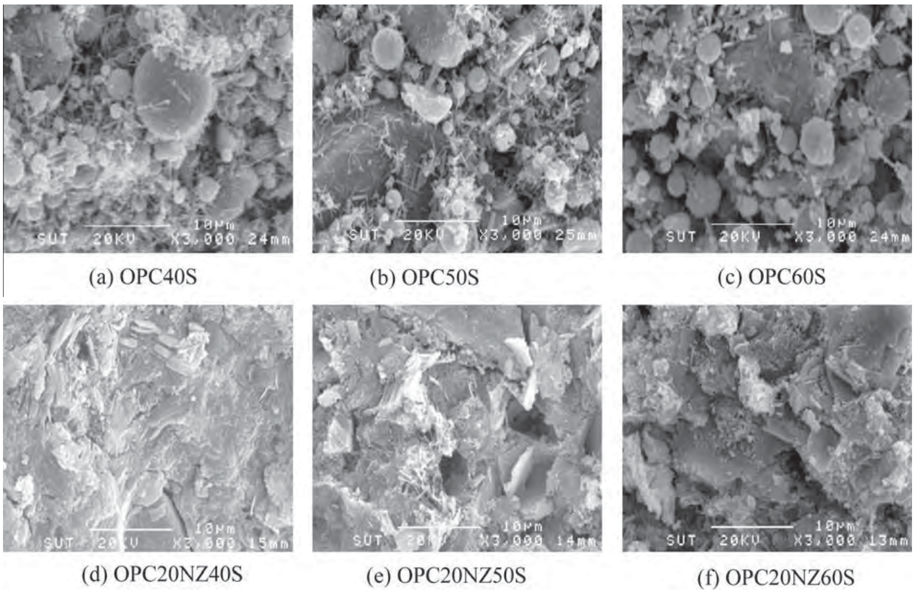

(a) OPC40S

(b) OPC50S

(c) OPC60S

(d) OPC20NZ40S

(e) OPC20NZ50S

(f) OPC20NZ60S

Fig. 8. Fracture surfaces of the solidified plating wastes at 28 days.

Table 5
Leachate pHs in TCLP leachates.

Sample	pH		
	Age 7 days	Age 28 days	Age 90 days
OPC100	6.3	6.5	6.6
OPC40S	6.4	6.6	6.7
OPC50S	7.1	7.2	7.2
OPC60S	7.7	7.7	7.7
OPC20SZ40S	7.6	7.5	7.4
OPC20SZ50S	7.9	7.9	7.8
OPC20SZ60S	7.8	7.9	7.9
OPC40SZ40S	9.8	9.5	9.5
OPC40SZ50S	8.8	8.8	8.7
OPC40SZ60S	8.5	8.5	8.6
OPC20NZ40S	11.4	11.5	11.5
OPC20NZ50S	11.2	11.2	11.2
OPC20NZ60S	11.1	11.1	11.1
OPC40NZ40S	11.2	11.1	11.1
OPC40NZ50S	10.8	10.8	10.9
OPC40NZ60S	9.7	9.6	9.6

Thus, replacing the Portland cement with some zeolites resulted in a dense paste.

Fig. 8 shows the fractured surfaces of the solidified plating waste at 28 days, as determined by SEM. The paste with more plating sludge showed a lower density because the proportion of binder in the mixture decreased. Because heavy metals inhibit hydration, the cement reaction was not completed, and some heavy metals did not react (Bishop et al., 2003). The replacement of Portland cement by zeolites showed a higher density than used Portland cement alone. The consequences of this are that the solidified waste was more porous, and the compressive strength of the solidified waste decreased significantly compared with those with the absence of plating sludge in the mixture.

4.2.7. Leaching analysis

Table 5 shows the leachate pH values in the TCLP leachates at 7, 28 and 90 days. The pH of the solution extracted from the solidified waste is increased from the initial pH. For example, the pH of pastes OPC100, OPC40S, OPC20SZ40S and OPC20NS40S pastes at 28 days were 6.5, 6.6, 7.5 and 11.5, respectively. The pH values increased because calcium hydroxide in the pores dissolved into the acid. Fig. 9 shows the metal concentrations in TCLP leachates, the results showed that the concentration of Cr in the leachate for all solidified waste samples was lower than the limit specified by the standards of the US EPA (<5.0 mg/l). It should be noted here that the untreated sludge also meets US EPA criteria for Cr. For example, the concentrations of Cr in the leachate of pastes

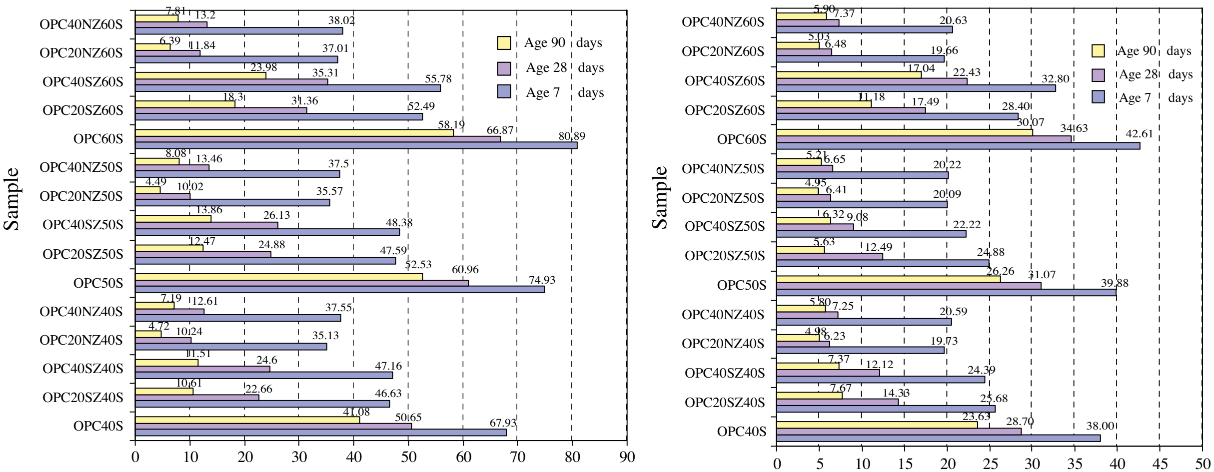

(a) concentration of Ni
(b) concentration of Cu

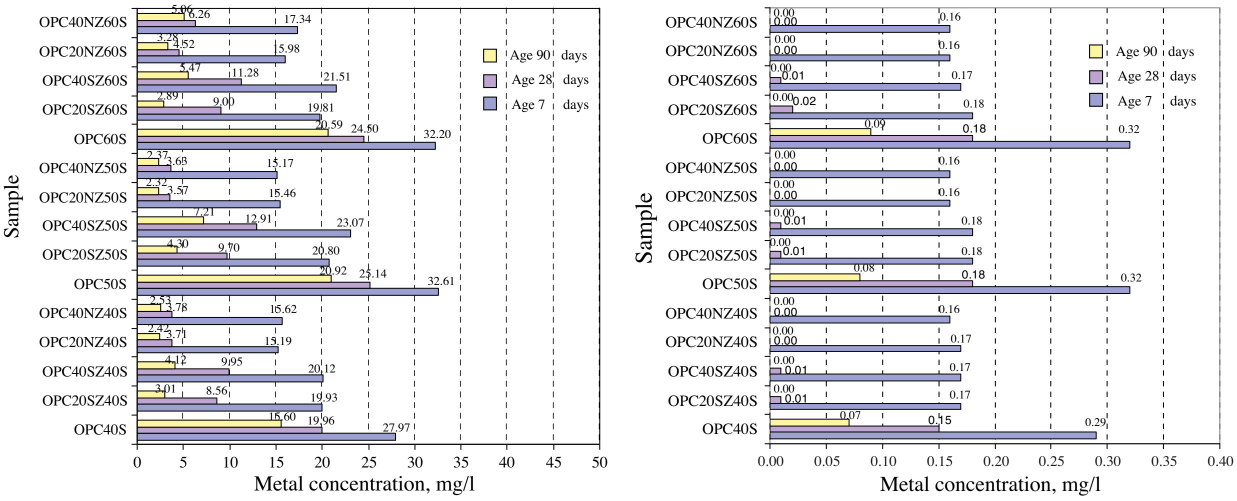

(c) concentration of Zn
(d) concentration of Cr

Fig. 9. Metal concentrations in TCLP leachates.

OPC20SZ40S, OPC20SZ50S, OPC20NZ40S and OPC20SZ50S at 7 days were 0.17, 0.18, 0.17 and 0.16 mg/l respectively. The Ni, Cu and Zn have no regulatory standards because these three metals are not classified as hazardous waste by the US EPA. The results showed that when sample age increased the effectiveness in reducing the leachability increased, For example, it was detected that OPC20NZ40S contained Ni of 35.13 mg/l at 7 days and this decreased to only 10.24 mg/l at 90 days. Using NZ as a binder effectively reduced leaching more than using SZ. For example, the concentrations of Ni in the leachate of pastes OPC40NZ40S and OPC40SZ40S at 28 days were 12.61 and 24.60 mg/l respectively. Additionally, the metal concentrations in the TCLP leachates that were extracted from the cement-based solidified plating waste were much lower than that extracted from the plating sludge. Effectiveness in reducing the leachability of solidified waste using SZ and NZ to replace OPC as a binder was higher than 80.0% at all ratios. This was because SZ and NZ mainly composed of SiO_2, Al_2O_3 and Fe_2O_3; and the structures of zeolites consist of three-dimensional frameworks of SiO_4 and AlO_4 tetrahedra. The aluminum ion is small enough to occupy the position in the center of the tetrahedron of four oxygen atoms, and the isomorphous replacement of Si^{4+} by Al^{3+} produces a negative charge in the lattice. The net negative charge is balanced by the exchangeable cation (Cheng and Bishop, 1992; Peralta et al., 1992). Thus, the effectiveness in reducing the leachability was higher using SZ and NZ than that with OPC alone. These results indicated that during the ion-exchange process, the metal ions had to move through the pores of zeolite mass and through channels of the lattice, and they had to replace exchangeable cations. The diffusion was fast through the pores, but was retarded when the ions moved through the smaller diameter channels. In this case, the metal ions uptake could mainly be attributed to the ion-exchange reactions in the microporous minerals of zeolite (Erdem et al., 2004).

5. Conclusions

On the basis of the results of this study, the following conclusions can be drawn.

1. The blended cement pastes containing synthesized zeolite and natural zeolite exhibited higher total porosity and capillary porosity than those containing Portland cement alone. This resulted in the lower compressive strengths of blended cement pastes compared to that of the control Portland cement paste.
2. The pore size distribution and the average pore diameter of the blended cement paste containing zeolites decreased with an increase in zeolite content which resulted in the dense structure of the paste. This effect was caused by the hydration reaction and the pozzolanic reaction.
3. The use of zeolites to partially replace Portland cement as a solidification binder produced solidified waste with lower strength. However, it is more effectiveness in terms of leachablity than the use of Portland cement alone.
4. The application of natural zeolite as a binder with Portland cement to reduce the leaching of heavy metals resulted in a better outcome than using synthetic zeolites with cement, or cement alone. The use of natural zeolite with Portland cement as a binder to solidify waste sludge is appropriate as the leachablity was reduced and the compressive strength complied with the US EPA standard.

Acknowledgments

The authors would like to acknowledge the financial support by the Higher Education Research Promotion and National Research University Project of Thailand, Office of the Higher Education Commission, through the Advanced Functional Materials Cluster of Khon Kaen University, and the Strategic Scholarships for Frontier Research Network for the Joint Ph.D. Program, Thai Doctoral degree. Thanks are also extended to the Thailand Research Fund (TRF) for financial support under the TRF Senior Research Scholar, Grant No. RTA5480004 and the TRF New Researcher Scholar, Grant No. MRG5280178.

References

Asavapisit, S., Nanthamontry, W., Polprasert, C., 2001. Influence of condensed silica fume on the properties of cement-based solidified wastes. Cement and Concrete Research 31, 1147–1152.

Asavapisit, S., Naksrichum, S., Harnwajanawong, N., 2005. Strength, leachability and microstructure characteristics of cement-based solidified plating sludge. Cement and Concrete Research 35, 1042–1049.

Bishop, M., Bott, S.G., Barron, A.R., 2003. A new mechanism for cement hydration inhibition: solid-state chemistry of calcium nitrilotris(methylene)-triphosphonate. Chemistry of Materials 15 (16), 3073–3088.

Cheng, K.Y., Bishop, P.L., 1992. Metals distribution in solidified/stabilized waste forms after leaching. Hazardous Waste and Hazardous Materials 9, 163–312.

Chindaprasirt, P., Jaturapitakkul, C., Sinsiri, T., 2005. Effect of fly ash fineness on compressive strength and pore size of blended cement paste. Cement and Concrete Composites 27, 425–428.

Chindaprasirt, P., Jaturapitakkul, C., Sinsiri, T., 2007. Effect of fly ash fineness on microstructure of blended cement paste. Construction and Building Materials 21, 1534–1541.

Deja, J., 2002. Immobilization of Cr^{6+}, Cd^{2+}, Zn^{2+} and Pb^{2+} in alkali-activated slag binder. Cement and Concrete Research 32, 1971–1979.

Erdem, E., Karapinar, N., Donat, R., 2004. The removal of heavy metal cations by natural zeolites. Journal of Colloid and Interface Science 280, 309–314.

Feng, N.-Q., Peng, G.-F., 2005. Applications of natural zeolite to construction and building materials in China. Construction and Building Materials 19, 579–584.

Feng, N.-Q., Xing, F., Leng, F.-G., 2000. Zeolite ceramsite cellular concrete. Magazine of Concrete Research 52, 117–122.

Isaia, G.C., Gastaldini, A.L.G., Moraes, R., 2003. Physical and pozzolanic action of mineral addition on the mechanical strength of high-performance concrete. Cement and Concrete Research 25, 69–76.

Li, X.D., Poon, C.S., Sun, H., Lo, I.M.C., Kirk, D.W., 2001. Heavy metal speciation and leaching behaviours in cement based solidified/stabilized waste materials. Journal of Hazardous Materials A 82, 215–230.

Peralta, G.L., Ballsteros, F.C., Cepeda, M.L., 1992. Treatment and Disposal of Heavy Metal Waste Using Cementitious Solidification. Nation Engineering Center, Philippines, pp. 2–37.

Poon, C.S., Wong, Y.L., Lam, L., 1997. The influence of different curing conditions on the pore structure and related properties of fly ash cement pastes and mortars. Construction and Building Materials 11, 383–393.

Poon, C.S., Lam, L., Kou, S.C., Lin, Z.S., 1999a. A study on the hydration rate of natural zeolite blended cement paste. Construction and Building Materials 13, 427–432.

Poon, C.S., Lam, L., Wong, Y.L., 1999b. Effect of fly ash and silica fume on interfacial porosity of concrete. ACI Material Journal, 197–205.

Poon, C.S., Lam, L., Wong, Y.L., 2000. A study on high strength concrete prepared with large volume of law calcium fly ash. Cement and Concrete Research 30, 447–455.

Qin, G., Sun, D.D., Tay, J.H., 2003. Characterization of mercury- and zinc-doped alkali-activated slag matrix Part II. Zinc. Cement and Concrete Research 33, 1257–1262.

Quanlin, N., Naiqian, F., 2005. Effect of modified zeolite on expansion of alkaline silica reaction. Cement and Concrete Research 35, 1784–1788.

RESEARCH ARTICLE

ScienceAsia 38 (2012): **175–181**

doi: 10.2306/scienceasia1513-1874.2012.38.175

Microstructure and strength of blended FBC-PCC fly ash geopolymer containing gypsum as an additive

Kornkanok Boonserm[a], **Vanchai Sata**[a], **Kedsarin Pimraksa**[b], **Prinya Chindaprasirt**[a,*]

[a] Sustainable Infrastructure Research and Development Centre, Department of Civil Engineering, Faculty of Engineering, Khon Kaen University, Khon Kaen 40002 Thailand

[b] Department of Industrial Chemistry, Faculty of Science, Chiang Mai University, Chiang Mai 50200 Thailand

*Corresponding author, e-mail: prinya@kku.ac.th

Received 21 Dec 2011
Accepted 12 May 2012

ABSTRACT: This study focused on the microstructure and strength of blended fluidized bed coal combustion fly ash (FBC-FA) and pulverized coal combustion fly ash (PCC-FA) geopolymers containing gypsum as an additive. The source materials consisted of 100% FBC-FA and a blend of 75% FBC-FA and 25% PCC-FA. Gypsum was used as an additive at the dosage levels of 0, 5, and 10%wt of the source materials. NaOH and Na_2SiO_3 were used to activate aluminosilicate sources and temperature curing to accelerate the geopolymer reaction. The microstructures of the geopolymer pastes were examined using XRD, FTIR, MIP and SEM tests. The compressive strengths of the geopolymer mortars were also tested. Test results showed that the blending of FBC-FA and PCC-FA improved the geopolymerization and resulted in a dense matrix with reduced porosity and increased compressive strength as compared to those of the FBC-FA geopolymer. The improvement is due primarily to the high glassy phase content of PCC-FA. In addition, the use of 5% gypsum as an additive further improved the geopolymerization. The sulphate ions enhanced the leaching of alumina from the source materials forming additional aluminosilicate and increased calcium in the system which resulted in the formation of additional CSH.

KEYWORDS: fluidized bed coal combustion, pulverized coal combustion, porosity, paste, mortar

INTRODUCTION

The pulverized coal combustion (PCC) process has been used to burn coal for almost a century. This technology requires less excess air whilst uses high firing temperature to improve thermal efficiency creating a spherical shape, highly amorphous phase contents, and reactive by-product materials such as fly ash. Fly ash from pulverized coal combustion (PCC-FA) is commonly used as a pozzolanic material for partial replacement of Portland cement in concrete work[1,2]. The recently developed fluidized bed coal combustion (FBC) technology for power plant supersedes PCC. The FBC process operates at lower burning temperatures and emits lower CO_2, sulphur, and nitrogen oxide. The process can use burnable material such as grubby coal, municipal waste, and all types of biomass, including wood, rice husks, sugarcane bagasse, olive/palm oil residues, fruit residues, or even wet coffee as fuel materials. Even though the FBC method is a clean coal technology, it provides poorer grade of by-product materials.

In Thailand, the fluidized bed power plant normally uses two types of fuel, viz., coal and coal plus biomass. Biomass burning can use biological waste material derived from plants and animal wastes. The composition of biomass ashes is, therefore, quite variable. For example, wood contains low silica and high CaO, while agricultural residues contains high silica and low calcium. The use of biomass to partially replace coal reduces the overall emission of greenhouse gas[3]. However, the FBC fly ash (FBC-FA) is irregular in shape, less reactive, and contains smaller proportion of glassy phase compare to the PCC-FA. It cannot replace cement replacement[4], but it can be used as a source material for making geopolymer[5]. Geopolymer is an alkali-activated aluminosilicate material. The source material, therefore, contains high amorphous silica and alumina contents. It offers good strength, improved mechanical properties, and reduced CO_2 emission[6,7]. Although FBC-FA can be used to produce geopolymer, the strength is low compared to that of the PCC-FA geopolymer[8,9]. The blending of FBC-FA with a high glassy phase material such as PCC-FA is recommended to improve the strength of FBC-FA geopolymer[5].

The degree of geopolymerization can be increased by incorporating additives such as $CaCl_2$, $CaSO_4$, or Na_2SO_4[10]. Sulphate additives give slightly better performance than the chloride additive. $CaSO_4$ or

Table 1 Chemical compositions of FBC-C, FBC-Bi, PCC-FA, and G.

Chemical composition	Materials			
	FBC-C	FBC-Bi	PCC-FA	G
CaO	15.8	40.0	24.5	58.8
SiO_2	38.8	22.6	35.2	–
Al_2O_3	17.6	10.0	16.5	–
Fe_2O_3	11.9	7.6	13.6	–
SO_3	8.1	12.7	1.6	41.2
Na_2O	0	0	2.7	–
MgO	4.0	3.4	3.2	–
K_2O	2.3	1.5	1.9	–
P_2O_5	0.5	1.1	0.2	–
TiO_2	0.7	0.7	0.3	–
LOI	0.5	0.5	0.4	–

gypsum is a good choice as it available in the market at very reasonable cost.

This study, therefore, attempted to improve the compressive strength of geopolymer from FBC-FA. Gypsum was used to improve the FBC-FA and PCC-FA blend reaction. This knowledge would be instrumental to understand and use FBC-FA to produce geopolymeric material.

MATERIALS AND METHODS

Materials

The source materials for making geopolymer were fly ashes from FBC and PCC power plants. Two types of FBC-FA, viz., 100% coal burning (FBC-C) and 70% coal with 30% biomass burning (FBC-Bi) from central area and PCC-FA from Mae Moh Power Plant in northern Thailand were the source materials. Commercial graded gypsum (G) was selected as an additive to improve the geopolymer properties. The chemical compositions of FBC-C, FBC-Bi, PCC-FA, and G were determined by XRF analysis and shown in Table 1. The FBC-C, FBC-Bi, and PCC-FA consisted of SiO_2, Al_2O_3, Fe_2O_3, and CaO as the main oxides. SO_3 was also present in a substantial quantity in FBC ashes. The main components of G were CaO and SO_3 oxides. The physical characteristics of materials are examined by analysing particle sizes, specific gravity, and percentages retained on No. 325 sieve and tabulated in Table 2. The median particle sizes of FBC-C, FBC-Bi, PCC-FA, and G were 22.6, 28.9, 63.5, and 6.4 µm, respectively, with the corresponding specific gravity of 2.69, 2.78, 2.52, and 2.31, respectively. Sodium silicate was a commercially available solution with 13.8% Na_2O, 32.2% SiO_2, and 54.0% H_2O by weight and sodium hydroxide (NH) solution at 10 M concentration was prepared one day before mixing to ensure equilibrium. The NH and NS (Na_2SiO_3) were used as alkali activators. Local river sand with specific gravity of 2.62 and fineness modulus of 2.85 was used to make geopolymer mortar.

Table 2 Physical characteristics of FBC-C, FBC-Bi, PCC-FA, and G.

Materials	Median particles size (µm)	Specific gravity	Retained on sieve #325 (%)
FBC-C	22.6	2.69	15.1
FBC-Bi	28.9	2.78	21.7
PCC-FA	63.5	2.52	50.0
G	6.4	2.31	3.0

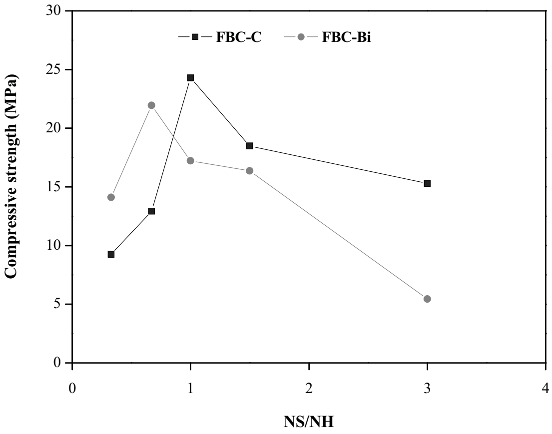

Fig. 1 Compressive strength of FBC-C and FBC-Bi geopolymers based on NS/NH ratios.

Details of mixing and testing

The source materials were the FBC-FA and the blend of 75%wt FBC-FA and 25%wt PCC-FA. Three levels of gypsum additive of 0, 5, and 10% by weight of solid binder content were used. The liquid/ash (L/A) ratio of 1.0 and sand/ash ratio of 2.75 were used for both FBC-C and FBC-Bi mixes. The NS/NH ratios of 1.0 and 0.67 for FBC-C and FBC-Bi geopolymers were selected from the optimum compressive strengths from the trial mixes (Fig. 1). The details proportion details are tabulated in Table 3. SiO_2/Al_2O_3 and Na_2O/Al_2O_3 ratios were calculated from the source materials and alkaline solution in the reaction.

The FBC-FA and PCC-FA were blended thoroughly to obtain a uniform blended source material. Gypsum was added to the source material and mixed in a container. NH solution was added and mixed for 5 min. After that, NS solution was added and

Table 3 Mix proportions and oxide molar ratio of blended FBC-FA and PCC-FA containing G as an additive.

Mixes	FBC-FA: PCC-FA	G (%)	SiO_2/ Al_2O_3	Na_2O/ Al_2O_3
FBC-C100-G0[†]	100:0	0	5.29	1.74
FBC-C100-G5		5	5.38	1.83
FBC-C100-G10		10	5.47	1.93
FBC-C75-G0	75:25	0	5.29	1.83
FBC-C75-G5		5	5.37	1.93
FBC-C75-G10		10	5.46	2.03
FBC-Bi100-G0[†]	100:0	0	6.02	3.22
FBC-Bi100-G5		5	6.14	3.39
FBC-Bi100-G10		10	6.26	3.58
FBC-Bi75-G0	75:25	0	5.64	2.87
FBC-Bi75-G5		5	5.74	3.01
FBC-Bi75-G10		10	5.85	3.18

[†] Control mix.

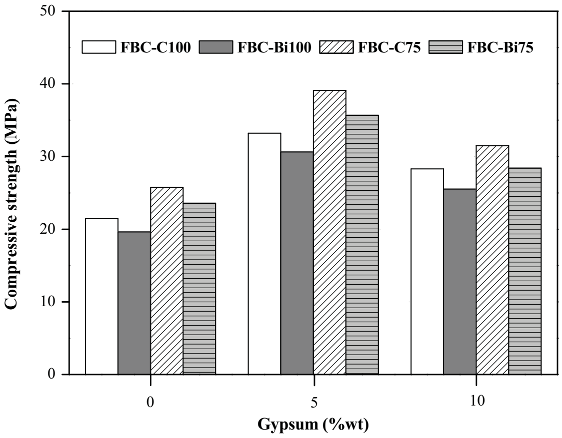

Fig. 2 Compressive strength of FBC-C and FBC-Bi based geopolymer mortars.

mixed for another 5 min. After mixing, the fresh paste was casted in 5 × 5 × 5 cm cubic plastic moulds in accordance with ASTM C109 and compacted in a vibrating table for 10 s. The mould was then wrapped with polyvinyl sheet to prevent a loss of moisture. Samples were cured in an electric oven at 40 °C for 48 h and then kept at 25 °C and 50% R.H. room until testing. The paste samples were used for the XRD, FTIR, MIP, and SEM analyses. For the geopolymer mortar, sand was added at the final stage and mixed again for 5 min. The curing regime was the same as the paste samples. The compressive strength of mortar was tested at the age of 7 days in accordance with ASTM C109.

RESULTS AND DISCUSSION

Compressive strength

The results of compressive strength of mortars are shown in Fig. 2. The strength of FBC-C mortar was slightly higher than that of FBC-Bi mortar. The compressive strengths of FBC-C100-G0 and FBC-Bi100-G0 control mortar mixes were 21.5 and 19.6 MPa, respectively. The FBC-C contained a higher percentage of silica and alumina than those of FBC-Bi (Table 1). Although the reactivity of both FBC-C and FBC-Bi were low, the high silica and alumina of FBC-C was responsible for its slightly better performance than that of FBC-Bi. Blends of FBC-FA and PCC-FA significantly improved the strengths of mortars compared to the control mortars with no PCC-FA. The compressive strengths of blended FBC-C and PCC-FA, and FBC-Bi and PCC-FA mortars increased to 25.8 and 23.4 MPa, respectively. In addition, calcium silicate hydrate (CSH) gel from the reaction between Ca^{2+} from ashes and silicate group could increase the strength of the matrix[10]. The increase in strength in this case was due to the increased reactive amorphous phase of the mixture resulted from the blending of FBC-FA with PCC-FA[11].

The incorporation of 5% G as an additive further improved the compressive strengths of the mortars (Fig. 2). Addition 5% G increases the compressive strengths of FBC-C100-G5 and FBC-Bi100-G5 mortars to 33.2 and 30.6 MPa, respectively. The additions of 10% G also produced geopolymer mortars with high strength but were slightly lower than those with the addition of 5% G. The high amount of G hindered the geopolymer reaction and slightly decreased the strength of the geopolymer mortars[10]. The compressive strengths of FBC-C100-G10 and FBC-Bi100-G10 were 28.3 and 25.5 MPa, respectively.

For the blended fly ash mortars, the addition of G also showed the same trend of results as that of the FBC-FA mortars. The optimum increase in strength was obtained with the addition of 5% G. For the blended FBC-C and PCC-FA, the maximum compressive strength was 39.1 MPa with the addition of 5% G. For the blended FBC-Bi and PCC-FA, the maximum compressive strength was 35.7 MPa also with the addition of 5% G. The increase in the strength is due to the Ca^{2+} ions from G entering the Si−O−Al−O framework and balancing the charge on Al ions[12]. This played an important role to form the CSH and the stronger aluminosilicate structure and contributed to strength improvement. Furthermore, the SO_4^{2-} ions from G attacked the Al ions from ashes[13, 14] and form

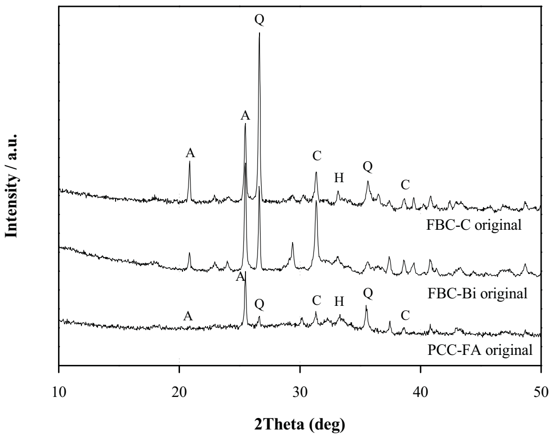

Fig. 3 XRD patterns of FBC-C, FBC-Bi, and PCC-FA originals (A = anhydrite, C = calcium oxide, H = haematite, Q = quartz).

aluminosilicate hydrate and geopolymer framework which help the strength development. However, the increase of G to 10%wt gave lower compressive strength than that of G 5%wt. There was an optimum SO_4^{2-} ions content which produced the highest compressive strength, with higher SO_4^{2-} ions content hindering the process of geopolymerization.

X-ray diffraction

The X-ray diffraction (XRD) patterns of the source materials are shown in Fig. 3. The crystalline phases of quartz (Q: SiO_2), anhydrite (A: $CaSO_4$), calcium oxide (C: CaO), and haematite (H: Fe_2O_3) were found in all FBC-Bi, FBC-C, and PCC-FA. The amount of CaO in FBC-Bi and quartz content were higher than those of FBC-C and PCC-FA. The FBC-C and FBC-Bi clearly showed lower content of amorphous phase than that of PCC-FA evident by a broad hump around 16–38° (2θ). This was due to the low combustion temperature of coal in the FBC system.

The XRD patterns of geopolymer paste are shown in Fig. 4. The XRD patterns of the source materials and those of geopolymer pastes differed in the amount of crystalline and amorphous phases. For the FBC-C and FBC-Bi pastes, the intensities of SiO_2 (Q) and CaO (C) peak decreased, while CSH (X), aluminosilicate (U), Magnesioferrite (F) and amorphous phase increased compared to those of the source materials. The broad humps of aluminosilicate gel around 30° (2θ) of the FBC-C pastes (Fig. 4a) were more pronounce than those of the FBC-Bi pastes (Fig. 4b). This suggested that the geopolymerizations of the FBC-C pastes were more advanced and agreed with the higher compressive strength of the FBC-C pastes compared to those of the FBC-Bi pastes. Moreover, two new compounds, viz., zeolite named vishnevite (V: $Na_8Al_6Si_6O_{24}(SO_4)\cdot 2\,H_2O$) and thenardite (T: $NaSO_4$) were detected.

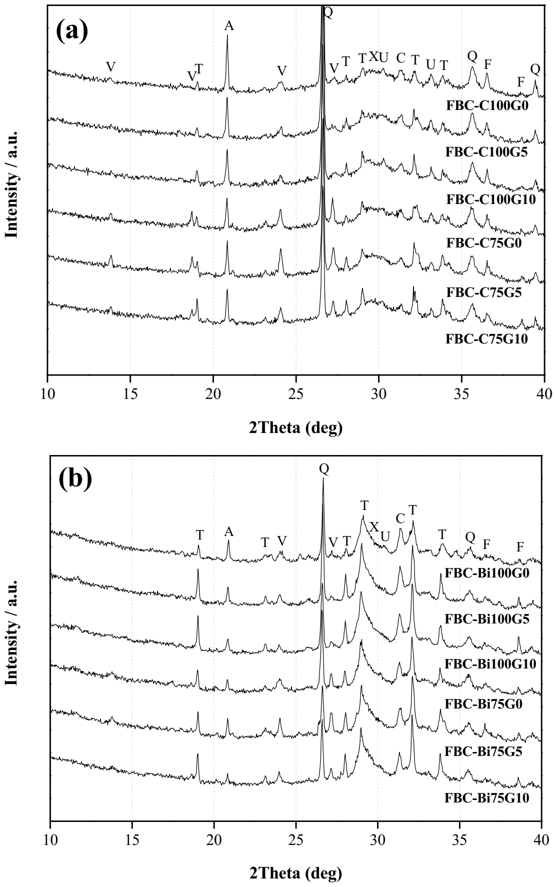

Fig. 4 XRD patterns of geopolymer pastes, (a) FBC-C and (b) FBC-Bi (A = anhydrite, C = calcium oxide, F = magnesioferrite, Q = quartz, T = thenardite, U = aluminosilicate, V = vishnevite, X = calcium silicate hydrate).

The blending of PCC-FA with FBC-C and FBC-Bi resulted in a reduction in the anhydrite content and an increase in the CSH, aluminosilicate, and vishnevite phases. The existence of some crystalline phase improved the strength of geopolymer paste[15]. Adding 5%wt G in FBC-C and FBC-Bi showed similar trend to those of the blending with PCC-FA with additional increases in, aluminosilicate, CSH, vishnevite, and thenardite phases. The addition of 10%wt G resulted in an increase in thenardite phase but decrease in vishnevite phase compared to the addition of

5%wt G. The reduction in the strength of geopolymer with the high amount of G was due to the reduction of vishnevite phase and the increase in the thenardite phase. It was suggested that the high percentage of Na_2SO_4 (T) existed as an impurity in the matrix[16]. Comparing the XRDs of Fig. 4a and Fig. 4b revealed that the phases of aluminosilicate and vishnevite of the mixes in FBC-C series were more pronounced than those of the mixes in FBC-Bi series. This confirmed that the higher strengths of FBC-C series compared to those of FBC-Bi series were probably due to the presence of the aluminosilicate and zeolite phase of vishnevite[17].

IR spectra

The Fourier Transform Infrared Spectroscopy (FTIR) was used to study the reaction of original materials and geopolymer pastes. The chemical bonding of IR spectra and results are shown in Fig. 5. The vibration of CO_3^{2-} at about 1500 cm^{-1} indicated the Na_2CO_3 from carbonation process[18]. The vibrations at 3700–3200 cm^{-1} of O−H stretching and 1700–1600 cm^{-1} of H−O−H bending showed the weak bond of water molecules which were easily adsorbed on the surface or trapped in large cavities between the rings of geopolymer materials. The Si−O−Si and Al−O−Si stretching of geopolymer pastes at the wavenumber of 1200–950 cm^{-1} were more prominent than in original materials. The blending with PCC-FA also showed all the common features of carbonation, O−H stretching and H−O−H bending, and Si−O−Si and Al−O−Si stretching. The noticeable difference was the larger Si−O−Si and Al−O−Si stretching band of the paste made from blending of FBC-FA with PCC-FA compared to that of the FBC-FA pastes. The increase in the Si−O−Si and Al−O−Si stretching band indicated the increase in the geopolymerization[5].

The addition of 5%wt G resulted in the increase of the intensity of Al−O−Si and S=O stretching at the wavenumber around 950–1200 cm^{-1} and vibration of Na_2SO_4 at the wavenumber of 636 cm^{-1}. The increase of G content to 10%wt resulted in the high calcium and SO_4^{2-} content. This provided the high band of Na_2SO_4 at the wavenumber of 636 cm^{-1}. The strength started to decline as Na_2SO_4 did not contribute to the strength of geopolymer.

Porosity

The total porosity of geopolymer pastes were measured by mercury intrusion porosimetry analysis (Fig. 6). For the control mixes, FBC-C100-G0 and FBC-Bi100-G0 contained the total porosity of 20.4% and 21.7%, respectively. The use of the blends of FBC-FA and PCC-FA significantly reduced the total porosity of the pastes compared to the control mixes. The total porosity of blended FBC-C and PCC-FA; and FBC-Bi and PCC-FA decreased to 14.3 and 16.2%, respectively. The spherical shape and smooth surface of PCC-FA particle offered better distribution than that of FBC fly ash which comprised with irregular shape and high porosity particle. Additionally, PCC-FA was more effective in adjusting pores and decreasing the porosity of paste[19].

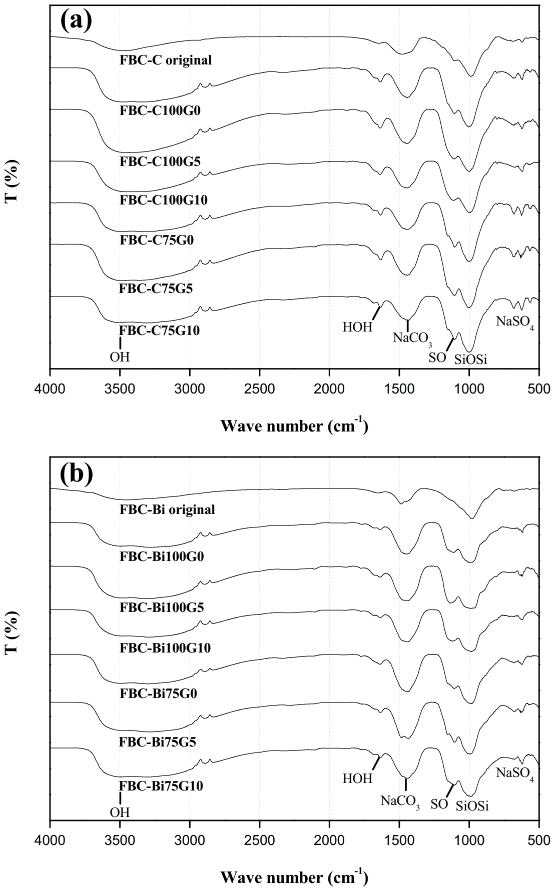

Fig. 5 FTIR spectra of original materials and geopolymer pastes, (a) FBC-C and (b) FBC-Bi.

The addition of G as an additive could reduce the total porosity. For the incorporation of 5% G, the total porosity of FBC-C100-G5 and FBC-Bi100-G5 pastes were decreased to 16.5 and 17.1%, respectively. Although the additions of 10% G reduced the total porosity of geopolymer pastes compared with that of the control 0% G, they were higher than those with the addition of 5% G. This confirmed that the addition of 5% G produced a dense matrix with low porosity and

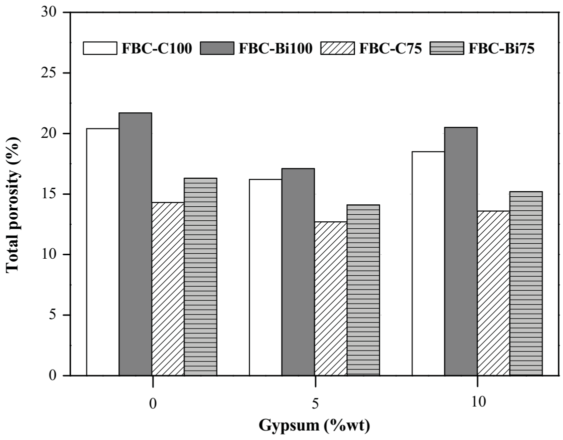

Fig. 6 Total porosity of geopolymer pastes from FBC-C and FBC-Bi.

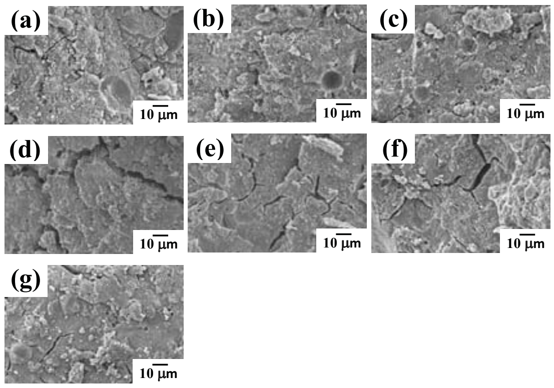

Fig. 7 SEM photography of geopolymer pastes, (a) FBC-C75G0, (b) FBC-C75G5, (c) FBC-C75G10, (d) FBC-Bi100G0, (e) FBC-Bi100G5, (f) FBC-Bi75G0, and (g) FBC-Bi75G5.

the increase in G content to 10% started to hinder the reaction. The total porosity of FBC-C100-G10 and FBC-Bi100-G10 were 18.5 and 20.5%, respectively.

For the blended fly ash pastes, the addition of G also showed a similar trend of results as that of the FBC-FA pastes. The optimum decreased in total porosity occurred with the addition of 5% G. For the blended FBC-C and PCC-FA, the total porosity was 12.7% with the addition of 5% G. For the blended FBC-Bi and PCC-FA, the minimum total porosity was 14.1% also with the addition of 5% G. The Ca^{2+} ions from G were interconnected with Si−O−Al−O chains thus provided the stronger structure and also decreased of the total porosity[20]. The incorporation of 10% G also produced geopolymer pastes with low total porosity but was slightly higher than those with the addition of 5% G. For the blended FBC-C and PCC-FA, the total porosity was 13.6% with the addition of 10% G. For the blended FBC-Bi and PCC-FA, the minimum total porosity was 15.2% with the addition of 5% G.

Scanning electron microscopy

The scanning electron microscopy (SEM) of geopolymer pastes are shown in Fig. 7. The matrix of FBC-C75 with 5% G was denser than that of FBC-C75 with 0 and 10% G as shown in Fig. 7a. This reflected an enhancement of geopolymerization by the addition of 5% G. With regard to the effect of PCC-FA, the results shown in Fig. 7b indicate that the replacement of 25% PCC-FA resulted in homogeneous and dense matrices in comparison to those without PCC-FA (FBC-Bi100) for both 0 and 5% G series. This confirmed that the PCC-FA was more reactive and contained a higher amount of amorphous phase than the FBC-FA[11].

CONCLUSIONS

The FBC-C and FBC-Bi could be used as source materials for the production of geopolymer. The blending with 25%wt PCC-FA improved the geopolymerization and resulted in geopolymer pastes with increased compressive strengths and reduced porosity. The improvement was due to the blending with the more reactive PCC-FA. The addition of G further improved the geopolymerization of the paste and resulted in additional increase in strength and reduction in porosity. The incorporation of 5%wt G was optimum. The increase in Ca^{2+} ions from G formed additional CSH and improved the strength and reduced the total porosity of geopolymer.

Acknowledgements: This work was financial supported by the Thailand Research Fund (TRF) under the TRF Senior Research Scholar, Grant No. RTA5480004 and the Royal Golden Jubilee Ph.D. program, Grant No. PHD/0210/2551 in collaboration with the SCG Paper Public Company Limited, Thailand.

REFERENCES

1. Malhotra VM (2002) Introduction: sustainable development and concrete technology. *ACI Concr Int* **24**, 22.
2. Sinsiri T, Teeramit P, Jaturapitakkul C, Kiattikomol K (2006) Effect of Finenesses of Fly Ash on Expansion of Mortars in Magnesium Sulfate. *Sci Asia* **32**, 63–9.
3. Prasertsan S, Sajjakulnukit B (2006) Biomass and biogas energy in Thailand: potential, opportunity and barriers. *Renew Energ* **31**, 599–610.

4. Jaturapitakkul C, Cheerarot R (2003) Development of bottom ash as pozzolanic material. *J Mater Civ Eng* **15**, 48–53.
5. Chindaprasirt P, Rattanasak U, Jaturapitakkul C (2011) Utilization of fly ash blends from pulverized coal and fluidized bed combustions in geopolymeric materials. *Cement Concr Compos* **33**, 55–60.
6. Davidovits J (1994) Properties of geopolymer cements. In: Krivenko PV (ed) *Proceedings of the 1st International Conference on Alkaline Cements and Concretes*, Ukraine, pp 131–49.
7. Duxson P, Provis JL, Grant C, Van Deventer JSJ (2007) The role of inorganic polymer technology in the development of 'green concrete'. *Cement Concr Res* **37**, 1590–7.
8. Chindaprasirt P, Chareerat T, Sirivivatnanon V (2007) Workability and strength of coarse high calcium fly ash geopolymer. *Cement Concr Compos* **29**, 224–9.
9. Chindaprasirt P, Jaturapitakkul C, Chalee W, Rattanasak U (2009) Comparative study on the characteristics of fly ash and bottom ash geopolymers. *Waste Manag* **29**, 539–43.
10. Rattanasak U, Pankhet K, Chindaprasirt P (2011) Effect of chemical admixtures on properties of high-calcium fly ash geopolymer. *Int J Miner Metall Mater* **18**, 364–9.
11. Chindaprasirt P, Rattanasak U (2010) Utilization of blended fluidized bed combustion (FBC) ash and pulverized coal combustion (PCC) fly ash in geopolymer. *Waste Manag* **30**, 667–72.
12. Fernández-Jiménez A, Palomo A, Sobrados I, Sanz J (2006) The role played by the reactive alumina content in the alkaline activation of fly ashes. *Micropor Mesopor Mat* **91**, 111–9.
13. Ma W, Liu C, Brown PW, Komarneni S (1995) Pore structures of fly ashes activated by $Ca(OH)_2$ and $CaSO_4 \cdot 2\,H_2O$. *Cement Concr Res* **25**, 417–25.
14. Pimraksa K, Chindaprasirt P (2009) Lightweight bricks made of diatomaceous earth, lime and gypsum. *Ceram Int* **35**, 471–8.
15. Rattanasak U, Chindaprasirt P (2009) Influence of NaOH solution on the synthesis of fly ash geopolymer. *Miner Eng* **22**, 1073–8.
16. Luke K (2007) The effect of natural zeolites on the composition of cement pore fluids at early ages. In: *Proceedings of 12th International Congress on the Chemistry of Cement*, Halliburton, USA.
17. Höller H, Wrisching U (1985) Zeolites formation from fly ash. *Fortschr Mineral* **63**, 21–43.
18. Barbosa VFF, MacKenzie KJD, Thaumaturgo C (2000) Synthesis and characterization of materials based on inorganic polymers of alumina and silica: sodium polysialate polymer. *Int J Inorg Mater* **2**, 309–17.
19. Sinsiri T, Chindaprasirt P, Jaturapitakkul C (2010) Influence of fly ash fineness and shape on the porosity and permeability of blended cement pastes. *Int J Miner Metall Mater* **17**, 683–90.
20. Škvára F, Kopecký L, Šmilauer V, Bittnar Z (2009) Material and structural characterization of alkali activated low-calcium brown coal fly ash. *J Hazard Mater* **168**, 711–20.

International Journal of Minerals*, *Metallurgy and Materials
Volume 19*, *Number 9*, *Sep 2012*, *Page 872
DOI: 10.1007/s12613-012-0641-z

Thermal treatment and utilization of Al-rich waste in high calcium fly ash geopolymeric materials

Prinya Chindaprasirt[1], *Ubolluk Rattanasak*[2], *Pimdao Vongvoradit*[2], *and Supichart Jenjirapanya*[3]

1) Sustainable Infrastructure Research and Development Center, Department of Civil Engineering, Faculty of Engineering, Khon Kaen University, Khon Kaen 40002, Thailand
2) Department of Chemistry, Faculty of Sciences, Burapha University, Chonburi 20131, Thailand
3) Applied Science Department, Faculty of Sciences, Chandrakasem Rajabhat University, Bangkok 10900, Thailand

(Received: 30 August 2011; revised: 18 October 2011; accepted: 8 December 2011)

Abstract: The Al-rich waste with aluminium and hydrocarbon as the major contaminant is generated at the wastewater treatment unit of a polymer processing plant. In this research, the heat treatment of this Al-rich waste and its use to adjust the silica/alumina ratio of the high calcium fly ash geopolymer were studied. To recycle the raw Al-rich waste, the waste was dried at 110°C and calcined at 400 to 1000°C. Mineralogical analyses were conducted using X-ray diffraction (XRD) to study the phase change. The increase in calcination temperature to 600, 800, and 1000°C resulted in the phase transformation. The more active alumina phase of active θ-Al_2O_3 was obtained with the increase in calcination temperature. The calcined Al-rich waste was then used as an additive to the fly ash geopolymer by mixing with high calcium fly ash, water glass, 10 M sodium hydroxide (NaOH), and sand. Test results indicated that the calcined Al-rich waste could be used as an aluminium source to adjust the silica/alumina ratio and the strength of geopolymeric materials. The fly ash geopolymer mortar with 2.5wt% of the Al-rich waste calcined at 1000°C possessed the 7-d compressive strength of 34.2 MPa.

Keywords: waste utilization; calcination; geopolymers; fly ash

[*This work was financially supported by the Higher Education Research Promotion and National Research University Project of Thailand, Office of the Higher Education Commission, through the Advanced Functional Materials Cluster of Khon Kaen University and the Thailand Research Fund (TRF) under TRF Senior Research Scholar contract No.RTA5480004.*]

1. Introduction

The Al-rich waste is generated at the wastewater treatment unit of a polymer processing plant. In this process, aluminium chloride ($AlCl_3$) is used as a catalyst for the polymerization of hydrocarbon resin [1]. Neutralization with sodium hydroxide (NaOH) solution is performed on the polymer product. The resulting sewage contains aluminium hydroxide ($Al(OH)_3$) gel and is discharged into the wastewater treatment unit. The sewage is then treated with sulphuric acid (H_2SO_4) solution in order to adjust the pH value and to coagulate the Al-rich waste. The solid waste is finally separated from the wastewater and disposed off in landfill. The leaching of aluminium ions and other contaminants into groundwater is the main concern. The flowchart of the waste generation and treatment process is shown in Fig. 1.

The aluminium waste contains many forms of aluminium compounds. $Al(OH)_3$ is the major compound, and aluminium and sodium sulphate are the minor ones. The high annual output of Al-rich sludge leads to the problems of waste management and increases the treatment costs. A number of researches [2-4] have been conducted to utilize this Al-rich industrial sludge as a filler in cement and ceramic products. Due to the high water content up to 85wt% and the impurity of this sludge, treatment is needed to improve its properties before it can be effectively used. After the filter pressing

Corresponding author: Ubolluk Rattanasak E-mail: ubolluk@buu.ac.th

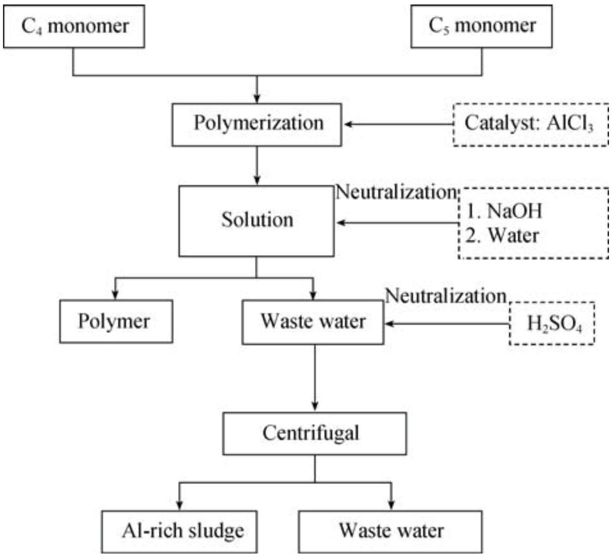

Fig. 1. Flow diagram of waste generation.

process, this sludge is basically the colloidal aluminium hydroxides with some soluble salts such as aluminium sulphate [2].

The high water content and the gel-like consistency of the sludge make it difficult to form the homogeneous mixture with other raw materials. This is the main reason for an increase in the drying shrinkage of ceramic bodies obtained from this sludge [3]. The pre-drying of Al-rich sludge at 100°C gives a strong agglomerated structure and also makes it difficult to obtain the proper mixing with other materials. Due to its high alumina content, calcination provides the opportunity for the application of this waste in the alumina-based materials such as mullite or mullite-alumina products.

In Thailand, the transportation cost for disposal is rather high at US$ 25-30/t and keeps rising. The amount of this waste increases every year and thus prompts the industry to find ways to utilize it. Therefore, this work aims to reuse the Al-rich waste by improving its properties with calcination. The calcined product should then be ready as an aluminium source material to produce the aluminosilicate binder or the geopolymeric material using low temperature curing [5-7]. Geopolymeric material is the aluminosilicate compound prepared at 40-90°C [6-7]. This material possesses high early compressive strength compared to the normal concrete at the same curing age.

Fly ash is widely used as an aluminosilicate source material for making geopolymer. It has been shown that high calcium fly ash is a suitable source material for making geopolymer [7-8]. The properties of the fly ash geopolymer can be further adjusted with the addition of chemical additives and mineral compounds such as rice husk ash [9-10]. In many instances, the source material contains low aluminium content, and the strength and other properties of the geopolymeric materials are impaired [11]. The utilization of the Al waste as an additional source material to increase the aluminium content of the geopolymer was therefore proposed.

2. Materials and methods

2.1. Materials

The Al-rich waste was obtained from a local polymer plant in Thailand. This waste contained high water content (ca. 80wt%); therefore, it was oven dried at 110±5°C for 24 h and the whitish yellow solid was obtained. The dry sample was then ground for 1 h using Rapid Mill 1105 (Compound Clay Ltd., Thailand) at 500 r/min. The median particle size of 15 μm measured by the particle size analyzer (Malvern Mastersizer S) was obtained. Grinding apparently reduced the grain size and promoted an amorphization, resulting in the enhancement of reactivity and structural changes of materials [12-13]. The chemical composition of this waste is presented in Table 1. The loss on ignition (LOI) was determined according to ASTM D7348. Differential scanning calorimetry (DSC) analysis was performed on the ground sample and on the commercial $Al(OH)_3$ sample using Pyris Diamond DSC (Perkin-Elmer) at a heating rate of 10°C/min, nitrogen purging at 20.0 mL/min, and the operation range from 50 to 400°C.

For the preparation of geopolymeric materials, the high calcium fly ash from the pulverized coal combustion process (PCC), sodium silicate solution (9wt% Na_2O, 30wt% SiO_2,

Table 1. Chemical composition of as-received Al-rich waste and fly ash **wt%**

Composition	Al-rich waste	Fly ash
$Al(OH)_3$	82.5	—
Na_2SO_4	4.7	—
NaCl	4.6	—
SiO_2	—	39.4
Al_2O_3	—	21.6
CaO	—	12.0
Fe_3O_4	—	11.4
SO_3	—	2.8
MgO	—	10.9
K_2O	—	2.1
LOI	8.2	0.8

and 61wt% H_2O), 10 M NaOH, and graded river sand with the fineness modulus of 2.8 were used [8].

2.2. Calcination of the ground sample

Since the Al-rich waste could not be used directly because of the high organic contents as indicated by the high LOI of 8.2%, the calcination was therefore employed. The LOI indicated the amount of organic compounds decomposed at 400-500°C since this waste was from a polymer plant. The ground samples were subjected to the thermal treatment at 400, 600, 800, and 1000°C for 1 h. The preliminary test indicated that 1-h calcination was sufficient. Although the cost of preparing this waste could be slightly higher than the normally used raw material, the method provides a new recycling opportunity for this kind of sludge. Mineralogical analysis was conducted using X-ray diffraction (XRD, PANalytical/Expert). Functional characterization of the calcined wastes was also performed by Fourier transform-infrared spectroscopy (FT-IR, Perkin-Elmer System 2000).

2.3. Preparation of geopolymeric materials

The Al-fly ash geopolymeric material was prepared by mixing the aluminosilicate source materials with sodium silicate solution (water glass), 10 M NaOH, and sand. The source materials were the blend of the calcined wastes (at 800 and 1000°C) and fly ash. The fly ash was replaced with 2.5wt% and 5.0wt% of the calcined wastes. The liquid was the mixture of water glass and 10 M NaOH with the mass ratio of 2:1. Powdery blend was then mixed with the liquid at the mass ratio of 60:40. Sand was used as a filler with a sand-to-powdery blend ratio of 2.0 [7-8]. The original pre-dried waste was also used to prepare the geopolymeric materials for comparison. Mix proportions are tabulated in Table 2.

Table 2. Mix proportion of geopolymeric materials g

Sample	Fly ash	Al waste	Water glass	10 M NaOH	Sand	Remark
Control	60	—	27	13	120	Control sample
2.5Al (PD)	58.5	1.5	27	13	120	Pre-dried waste
5Al (PD)	57	3	27	13	120	
2.5Al (800)	58.5	1.5	27	13	120	Calcined waste (800°C)
5Al (800)	57	3	27	13	120	
2.5Al (1000)	58.5	1.5	27	13	120	Calcined waste (1000°C)
5Al (1000)	57	3	27	13	120	

The pastes were cast into 5 cm cube acrylic plastic molds and cured at 60°C for 24 h to activate the reaction [7-8]. Specimens were then demolded and left in the controlled room of 23±2°C and with the relative humidity (RH) of 50%. The compressive strengths of specimens were measured at the age of 7 d using the compression testing machine (CB-10M, CBN Co.). The specimen was placed between the two steel plates and compressed at a uniform loading rate in accordance with the ASTM C109. Compressive strength was calculated by dividing the maximum load by the cross-sectional area of the specimen. The reported results are the averages of three samples.

The microstructural study of the hardened pastes was performed using scanning electron microscopy (SEM, Leo 1455VP SEM, Zeiss). Nonconductive specimens were coated with gold before the examination with the microscope.

3. Results and discussion

3.1. Characterization of pre-dried waste

DSC was used to study the thermal transition of the commercial pure $Al(OH)_3$ and the ground pre-dried waste. This technique observes the exothermic and endothermic events such as glass transition temperature (T_g), crystallization temperature (T_c), and melting temperature (T_m). The temperature range of the investigation was from 50 to 400°C. The results of the DSC-thermogravimetric (TG) analysis (endothermic up) are presented in Fig. 2. The commercial $Al(OH)_3$ exhibits T_c of 240°C. At this temperature, the crystalline arrangement occurred as indicated by the drop in the heat flow. The material gave off heat when it crystallized in the exothermic transition. Endothermic transition (T_g) was also found at 345°C as heat was absorbed for phase transformation and the broad peak appeared. For the ground pre-dried waste, only the crystallization peak T_c was found at 165°C. These endothermic peaks indicated the transition of gibbsite ($Al(OH)_3$) to boehmite ($AlO{\cdot}OH$) at ~250°C and the transition of boehmite to γ-alumina (γ-Al_2O_3) at ~350°C [14-15]. The change in location of T_c was due to contaminants in the waste. The contaminants were the unreacted hydrocarbons, polymer residue, and sodium sulphate from the polymerization and neutralization processes. These impurities of

Al-rich sludge hindered the homogeneous formation; therefore, the removal was needed to increase its efficiency. Calcination was consequently applied to this waste.

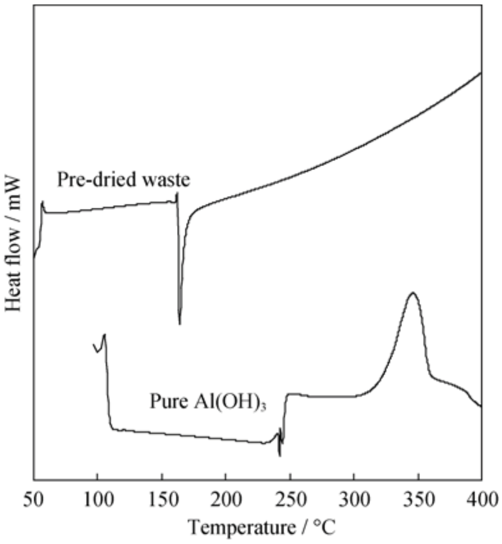

Fig. 2. DSC-TG curves of commercial pure $Al(OH)_3$ and pre-dried waste.

3.2. Characterization of the calcined waste

3.2.1. XRD analysis

The XRD results of the waste after calcination are shown in Fig. 3. The calcination duration and the temperature are significant factors for the phase change and removal of impurities. The calcination resulted in the amorphous phase with some crystalline phases [16]. The compounds detected in the pre-dried sample were gibbsite ($Al(OH)_3$), sodium sulphate ($NaSO_4$), and sodium chloride (NaCl) as shown in Table 1. At the calcination temperature of 400°C, γ-Al_2O_3 was formed. For the calcination temperatures of 600, 800, and 1000°C, two distinct peaks at 37° and 46° indicated the incipient phase of active θ-Al_2O_3. The glassy phase was increased due to the increase in calcination temperature as indicated by the appearance of broad peaks. The θ-Al_2O_3 was formed in large quantity with some impurities of NaCl and Na_2SO_4 at 600 and 800°C. The decomposition temperatures of NaCl and Na_2SO_4 were 780 and 880°C, respectively. At 1000°C, NaCl disappeared and the sample contained a higher amount of the amorphous phase. The calcination of gibbsite produced a series of transitions of alumina as shown in the following equation [14, 17]:

$$\text{Gibbsite} \xrightarrow{200^\circ\text{C}} \gamma\text{-boehmite} \xrightarrow{400^\circ\text{C}}$$

$$\gamma\text{-}Al_2O_3 \xrightarrow{750^\circ\text{C}} \delta \xrightarrow{900^\circ\text{C}} \theta \xrightarrow{1200^\circ\text{C}} \alpha\text{-}Al_2O_3.$$

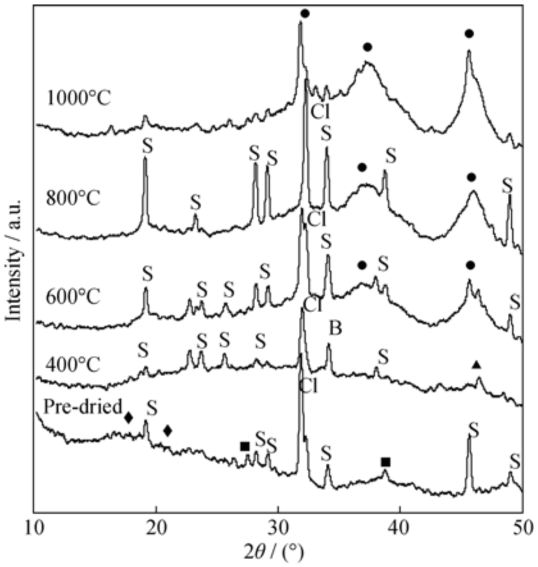

Fig. 3. XRD patterns of the Al-rich waste. Cl—NaCl; S—Na_2SO_4; ♦—gibbsite; ■—boehmite; ▲—γ-Al_2O_3; ●—θ-Al_2O_3.

All transition phases are stable at room temperature. It has been pointed out that the transformation temperatures are somewhat variable depending on the impurities of the starting materials [3, 17]. Practically, various substances can be produced with mixed crystalline forms of $Al(OH)_3$, $AlO{\cdot}OH$, and aluminium oxide (Al_2O_3) with water molecules. These are known as hydrated alumina. Calcination of the hydrated hydroxide resulted in the loss of water and produces various kinds of active alumina. They differ in porosity, number of remaining –OH groups, and particle size. They can be used as catalyst supports and in chromatography.

3.2.2. IR spectra

Fig. 4 shows the FT-IR spectra of the pre-dried and the calcined samples at 800 and 1000°C. Spectrum characterization of the products is based on the analysis of the absorption bands, which are due to the vibrations of –OH groups in the ranges of 800 to 1300 cm^{-1} (bending vibrations) and 3000 to 3800 cm^{-1} (stretching vibrations). Despite the significant similarity of the structures, the arrangements of the layers in some hydroxides were different in the O–H···O–H distances (predetermining the length of the hydrogen bond), which led to a change in the arrangement of the IR bands [18]. The vibration stretching of S=O of the sulfonate group of Na_2SO_4 was located at ~1100 cm^{-1}. The absorption peaks in the region of 700 to 400 cm^{-1} corresponded to the existence of $Al(OH)_3$ and Al_2O_3. The IR spectra of the calcined samples were slightly different from that of the pre-dried sample. In the region of 1000 to 400 cm^{-1}, the calcined samples showed a noticeable change with peak shift compared to that of the pre-dried sample and a broader peak at 1000 to 800 cm^{-1} resulting from the phase transformation of gibbsite to active θ-Al_2O_3. At high calcination temperature, $Al(OH)_3$ dehydrated to Al_2O_3, resulting in the absorption band shift. The change of the crystal structure could also be responsible for the differences. In addition, the band of gibbsite could partially overlap with that of boehmite at 1070 cm^{-1} as in the pre-dried sample. From the results of XRD and IR spectra, the waste samples with the calcination temperatures of 800 and 1000°C were selected to blend with fly ash for making the geopolymeric materials.

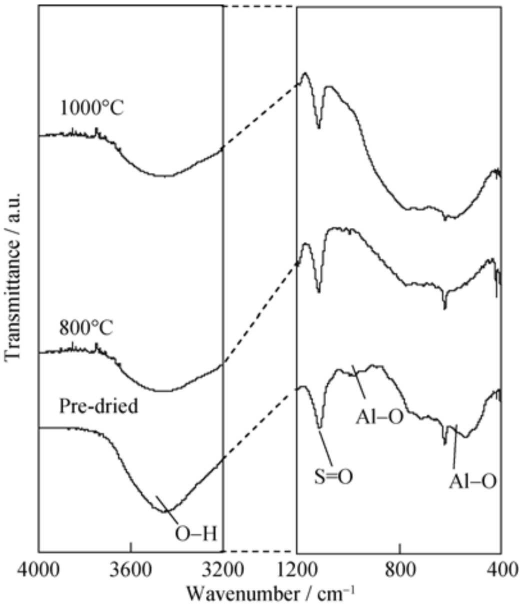

Fig. 4. IR spectra of the pre-dried and calcined samples.

3.2.3. Compressive strength

The pre-dried sample and calcined samples (if applicable) were mixed with fly ash, water glass, 10 M NaOH, and sand to form geopolymeric materials. The compressive strengths of the specimens are presented in Fig. 5. The control geopolymeric specimen had the compressive strength of 27.6 MPa. Blending of the fly ash with the pre-dried waste gave slightly lower strengths of 27.4 and 24.8 MPa for 2.5wt% and 5.0wt% replacements, respectively. The pre-died waste contained impurities and the low strength geopolymers were thus obtained. The low replacement level of 2.5wt% pre-dried waste resulted in a small decrease in strength. However, at the 5wt% replacement level, the strength was significantly reduced. In contrast, the calcined waste at 800 and 1000°C gave higher strengths than that of the control. For the calcined waste at 800°C, the 7-d compressive strengths of the mixes with 2.5wt% and 5wt% replacements were 31.2 and 29.9 MPa, respectively. At a high calcination temperature of 1000°C, the compressive strengths of the 2.5wt% and 5wt% replacements were significantly increased to 34.2 and 31.6 MPa, respectively. The higher strength was obtained as a result of the increase in amorphous phase of the calcined waste at high temperature. The amorphous phase was relatively active and enhanced a chemical bonding between the Al-compound and sodium silicate. The Al dissolved in sodium silicate solution and replaced the four-coordinate Si in the silicate network leading to a strong chemical bonding [13, 19]. The presence of gibbsite ($Al(OH)_3$) increased the strength of geopolymer compared with that containing both boehmite and gibbsite. The gibbsite readily dissolves at moderate hydroxide concentrations and temperatures. The dissolution of θ-Al_2O_3 and other Al forms, however, requires more rigorous conditions and generally is kinetically slow [20]. As a result, NaOH in the mixture helped the dissolution of gibbsite, resulting in the strength enhancement of geopolymeric materials. In addition, calcination removed impurities and promoted the phase transformation.

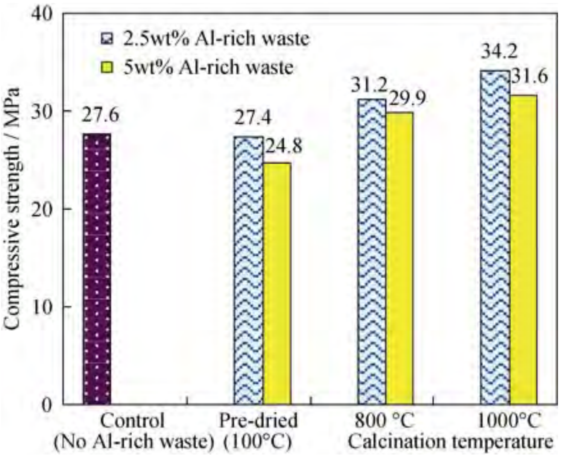

Fig. 5. Compressive strength of Al-fly ash geopolymeric materials at the 7-d curing.

However, the increase in Al content could adversely affect the strength. The surplus aluminium acted as the filler because of the insufficient amount of Si for geopolymerization reaction. However, for the source material with high silica content such as rice husk ash, the high Al dosage is beneficial for the strength development of the geopolymer [21]. The mechanical strength of the material is known to be enhanced by a high initial silica-to-alumina (SiO_2/Al_2O_3) ratio, which increases the number of strong Si–O–Si bonds in the final product [22]. The Al_2O_3 content in the system also plays an important role in the controlling process kinetics

[23-24]. The SiO_2/Al_2O_3 ratios of the specimens are shown in Table 3.

Table 3. SiO_2-to-Al_2O_3 ratio in geopolymer mixtures

Geopolymer sample	SiO_2-to-Al_2O_3 molar ratio
Control	4.32
2.5wt% Al-rich waste	3.88
5wt% Al-rich waste	3.51

It was reported that the optimum SiO_2/Al_2O_3 ratio was between 3.5 and 4.0 for good strength geopolymer. The use of low SiO_2/Al_2O_3 ratio resulted in an Al-rich aluminosilicate gel and a low strength geopolymer. The mechanical strength rose during the transformation of the Al-rich into a Si-rich aluminosilicate gel [23]. In addition, some calcium silicate hydrate (C–S–H) was also formed and coexisted with the class C fly ash geopolymeric products [24]. The formation of C–S–H contributed partly to the strength development and resulted in less silica available for the geopolymerization reaction. The aluminosilicate phase with a low Si/Al ratio was therefore obtained [25]. A decrease in Si/Al ratio could lead to the aluminosilicate compound of lower strength accompanied by the increase in crystalline phase [26]. Therefore, the increase in the fly ash replacement level of the Al-rich waste from 2.5wt% to 5wt% resulted in the geopolymer with a lower strength.

3.2.4. Microstructural study

The microstructures of Al-fly ash geopolymer pastes prepared by the pre-dried and the calcined samples (1000°C) with 2.5wt% replacement were investigated using SEM. Fig. 6 shows the geopolymer gel formation on the fly ash particles. The hardened gel prepared using the non-calcined Al-rich waste was not homogenous and agglomerations of the gel were easily detected. Partially reacted fly ash particles were easily detected as a result of the low reactivity of the waste. For the calcined Al-rich waste, the formation of the gel fully covered the fly ash particles resulting in the more homogenous matrix compared with the pre-dried Al waste sample due primarily to the increased reaction of active alumina (θ-Al_2O_3). The gel bound the fly ash particles and formed a dense geopolymer matrix, resulting in an increase in compressive strength. Therefore, calcination enhanced the reactivity of Al-rich waste, making it suitable for use as an alternative aluminium source material.

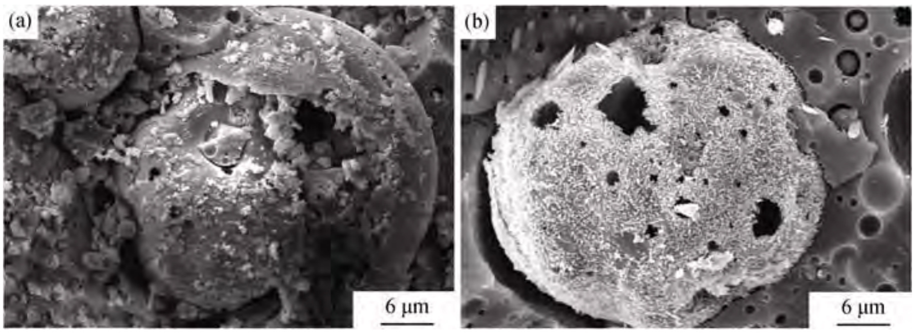

Fig. 6. SEM images of Al-fly ash geopolymer: (a) 2.5Al (PD) sample; (b) 2.5Al (1000) sample.

4. Conclusions

The improvement of the Al-rich waste from a polymer plant can be made by grinding and calcination. The calcination transformed the inactive boehmite to active alumina (θ-Al_2O_3). According to the XRD pattern, the calcination temperature of the waste needs to be higher than 800°C to obtain the phase transformation. The ground calcined waste with a median particle size of 15.0 μm can be used as an additional source material for adjusting the silica-to-alumina ratio of the fly ash geopolymeric materials. A reasonable compressive strength of 34.2 MPa was obtained at the age of 7 d for fly ash geopolymer mortar with 2.5wt% replacement of the Al-rich waste (calcined at 1000°C) compared with the strength of 27.6 MPa of the control.

References

[1] G.T. Austin, *Shreve's Chemical Process Industries*, 5th Ed., McGraw-Hill, Singapore, 1985, p.658.

[2] D.A. Pereira, Barroso de Aguiar, F. Castro, M.F. Almeida, and J.A. Labrincha, Mechanical behavior of Portland cement mortars with incorporation of Al-containing salt slags, *Cem. Concr. Res.*, 30(2000), p.1131.

[3] M.J. Ribeiro, D.U. Tulyaganov, J.M. Ferreira, and J.A. Labrinacha, Recycling of Al-rich industrial sludge in refractory ceramic pressed bodies, *Ceram. Int.*, 28(2002), No.3, p.319.

[4] M.J. Ribeiro, D.U. Tulyaganov, J.M. Ferreira, and J.A. Labrinacha, High temperature mullite dissolution in ceramic bodes derived from Al-rich sludge, *J. Eur. Ceram. Soc.*, 25(2005), No.5, p.703.

[5] J. Davidovit, Geopolymer: Inorganic polymeric new materi-

als, *J. Therm. Anal.*, 37(1991), No. 8, p.1633.

[6] J.G.S. Van Jaarsveld and J.S.J. Van Deventer, Effect of the alkali metal activator on the properties of fly ash-based geopolymers, *Ind. Eng. Chem. Res.*, 88(1999), No.10, p.3932.

[7] P. Chindaprasirt, C. Jaturapitakkul, W. Chalee, and U. Rattanasak, Comparative study on the characteristics of fly ash and bottom ash geopolymers, *Waste Manage.*, 29(2009), No.2, p.539.

[8] U. Rattanasak and P. Chindaprasirt, Influence of NaOH solution on the synthesis of fly ash geopolymer, *Miner. Eng.*, 22(2009), No.12, p.1073.

[9] S. Detphan and P. Chindaprasirt, Preparation of fly ash and rice husk ash geopolymer, *Int. J. Miner. Metall. Mater.*, 16(2009), No.6, p.720.

[10] U. Rattanasak, K. Pankhet, and P. Chindaprasirt, Effect of chemical admixtures on properties of high-calcium fly ash geopolymer, *Int. J. Miner. Metall. Mater.*, 18(2011), No.3, p.364.

[11] S. Songpiriyakij, T. Kubprasit, C. Jaturapitakkul, and P. Chindaprasirt, Compressive strength and degree of reaction of biomass- and fly ash-based geopolymer, *Constr. Build. Mater.*, 24(2010), No.3, p.236.

[12] J. Kano, S. Saeki, F. Saito, M. Tanjo, and S. Yamazaki, Application of dry grinding to reduction in transformation temperature of aluminum hydroxides, *Int. J. Miner. Process.*, 60(2000), No.2, p.91.

[13] T. Shiono, S. Okumura, H. Shiomi, T. Nishida, M. Kitamura, and M. Kamitani, Preparation of inorganic consolidated body using aluminium hydroxide mechanically activated by dry milling, *J. Mater. Synth. Process.*, 8(2000), No.5-6, p.351.

[14] A.R. Farinha, J.B. Ribeiro, R. Mendes, and M.T. Vieira, Shock activation of α-alumina from calcinated Al-rich sludge, *Ceram. Int.*, 35(2009), No.5, p.1897.

[15] B.Q. Zhu, B.X. Fang, and X.C. Li, Dehydration reactions ad kinetic parameters of gibbsite, *Ceram. Int.*, 36(2010), No.8, p.2493.

[16] V.P. Della, I. Kühn, and D. Hotza, Rice husk ash as an alternate source for active silica production, *Mater. Lett.*, 57(2002), No.4, p.818.

[17] A. Tonejc, M. Stubiċar, A. Tonejc, C. Kosanović, B. Subotić, and I. Šmit, Transformation of γ-AlOOH (boehmite), and $Al(OH)_3$ (gibbsite) to α-Al_2O_3 (corundum) induced by high energy ball milling, *J. Mater. Sci. Lett.*, 13(1994), No.7, p.519.

[18] E. Wolska and W. Szajda, Use of infrared spectroscopy to identify crystalline aluminum hydroxides of the $Al(OH)_3$-$Fe(OH)_3$ system, *J. Appl. Spectrosc.*, 38(1983), No.1, p.137.

[19] M. Mora, D. Gutiérrez-Campos, C. Lavelle, and R.M. Rodríguez, Evaluation of Bayer process gibbsite reactivity in magnesium aluminate spinel formation, *Mater. Sci. Eng. A*, 454-455(2007), No.1, p.139.

[20] X. Gong, Z. Nie, M. Qian, J. Liu, L.A. Pederson, D.T. Hobbs, and N.G. McDuffie, *Gibbsite to Boehmite Transformation in Strongly Caustic and Nitrate Environments*, Report No. WSRC-MS-2002-00850 submitted to the U.S. Department of Energy, 2002.

[21] U. Rattanasak, P. Chindaprasirt, and P. Suwanvitaya, Development of high volume rice husk ash alumino silicate composites, *Int. J. Miner. Metall. Mater.*, 17(2010), No.5, p.654.

[22] G. Kovalchuk, A. Fernández-Jiménez, and A. Palomo, Alkali-activated fly ash: Effect of thermal curing conditions on mechanical and microstructural development: Part II. *Fuel*, 86(2007), No.3, p.315.

[23] A. Fernández-Jiménez, A. Palomo, I. Sobrados, and J. Sanz, The role played by the reactive alumina content in the alkaline activation of fly ashes, *Microporous Mesoporous Mater.*, 91(2006), No.1-3, p.111.

[24] X.L. Guo, H.S. Shi, and A.D. Warren, Compressive strength and microstructural characteristics of class C fly ash geopolymer, *Cem. Concr. Compos.*, 32(2010), No. 2, p.142.

[25] K. Somna, C. Jaturapitakkul, P. Kajitvichyanukul, and P. Chindaprasirt, NaOH-activated ground fly ash geopolymer cured at ambient temperature, *Fuel*, 90(2011), No.6, p.2118.

[26] P. De Silva, K. Sagoe-Crenstil, and V. Sirivivatnanon, Kinetics of geopolymerization: Role of Al_2O_3 and SiO_2, *Cem. Concr. Res.*, 37(2007), No.4, p.512.

Computers and Concrete, Vol. 10, No. 4 (2012) 331-342

Permeability and abrasion resistance of concretes containing high volume fine fly ash and palm oil fuel ash

S. Homwuttiwong[1], C. Jaturapitakkul[2] and P. Chindaprasirt*[3]

[1] *Department of Civil Engineering, Faculty of Engineering, Mahasarakham University, Mahasarakham 44150, Thailand*
[2] *Department of Civil Engineering, Faculty of Engineering, King Mongkut's University of Technology Thonburi (KMUTT), Bangkok 10140, Thailand*
[3] *Sustainable Infrastructure Research and Development Center, Department of Civil Engineering, Faculty of Engineering, Khon Kaen University, Khon Kaen 40002, Thailand*

(Received June 22, 2011, Revised February 5, 2012, Accepted April 17, 2012)

Abstract. In this paper, compressive strength, water permeability and abrasion resistance of concretes containing high volume fine fly ash (FFA) and fine ground palm oil fuel ash (GPA) were studied. Portland cement type I was replaced with FFA and GPA at dosages up to 70% by weight of binder. Ground river sand (GRS) was also used to replace Portland cement in order to indicate the level of filler effect. Results indicated that FFA was slightly more reactive than GPA. The replacement of 40-70% of FFA produced concretes with compressive strength, permeability and abrasion resistance comparable to those of normal concretes. The incorporation of GPA slightly reduced the performances of concretes as compared to those of FFA concretes. The reduction of Portland cement was partly compensated by the increase in pozzolanic activity of the fine fly ash and palm oil fuel ash and thus enabled the large replacement levels.

Keywords: concrete; water permeability; abrasion resistance; fly ash; palm oil fuel ash.

1. Introduction

Strength, water permeability and abrasion resistance of concrete are recognized as important properties of concrete. They indicate the quality of concrete, its durability and service life. The most critical parameters controlling durability of concrete are governed by the transportation of liquid or fluid in concrete. Therefore, durability of concrete can be monitored as a function of water permeability. The deterioration of concrete during its service life arises primarily from its high permeability (Naik *et al*. 1996, Basheer *et al*. 2001, Khan 2003). It has been shown that incorporation of pozzolans with suitable dosage level can improve the permeability of concrete (Vedalakshmi 2003).

Abrasion resistance also indicates the durability, especially for concretes which require strong surface such as hydraulic structure, traffic pavement and parking lots. The abrasion is caused by the rolling or grinding of any element against the concrete surface. This phenomenon induces damage to concrete and can jeopardize the whole structure integrity. Abrasion resistance of concrete is

---

* Corresponding author, Professor, E-mail: prinya@kku.ac.th

influenced by various factors, such as mixture proportion, aggregate property and supplementary cementitious materials. Researches indicated that the abrasion resistance depended primarily on the strength of concrete (Siddique 2003, Li *et al.* 2006).

Fly ash, a well-known pozzolan, has been extensively used in concrete work. Its use increases the durability of concrete through pore refinement and reduction in calcium hydroxide of cement paste matrix (Chindaprasirt *et al.* 2007, Malhotra 2002). Properties of concrete are affected by both quality and quantity of fly ash. It is generally agreed that fine fly ash is more reactive and thus improves the properties of mortar and concrete than as-received coarse fly ash (Chindaprasirt *et al.* 2004, Chindaprasirt *et al.* 2010a, Erdogdu and Turker 1998, Sata *et al.* 2011).

Palm oil fuel ash has been recently introduced as a new pozzolanic material. It has to be properly ground to obtain satisfactory reactivity (Tangchirapat *et al.* 2009). Properties of concrete such as compressive strength, chloride penetration resistance and alkali-silica reaction can be improved when incorporated with palm oil fuel ash (Awal and Hussin 1997, Chindaprasirt *et al.* 2010b, Rukzon and Chindaprasirt 2009a, 2009b, Tay 1990). However, palm oil fuel ash is not yet being used commercially in concrete industry and almost all of it is discarded in landfills.

Because the global price of Portland cement is increasing and the production process consumes large amount of energy which leads to greenhouse effect (Malhotra 2002), many attempts are being made to utilize higher percentage of supplementary cementitious materials or pozzolans to replace conventional Portland cement. It is generally accepted that the use of supplementary material at low replacement level produced good concrete with reduced porosity, increased durability and acceptable strength (Chindaprasirt *et al.* 2005, Malhotra 2002, Ramezanianpour and Malhotra 1995). The reactivity of the pozzolanic materials increases with the increase in their finenesses (Chindaprasirt *et al.* 2004, Erdogdu and Turker 1998, Sathonsaowaphak *et al.* 2009). This should allow a higher replacement level of these pozzolanic materials in the concrete industry.

Inert materials such as ground sand are incorporated to Portland cement to produce silica cement (Neville 1995). This is to adjust some of the properties of the cement, lower the cost and reduce the use of Portland cement. It is also successful to use inert material to replace part of cement to study the filler effect on the strength development of concrete (Tangpagasit *et al.* 2005).

This work aims to investigate the water permeability and abrasion of concrete containing high volume FFA and GPA. The results will be useful and lay some ground work for utilization of high fine pozzolan replacement of Portland cement.

2. Experimental program

2.1 Materials and concrete mixtures

Ordinary Portland cement (OPC) was used for all concrete mixtures. Lignite fly ash from Mae Moh power plant in the north of Thailand was used. FFA was obtained from air classifier. GPA was obtained from ball mill grinding of palm oil fuel ash; a waste material from the palm oil extraction factory. In addition, ground river sand (GRS) with similar fineness to FFA and GPA was used to indicate the filling effect (Isaia *et al.* 2003, Nehdi 1998, Tangpagasit *et al.* 2005). Physical properties and chemical compositions of the OPC and replacement materials (*R*) are reported in Tables 1 and 2. FFA, GPA and GRS finenesses were similar with percentages retained on No. 325 sieve (45 μm opening) of 1.0-2.5% by weight. Natural river sand with a fineness modulus of 2.44 and specific gravity of 2.65 and crushed limestone with nominal size of 20 mm and specific gravity of 2.67

Table 1 Physical properties of cement and replacement materials

Material	Specific gravity	Retained on a sieve No. 325 (%)	Median particle size, d_{50} (μm)
Portland cement type I (OPC)	3.14	-	14.7
Classified fly ash (FFA)	2.52	2.43	5.5
Ground palm oil fuel (GPA)	2.43	1.0	8.1
Ground river sand (GRS)	2.65	2.02	6.0

Table 2 Chemical composition of cement and replacement materials

Compositions	OPC	FFA	GPA	GRS
SiO_2	20.9	41.1	57.8	92.8
Al_2O_3	4.8	22.5	4.6	3.2
Fe_2O_3	3.4	11.6	3.3	0.3
CaO	65.4	15.3	6.6	0.6
MgO	1.2	2.8	4.2	0.5
Na_2O	0.2	1.7	0.5	0.4
K_2O	0.3	2.9	8.3	0.3
SO_3	2.7	1.5	0.3	0.5
LOI	0.9	0.2	10.1	0.6

Table 3 Concretes mix proportions

Mixes	OPC (kg)	FAA (kg)	GPA (kg)	GRS (kg)	Fine (kg)	Coarse (kg)	Water (kg)	*W/C+R*	Slump (mm)
Control	300	-	-	-	915	1080	213	0.71	75
FFA20	240	60	-	-	920	1084	200	0.67	85
FFA40	180	120	-	-	933	1098	185	0.62	80
FFA55	135	165	-	-	928	1093	189	0.63	80
FFA70	90	210	-	-	902	1067	202	0.67	90
GPA20	240	-	60	-	907	1072	220	0.73	65
GPA40	180	-	120	-	900	1064	222	0.74	70
GPA55	135	-	155	-	894	1059	225	0.75	90
GPA70	90	-	210	-	889	1011	228	0.76	70
GRS20	135	-	-	60	905	1070	212	0.71	75
GRS40	180	-	-	120	896	1060	216	0.72	60
GRS55	135	-	-	165	882	1046	222	0.74	65
GRS70	90	-	-	210	886	1050	228	0.76	60

were used as fine and coarse aggregates in concrete mixtures, respectively.

Table 3 shows the concrete mixture proportions. The controlled concrete with water to cement ratio of 0.71 and slump of 75 mm was selected so that the effects of incorporating FFA and GPA can be gauged with confidence. Slumps were maintained at 75±15 mm and water to cement and replacement material ratios (*W*/(*C*+*R*)) were controlled within 0.71±0.05 except for FFA as it improved workability and slightly lowered the $W/C{+}R$ ratios of concretes. These were achieved without the aid of plasticizer. The concretes with Portland cement replaced with 20, 40, 55 and 70% of FFA, GPA and GRS were prepared and tested.

2.2 Testing procedure

2.2.1 Compressive strength

Concrete cylinders of 100 mm in diameter and 200 mm in height were cast, demolded at 24 hours and cured in water. The compressive strength of concretes was tested at 28 and 90 days. The report results are the average of three samples.

2.2.2 Water permeability

For permeability testing, concrete cylinder was sliced to discs of 40 mm thickness and the ends were discarded. The disc was installed in permeability cell as suggested by Khatri and Sirivivatnanon (1997). Distilled water was used as fluid to flow through concrete disc under constant pressure. The pressure of 0.5 MPa (5 bars) recommended by concrete society (1987) was employed. Report results are averages of four samples. Flow rate was monitored and the steady flow rate was used to calculate permeability using equation based on Darcy's law and equation of continuity.

$$K = \frac{\rho L g Q}{PA}$$

K - coefficient of permeability, ρ - density of water, L - thickness of concrete sample, g - gravity acceleration, Q - flow rate, P – pressure of water, A - cross sectional area of sample

2.2.3 Abrasion resistance

Abrasion resistance of concrete was evaluated according to ASTM C1138 (Underwater method). Samples of 300 mm in diameter and 100 mm in height were cast and cured in moist condition for 28 days. The samples were installed in the abrasion machine containing 70 chrome steel balls placed on the concrete upper surface. Fresh water was filled to the specified level and stirring of steel balls with blade was performed for 12 hours. This procedure was repeated 6 times. The abrasion of concrete was calculated from the weight loss of the samples.

3. Results and discussion

3.1 Properties and particle shape of materials

The chemical compositions of the materials as shown in Table 2 revealed that the classified fly ash could be assigned as class F as prescribed by ASTM C 618. For GPA, the contents of SiO_2 + Al_2O_3 + Fe_2O_3 were 65.7%, while the GRS consisted of 92.8% SiO_2.

Fig. 1 shows the particle size distribution curves of OPC, FAA, GPA and GRS and their median particle sizes (d_{50}) are 14.7, 5.5, 8.1 and 6.0 μm, respectively. The particle size distribution curves of FFA, GPA and GRS are similar. Their particle sizes are slightly finer than the OPC. As shown in Fig. 2, the FFA is spherical in shape and its surface is relatively smooth. On the other hand, OPC, GPA and GRS contain particles with angular and irregular shape as a result of crushing and milling processes.

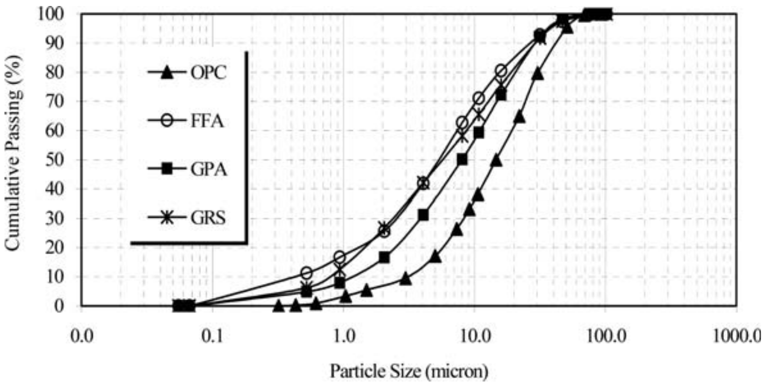

Fig. 1 Particle size distribution of cement and replacement materials

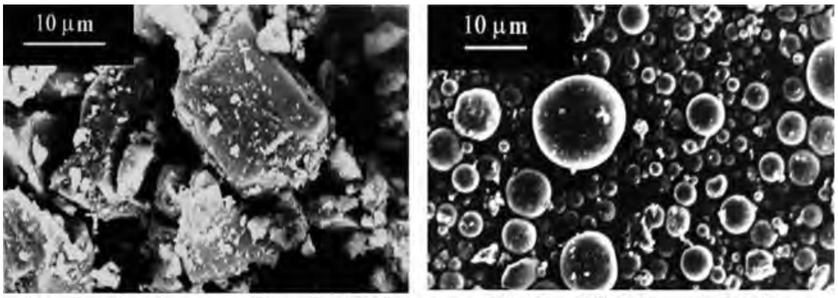

(a) Portland cement Type I (OPC) (b) Classified fly ash (FFA)

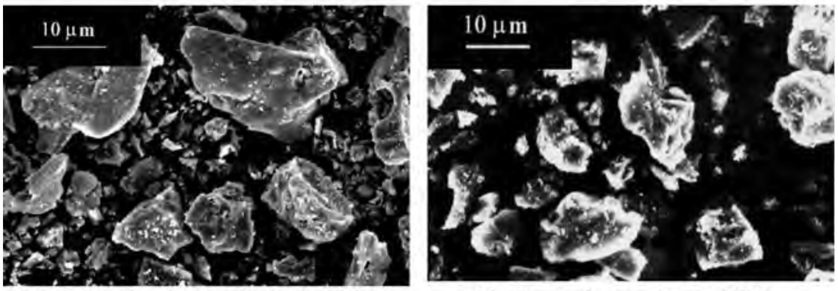

(c) Ground palm oil fuel ash (GPA) (d) Ground river sand (GRS)

Fig. 2 Scanning electron microscopy (SEM) of cement and replacement materials

3.2 Water requirement in concrete mixes

The amounts of mixing water are shown in Table 3. The use of FFA reduced the $W/(C+R)$ ratios of fly ash concrete compared to that of the control concrete. For example, the $W/(C+R)$ ratios of the control concrete, FFA20 (mix with 20% FFA), FFA40, FFA55 and FFA70 concretes were 0.71, 0.67, 0.62, 0.63 and 0.67, respectively. The reduction in water requirement was the result of the ball bearing effect of the spherical FFA particles. For the GPA and GRS concretes, the opposite trend of results was obtained. The $W/C+R$ ratios of both GPA and GRS concretes were slightly higher than that of control concrete and increased with the increase in the replacement level. The angular and irregular particles of GPA and GRS increased the water requirement to maintain the same workability compared to that of the control concrete.

3.3 Compressive strength

Table 4 shows compressive strengths and normalized compressive strengths of concretes containing FFA, GPA and GRS in comparison with that of control concrete. The relationship between the compressive strengths of concretes and the replacement levels are shown in Fig. 3.

The compressive strengths of FFA20 were 32.5 and 35.4 MPa or 123% and 126% of the control concrete at 28 and 90 days, respectively. The strengths of FFA concretes with the 55% replacement were still higher than that of the original concrete. When the cement replacement by FFA was 70%, the compressive strength of FFA concrete was slightly lower than that of control concrete. The

Table 4 Compressive strength, water permeability and abrasion of concretes

Mixes	Comp. Strength (MPa) –Normalized (%)		$k \times 10^{-12}$ (m/s) - k/k_{CON}		Abrasion depth
	28 days	90 days	28 days	90 days	(mm)
Control	26.1 – 100	28.2 - 100	2.89 - 1.00	2.05 - 1.00	2.55
FFA20	32.5 – 123	35.4 - 126	1.32 - 0.46	0.44 - 0.21	2.38
FFA40	31.9 – 122	34.0 - 121	0.51 - 0.18	0.32 - 0.16	2.41
FFA55	29.1 – 111	31.8 - 113	0.72 - 0.25	0.42 - 0.21	2.67
FFA70	25.5 – 98	27.1 - 96	1.85 - 0.64	1.54 - 0.90	3.45
GPA20	23.9 – 92	29.4 - 104	0.59 - 0.20	0.25 - 0.12	2.75
GPA40	20.7 – 79	23.7 - 84	0.41 - 0.14	0.26 - 0.13	3.23
GPA55	18.1 – 69	22.3 - 79	3.30 - 1.14	2.38 - 1.16	3.67
GPA70	14.9 – 57	17.5 - 62	37.30 - 12.9	23.10 - 11.27	4.34
GRS20	22.2 – 85	25.9 - 92	8.16 - 2.83	5.91 - 2.88	3.54
GRS40	16.0 – 61	17.2 - 61	22.60 - 7.83	10.20 - 4.98	4.62
GRS55	9.1 – 35	9.3 - 33	630 - 218	447 - 218	5.73
GRS70	5.1 - 20	5.2 - 18	2250 - 780	2450 - 1195	6.52

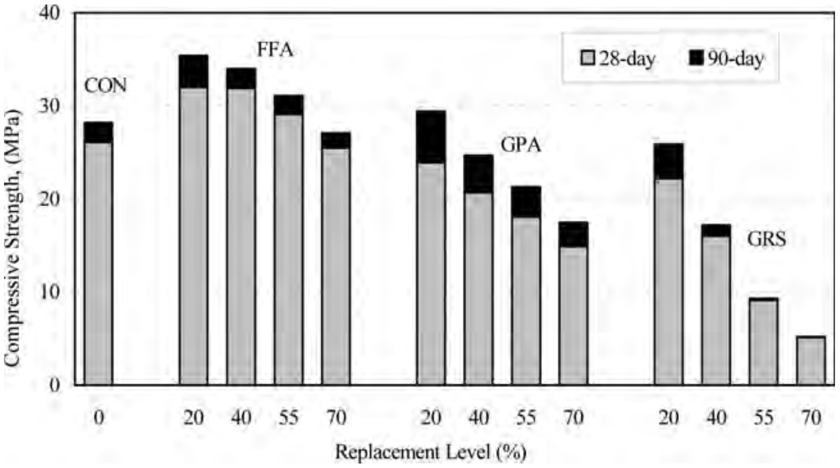

Fig. 3 Relationship between the compressive strength of concrete and the cement replacement level

results indicated better performance of high volume FFA concrete compared to that of high volume normal fly ash concrete (Jiang and Malhotra 2000, Serdar *et al.* 2007). The good performance of FFA was due to the ball bearing effect, the dispersion effect and the enhancement of the pozzolanic reaction of small particle size of FFA (Erdogdu and Turker 1998, Chindaprasirt *et al.* 2004).

The compressive strength of GPA concretes decreased with the increase in the replacement levels. The 28-day compressive strengths of GPA20, GPA40, GPA55 and GPA70 concretes were 23.9, 20.7, 18.1 and 14.9 MPa or 92, 79, 69 and 57% of the control concretes, respectively. These results were due to the less Portland cement content and the slightly larger amount of water in the concrete mixture. At 90 days, the compressive strength of GPA20 concrete was, however, improved compared to the compressive strength at 28 days. This confirmed that a substantial amount of pozzolanic reaction was obtained with the use of GPA in concrete. High volume 40-70% GPA could also be used to produce concrete with acceptable 28-day compressive strength of 15-20 MPa. It should be pointed out here that higher strength concretes could be obtained with lower water to cement ratio with the aid of superplasticizer (Jiang and Malhotra 2000, Serdar *et al.* 2007).

For GRS concretes, the 28-day and 90-day normalized compressive strengths of GRS20 concrete were 85 and 92% of control concrete. At low level of replacement, the filler effect is significant and this resulted in only slight reduction in strengths. The compressive strengths of GRS concretes, however, decreased substantially as the level of replacement was increased. The GRS produced filler effect from its small particle size without pozzolanic effect (Tangpagasit *et al.* 2005) and was thus not effective in terms of maintaining the acceptable strengths with high replacement level. At high replacement level, the pozzolanic effect played the dominant role in maintaining the acceptable level of strengths.

3.4 Permeability of concrete

The permeability of concretes and the ratios of permeability are given in Table 4. The ratio of permeability is defined as the permeability of concrete containing replacement materials divided by that of the control concrete. The values of water permeability of the control concrete at 28 and 90 days were 2.89×10^{-12} m/s and 2.05×10^{-12} m/s, respectively.

Fig. 4 shows the relationship between permeability and replacement levels of materials. The values of permeability of concretes decreased with the age of samples. This was the result of the increase in hydration and pozzolanic reaction with time (Ramezanianpour and Malhotra 1995). The permeability values of FFA concretes were lower than those of the control concretes for all replacement levels. The lowest permeability was obtained with the replacement of 40%. This result can be attributed to the pozzolanic reaction from FFA, and the less amount of mixing water influenced the reduction in volume and size of pores in cement paste (Poon *et al.* 2001). Moreover, the filler effect of the smaller particles of FFA also assisted to produce a denser cement matrix (Govindarajan and Gopalakrishnan 2009).

GPA concretes also showed the same characteristic of permeability as FFA concretes when the replacement levels were up to 40% by weight of binder. The 90-day water permeability of GPA20 and GPA40 concretes were 0.25×10^{-12} m/s and 0.26×10^{-12} m/s or 0.12 and 0.13 of those of the control concretes, respectively. For the GPA40 concrete, its water permeability was also lower than that of control concrete in spite of the slightly higher water content (0.74 for GPA40 concrete and 0.71 for control concrete). Although the pozzolanic reaction of GPA was lower than that of FFA as indicated by the strength development characteristics, the permeability values were similar at this

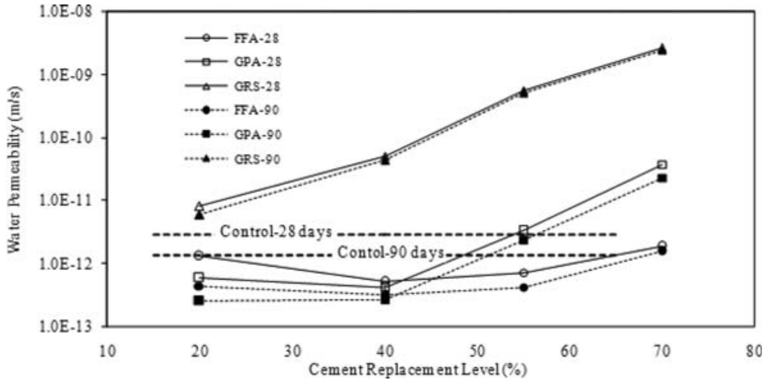

Fig. 4 Relationship between water permeability of concrete and cement replacement level

range of replacement. This suggested that filler and pozzolanic effects were comparatively high up to replacement level of 40% of GPA and contributed to the low permeability of the concretes.

At higher replacement level of 55 and 70% of GPA, the permeability increased significantly. The 90-day ratios of permeability of GPA55 and GPA70 concretes were 1.16 and 11.27, respectively. This resulted from the slightly higher water content of the mixes, the low pozzolanic reaction and the low filler effect which were not sufficient at the high level of replacement.

The ratios of water permeability of GRS20, GRS40, GRS55 and GRS70 concretes at 28 days were 2.83, 7.83, 218 and 780, respectively. Only the GRS20 concrete gave the acceptable level of permeability. For high level of replacement, the filling effect alone was not able to maintain the low level of permeability of the concretes. At high replacement level, the pozzolanic effect also played the dominant role similar to that of strength.

The relationships between water permeability and compressive strength of concrete at 90 days are presented in Fig. 5. In general, the permeability decreased when concrete compressive strengths were higher. The high volume FFA concrete showed both high strength and low permeability. The high volume GPA concrete showed slightly lower strength and higher permeability than those of

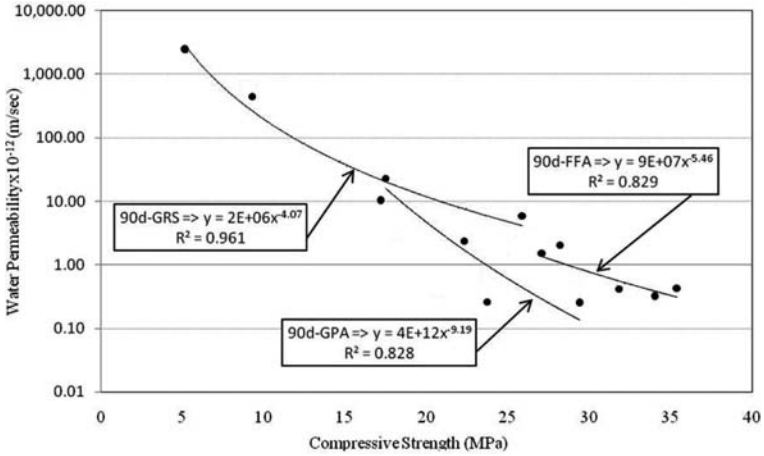

Fig. 5 Relationship between water permeability and compressive strength of concrete at 90 days

FFA concrete. At high level of replacement, the filler effect became less significant and the performances of concrete relied mainly on the pozzolanic reaction.

3.5 Abrasion resistance of concrete

The abrasion of concretes is shown in Table 4 and the relationship between abrasion and replacement levels of materials is shown in Fig. 6. The abrasion of concrete in this investigation ranged from 2.38-5.52 mm. The abrasion of FFA concrete was slightly lower than that of the OPC concrete with the replacement level up to 40% and the lowest value was 2.38 mm for FFA20 concrete compared to 2.55 mm of the OPC concrete. A similar trend of result of decreasing abrasion resistance with OPC replacement level of above 50% with class C fly ashes was reported by Naik *et al.* (2002).

For GPA concretes, the abrasion increased as the content of GPA increased. The depth of wear of GPA20 was slightly higher at 2.75 mm than those of FFA and OPC concretes. The abrasion resistance of GRS concrete significantly increased with the increase in the replacement level. This indicated that although the incorporation of GRS produced filling effect, it had an adverse effect on the abrasion resistance of concrete. The filling of GRS did not have a cementing property which helped to resist the abrasion.

Fig. 7 presents the relationships between the depth of abrasion, permeability and compressive strength of concrete at 28 days. The compressive strength of concrete with the incorporation of supplementary material is related to the abrasion resistance. The abrasion resistance increased with increasing compressive strength and could be expressed in terms of exponential equation with R^2 of 0.945. The previous researches also reported that the abrasion resistance was strongly governed by its compressive strength (Siddique 2003, Li *et al.* 2006).

The relationship between water permeability and depth of abrasion of concrete is also shown in Fig. 7. As expected, the high permeability concrete produced low abrasion resistance. The relationship could also be expressed in terms of exponential relation with R^2 of 0.899. This result agreed with

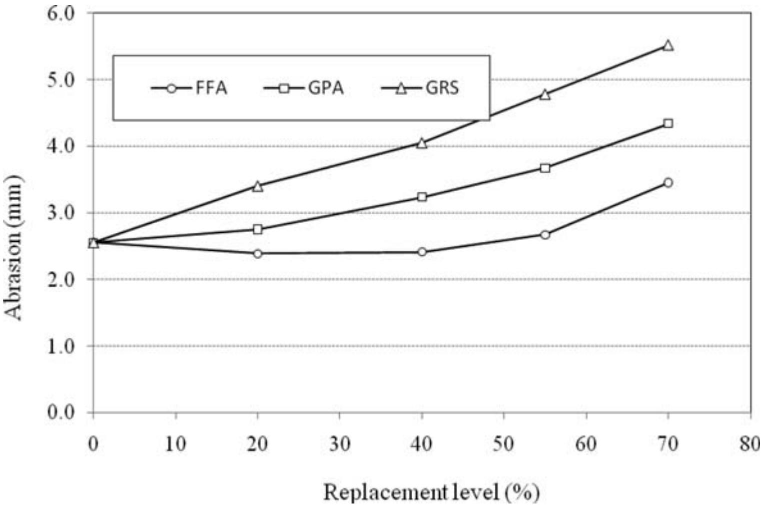

Fig. 6 Relationship between abrasion and replacement level at 28 days

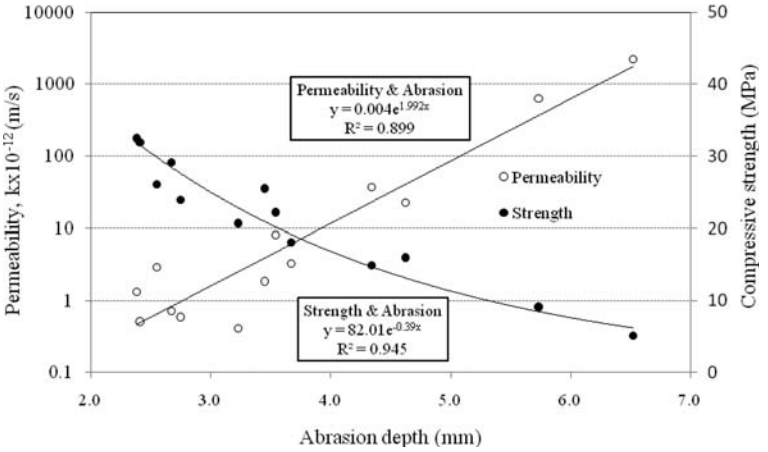

Fig.7 Relationship between abrasion, permeability and compressive strength at 28 days

that of Liu *et al.* (2006) who studied the abrasion erosion of concrete using the water-borne sand and found that the concrete with high coefficient permeability exhibited the low abrasion erosion resistance.

4. Conclusions

From this study, it can be concluded that high volume fine fly ash (FFA) and fine ground palm oil fuel ash (GPA) can produce concrete with acceptable strength, water permeability and abrasion resistance. FFA is an effective pozzolan for use in high volume as it produces good pozzolanic reaction through the small particle size and requires less water through the ball bearing effect of the spherical particles. GPA is slightly less effective pozzolan compared to FFA and its use in high volume resulted in slightly lower strength and higher water permeability.

Acknowledgments

The writers gratefully acknowledge the financial support from the Higher Education Research Promotion and National Research University Project of Thailand, Office of the Higher Education Commission, through the Advanced Functional Materials Cluster of Khon Kaen University, the Thailand Research Fund (TRF) and the Higher Education Commission under grant No. MRG5280013 and the TRF Senior Research Scholar under grant No. RTA5480004.

References

ASTM C1138-97, *Standard test method for abrasion resistance of concrete (Underwater method)*, Philadelphia.

ASTM C618-08a, *Standard specification for coal fly ash and raw or calcined natural pozzolan for use in concrete*, philadelphia.

Awal, A.S.M.A. and Hussin, M.W. (1997), "The effectiveness of palm oil fuel ash in preventing expansion due to alkali-silica reaction", *Cement Concrete Comp.*, **19**(4), 367-372.

Basheer, L., Kropp, J. and Cleland, D.J. (2001), "Assessment of the durability of concrete from its permeation properties: a review", *Constr. Build. Mater.*, **15**(2-3), 93-103.

Chindaprasirt, P., Chareerat, T., Hatanaka, S. and Cao, T. (2010a), "High strength geopolymer using fine high calcium fly ash", *J. Mater. Civil Eng.,* **23**(3), 264-270.

Chindaprasirt, P., Chotetanorm, C. and Rukzon, S. (2010b), "The use of palm oil fuel ash to improve the chloride and corrosion resistance of high-strength and high-workability concrete", *J. Mater. Civil Eng.,* **23**(4), 499-503.

Chindaprasirt, P., Homwuttiwong, S. and Sirivivatnanon, V. (2004), "Influence of fly ash fineness on strength, drying shrinkage and sulfate resistance of blended cement mortar", *Cement Concrete Res.*, **34**(7), 1087-1092.

Chindaprasirt, P., Jaturapitakkul, C. and Sinsiri, T. (2005), "Effect of fly ash fineness on compressive strength and pore size of blended cement paste", *Cement Concrete Comp.*, **27**(4), 425-428.

Chindaprasirt, P., Jaturapitakkul, C. and Sinsiri, T. (2007), "Efffect of fly ash fineness on microstructure of blended cement paste", *Constr. Build. Mater.*, **21**(7), 1534-1541.

Concrete Society Ltd. (1987), "Permeability testing of site concrete: a review of methods and experience", Report No. 31. Report of a concrete society working party. *The Concrete Society,* London.

Erdogdu, K. and Turker, P. (1998), "Effects of fly ash particle size on strength of Portland cement fly ash mortars", *Cement Concrete Res.*, **28**(9), 1217-1222.

Govindarajan, D. and Gopalakrishnan, R. (2009), "Magnetic susceptibility measurements on metakaolin admixtured cement hydrated with ground water and sea water", *Int. J. Miner. Metall. Mater.*, **16**(3), 349-354.

Isaia, G.C., Gastaldini, A.L.G. and Moraes, R. (2003), "Physical and pozzolanic action of mineral additions on the mechanical strength of high-performance", *Cement Concrete Comp.*, **25**(1), 69-76.

Jiang, L.H. and Malhotra, V.M. (2000), "Reduction in water demand of non-air-entrained concrete incorporating large volumes of fly ash", *Cement Concrete Res.*, **30**(11), 1785-1789.

Khan, M.I. (2003), "Permeation of high performance concrete", *J. Mater. Civil Eng.,* **15**(1), 84-92.

Khatri, R.P. and Sirivivatnanon, V. (1997), "Methods for the determination of water permeability of concrete", *ACI Mater. J.*, **94**(3), 257-261.

Li, H., Zhang, M.H. and Ou, J.P. (2006), "Abrasion resistance of concrete containing nano-particles for pavement", *Wear*, **260**(11-12), 1262-1266.

Liu, Y.W., Yen, T. and Hsu, T.H. (2006), "Abrasion erosion of concrete by water-borne sand", *Cement Concrete Res.*, **36**(10), 1814-1820.

Malhotra, V.M. (2002), "Introduction: sustainable development and concrete technology", *ACI Concrete Int.*, **24**(7), 22.

Naik, T.R., Singh, S.S. and Hossain, M.M. (1996), "Permeability of high-strength concrete containing low cement factor", *J. Energy Eng.,* **122**(1), 21-39.

Naik, T.R., Singh, S.S. and Ramme, B.W. (2002), "Effect of source of fly ash on abrasion resistance of concrete", *J. Mater. Civil Eng.,* **14**(5), 417-426.

Nehdi, M., Mindess, S. and Aitcin, P.C. (1998), "Rheology of high-performance concrete: effect of ultrafine particles", *Cement Concrete Res.*, **28**(5), 687-697.

Neville, A.M. (1995), *Properties of concrete*, 4th and final edition, London, Addison Wesley Longman Limited.

Poon, C.S., Azhar, S., Anson, M. and Wong, Y.L. (2001), "Comparison of the strength and durability performance of normal and high-strength pozzolanic concretes at elevated temperatures", *Cement Concrete Res.*, **31**(9), 1291-1300.

Ramezanianpour, A.A. and Malhotra, V.M. (1995), "Effect of curing on the compressive strength, resistance to chloride-ion penetration and porosity of concretes incorporating slag, fly ash or silica fume", *Cement Concrete Comp*., **17**(2), 125-133.

Rukzon, S. and Chindaprasirt, P. (2009a), "Strength and chloride penetration of Portland cement mortar containing palm oil fuel ash and ground river sand", *Comput. Concrete,* **6**(5), 391-401.

Rukzon, S. and Chindaprasirt, P. (2009b), "Strength and chloride resistance of blended Portland cement mortar containing palm oil fuel ash and fly ash", *Int. J. Miner., Metall. Mater.*, **16**(4), 475-481.

Sata, V., Khammathit, P. and Chindaprasirt, P. (2011), "Efficiency factor of high calcium Class F fly ash concrete", *Comput. Concrete*, **8**(5), 583-595.

Sathonsaowaphak, A., Chindaprasirt, P. and Pimraksa, K. (2009), "Workability and strength of lignite bottom ash geopolymer mortar", *J. Hazard. Mater.*, **168**(1), 44-50.

Serdar, A., Halit, Y., Hüseyin, Y. and Bülent, B. (2007), "Sulfuric acid resistance of high-volume fly ash concrete", *Build. Environ.*, **42**(2), 717-721.

Siddique, R. (2003), "Effect of fine aggregate replacement with Class F fly ash on the abrasion resistance of concrete", *Cement Concrete Res.*, **33**(11), 1877-1881.

Tangchirapat, W., Jaturapitakkul, C. and Chindaprasirt, P. (2009), "Use of palm oil fuel ash as a supplementary cementitious material for producing high-strength concrete", *Constr. Build. Mater.*, **23**(7), 2641-2646.

Tangpagasit, J., Cheerarot, R., Jaturapitakkul, C. and Kiattikomol, K. (2005), "Packing effect and pozzolanic reaction of fly ash in mortar", *Cement Concrete Res.*, **35**(6), 1145-1151.

Tay, J.H. (1990), "Ash from oil-palm waste as concrete material", *J. Mater. Civil Eng.,* **2**(2), 94-105.

Vedalakshmi, R., Sundara Raj, A., Srinivasan, S. and Ganesh Babu, K. (2003), "Quantification of hydrated cement products of blended cements in low and medium strength concrete using TG and DTA technique", *Thermochim Acta*, **407**(1-2), 49-60.

CC

Ferroelectrics Letters, 39:76–80, 2012
Copyright © Taylor & Francis Group, LLC
ISSN: 0731-5171 print / 1563-5228 online
DOI: 10.1080/07315171.2012.738595

Dielectric Properties of 2–2 PMN-PT/Cement Composites

A. CHAIPANICH,[1,*] R. RIANYOI,[1] R. POTONG,[1] W. SURIYA,[1]
N. JAITANONG,[2] AND P. CHINDAPRASIRT[3]

[1]Department of Physics and Materials Science, Faculty of Science, Chiang Mai University, Chiang Mai 50200, Thailand
[2]Materials Science Program, Faculty of Science, Maejo University, Chiang Mai 50290, Thailand
[3]Sustainable Infrastructure Research and Development Center, Department of Civil Engineering, Faculty of Engineering, Khon Kaen University, Khon Kaen 40002, Thailand

Communicated by Dr. George W. Taylor
(*Received in final form June 20, 2012*)

Dielectric properties of 2–2 connectivity lead magnesium niobate-lead titanate (PMN-PT)/Cement composites were investigated at 0.1–20 kHz. PMN-PT of 60–80% by volume was used. The composites were fabricated using a dice and fill technique and cured in 98%RH curing chamber for 7 days before measurements. Dielectric constant (ε_r) at 1 kHz increased with PMN-PT volume, having values of 1504, 1645 and 2390 respectively. Dielectric loss (tanδ) values are 0.382, 0.185 and 0.188 at 1 kHz. In addition, the dielectric constant was found to decrease with an increase in the frequency tested having value of 1692, 1504 and 1322 for 0.1, 1 and 20 kHz respectively. The dielectric loss was found to be less with increasing frequency at 0.702, 0.382 and 0.179 for 0.1, 1 and 20 kHz respectively.

Keywords PMN-PT; cement; composites; 2–2 connectivity; dielectric properties

1. Introduction

A number of research developments have been made very recently on the composite material which consists mainly of a piezoelectric ceramic and a cement-based material [1–19]. Among those, many dielectric and piezoelectric properties of 0–3 connectivity composites were reported [1–4, 6–13, 15–19]. One of the mostly used piezoelectric ceramic materials is lead zirconate titanate (PZT) as it has very high piezoelectric coefficient (d_{33}) and dielectric constant (ε_r) [20, 21] and most of the piezoelectric-cement based composites were produced using PZT as the piezoelectric ceramic in the composite [1–14, 17–19]. Another piezoelectric material such as lead magnesium niobate-lead titanate, $Pb(Mg_{1/3}Nb_{2/3})O_3$-$PbTiO_3$ (PMN-PT) may also be used as PMN-PT ceramic has a high dielectric constant (ε_r) and high piezoelectric coefficient [22]. For cement-based composite produced with

---

[*] Corresponding author. E-mail: arnon@chiangmai.ac.th

piezoelectric materials other than PZT such as PMN-PT very little is know. In this research work, PMN-PT/cement composite material was produced from PMN-PT with normal Portland cement (PC) as a composite of 2–2 connectivity PMN-PT/PC composite and dielectric properties were investigated at 0.1–20 kHz.

2. Experimental

A columbite technique was first used to produce PMN powder where $MgNb_2O_6$ or MN powder was produced by calcining magnesium carbonate hydroxide pentahydrate $(MgCO_3)_4Mg(OH)_2.5(H_2O)$ and Nb_2O_5 at 1150°C. MN powder was mixed with lead oxide (PbO) in ethanol and milled together in a zirconia ball mill for 24 h, and were calcined at 800°C to produce PMN powder. Lead titanate ($PbTiO_3$) was produced in a similar manner using mixed oxide method from PbO and TiO_2. PMN and PT were then mixed together at a molar ratio of 0.67PMN – 0.33PT in ethanol and milled together for 30 minutes. PMN and PT powder were then pressed into pellets before sintering at 1250°C for 2 h to finally produce PMN-PT ceramic disc of ≈15 mm in diameter and ≈2 mm thick. The composites were fabricated using a dice and fill technique where Portland cement paste was filled in the gaps after cutting and cured in 98%RH 60°C curing chamber for 7 days before measurements. An impedance meter (Hewlett Packard 4194A) was used to obtain the capacitance and the dissipation factor (dielectric loss: tanδ) of the composites at room temperature and at frequency of 0.1, 0.5, 1, 5, 10 and 20 kHz. The relative dielectric constant (ε_r) was the calculated from the following equation:

$$\varepsilon_r = \frac{Ct}{\varepsilon_0 A}$$

where C is the sample capacitance, t is the thickness, ε_0 is the permittivity of free space constant (8.854×10^{-12} Farad per meter), and A is the electrode area.

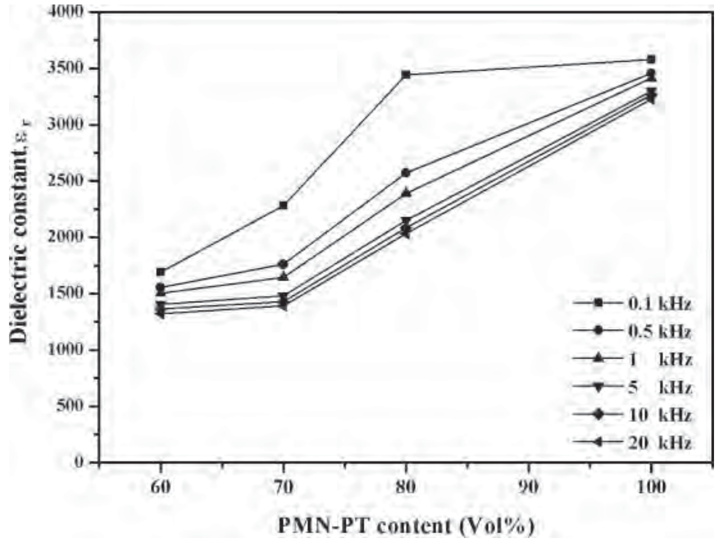

Figure 1. Dielectric constant results of 2–2 PZT-cement composites at 0.1 to 20 kHz.

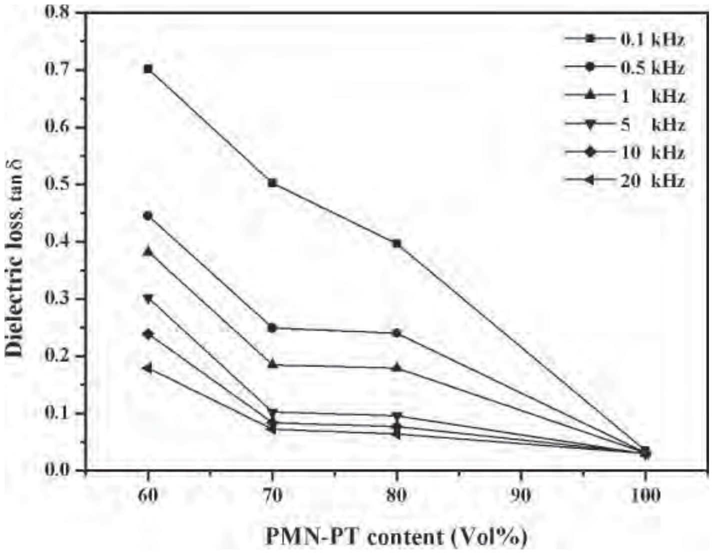

Figure 2. Dielectric loss results of 2–2 PZT-cement composites at 0.1 to 20 kHz.

3. Results and Discussion

The effect of PMN-PT on the dielectric constant at various frequencies (0.1 kHz–20 kHz) can be seen in Fig. 1 where the dielectric constant is plotted against PMN-PT content. The dielectric constant of the 2–2 composites can be seen to increase with PMN-PT content for all frequencies. Moreover, the dielectric constant can be seen to decrease with an increase in the frequency used. The dielectric constant values are 1692, 1504 and 1322 at 0.1 kHz, 1 kHz and 20 kHz for 60% PMN-PT composite respectively. At a certain frequency, i.e. at 0.1 kHz the ε_r values can be seen to increase with increasing PMN-PT vol. content which are 1692, 2283 and 3444 for composite with 60%, 70% and 80% PMN-PT respectively. At 1 kHz, the ε_r values are 1504 and 2390 for composite with 60% and 80% PMN-PT respectively. These values are noticeably higher than reported values at 1 kHz of 0–3 piezoelctric-cement composites [4–7] where the dielectric value is in the region of 200–300 for 50–70% by volume.

The effect of PMN-PT on the dielectric loss measured at the frequency from 0.1 kHz to 20 kHz can be seen in Fig. 2. In general, the dielectric loss of 2–2 PMN-PT/cement composites was found to reduce with increasing frequency, for 60% PMN-PT composite the tanδ values are 0.702, 0.38, 0.239 and 0.179 at 0.1, 1, 10 and 20 kHz respectively. The tanδ values were also found to reduce with increasing PMN-PT content at all frequency tested.

4. Conclusions

PMN-PT ceramic/ cement composites of 2–2 connectivity were produced using a dice and fill method. Dielectric constant (ε_r) of 2–2 composites at 1 kHz increased with PMN-PT volume, having values of 1504, 1645 and 2390 respectively. Dielectric loss (tanδ) values are 0.382, 0.185 and 0.188 at 1 kHz. In addition, the dielectric constant was found to decrease with an increase in the frequency tested having value of 1692, 1504 and 1322 for 0.1, 1 and

20 kHz. The dielectric loss was found to be less with increasing frequency at 0.702, 0.382 and 0.179 for 0.1, 1 and 20 kHz respectively.

Acknowledgments

The authors are grateful to members of staff at the Electroceramics Research Laboratory, Faculty of Science, and Chiang Mai University for the research facilities made possible for this research work. The authors would like to express their gratitude for the Thialand Research Fund (TRF) Research Scholar grant awarded to Assistant Prof. Dr. Arnon Chaipanich by the Thailand Research Fund (TRF). This work was also financially supported by the Thailand Research Fund (TRF) under the TRF Senior Research Scholar Contract No. RTA5480004.

References

1. A. Chaipanich, and N. Jaitanong, Effect of poling time on piezoelectric properties of 0–3 PZT-Portland cement composite. *Ferr. Lett.* **35**, 73–78 (2008).
2. N. Jaitanong, and A. Chaipanich, Effect of poling temperature on piezoelectric properties of 0–3 PZT-Portland cement composite. *Ferr. Lett.* **35**, 17–23 (2008).
3. A. Chaipanich, and N. Jaitanong, Effect of PZT particle size on the electromechanical coupling coefficient of 0–3 PZT-cement composites, *Fer. Lett.* **36** 37–44 (2009).
4. Z. Li, D. Zhang, and K. Wu, Cement-Based 0–3 Piezoelectric Composites. *J. Am. Ceram. Soc.* **85**, 305–13 (2002).
5. B. Dong and Z. Li, Cement-based piezoelectric ceramic smart composites. *Comp. Sci. Tech.* **65**, 1363–1371 (2005).
6. Z. Li, B. Dong, and D. Zhang, Influence of polarization on properties of 0–3 cement-based PZT composites. *Cem. Con. Comp.* **27**, 27–32 (2005).
7. A. Chaipanich, N. Jaitanong, and T. Tunkasiri, Fabrication and properties of PZT-ordinary Portland cement composites. *Matls. Letts.* **61**, 5206–5208 (2007).
8. A. Chaipanich, G. Rujijanagul, and T. Tunkasiri, Properties of Sr and Sb doped PZT-Portland Cement Composites, *Appl. Phys. A.* **94**, 329–337 (2008).
9. A. Chaipanich, Effect of PZT particle size on dielectric and piezoelectric properties of PZT-cement composites. *Curr. Appl. Phys.* **7**, 574–577 (2007).
10. N. Jaitanong, A. Chaipanich, and T. Tunkasiri, Properties 0–3 PZT–Portland cement composites. *Ceram. Inter.* **34**, 793–795 (2008).
11. A. Chaipanich, Effect of PZT particle size on dielectric and piezoelectric properties of PZT-cement composites. *Curr. Appl. Phys.* **7**, 574–577 (2007).
12. A. Chaipanich, N. Jaitanong, and R. Yimnirun, Ferroelectric hysteresis behavior in 0–3 PZT-cement composites: Effects of frequency and electric field. *Ferr. Lett.* **36**, 59–66 (2009).
13. S. Huang, J. Chang, R. Xu, F. Liu, L. Lu, Z. Ye, X. Cheng, Piezoelectric properties of 0–3 PZT/sulfoaluminate cement composites. *Smart Mater. Struct.* **13**, 270–274 (2004).
14. C. Xin, S. Huang, C. Jun, X. Ronghua, L. Futian, L. Lingchao, Piezoelectric and dielectric properties of piezoelectric ceramic-sulphoaluminate cement composites. *J. Eur. Ceram. Soc.* **25**, 3223–3228 (2005).
15. R. Potong, R. Rianyoi, A. Chaipanich, Dielectric properties of lead-free composites from 0–3 barium zirconate titanate-portland cement composites. *Ferr. Lett.* **38**, 18–23 (2011).
16. N. Jaitanong, R. Yimnirun, A. Chaipanich, Effect of compressive stress on the ferroelectric hysteresis behavior in 0–3 PMN-PT/cement composites. *Ferr. Lett.* **38**, 11–17 (2011).
17. A. Chaipanich, R. Rianyoi, R. Potong, N. Jaitanong, Effect of temperature on the dielectric properties of 0–3 PZT-cement composites. *Ferr. Lett.* **37**, 76–81 (2010).

18. N. Jaitanong, K. Wongjinda, P. Tammakun, G. Rujijanagul, A. Chaipanich, Effect of carbon addition on dielectric properties of 0–3 PZT-Portland cement composite. *Adv. Mater. Res.* **55–57**, 377–380 (2008).
19. A. Chaipanich, N. Jaitanong, Effect of polarization on the microstructure and piezoelectric properties of PZT-cement composites. *Adv. Mater. Res.* **55–57**, 381–384 (2008).
20. S. Schwarzer, A. Roosen, Tape casting of piezo ceramic/polymer composites. *J. Eur. Ceram. Soc.* **19**, (6–7) 1007–1010 (1999).
21. S. T. Lau, K. W. Kwok, H. L. W Chan, C. L. Choy, Piezoelectric composite hydrophone array. *Sens. Actuators A.* **96**, 14–20 (2002).
22. L. Cao, X. Yao, Z. Xu, Y. Feng Research on dielectric and piezoelectric properties of Ta-doped $0.68Pb(Mg_{1/3}Nb_{2/3})O_3$–$0.32PbTiO_3$ ceramics. *Ceram. Int.* **30**, 1373–1376 (2004).

Environmental Engineering and Management Journal

August 2012, Vol.11, No. 8, 1425-1432
http://omicron.ch.tuiasi.ro/EEMJ/

"Gheorghe Asachi" Technical University of Iasi, Romania

FACTORS AFFECTING THE WORKABILITY AND STRENGTH OF ALKALI-ACTIVATED HIGH CALCIUM FLY ASH CONCRETE

Krit Chaimoon[1], Sittiporn Pantura[1], Sahalaph Homwuttiwong[1],
Athika Wongkvanklom[1], Prinya Chindaprasirt[2*]

[1]Division of Civil Engineering, Faculty of Engineering, Mahasarakham University, Mahasarakham 44150, Thailand
[2]Sustainable Infrastructure Research and Development Center, Department of Civil Engineering, Faculty of Engineering,
Khon Kaen University, Khon Kaen 40002, Thailand

Abstract

The effects of several parameters on the workability and strength of alkali-activated high calcium fly ash (AAHCFA) concrete were investigated in this study. The AAHCFA concretes were activated with alkali sodium hydroxide solution (NaOH), sodium silicate solution (Na_2SiO_3) and heat. Three alkali liquid to fly ash (L/S) ratios of 0.55, 0.60 and 0.65, three NaOH concentrations of 10, 15 and 20 molars (M) and three Na_2SiO_3/NaOH ratios of 1.0, 1.5 and 2.0 were used. The workability was obtained by measuring the slump and the compressive strength was tested to gauge the strength of concrete. The results revealed that the workability of AAHCFA concrete was related to the molar ratio of H_2O/Na_2O in activator, the NaOH concentration, and the L/S ratio. The improvement in compressive strength was mainly related to the increase in the NaOH concentrations. The strength was, however, reduced with the increase in the Na_2SiO_3/NaOH ratio. The obtained slumps were in the range of 70 to 260 mm and the 28-day compressive strength ranged from 9.0 to 47.5 MPa. The influence of delay time (the time taken from the completion of specimen casting to the start of heat curing), curing temperature and curing duration on compressive strength were also presented.

Key words: alkali-activated material, compressive strength, concrete, high calcium fly ash, workability

Received: September 2010; Revised final: August, 2011; Accepted: September, 2011

---

[*] Author to whom all correspondence should be addressed: email: prinya@kku.ac.th; Phone: +66 4320 2355; Fax: +66 4320 2355 x 12

Portland cement materials in many aspects such as fire resistance, acid resistance and solidification of heavy metal wastes (Duxson et al., 2007). The binding property of alkali-activated binders depends on various factors such as source materials used, processing conditions and curing conditions. Various source materials such as blast furnace slag, clay, metakaolin and fly ash have been investigated over the past decades. A review on alkali-activated binders can be found in Pacheco-Torgal et al. (2008).

For fly ash, researchers have made intensive studies on alkali-activated low calcium or class F fly ash (FFA) mortar and concrete (Chindaprasirt et al., 2009; Hardjito and Rangan, 2005; Palomo et al., 1999). However, few papers have been published regarding the use of high calcium or class C fly ash (CFA) in making alkali-activated materials in particular alkali-activated concrete. The worldwide availability of fly ash worldwide, both FFA and CFA, has been increasing annually (Malhotra, 2002).

For the use of CFA, the presence of high amounts of calcium may have effects in the polymerization process and the microstructure. Nevertheless, the presence of calcium can greatly improve the compressive strength of alkali-activated materials and accelerates the hardening process (Yip et al., 2005). The studies on microstructures (Guo et al., 2010; Yip et al., 2005; Yip et al., 2008) have been conducted to explain this observation, however, it is still not clear why and how the presence of calcium plays such a significant role in determining the properties of an alkali-activated binder. Understanding of the use of CFA in producing alkali-activated concrete would be useful to the future applications.

This study focused on the investigation of the effects of several parameters on the mechanical properties of alkali-activated high calcium fly ash (AAHCFA) concrete. The mass ratio of alkaline liquid to fly ash (L/S), concentration of sodium hydroxide solution (NaOH), mass ratio of sodium silicate solution to sodium hydroxide solution (Na_2SiO_3/NaOH), delay time (the time taken from the completion of specimen casting to the start of heat curing), curing temperature and curing duration were the main parameters examined in the current study.

2. Materials

Fly ash from Mae Moh power station in the north of Thailand was used in this study as the source material. The loss on ignition (LOI) and chemical composition of this fly ash obtained by X-Ray Fluorescence (XRF) analysis using a Philips PW-2404 instrument is given in Table 1. The fly ash conforms to the class C, as per ASTM C 618-03 (2003), as the sum of SiO_2, Al_2O_3 and Fe_2O_3 is between 50 and 70% and the fly ash contains more than 20% of CaO. This fly ash has Blaine fineness of 3100 cm^2/g in accordance with ASTM C 204-00 (2000). The molar Si-to-Al ratio is about 1.3 which is slightly low for concrete application compared with the value of 2 suggested by Davidovits (1999). The XRD of the high calcium fly ash is shown in Fig. 1. The fly ash consisted mainly of the glassy phase which is highly disordered as indicated by the hump between 21 to 38 °2θ with some crystalline phases consisted of anhydrite, calcium oxide, magnesioferrite, hematite and quartz.

Sodium hydroxide pellets (99% purity) and sodium silicate solution (9.5 wt% Na_2O, 29.0 wt% SiO_2 and 61.5 wt% H_2O) were used for the preparation of alkaline solution. The sodium silicate solution used in this test was slightly higher in water content than the normally used one and this could affect the workability and other test results. However, it was selected as it gave a satisfactory wide range of relatively workable concretes. Local river sand with specific gravity of 2.58 and crushed stone (12.5 mm nominal size) with specific gravity of 2.65 were used as fine and coarse aggregate, respectively. Both aggregates were in saturated surface dry (SSD) condition.

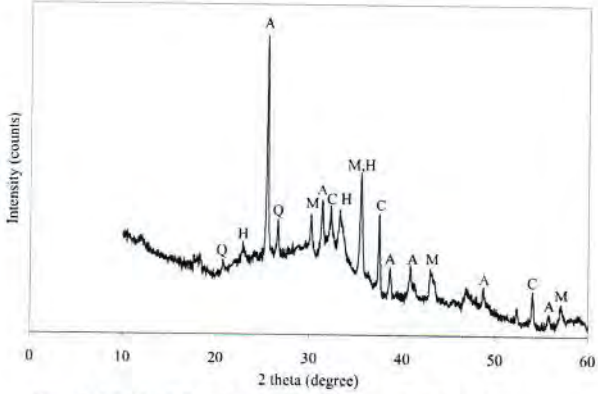

Fig. 1. XRD of fly ash: A = anhydrite ($CaSO_4$), C = calcium oxide (CaO), M = magnesioferrite ($MgFe_2O_4$), H = hematite (Fe_2O_3) and Q = quartz (SiO_2)

3. Experimental

3.1. Test on delay time, heat curing temperature and heat curing duration

For the first part, the effects of curing conditions including delay time, heat curing temperature and heat curing duration were investigated on compressive strength. The compressive strength tests were carried out at the age of 7 days.

Table 1. Chemical composition of fly ash

Oxides	SiO_2	Al_2O_3	Fe_2O_3	CaO	Na_2O	TiO_2	MgO	K_2O	P_2O_5	SO_3	LOI
Mass (%)	24.83	18.93	15.61	27.41	1.92	0.44	2.33	2.62	0.22	4.71	0.40

The mix of Na_2SiO_3/NaOH ratio of 1, NaOH concentration of 20M and L/S ratio of 0.60 were used. The mix constituents in one cubic meter are 1294 kg crushed stone, 554 kg sand, 345 kg fly ash, 103.5 kg Na_2SiO_3 and 103.5 kg NaOH.

3.1.1. Effect of delay time

The delay times of 0, 1, 8 and 24 hours were used before heat curing of the concrete specimens at 60 °C for a period of 1 day. Some delay time was found to be beneficial to strength (Hardjito and Rangan, 2005) as it allowed the dissolving of silica and alumina (Chindaprasirt et al., 2007).

3.1.2. Effect of temperature of heat curing

For this test, a constant delay time of one hour was used based on the result obtained from the test of the effect of delay time. The concrete specimens were heat cured for a period of 1 day. The curing temperatures of 25, 40, 60, 75 and 90°C were selected for this test based on the previous work. Hardjito and Rangan (2005) worked on the alkali-activated low-calcium fly ash (AALCFA) concrete and found that curing at temperatures of 60, 75 and 90°C gave AALCFA concrete with good compressive strengths. At low curing temperatures of 30 and 45 °C the strengths were rather slow. For AAHCFA pastes and mortars, the curing at moderate temperatures of 60 to 90°C was also required to obtain reasonable strength (Chindaprasirt et al., 2007; Guo et al., 2010).

3.1.3. Effect of duration of heat curing

In this test, a constant delay time of one hour and a temperature of heat curing of 60 °C were used. The heat curing durations of 0.5, 1, 2, 3 and 4 days were selected also based on the previous work. Hardjito and Rangan (2005) reported that the strength of AALCFA concrete increased with increasing curing duration of up to 4 days. Chindaprasirt et al. (2007) also reported the same trend of results with the curing duration up to 3 days.

3.2. Details of main test and mix design

In order to examine the potential influencing factors on the workability and strength of AAHCFA concrete, the effects of L/S ratio, NaOH concentration and Na_2SiO_3/NaOH ratio were investigated. Three L/S ratios of 0.55, 0.60 and 0.65, three NaOH concentrations of 10M, 15M and 20M and three Na_2SiO_3/NaOH ratios of 1.0, 1.5 and 2.0 were used. It should be pointed out that the concentrations of NaOH of 15M or 20M are high and may lead to difficulty in handling and to the increased cost. From a preliminary test, the use of low L/S ratios of 0.3 to 0.4 gave mixes with low slumps. The suitable workability range was obtained with the slightly higher values of L/S of 0.55-0.65 to avoid adding extra water in order to maintain the concentration of NaOH for better comparison of test results. The range of L/S of 0.52-0.71 was used to produce workable alkali-activated high calcium bottom ash mortar (Sathonsaowaphak et al., 2009). For reasons of cost and environmental gain, it is advisable to use slightly lower workable mix with lower L/S ratio in practice to reduce the amount of NaOH and Na_2SiO_3 usage. For example, the mix No.1 as shown in Table 2 (Na_2SiO_3/NaOH = 1, 10M NaOH and L/S = 0.55) consists of 1294 kg crushed stone, 554 kg sand, 356 kg fly ash, 98 kg Na_2SiO_3 and 98 kg NaOH. The delay time of 1 hour, the temperature of heat curing of 60 °C and the duration of heat curing of 1 day were employed based on the results obtained from the Section 3.1. The details of the mixes and their main molar ratios are given in Table 2.

The main oxide molar ratios of the mixes were varied in the following ranges: SiO_2/Al_2O_3 = 2.94-3.35, Na_2O/Al_2O_3 = 0.96-1.62 and H_2O/Na_2O = 7.06-12.20 as compared to SiO_2/Al_2O_3 = 3.5-4.5, Na_2O/Al_2O_3 = 0.8-1.2 and H_2O/Na_2O = 15-17.5 as suggested by Davidovits (1982). The 1.92 wt.% Na_2O in the fly ash was taken into account to calculate the overall ratio of H_2O/Na_2O as commonly practiced (Hardjito and Rangan, 2005; Sathonsaowaphak et al., 2009). Admittedly, it is questionable whether this Na_2O in the fly ash is present in a reactive phase and thus not all takes part in the reaction. Therefore, H_2O/Na_2O in the activator denoted by H_2O/Na_2O^* and modulus of the activator (Ms) viz., molar ratio of SiO_2/Na_2O are also given in Table 2.

3.3. Specimen preparations and tests

For each mix, the alkaline solution was obtained by dissolving sodium hydroxide pellets in water and then mixed with the sodium silicate solution. The liquid was then left to cool down to the temperature of 25-28 °C prior to using. This was done to eliminate the uncontrolled temperature effect. Prior mixing of sodium hydroxide solution and sodium silicate solution in the making of alkali-activated concrete is suggested by Hardjito and Rangan (2005) for the purpose of the reduction of bleeding and segregation.

The mixing of AAHCFA concrete started with the mixing of alkaline liquid and fly ash for 5 minutes. From trial mixes using different mixing times, it was found that the use of mixing time of 5 minutes gave a consistence paste and concrete with high compressive strength. The mixing of fly ash and NaOH solution for 5 minutes was used in the previous work (Chindaprasirt et al., 2007; Sathonsaowaphak et al., 2009). Sand and crushed stone in SSD condition were mixed together for 2 minutes in a pan mixer. This was followed by the addition of the premixed alkaline liquid and fly ash and continued the mixing for another 2 minutes. Right after the mixing, the slump test was performed in accordance with ASTM C 143/C 143M-00 (2000).

Table 2. Na_2SiO_3/NaOH, NaOH concentration, L/S, SiO_2/Al_2O_3, Na_2O/Al_2O_3, H_2O/Na_2O, H_2O/Na_2O* and Ms of the mixes

Mix No.	*Na_2SiO_3/ NaOH*	*NaOH concentraion*	*L/S*	*SiO_2/ Al_2O_3*	*Na_2O/ Al_2O_3*	*H_2O/ Na_2O*	*H_2O/ Na_2O**	*Ms*
1	1	10M	0.55	2.94	0.96	11.87	14.38	0.91
2	1	10M	0.60	3.01	1.03	12.05	14.38	0.91
3	1	10M	0.65	3.07	1.10	12.20	14.38	0.91
4	1	15M	0.55	2.94	1.18	8.97	10.44	0.71
5	1	15M	0.60	3.01	1.27	9.07	10.44	0.71
6	1	15M	0.65	3.07	1.36	9.16	10.44	0.71
7	1	20M	0.55	2.94	1.39	7.06	8.02	0.58
8	1	20M	0.60	3.01	1.51	7.13	8.02	0.58
9	1	20M	0.65	3.07	1.62	7.19	8.02	0.58
10	1.5	15M	0.55	3.08	1.07	9.82	11.64	0.95
11	1.5	15M	0.60	3.16	1.15	9.95	11.64	0.95
12	1.5	15M	0.65	3.24	1.23	10.06	11.64	0.95
13	1.5	20M	0.55	3.08	1.24	7.99	9.23	0.80
14	1.5	20M	0.60	3.16	1.34	8.08	9.23	0.80
15	1.5	20M	0.65	3.24	1.43	8.16	9.23	0.80
16	2	15M	0.55	3.18	0.99	10.49	12.61	1.15
17	2	15M	0.60	3.27	1.07	10.64	12.61	1.15
18	2	15M	0.65	3.35	1.14	10.77	12.61	1.15
19	2	20M	0.55	3.18	1.14	8.74	10.25	0.98
20	2	20M	0.60	3.27	1.22	8.85	10.25	0.98
21	2	20M	0.65	3.35	1.31	8.95	10.25	0.98

After that, specimens were cast in steel cylindrical moulds 100 mm in diameter and 200 mm in height. The fresh AAHCFA concrete was placed in three equal layers. Each layer was vibrated for 15 seconds on a vibrating table. After casting, the moulds were covered with vinyl sheet and left at 25-28 °C standing at a predetermined delay time before the temperature curing for a specified curing time in the oven. After heat curing, the specimens were put in the laboratory to cool down and then demolded. Finally, each specimen was wrapped with plastic film and left at 25-28 °C until the day of test. The compressive strength tests were conducted as per ASTM C 39/C 39M-01 (2001). The strength at the ages of 1, 3, 7 and 28 days were determined. The reported strengths are the average of three tests. The standard deviations are also plotted on the test data points as the error bar.

4. Results and discussion

4.1. Results of test for delay time, heat curing temperature and duration

4.1.1. Delay time

The results of the effect of delay time on compressive strength are shown in Fig. 2. The strength of 21.8 MPa was obtained by the sample with no delay time before the curing. When the delay time was 1 hour, the strength increased slightly to a maximum of 28.6 MPa. This is in agreement with the previous study (Chindaprasirt et al., 2007) on AAHCFA mortar, where a delay time longer than 1 hour slightly reduced the strength of mortar. For AALCFA concrete, a delay time of up to 72 hours was found to be beneficial to strength (Hardjito and Rangan, 2005). Some delay time allowed the dissolving of silica and alumina (Chindaprasirt et al., 2007) and therefore enhance the strength development of alkali-activated binder. Some delay time is highly desirable in practice especially in precast concrete industry as this gives sufficient time between casting products and preparing them for the heat curing.

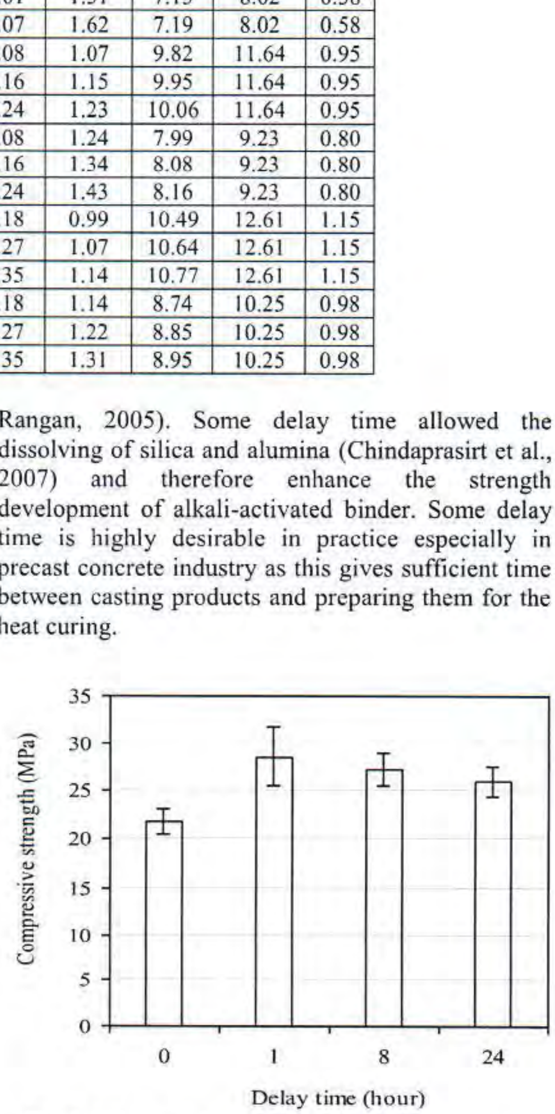

Fig. 2. Effect of delay time on the 7-day compressive strength of the Na_2SiO_3/NaOH = 1, 20M NaOH and L/S = 0.60 mixes

4.1.2. Effect of temperature of heat curing

The results of the temperature of heat curing on the strength are given in Fig. 3. The low curing temperatures of 25 and 40 °C gave the low compressive strengths of 7.5 and 10.5 MPa. The curing temperature of 60 °C gave the highest compressive strength of 28.6 MPa and when the temperature increased to 75 and 90 °C the compressive strength slightly dropped to 25.9 and 25.7 MPa, respectively. Similar reductions in strength with high curing temperature were reported for AAHCFA paste (Guo et al., 2010) and mortar (Chindaprasirt et al., 2007). The reductions in strengths were found when the curing temperature exceeded 75 °C.

4.1.3. Effect of duration of heat curing

The relation between compressive strength and duration of heat curing is displayed in Fig. 4. The highest strength of 28.6 MPa was obtained at the curing duration for 1 day and increased curing duration resulted in a slight decrease in strength. The previous study (Chindaprasirt et al., 2007) on AAHCFA mortar indicated that the optimum curing time was 3 days. The prolonged curing at elevated temperature could weaken the microstructure of alkali-activated fly ash binders (van Jaarsveld et al., 2002).

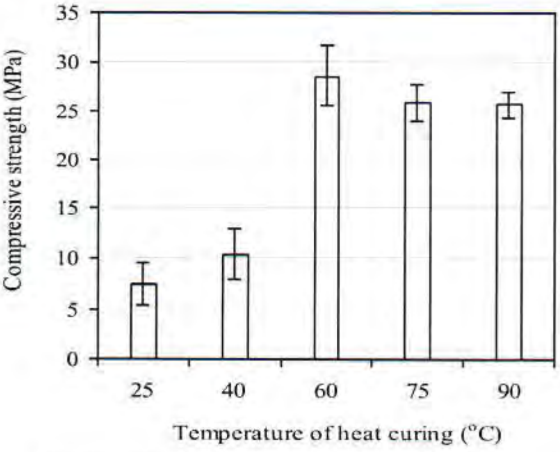

Fig. 3. Effect of temperature of heat curing on the 7-day compressive strength of the $Na_2SiO_3/NaOH = 1$, 20M NaOH and L/S = 0.60 mixes with heat curing duration of 1 day

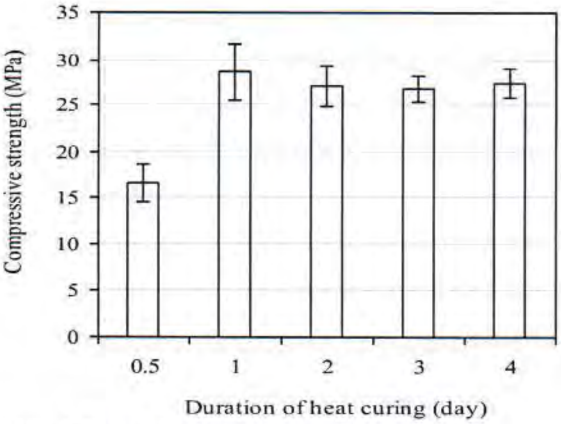

Fig. 4. Effect of duration of heat curing on the 7-day compressive strength of the $Na_2SiO_3/NaOH = 1$, 20M NaOH and L/S = 0.60 mixes with temperature of curing of 60 °C

4.2. Results of the main test series

4.2.1. Workability of the mixes

The details of the mixes are summarized in Table 2. For mixes with high $Na_2SiO_3/NaOH$ ratios of 1.5 and 2.0; and NaOH concentration of 10M, the setting of AAHCFA concrete was quite fast and there were not sufficient time for proper compaction. These mixes were discarded and not used to compare with the other results. The polymeric reactions of mixes using alkaline liquid contained soluble silicate occurred at a higher rate than those using only alkaline hydroxides (Palomo et al., 1999; Xu and Van Deventer, 2000). The presence of calcium played an important role in the fast setting of concrete. It was reported that the solubility of calcium increased with decreasing pH (Phair et al., 2000). The calcium concentration in the low 10M NaOH solution should therefore be higher than those in the higher 15M and 20M NaOH solutions. The high calcium content in the fly ash led to the formation of C-S-H which co-existed with the alkali-activated products (Xiaolu et al, 2010). It was highly likely that calcium silicates precipitated and performed as nucleation sites. This caused extra precipitation of dissolved species and rapid hardening (Lee and van Deventer, 2002; van Deventer et al., 2007). The results of slumps of AAHCFA concrete are shown in Fig. 5. For $Na_2SiO_3/NaOH = 1$, the slump increased with increasing L/S but decreased with increasing NaOH concentration as shown in Fig. 5(a). The high liquid content naturally improved the workability of the mixes. For the high NaOH concentration, the liquid became more viscous reducing the workability of the mixes. This happened despite the fact that at high NaOH concentration there was less chance of Ca ion entered into the solution from free lime, which would prevent C-S-H type phases to be formed and therefore increased the workability. At higher $Na_2SiO_3/NaOH$ ratios of 1.5 and 2.0 (Figs. 5(b) and 5(c)) the effect of L/S ratios was slightly less significant but the effect of NaOH concentrations was negligible. The slumps of the mixes as shown in Figs. 5(b) and 5(c) varied between 180-250 mm. It is known that the workability of alkali activated fly ash mortar and concrete is dependent on the water content of the mixes. From the results of a molar ratio analysis as shown in Table 2, the ratios of H_2O/Na_2O^* of the mixes with complete test results ranged between 8.02 - 14.38. Fig. 6 shows the plot of slump and H_2O/Na_2O^* molar ratio, it is confirmed that the important parameter affecting the slump of alkali activated fly ash concrete was the H_2O/Na_2O^* molar ratio. The increase in the H_2O/Na_2O^* molar ratio within the range of 8.02 to 9.23 (Table 2; Fig. 6) had a very strong influence on slump as it increased the slump from approximately 100 mm to 200 mm. The additional increase in the H_2O/Na_2O^* molar ratio led to a smaller increase in the slumps since the values were approaching the obtainable maximum slump values.

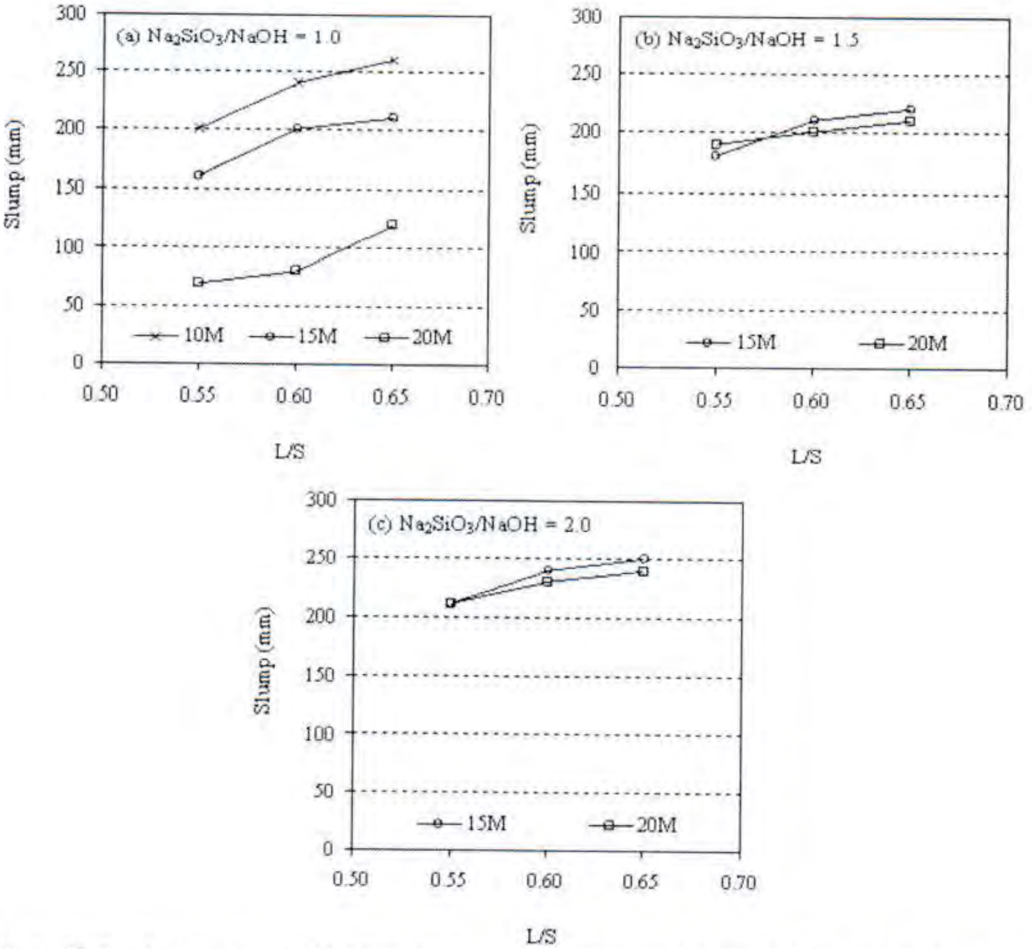

Fig. 5. Effects of L/S and concentration of NaOH on the slump of the mixes with delay time of 1 hour, curing temperature of 60 °C, curing duration of 1 day: (a) $Na_2SiO_3/NaOH = 1.0$, (b) $Na_2SiO_3/NaOH = 1.5$ and (c) $Na_2SiO_3/NaOH = 2.0$

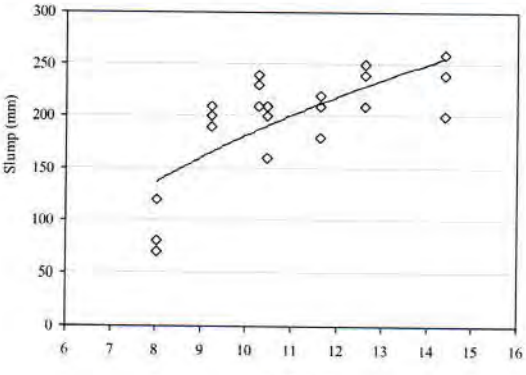

Fig. 6. Effect of molar ratio of H_2O/Na_2O in activator (H_2O/Na_2O^*) on the slump of mix with delay time of 1 hour, curing temperature of 60 °C and curing duration of 1 day

4.2.2. Strength of the AAHCFA concretes

In the presence of calcium, it has been reported that it is possible to have polymeric gel and C-S-H gel forming simultaneously (Alonso and Palomo, 2001; Yip et al., 2005). The C-S-H gel is believed to be different from the one resulting from the hydration of Portland cement. At high alkalinity (Ms = 1.2), the polymeric gel contributes to the strength of the binder whereas C-S-H gel contribute significantly to the binder compressive strength at lower alkalinity (Ms = 2.0) (Yip et al., 2005). In this study, the Ms of the mixes with complete test results ranged between 0.58-1.15 as shown in Table 2; therefore, polymeric gel should be the dominant phase contributing to the strength of the AAHCFA concretes.

The results of the compressive strength are shown in Fig. 7. The strength of AAHCFA concrete increased with increasing NaOH concentration and decreasing $Na_2SiO_3/NaOH$ ratio. The increase in strength with increasing NaOH concentration was directly related to the ability of the dissolution of silica and alumina into the solution (Rattanasak and Chindaprasirt, 2009). The dissolution from fly ash particles is usually better in higher NaOH concentrations. Regarding the effect of $Na_2SiO_3/NaOH$ ratio, the low $Na_2SiO_3/NaOH$ ratio of 1.0 resulted in high strength concrete compared to those of higher $Na_2SiO_3/NaOH$ ratios of 1.5 and 2.0. A similar strength reduction of alkali-activated mortar was reported for solutions of high

Na_2SiO_3/NaOH ratio of 2.0 and NaOH concentrations of 10M and 15M (Rattanasak and Chindaprasirt, 2009). The reduction in strength with high Na_2SiO_3/NaOH ratio should again relate to the amount of silica and alumina dissolved into the solution. At high Na_2SiO_3/NaOH ratio, the amount of silicate is high and the water content is also high since this Na_2SiO_3 contained relatively high amount of water. At high Na_2SiO_3/NaOH ratio, the amount of NaOH was low and the dissolving of both silica and alumina were also low. The alkali-activated fly ash products with high silica to alumina ration were obtained. The strength reduction was likely related to the increase in the water content of the mixes and the high silica to alumina ratio of the products (Detphan and Chindaprasirt, 2009; Fletcher et al., 2005).

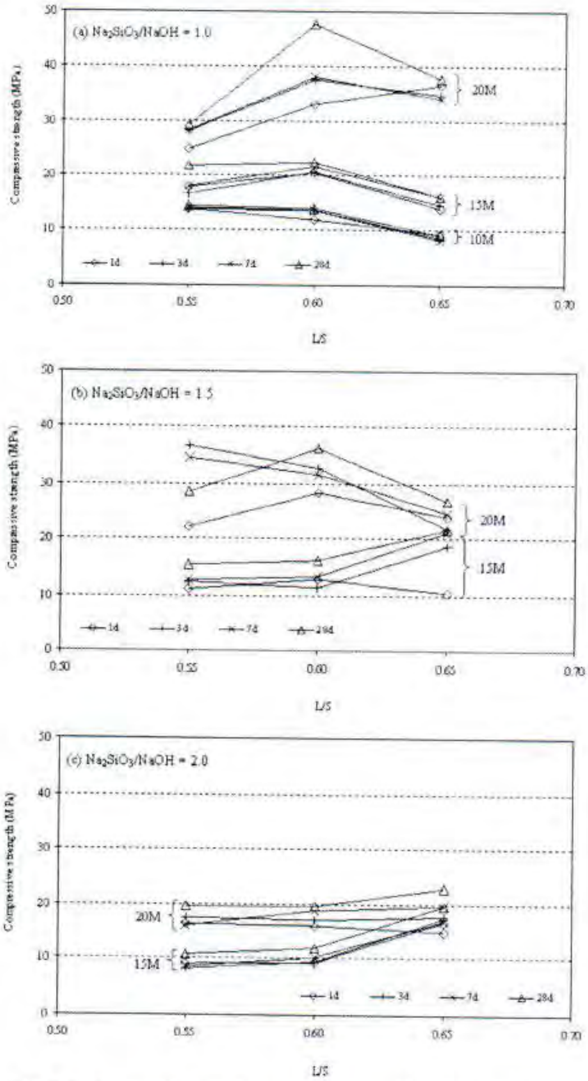

Fig. 7. Effects of L/S and concentration of NaOH on the compressive strength of the mixes with delay time of 1 hour, curing temperature of 60 °C, curing duration of 1 day: (a) Na_2SiO_3/NaOH = 1.0, (b) Na_2SiO_3/NaOH = 1.5 and (c) Na_2SiO_3/NaOH = 2.0

The L/S ratio also had a small effect on the compressive strength. At low NaOH concentration of 10M, the compressive strengths of the mixes with L/S ratios of 0.55 and 0.60 were approximately the same, but the strengths of the mixes with L/S ratio of 0.65 were slightly lower. At high alkali liquid content (L/S ratio of 0.65), the mixes contained low amount of fly ash. This should result in the lower amount of silica and alumina dissolved into the solution and also in a higher water volume that will evaporate leaving empty spaces in the microstructures.

At Na_2SiO_3/NaOH ratio of 1 and NaOH concentrations of 15M and 20M, the mixes with L/S ratio of 0.60 gave optimum strengths as shown in Fig. 7(a). At the lower L/S ratio of 0.55, the amount of liquid was low and the dissolving of the silica and alumina was therefore slowed down as the results of the increased concentration of the silica and alumina in the solution. Water is an essential part of polymerization and hydration reaction. However, the increase in the water content as a result of the increase in the L/S ratio produced a weak matrix in a similar manner to the high water to cement ratio in the Portland cement system.

As mentioned before, the sodium silicate solution used in this test was high in water content and the workability and strength results were therefore influenced by this. Furthermore, the results reported on the influence of the high calcium content might have been influenced by the method of mixing the alkali-activated fly ash concrete adopted.

5. Conclusions

The effects of several parameters on the slump and strength of alkali-activated high calcium fly ash (AAHCFA) concrete have been investigated. Based on results obtained with the materials and the method of mixing used in this experiment, the following conclusions could be made.

1. The use of high calcium fly ash and NaOH with low concentration of 10M resulted in relatively fast setting of the alkali-activated fly ash concrete.
2. The workability of AAHCFA concrete was related to the molar ratio of H_2O/Na_2O in activator. The L/S ratio and NaOH concentration also had some effects on the workability.
3. The compressive strength increased with the increase in the NaOH concentrations and reduced with the increase in the Na_2SiO_3/NaOH ratio. The L/S ratio also had some effect on strength but to a lesser extent.
4. The AAHCFA concretes with high strengths were obtained when the delay time of 1 hour, the heat curing temperature of 60 °C and the heat curing duration of 1 day were employed.

Acknowledgements

The authors would like to acknowledge the financial support from the Faculty of Engineering, Mahasarakham University. The support from the Thailand Research Fund (TRF) under the TRF Senior Research Scholar, Grant No. RTA5480004 is also gratefully acknowledged.

References

ASTM C 39/C 39M-01, (2001), Standard Test Method for Compressive Strength of Cylindrical Concrete Specimens, American Society for Testing and Materials, ASTM International, Philadelphia, USA.

ASTM C 143/C 143M-00, (2000), Standard Test Method for Slump of Hydraulic-Cement Concrete, American Society for Testing and Materials, ASTM International, Philadelphia, USA.

ASTM C 204-00, (2000), Standard Test Methods for Fineness of Hydraulic Cement by Air-Permeability Apparatus, American Society for Testing and Materials, ASTM International, Philadelphia, USA.

ASTM C 618-03, (2003), Standard Specification for Coal Fly Ash and Raw or Calcined Natural Pozzolan for Use as a Mineral Admixture in Concrete, American Society for Testing and Materials, ASTM International, Philadelphia, USA.

Alonso S., Palomo A., (2001), Calorimetric study of alkaline activation of calcium hydroxide-metakaolin solid mixtures, *Cement and Concrete Research*, **31,** 25-30.

Chindaprasirt P., Chareerat T., Sirivivatnanon, V., (2007), Workability and strength of coarse high calcium fly ash geopolymer, *Cement and Concrete Composites*, **29,** 224-229.

Chindaprasirt P., Jaturapitakkul C., Chalee W., Rattanasak U., (2009), Comparative study on the characteristics of fly ash and bottom ash geopolymers, *Waste Management*, **29,** 539-543.

Davidovits J., (1982), Mineral Polymers and Methods of Making Them. USA Patent, No. 4, *349,386*.

Davidovits J., (1999), *Chemistry of geopolymeric systems terminology*, The 2nd International Conference Geopolymere'99, Saint-Quentin, France, 9–40.

Detphan S., Chindaprasirt P., (2009), Preparation of fly ash and rice husk ash geopolymer, *International Journal of Minerals, Metallurgy and Materials*, **16,** 720-726.

Duxson P., Fernández-Jiménez A., Provis, J., Lukey, G., Palomo, A., Van Deventer, J., (2007), Geopolymer technology: the current state of the art, *Journal of Materials Science*, **42,** 2917-2933.

Fletcher R.A., Mackenzie K.J.D., Nicholson C.L., Shimada S., (2005), The composition rang of aluminosilicate geopolymers, *Journal of the European Ceramic Society*, **25,** 1471-1477.

Guo X., Shi H., Dick W.A., (2010), Compressive strength and microstructural characteristics of class C fly ash geopolymer, *Cement and Concrete Composites*, **32,** 142-147.

Hardjito D., Rangan B.V., (2005), *Development and properties of low-calcium fly ash based geopolymer concrete*, Research Report GC1, Faculty of Engineering, Curtin University of Technology, Perth, Australia.

Lee W.K.W., van Deventer J.S.J., (2002), The effect of ionic contaminants on the early-age properties of alkali-activated fly ash-based cements, *Cement and Concrete Research*, **32,** 577-584.

Malhotra V.M., (2002), High-Performance High-Volume Fly Ash Concrete, *ACI Concrete International*, **24,** 1-5.

Pacheco-Torgal F., Castro-Gomes J., Jalali S., (2008), Alkali-activated binders: A review: Part 1. Historical background, terminology, reaction mechanisms and hydration products, *Construction and Building Materials*, **22,** 1305-1314.

Palomo A., Grutzeck M.W., Blanco M.T., (1999), Alkali-activated fly ashes: A cement for the future, *Cement and Concrete Research*, **29,** 1323-1329.

Phair J.W., van Deventer J.S.J., Smith J.D., (2000), Mechanism of Polysialation in the Incorporation of Zirconia into Fly Ash-Based Geopolymers, *Industrial & Engineering Chemistry Research*, **39,** 2925-2934.

Rattanasak U., Chindaprasirt P., (2009), Influence of NaOH solution on the synthesis of fly ash geopolymer, *Minerals Engineering*, **22,** 1073-1078.

Sathonsaowaphak A., Chindaprasirt P., Pimraksa K., (2009), Workability and strength of lignite bottom ash geopolymer mortar, *Journal of Hazardous Materials*, **168,** 44-50.

van Deventer J.S.J., Provis J.L., Duxson P., Lukey G.C., (2007), Reaction mechanisms in the geopolymeric conversion of inorganic waste to useful products, *Journal of Hazardous Materials*, **139,** 506-513.

van Jaarsveld J.G.S., Van Deventer J.S.J., Lukey G.C., (2002), The effect of composition and temperature on the properties of fly ash- and kaolinite-based geopolymers, *Chemical Engineering Journal*, **89,** 63-73.

Xiaolu G., Huisheng S., Warren A.D., (2010), Compressive strength and microstructural characteristics of class C fly ash geopolymer, *Cement and Concrete Composites*, **32,** 142–147.

Xu H., van Deventer J.S.J., (2000), The geopolymerisation of alumino-silicate minerals, *International Journal of Mineral Processing*, **59,** 247-266.

Yip C.K., Lukey G.C., van Deventer J.S.J., (2005), The coexistence of geopolymeric gel and calcium silicate hydrate at the early stage of alkaline activation, *Cement and Concrete Research*, **35,** 1688-1697.

Yip C.K., Lukey G.C., Provis, J.L., van Deventer, J.S.J., (2008), Effect of calcium silicate sources on geopolymerisation, *Cement and Concrete Research*, **38,** 554-564.

Journal of Cleaner Production 41 (2013) 31–41

Contents lists available at SciVerse ScienceDirect

Journal of Cleaner Production

journal homepage: www.elsevier.com/locate/jclepro

Cement mortars hybridized with zeolite and zeolite-like materials made of lignite bottom ash for heavy metal encapsulation

Kedsarin Pimraksa [a,b,*], Prinya Chindaprasirt [c], Tanwalak Huanjit [a], Clarence Tang [d], Tsugio Sato [e]

[a] *Department of Industrial Chemistry, Faculty of Science, Chiang Mai University, Chiang Mai 50200, Thailand*
[b] *Materials Science Research Center, Faculty of Science, Chiang Mai University, Chiang Mai 50200, Thailand*
[c] *Sustainable Infrastructure Research and Development Center, Department of Civil Engineering, Faculty of Engineering, Khon Kaen University, 40002, Thailand*
[d] *Siam Research and Innovation Co., Ltd., Saraburee 18260, Thailand*
[e] *Institute of Multidisciplinary Research for Advanced Materials, Tohoku University, 980-8577, Japan*

ARTICLE INFO

Article history:
Received 28 August 2012
Received in revised form
1 October 2012
Accepted 3 October 2012
Available online 22 October 2012

Keywords:
Natrolite-K
Potassium aluminosilicate hydrate
Zeolite hybridized cement mortar
Pozzolanic reaction
Heavy metal encapsulation

ABSTRACT

Bottom ash (BA) from Mae Moh lignite power plant was used to synthesize zeolite and zeolite-like materials. Low temperature synthesis (100–110 °C) was completed using SiO_2 to Al_2O_3 with molar ratios of 2.94 and 2.92, respectively. Factors investigated that affect synthesis include particle size distribution, pretreatment of BA, concentration of alkali solution and liquid to solid ratio. The synthesized product qualities were characterized by mineralogical composition, morphology, specific surface area, pore size, pore volume and cation exchange capacity. Natrolite-K zeolite (NAT-K) was obtained with a solution of BA and 7 M KOH. Zeolite-like material (potassium aluminosilicate hydrate: KASH) was obtained using very fine BA and 9 M KOH solution. The NAT-K, KASH and BA powders were used to replace type I Portland cement at 0, 5, 10, 20 and 30% by weight to produce composite materials for heavy metal encapsulation. The compressive strength and bulk density of the NAT-K- or KASH-hybridized cement mortars were tested at 1, 7 and 28 days. The heavy metal encapsulation capacity was also tested using the 28-day cement mortar containing either 5 wt% NAT-K or KASH adsorbed with Cr, Ni and Cd ions. The results showed that 5 wt% of NAT-K could improve early strength of cement mortar and the 28-day specimens with 5–10 wt% of NAT-K replacement had compressive strength similar to that of the normal cement mortar. The NAT-K and KASH encapsulate Cr, Ni and Cd ions in the structures of cement mortar matrices more than 97%.

1. Introduction

Worldwide, the coal industry annually produces several million metric tons of by-products such as fly ash (FA), bottom ash, boiler slag and flue gas desulfurization material (Ríos and Williams, 2008). The yearly output of lignite bottom ash (BA) produced at the Mae Moh power plant in Thailand is approximately 0.8 MT, and it is discarded in landfills as solid wastes. The BA needs proper grinding to obtain a reasonably fine particle size for use as pozzolan (Sathonsaowaphak et al., 2009). The BA from the coal industry contains heavy metals and is harmful to the environment. It is often used as a low-cost replacement for more expensive sand in the production of concrete blocks. In many countries, it is used as a base course in road construction (Cheriaf et al., 1999). Synthesis of zeolites from BA is one of the promising ways to create a more environmentally friendly use of the unused solid waste. One of the good examples is synthesis of zeolite A from BA obtained from coal-fired boilers within the paper industries in Thailand (Chareonpanich et al., 2011). The BA obtained from the paper industry contains more crystalline silica content than that obtained from steam boilers at Mae Moh power plant. Moreover, due to the different coal source, their chemical and mineralogical compositions are not similar. In this study, low temperature zeolite synthesis from lignite BA obtained from Mae Moh power plant is investigated.

Zeolite has a crystalline aluminosilicate structure with a SiO_4 tetrahedra framework. Parts of the structure are substituted with AlO_4 tetrahedra which require charge-compensating cations. These tetrahedral units are connected with each other as repeating units forming 3-D porous framework structures in a molecular size (Kadono et al., 2008). The advantage of zeolites over resins, apart

---

[*] Corresponding author. Department of Industrial Chemistry, Faculty of Science, Chiang Mai University, Chiang Mai 50200, Thailand. Tel.: +66 819506645; fax: +66 53892262.

E-mail addresses: kpimrak.p@cmu.ac.th, kedsarin.p@cmu.ac.th (K. Pimraksa).

0959-6526/$ – see front matter © 2012 Elsevier Ltd. All rights reserved.
http://dx.doi.org/10.1016/j.jclepro.2012.10.003

from their much lower cost, is their ion selectivity. Because of the characteristics of zeolite structures and their adsorbent properties, they have been applied as chemical sieve, water softener and adsorbents (Hui et al., 2005). Various types of zeolites can be synthesized from different source materials and under different conditions. BA, like fly ash, is considered as a starting material because of its promising chemical and mineralogical compositions and abundant availability. Although coming from the same source, mineralogical compositions of BA are totally different from FA due to their combustion temperature. For example, FA contains inert material such a mullite which is not easy to be dissolved (Chindaprasirt and Pimraksa, 2008). However, BA has been utilized less because its particle size is large and grinding is required to reduce the particle size and to increase its reactivity.

In previous work, we found that the optimum refluxing conditions for zeolite synthesis from Mae Moh BA with $d_{[4,3]}$ of 23 micron and Si/Al molar ratio of 1.5 or SiO_2/Al_2O_3 ratio of 3.06 were 5 M KOH solution, liquid to BA ratio (L/S ratio) of 8 and reaction time of 24 h (Pimraksa et al., 2010). This resulted in the formation of a zeolite-like material in the form of potassium aluminum silicate hydrate (KASH) ($KAlSiO_4.15H_2O$) as a main composition and phillipsite-K ($K_2[Al_2Si_{2.2}O_{6.4}].2H_2O$) as a minor phase. When 3 M NaOH solutions were used, there was no zeolite formation. This research, therefore, aims to study further the synthesis of zeolite phases from Mae Moh BA to discover more potential uses of BA for heavy metal encapsulation. Various factors affecting this synthesis, including KOH concentration, liquid to solid ratio, iron content and particle size distribution of BA were investigated. The quality of the synthesized zeolite is characterized in terms of mineralogical composition, microstructure, pore size, pore volume and CEC.

There are many kinds of zeolites suitable for use in encapsulation. Among those that perform best for ion exchange are the ones with a large number of negative charges in the framework. For ion adsorption capacity, zeolites with a large number of cavities and large surface areas in the framework works best (Alex and Dong-ke, 2003). Zeolite-like materials have also been considered for adsorption applications because of their high specific surface area (Gao et al., 2009). Waste encapsulation is now in high demand as huge amount of toxic industrial wastes have been disposed of in landfills. Therefore, it is very important to find a high potential waste encapsulation material. Zeolites possess some pozzolanic properties and they can be used as a pozzolanic material by blending with normal cement (Poona et al., 1999; Jana, 2007). They contribute to concrete strength mainly through the pozzolanic reaction, similar to other widely used pozzolans such as silica fume, metakaolin and fly ash. The zeolite is a meta-stable phase that readily undergoes dissolution under basic conditions with different manner from BA and one of the most reactive pozzolans such a metakaolin due to their molecular structures (Pelisser et al., 2012). The demand for such supplementary cementing materials has been markedly increasing in order to reduce cement production to cope with global warming (Yilmaz et al., 2007). In addition to the strength improvement, zeolites, when present in cement and concrete structures, also play an important role in the encapsulation of several types of heavy metals (Atkins et al., 1995; Olmo et al., 2003; Ok et al., 2007). Both the pozzolanic reactivity and waste encapsulation of zeolites are thus of much interest to cement chemists, concrete technologists and environmental scientists. Therefore, this study aims to use BA obtained from the Mae Moh power plant (Thailand) as a starting material for zeolite synthesis and to find the optimum condition for synthesis. The pozzolanic reactivity of the synthesized zeolite is then studied and compared with the ground BA. A comparison in pozzolanic reactivity of BA synthesized zeolites and BA was performed in this study for the first time. Not only pozzolanic reactivity, the heavy metal (chromium (III), nickel (II) and cadmium (II)) encapsulation ability of the zeolite materials and zeolite-like-hybridized cement mortars is also studied. It is commonly known, that Cr, Ni and Cd ions are typically found in electroplating wastes (Telukdarie et al., 2006). Moreover, Cr ion is one of the carcinogenic metals which can be very harmful to the ground and water, seriously concerned in many countries which run a leather industry as their main market. Active absorbers for those heavy metal removal are, therefore, very important for mitigation of the negative impact (Giannetti et al., 2004). The knowledge obtained from this study will no doubt lay a solid groundwork for the conversion of lignite BA into zeolite and zeolite-like materials, for waste encapsulation using zeolite-hybridized cement material as well as for the utilization of BA in a high potential way.

2. Experimental methods

2.1. Materials

Lignite BA used for zeolite synthesis was obtained from the Mae Moh power plant. The BA was ground by ball milling to obtain various particle size distributions. The BA volumetric mean diameter ($d_{[4,3]}$) after grinding for 12, 24 and 48 h were 13.3, 6.6 and 3.0 μm, respectively. The ground BA was treated to remove the iron compound using the looped magnetic separator until the iron content was lowered by 50%. The chemical composition of BA determined using X-ray fluorescence spectrometry (XRF) is shown in Table 1. BA was stirred in 5–9 M KOH solutions for 24 h in a 25 °C room to investigate the concentrations of reactive cations (Si^{4+} and Al^{3+}). The investigated condition, shown in Table 2, was determined to be the best condition based on the results of a previous study (Pimraksa et al., 2010). The reactive ions were measured using Atomic Absorption Spectroscopy (AAS). The total content of heavy metals contained in BA and type I Portland cement were determined using AAS and Inductively Coupled Plasma-Mass Spectroscopy (ICP-MS) carried out in accordance with ASTM D3688-78.

2.2. Zeolite synthesis

The as-received BA and the BA from which iron was removed BA, with SiO_2/Al_2O_3 molar ratios of 2.94 and 2.92, respectively, were used as starting materials. The conditions of zeolite synthesis are shown in Table 2. The effects of ground BA particle size, iron oxide removal from BA, KOH concentration and liquid to solid ratios on zeolite quality were studied. It was shown that the zeolite phase obtained from the refluxing method was better than that from the hydrothermal method (Pimraksa et al., 2010). Therefore, the refluxing method was selected for synthesis. The ground BA was stirred with the KOH solution for 30 min to allow the dissolution of silicate and aluminate ions. Refluxing was carried out at 100–110 °C for 24 h. The reaction time and temperature were taken from

Table 1
Chemical compositions of as-received BA and magnetically treated BA.

Compositions	As-received BA (%)	Magnetic treated BA (%)
SiO_2	38.69	41.19
Al_2O_3	22.25	24.19
Fe_2O_3	13.75	6.89
CaO	13.16	13.14
MgO	2.83	2.62
Na_2O	0.53	0.73
K_2O	1.97	2.25
TiO_2	0.39	0.38
SO_3	0.82	0.71
P_2O_5	0.16	0.16
LOI	5.19	3.50

Table 2
Conditions for synthesis.

No.	Particle size, $[d]_{4,3}$ (μm)	Iron compound removal	KOH concentration (molar)	Liquid:solid ratio (L/S ratio)
1	13.3	✓	5	8
2	6.6	✗	5	8
3	3.0	✓	5	8
4	6.6	✗	5	6
5	6.6	✗	5	10
6	6.6	✓	5	8
7	6.6	✗	7	8
8	6.6	✓	7	8
9	6.6	✗	9	8
10	6.6	✓	9	8
11	3.0	✗	9	8
12	3.0	✓	9	8
13	3.0	✗	7	8
14	3.0	✓	7	8

a previous work (Pimraksa et al., 2010). The solid products were filtered and washed with deionized water until the pH of the filtrate reached 10. The sample was then dried at 110 °C for 24 h. The solid phases obtained after drying were characterized in terms of the mineralogical composition using X-Ray Diffractometry (XRD) and morphology using Scanning Electron Microscopy (SEM) and Energy Dispersive Spectroscopy (EDS). Specific surface area was determined using Brunauer–Emmett–Teller (BET) and mercury porosimetry (MIP) was used to determined pore sizes. The cation exchange capacity (CEC) was measured using the ammonium exchange capacity by the titration method in accordance with the method of the soil analysis method (Rhoades, 1982). The exchangeable cations of the zeolites were replaced by NH_4^+ using 1 N ammonium acetate solution.

2.3. NAT-K and KASH used as hybrid materials

The cement mortar samples were prepared using a water to cement ratio of 0.6 and cement to sand ratio of 1:2.75, by weight. The synthesized NAT-K, KASH and BA were used to replace Portland cement by weight at 0%, 5%, 10%, 20% and 30%. The prepared mortars were cast in 2 × 2 × 2 cm^3 brass molds. The samples were removed from the molds after 1 day and then cured in a lime-saturated solution in a temperature-controlled room at 25–27 °C until testing. The compressive strength was tested at 1, 7 and 28 days using a universal strength testing machine (Tinius Olsen, H50KT). Microstructure investigations using XRD and SEM-EDS were conducted on the cement pastes at 1, 7 and 28 days. The hydration of the cement pastes was stopped by soaking in acetone for 2 days and drying at 60 °C until a constant weight was obtained.

2.4. Waste encapsulation capacity of cement mortars hybridized with NAT-K and KASH

The $Cr(NO_3)_3.9H_2O$, $Ni(NO_3)_2.6H_2O$ and $Cd(N_2O_3)_2.4H_2O$ solutions were used as sources of Cr^{3+}, Ni^{2+} and Cd^{2+} ions, respectively, where 100 ppm of each solution was prepared. 100 g of NAT-K, KASH and BA were soaked separately in 100 ppm solutions of Cr^{3+}, Ni^{2+} and Cd^{2+} for 24 h. The amount of heavy metal adsorption on each material was confirmed by ICP detection, which was performed on the solutions after soaking. The heavy metals adsorbed on the materials were then dried at 60 °C until constant weights were obtained. To prepare the cement mortar, 5 wt% of heavy metal-adsorbed materials were used to replace Portland cement. Adsorbed heavy metal contents on hybrid materials before leaching test were calculated from the used material by weight obtained from the heavy metal adsorption test. After 28 days, the cured mortars were tested for leaching of heavy metal in accordance with TCLP. The 2 × 2 × 2 cm^3 mortar specimen was soaked in diluted acetic acid solution with a solid to liquid ratio of 1:20. The solution was then subjected to circulation using magnetic stirring for 20 ± 2 h in accordance with DIN 38414-S4. The leachate solutions were analyzed for heavy metal concentration using ICP-MS. The heavy metal encapsulation capacity was estimated by the subtraction of the adsorbed heavy metal content and the leached heavy metal content.

3. Results and discussion

3.1. Materials

Chemical compositions of as-received BA and magnetic treated BA are shown in Table 3. Mineralogical compositions of as-received BA consisted of anorthite ($CaAl_2Si_2O_8$), augite ($(Na, Ca, K)_2(Al, Si)_2O_6$), quartz ($SiO_2$), maghemite ($\gamma$-$Fe_2O_3$), magnetite ($Fe_3O_4$) and glassy phase. With the use of magnetic separation, the iron oxide content mostly in the form of magnetite was reduced by 50 wt%. Therefore, the starting materials without iron removal and with iron removal contained SiO_2/Al_2O_3 molar ratios of 2.94 and 2.92, respectively. The amounts of dissolved aluminum and silicon species as described by Si/Al ratios in various synthesized conditions are shown in Table 3. The starting SiO_2/Al_2O_3 and Si/Al ratio of BA was 2.94 and 1.74, respectively. The reactive Si^{4+} and Al^{3+} ions dissolved from BA with 5 M KOH solution were 871 and 527 ppm, respectively, giving a Si/Al ratio of 1.65. This ratio was slightly lower than that of BA confirming that there was some undissolved silica left behind with the alkali activation. With a decrease in particle size from 13.3 to 3.0 μm, the Si/Al ratios decreased. The aluminum

Table 3
Dissolved aluminum (Al^{3+}) and silicon (Si^{4+}) contents, Si/Al ratios of BA activated by various synthesized conditions and specific surface areas of synthesized products.

Particle sizes (μm)	Iron removal	KOH conc. (M)	Liquid to solid ratios	Dissolved amounts (ppm)			Major products	Spec. surf. areas of products (m^2/g)
				Si	Al	Si/Al ratios		
13.3	✓	5	8	767	415	1.85	NAT-K	18.26
6.6	✗	5	8	927	582	1.60	NAT-K	20.66
3.0	✓	5	8	1157	768	1.51	NAT-K	19.39
6.6	✗	5	6	1052	658	1.60	NAT-K	21.74
6.6	✗	5	10	1149	757	1.52	NAT-K	22.81
6.6	✓	5	8	1030	642	1.60	NAT-K	23.43
6.6	✗	7	8	1186	669	1.77	NAT-K	26.56
6.6	✓	7	8	1424	891	1.60	NAT-K	30.92
6.6	✗	9	8	1234	746	1.65	KASH	33.28
6.6	✓	9	8	1280	771	1.65	KASH	32.55
3.0	✗	9	8	1511	931	1.62	KASH	30.19
3.0	✓	9	8	1544	966	1.60	KASH	30.94
3.0	✗	7	8	1403	875	1.60	KASH	33.42
3.0	✓	7	8	1533	977	1.57	KASH	36.97

phases with the smaller particle sizes were more susceptible to dissolution. However, for the same particle size, the use of a high L/S ratio resulted in low Si/Al. For a high KOH concentration, the Si/Al ratio tended to increase because of the increased susceptibility of the silicate phases. When the fine particle size and high KOH concentration were used, the leaching of both aluminate and silicate phases was enhanced.

The total heavy metal concentrations of BA and Portland cement type I are shown in Table 4. The major heavy metals contained in BA were Mn (556.75 ppm), Se (270.81 ppm), Zn (83.47 ppm) and Ni (72.80 ppm). For ordinary Portland cement, the major heavy metals were Zn (956.62 ppm), Mn (431.18 ppm), Cu (281.87 ppm) and Cr (75.30 ppm). Both of them consisted mainly of Mn and Zn. The Portland cement contained a large amount of Zn likely due to the utilization of Zn-bearing waste, such as used tires, as alternative fuel, which leads to the changes in chemical reaction of cement minerals (Trezza, 2007). The Mn was likely present in BA, as it was commonly found in some minerals in coal mines (Larsen and Mann, 2005).

3.2. Zeolite synthesis

Four factors, including particle size, liquid/solid ratio (L/S ratio), KOH concentration and iron compound removal, were considered. Fig. 1 shows the results of the XRD patterns of products obtained from different BA particle sizes. With the same refluxing condition (100–110 °C for 24 h and 5 M KOH), 6.6 μm BA showed the highest peak intensity of zeolite in a form of natrolite-K ($(K_{0.988}Na_{0.012})(AlSi_{1.5}O_5)(H_2O)$ or NAT-K) which was observed at $2\theta = 12.8°$. To form NAT-K, SiO_2/Al_2O_3 or Si/Al molar ratios of about 3.0 or 1.5 were theoretically required. The starting SiO_2/Al_2O_3 and Si/Al ratios of used BA were 2.94 and 1.47, respectively, which conformed to the requirement of the NAT-K chemical pattern. Using a similar synthesis routine but with a different BA particle size, the obtained zeolite type was different from the previous work. With 23 μm BA used in the previous work, zeolite-like material in the form of potassium aluminum silicate hydrates ($KAlSiO_4.15H_2O$) with a Si/Al ratio of 1.0 and a small amount of zeolite (phillipsite-K) with a Si/Al ratio of 1.1 were obtained (Pimraksa et al., 2010). It was shown that for coarse BA, some of the silicon ion bearing phases did not dissolve. In this work, for the fine BA, quartz, augite and glassy phases changed to NAT-K with a Si/Al ratio of 1.5. However, anorthite ($(Ca, Na)(Al, Si)_2Si_2O_8$) which was one of the inert silicon-bearing mineral was still left behind. The natrolite zeolite group was one of the key players for ion exchange and adsorption (Noroozifar et al., 2009; Singh et al., 2011); therefore, it was used for waste encapsulation in this study. With the use of 3.0, 6.6 and 13.3 μm BA, in addition to NAT-K formation, calcium silicate hydrate in the form of jusite ($(Ca, Na, K)_5(Si, Al)_6O_{15}.5H_2O$) and rosenhahnite ($Ca_3Si_3O_9.H_2O$) and non-hydrated and iron-bearing products such as hedenbergite ($Ca(Fe, Mg)(SiO_3)_2$), were also found as minority species. With respect to the effect of particle size, the reduction in BA particle size from 13.3 to 6.6 μm facilitated the dissolubility of Si^{4+} and Al^{3+} and other ions such as Fe^{3+} and Ti^{4+} because of the increase in the surface areas resulting from the broken edges. This hindered zeolite precipitation (Wang et al., 2008) and led to the formation of a more stable phase of potassium aluminum silicate hydrate.

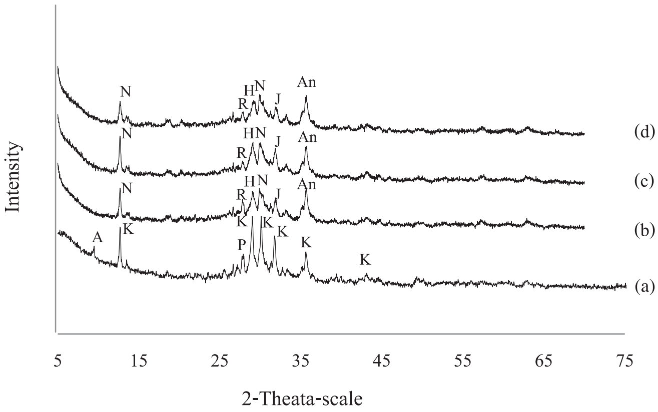

Fig. 1. XRD-pattern of products obtained from different BA particle sizes (a) 23 μm, (b) 13.3 μm, (c) 6.6 μm and (d) 3.2 μm. N = Natrolite-K [$K_{15.8}Na_{0.2}(Al_{16}Si_{24}O_{80}).16H_2O$], An = Anorthite [$(Ca,Na)(Al,Si)_2Si_2O_8$], H = Hedenbergite [$Ca(Fe, Mg)(SiO_3)_2$], J = Jusite [$(Ca,Na,K)_5(Si,Al)_6O_{15}.5H_2O$], R = Rosenhanite [$Ca_3Si_3O_9.H_2O$], Q= Quartz [$SiO_2$], P = Philipsite-K, K = Potasium Aluminum Silicate Hydrate [$KAlSiO_4.1.5H_2O$], A = Aluminum Titanium Phosphorus Silicon Oxide

The XRD results of the synthesized products for the L/S ratios 6, 8 and 10 are shown in Fig. 2(a), (b) and (c). The tests were performed using 6.6 μm BA, 5 M KOH solution and 100–110 °C for 24 h refluxing. The highest peak intensity of NAT-K was obtained when the L/S ratio was 8. At the dissolution stage, the increase in the L/S ratio resulted in the increased solubility of Si^{4+} and Al^{3+} including the counter ions such as Fe^{3+}. Walex et al. (2008) found that at a high L/S ratio, the dissolution of raw materials in an alkaline solution increased and also contributed to a high degree of crystallization. However, for practical applications, the favorable condition for dissolution was not desirable for zeolite crystallization. The system with the high L/S ratio contained a high water content, which caused the suppression of ion saturation and crystallization. As a result, 6.6 μm BA with an L/S ratio of 8 was chosen for further experimentation in the removal of iron oxide compounds from BA.

Table 3 shows the result of iron oxide contents removed from BA. The reduction of iron oxide was approximately 50% when BA was treated by the looped magnetic separator. According to the XRD patterns of synthesized products shown in Fig. 3(a) and (b), the NAT-K peak intensities of treated and untreated BA in 5 M KOH were quite similar, with a slight decrease in anorthite phase. All iron oxides in BA were not dissolved in the 5 M KOH solution and thus could not form precipitates of insoluble iron hydroxides. The insoluble $Fe(OH)_3$ acted as an inducer for the formation of hydrogarnet which could then compete with the zeolitization reaction (Wang et al., 2008).

Slightly higher KOH concentrations of 7 M and 9 M were used to compare the untreated BA and the magnetically treated BA. The results shown in Fig. 3(c) and (d) suggested that the use of treated BA and 7 M KOH produced the partial collapse of the anorthite structure and the NAT-K quantity was enhanced. For 9 M KOH, the XRD patterns shown in Fig. 3(e) and (f) revealed the crystals of potassium aluminum silicate hydrate (KASH: $KAlSiO_4.15H_2O$) with the presence of a small amount of kaliophilite ($KAlSiO_4$). However,

Table 4
Total heavy metal contents of BA and ordinary Portland cement (OPC); unit: ppm.

Samples	As	Cd	Cr	Cu	Hg	Mn	Ni	Pb	Se	Zn
BA	8.06	<0.01	59.25	58.60	<0.01	556.75	72.81	<0.01	270.81	83.47
OPC	4.16	2.36	75.30	281.87	<0.01	431.18	35.36	68.45	<0.01	956.62

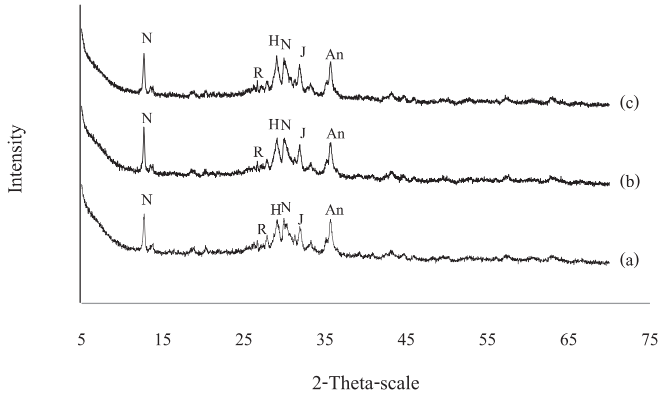

Fig. 2. XRD-patterns of products obtained from different L/S ratios (a) 6, (b) 8 and (c) 10. N = Natrolite-K [$K_{15.8}Na_{0.2}(Al_{16}Si_{24}O_{80}).16H2O$], An = Anorthite [$(Ca,Na)(Al,Si)_2Si_2O_8$], H = Hedenbergite [$Ca(Fe, Mg)(SiO_3)_2$], J = Jusite [$(Ca,Na,K)_5(Si,Al)_6O_{15}.5H_2O$], R = Rosenhanite [$Ca_3Si_3O_9.H_2O$]

the dissolved Si^{4+} and Al^{3+} concentrations were slightly different from that of 7 M KOH. At this high alkali concentration, the more stable phases of KASH and kaliophilite in the form of a tectosilicate Al–Si framework structure were developed. However, kaliophilite contained no zeolitic water in its structure. Fig. 4(a)–(d) show the XRD patterns of KASH obtained at various synthesized conditions. For 6.6 μm BA using 9 M KOH, KASH was formed. Increase in the fineness of BA to 3.0 μm did not increase the specific surface area of the matrix. With 7 M KOH, the surface area increased and approached the highest value (36.97 m^2/g). This was even superior to NAT-K when using magnetically treated BA. For the same starting material particle size, KASH possessed a higher surface area than NAT-K as shown in Table 3 because of the finer crystal sizes.

Thus, the highly purified NAT-K with high specific surface area (30.92 m^2/g) could be synthesized from magnetically treated 6.6 μm BA in 7 M KOH using L/S of 8 and 100–110 °C of refluxing for 24 h. The best condition of KASH synthesis was similar to that of NAT-K regardless of the BA particle size. It is noted that the particle size of BA is very critical to provide the proper amount of dissolved aluminum and silicon species. The CEC values of 6.6 μm BA, NAT-K and KASH were 8.9, 160.9 and 196.7 cmol(+)/kg, respectively. The zeolite-like material (KASH) was capable of exchanging the cations similarly to the NAT-K. Moreover, its CEC value, like the specific surface area, was superior to that of NAT-K. From the synthesis, the reactive glassy phases with some crystalline phases of BA were

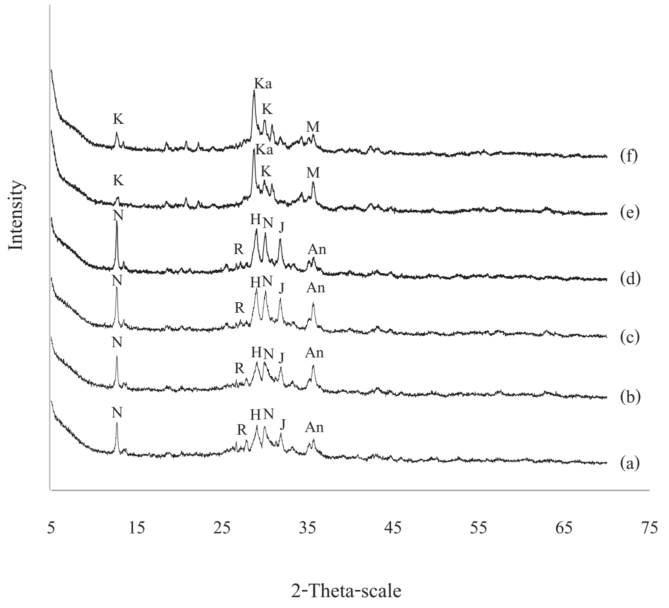

Fig. 3. XRD-patterns of products obtained from 6.6 μm BA with different synthesis conditions (a) untreated BA and 5 M KOH, (b) treated BA and 5 M KOH, (c) untreated BA and 7 KOH, (d) treated BA and 7 M KOH, (e) untreated BA and 9 M KOH and (f) treated BA and 9 M KOH. N = Natrolite-K [$K_{15.8}Na_{0.2}(Al_{16}Si_{24}O_{80}).16H_2O$], An = Anorthite [$(Ca,Na)(Al,Si)_2Si_2O_8$], H = Hedenbergite [$Ca(Fe, Mg)(SiO_3)_2$], J = Jusite [$(Ca,Na,K)_5(Si,Al)_6O_{15}.5H_2O$], R = Rosenhanite [$Ca_3Si_3O_9.H_2O$], K = Potassium aluminum silicate hydrate [$KAlSiO_4.1.5H_2O$], Ka = Kaliophillite [$KAlSiO_4$], M = Maghemite [Fe_2O_3]

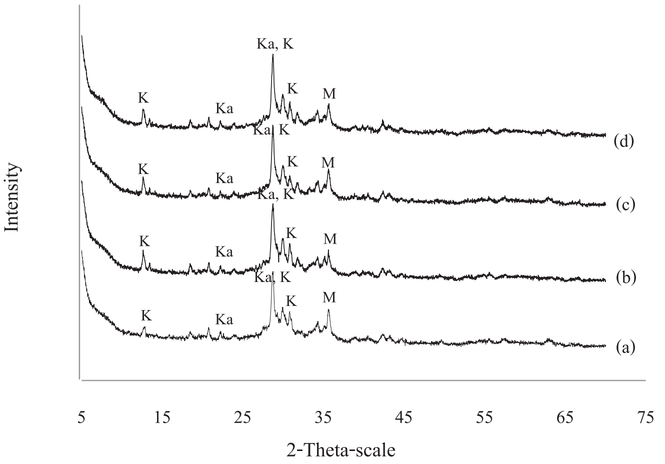

Fig. 4. XRD-patterns of products obtained from 3.0 μm BA with different synthesis conditions (a) untreated BA and 7 M KOH, (b) treated BA and 7 M KOH, (c) untreated BA and 9 M KOH and (d) treated BA and 9 M KOH. K = Potassium aluminum silicate hydrate [$KAlSiO_4.1.5H_2O$], Ka = Kaliophillite [$KAlSiO_4$], M = Maghemite [Fe_2O_3]

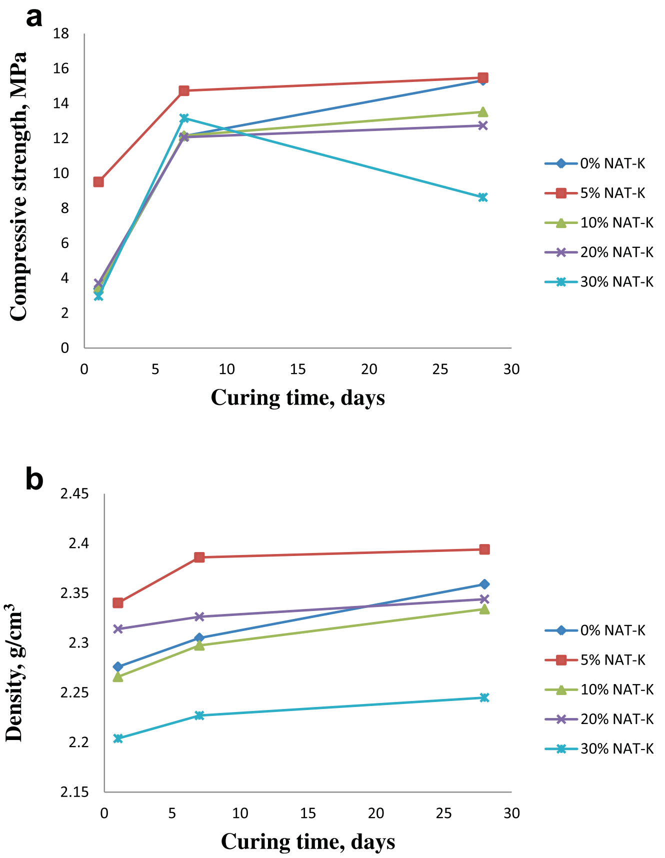

Fig. 5. (a) Strength development and (b) density of NAT-K-blended cement mortars.

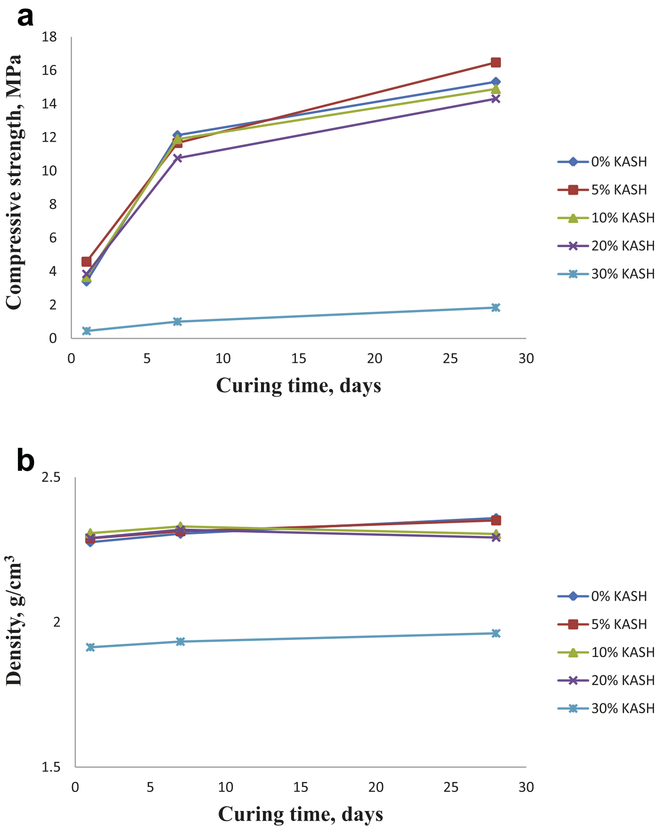

Fig. 6. (a) Strength development and (b) density of KASH-blended cement mortars.

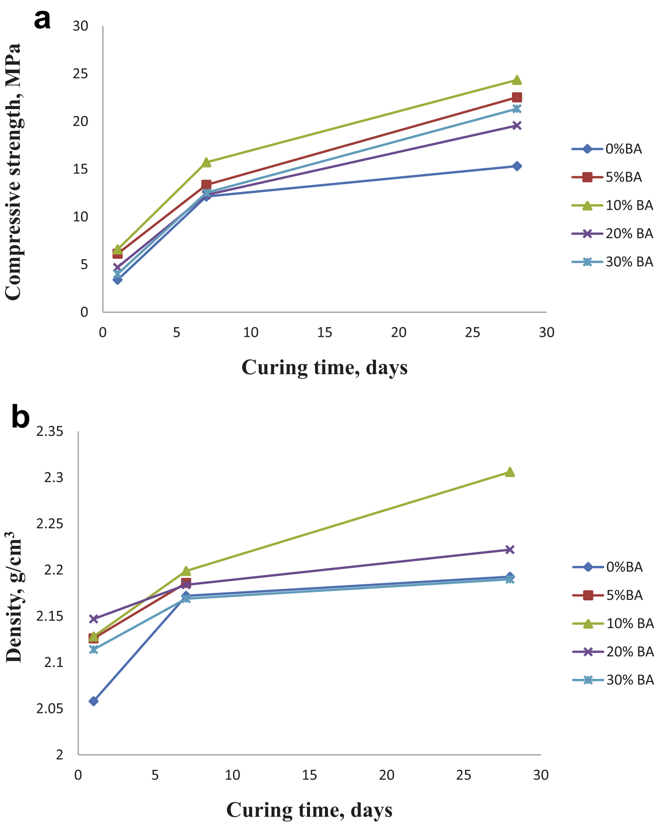

Fig. 7. (a) Strength development and (b) density of BA-blended cement mortars.

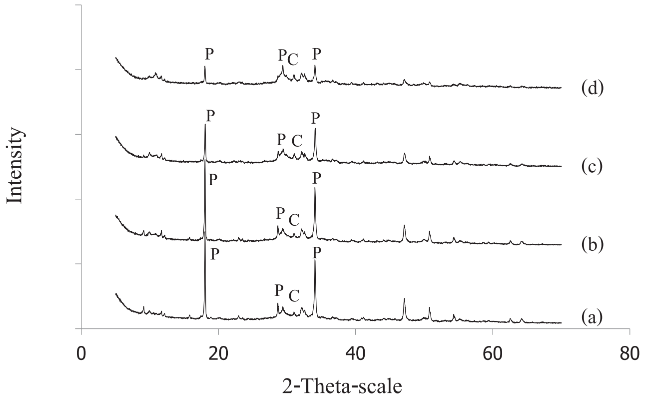

Fig. 8. XRD patterns of NAT-K used as supplementary cementing material for (a) 5 wt%, (b) 10 wt%, (c) 20 wt% and (d) 30 wt% at 28-day curing time. P = Portlandite [$Ca(OH)_2$], C = Calcite [$CaCO_3$]

transformed to zeolite phase (NAT-K) and zeolite-like material (KASH).

3.3. NAT-K and KASH used as hybrid materials

3.3.1. Mechanical property of NAT-K and KASH hybridized cement mortars

Fig. 5 shows the compressive strength and density of NAT-K-blended cement. The 1-day and 28-day compressive strengths of Portland cement mortar were 3.4 and 15.3 MPa, respectively. For 5 wt% zeolite replacement, the 1-day mortar strength increased substantially to 9.5 MPa indicating that the early strength of zeolitic cement was greater than that of the BA-blended cement, similar to the result shown in other works (Jana, 2007). The increase in the early strength should come from the ion exchange between Ca^{2+} in the cement matrix and K^+ in the zeolite structure, resulting in the increase in pH; hence, the hydration was accelerated. A small amount of NAT-K improved the early strength of mortar. The density also increased with the NAT-K addition. Addition of a natural zeolite such as clinoptilolite improved the strength of the cement concrete due, not only to the pozzolanic effect, but also to the microfiller effect (Jana, 2007). After curing for 28 days, the compressive strength of 5 wt% NAT-K-blended mortar was slightly higher than that of Portland cement mortar. Different from the result in this study, a report from Caputo et al.

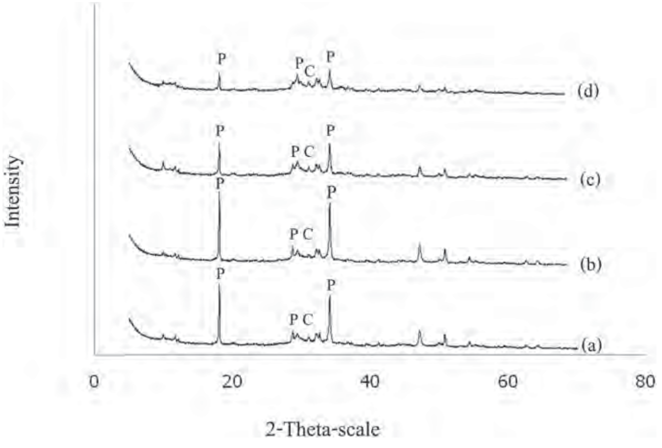

Fig. 9. XRD patterns of KASH used as supplementary cementing material for (a) 5 wt%, (b) 10 wt%, (c) 20 wt% and (d) 30 wt% at 28-day curing time. P = Portlandite [$Ca(OH)_2$], C = Calcite [$CaCO_3$]

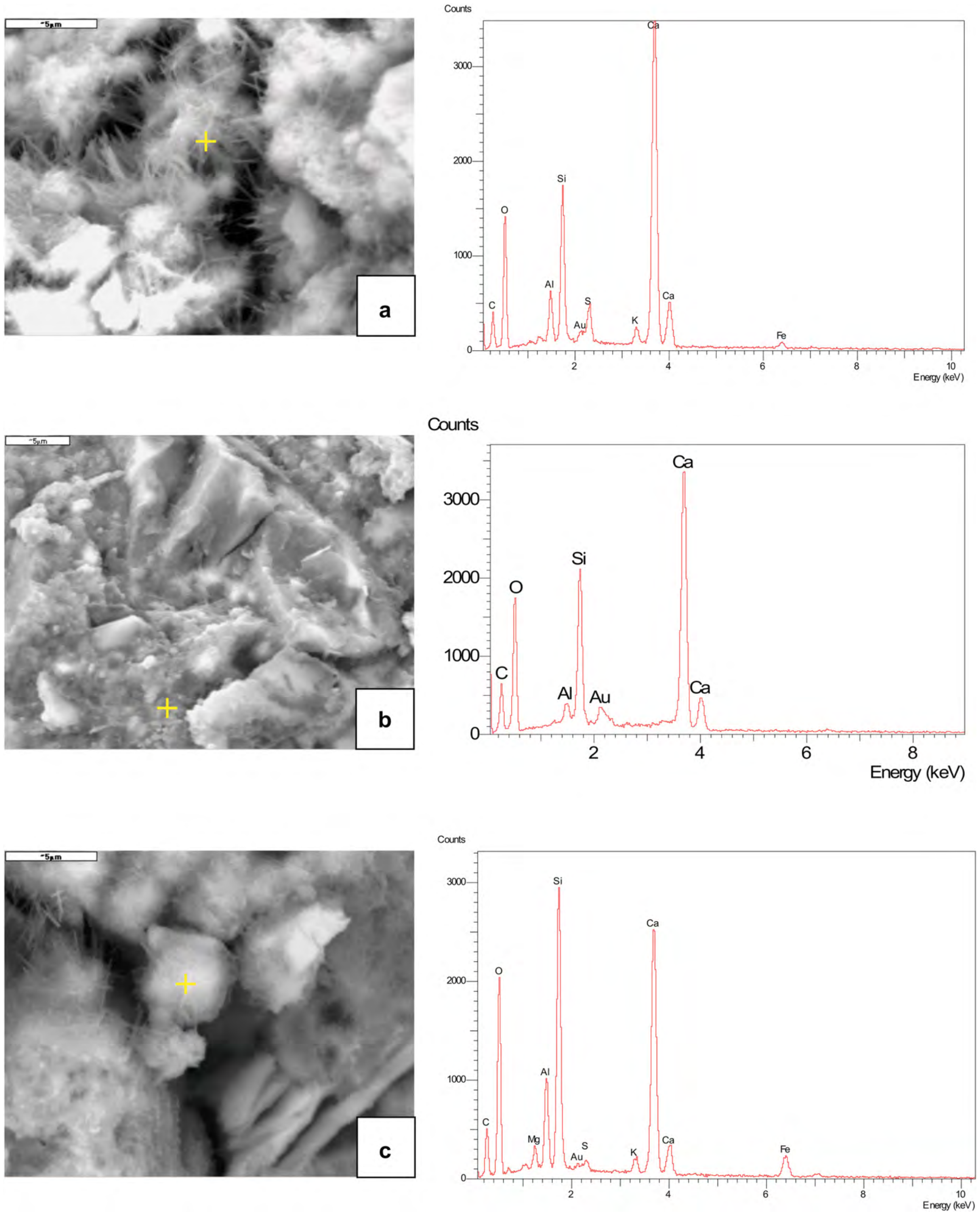

Fig. 10. SEM photomicrographs of (a) 1 day of cement mortar with no replacement (×5000), (b) 28 days of cement mortar with no replacement (×3500), (c) 7 days of 5 wt% NAT-K-replaced cement mix (×5000), (d) 28 days of 5 wt% NAT-K-replaced cement mix (×3500), (e) 7 days of 5 wt% KASH-replaced cement mix (×3500) and (f) 28 days of 5 wt% KASH-replaced cement mix.

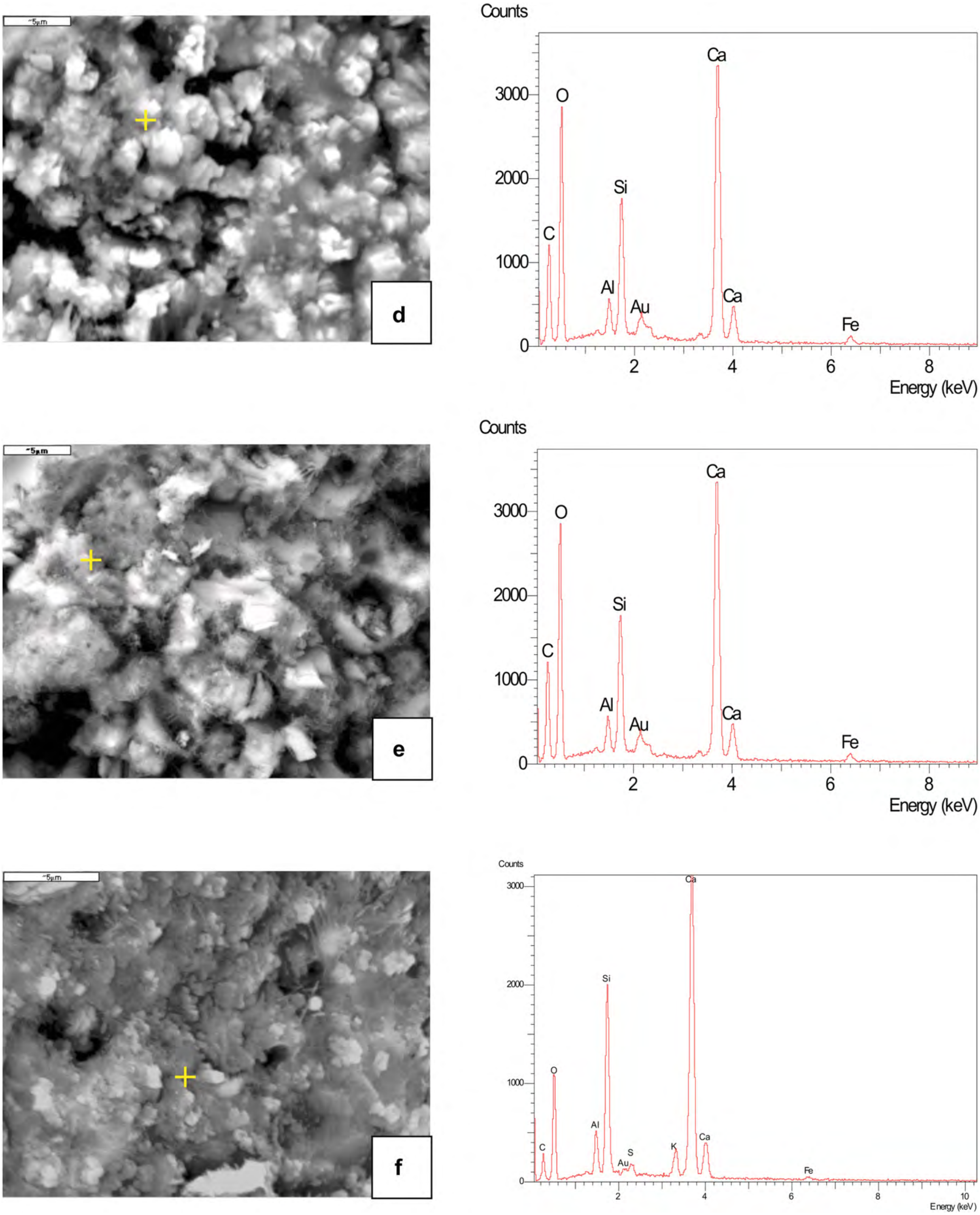

Fig. 10. (*continued*).

(2008) showed that LTA and FAU zeolites which contained very similar Si/Al molar ratio did not improve the early strength of cement mortar. This was owing to the different characteristics of NAT-K from those zeolites in which NAT-K had higher basic site density resulting in the better pozzolanic reactivity. An increase in NAT-K content to 10 wt% resulted in a mortar with similar strength at 7 days but with lower strength at 28 days compared with that of the control. The density substantially decreased with the replacement of 30 wt% NAT-K. With 20 and 30 wt% NAT-K replacement, their strength values were identical to that of normal cement mortar at 7 days curing and were lower at 28 days curing. The results were in good agreement with other researchers (Perraki et al., 2003; Yılmaz and Ediz, 2008) which indicated that the use of zeolite resulted in a smaller amount of Portland cement used. This led to less $Ca(OH)_2$ from cement hydration which was not sufficient for the pozzolanic reaction. In addition, the strength over time of zeolite-blended mortar was superior to that of the Portland cement mortar when the fine cement was used (Perraki et al., 2010; Canpolat et al., 2004; Un, 2005). The density greatly decreased with the addition of 30 wt% NAT-K. The zeolitic phase used in this investigation was highly porous and greatly affected the properties of the blended cement.

The strength development of KASH blended cement mortars was also investigated and shown in Fig. 6. There was no difference in compressive strength values when KASH was used to replace Portland cement up to 10 wt%. The compressive strengths at 1, 7 and 28 days were 4.5, 12.0 and 15.0 MPa, respectively. Their density was approximately 2.3 g/cm^3 for the range of KASH replacement of 5–20 wt%. With 20 wt% replacement, the strength slightly decreased. For the 30 wt% replacement, the 28-day strength and density were drastically reduced to 2.0 MPa and 1.9 g/cm^3, respectively, because of the high specific surface of KASH. Thus, the workability of the mortar was drastically reduced with the presence of the high amount of KASH at the fixed water content. This led to difficulty in the compaction and the reduced strength.

The mortar with only 6.6 μm BA only provided the best strength when compared to those with NAT-K and KASH, as shown in Fig. 7. The addition with 10 wt% BA attained the highest compressive strength. The density of the BA-blended mortar was also improved. The fine BA possessed a high surface area and increased the pozzolanic activity; hence, the strength of the mortars was increased (Jaturapitakkul and Cheerarot, 2003). The use of 5 wt% NAT-K, KASH and BA produced mortars with strengths higher than that of the control. Particularly, the use of BA resulted in mortar with improved strength at the later age because of the good pozzolanic reaction. BA that was mainly composed of the aluminosilicate glassy phase dissolved more readily in the lime solution than those of NAT-K and KASH.

3.3.2. Microstructures of NAT-K and KASH hybridized cement mortars

Fig. 8(a)–(d) show XRD patterns of 28-day paste containing NAT-K. Portlandite ($Ca(OH)_2$) from cement hydration was easily detected in all samples. The higher the NAT-K content, the less $Ca(OH)_2$ was left behind because of less cement in the mixes. After the pozzolanic reaction, binding compounds, such as calcium silicate hydrate (C-S-H) and calcium aluminosilicate hydrate (C-A-S-H), should be expected. Because of their semicrystalline characteristics and the XRD peak overlapping with portlandite, C-S-H and C-A-S-H were difficult to be identified. Fig. 9(a)–(d) show XRD-patterns of 28-day paste containing KASH. Again, the portlandite was easily identified and the binding phases were difficult to detect, similar to the NAT-K paste. Therefore, the pozzolanic reaction was confirmed by the reduction in the portlandite and the strength improvement of the cement mix with the presences of 5 wt% of NAT-K, KASH and BA.

Fig. 10 shows the photomicrographs of the hydration products with and without the supplementary cementing materials. At an early age (1 day), as shown in Fig. 10(a), ettringite and unreacted C_2S phases were found in normal cement. Potassium, which was found by EDS, was from the originally used BA. At 28 days, shown in Fig. 10(b), C-S-H was distributed quite evenly in the matrix and was easy to detect. For the 5 wt% NAT-K paste cured for 7 days, shown in Fig. 10(c), C-A-S-H was found at the surfaces of the NAT-K particles indicating the progress of the pozzolanic reaction. The reduction in the portlandite XRD peaks was also evident, which indicated the lime consumption of NAT-K. At the late curing age, shown in Fig. 10(d), C-A-S-H was found as a major phase. For 5 wt% KASH in Fig. 10(e) and (f), C-A-S-H can be detected in 7- and 28-day cured mortar.

3.3.3. Heavy metal adsorption capacity

Table 5 shows the percentages of heavy metal adsorption on NAT-K, KASH and BA. The cation exchange capacity (CEC) values of NAT-K and KASH were much higher than that of BA because of molecular pores and negative charges contained in their structures. Thus, NAT-K and KASH gave considerably higher adsorption of Ni and Cd than BA. NAT-K and KASH showed a similar adsorption capacity of 99.5–99.8% for Cr^{3+}, 97.5–98.0% for Ni^{2+} adsorption and 95.0% for Cd^{2+} adsorptions. The ionic radii of Cr, Ni and Cd were 0.097, 0.072 and 0.052 nm, respectively. The smaller ionic radii and the higher ionic valency led to the higher ionic strength. The increase in pH also resulted in an increase in Cd^{2+} adsorption (Hetzer et al., 2006; Quintelas et al., 2009). However, BA showed the effective adsorption for Cr ions and the poor adsorption for Ni and Cd ions. The small ionic radius and the high ionic valency of the Cr ion led to the higher ionic strength. Several researchers (Bayat, 2002; Mohan and Gandhimathi, 2009) reported that the functional oxidized groups of SiO_2 and Al_2O_3, as well as a basic testing condition, resulted in the negatively charged surfaces. The surface of the SiO_2 tended to form SiOH groups, which acted as a weak acid, and their surface charges were pH dependent. The negative charge for the high pH and the positive charge for the low pH would exist, and the positive charge was prone to dispel the positive ion. BA surfaces adsorbed the positive charges, which were attracted to the $Cr(OH)_3$ and $[Cr(OH)_6]^{3-}$ and $[Cr(OH)_4]^-$ at pH ~ 6–8 (Mollah et al., 1992). This induced Cr ion adsorption on BA surfaces. However, the pelletized lignite fly ash from the work of Papandreou et al. (2007) showed the same Cd^{2+} adsorption capacity on BA as this work at around pH 6.3. Its adsorption could reach 100% above pH 9.

However, in this work, the heavy metal adsorption was carried out without pH adjustment. The initial and final pH of the systems containing NAT-K, KASH and BA soaked in $Cr(NO_3)_3.9H_2O$, $Ni(NO_3)_2.6H_2O$ and $Cd(NO_3)_2.4H_2O$ solutions were ranged from weak acid to the neutral condition (pH ~ 6–8). In this condition, the NAT-K and KASH were highly effective in the adsorption of Cr, Ni and Cd ions. The heavy metal adsorption that occurred was because of ion exchange with K^+ for NAT-K and electrostatic attractive forces for KASH and BA. In multi-metal system, the zeolite adsorption mechanism was different. It was reported that, except for ion exchange, the formation of solid metal hydroxide occurred and depended on the ion species (Jha et al., 2009). For example in binary system of Cd^{2+} and Ni^{2+}, Jha et al. suggested that

Table 5
Capacity of heavy metal adsorption on NAT-K, KASH and BA; unit: percentage (%).

	CEC[a] cmol(+)/kg	Cr^{3+} adsorption	Ni^{2+} adsorption	Cd^{2+} adsorption
NAT-K	160.91	99.8	98.0	95.0
KASH	196.68	99.5	97.5	95.0
BA	8.87	95.0	29.0	30.0

[a] CEC, cation exchange capacity.

Table 6
Concentrations of Cr, Ni and Cd ions leached from cement mortars blended with hybrid materials.

Hybrid materials	Adsorbed concentration in 100 g zeolite (ppm)			Adsorbed concentration in cement mix (ppm)			Leached concentration (ppm)			Percentage of adsorption (%)		
	Cr	Ni	Cd	Cr	Ni	Cd	Cr	Ni	Cd	Cr	Ni	Cd
NAT-K	72.81	55.68	67.51	3.64	2.78	3.37	0.08	0.06	0.48	97.6	97.9	85.8
KASH	72.82	55.52	67.59	3.64	2.77	3.38	0.08	0.03	0.47	98.0	98.7	86.0
BA	69.75	16.5	23.55	3.49	0.83	1.18	0.21	0.10	0.30	94.0	88.0	74.5

the Ni^{2+} removal was caused by ion exchange with monovalent cation contained in zeolite structure, while Cd^{2+} removal involved the formation of metal hydroxide. In this study, Ni^{2+} was, therefore, removed by K^+ exchange and Cd^{2+} was precipitated in the form of cadmium hydroxide. For tertiary system, Jha et al. investigated the combination of Ni^{2+}, Cd^{2+} and Cu^{2+}. In this case, Ni^{2+} and Cd^{2+} were removed mainly via ion exchange and Cu^{2+} was done by metal hydroxide precipitation. In this study, for Cr^{3+} instead of Cu^{2+} combined with Ni^{2+} and Cd^{2+}, the Cr^{3+} removal was performed via both cation exchange due to its ionic strength and new phase formation as $CaCrO_4$ in Portland cement based system that also enhanced the cement strength (Shi and Fernandez-Jimenez, 2006). Therefore, the removal of Ni^{2+} and Cd^{2+} should be dependent on the metal hydroxide precipitation.

3.3.4. *Leaching of heavy metal encapsulated in cement mortar matrix*

The results of the leaching test of heavy metal from mortars are shown in Table 6. KASH gave a slightly better encapsulation than NAT-K. NAT-K and KASH encapsulated 97.6% Cr, 97.9% Ni and 85.8% Cd and 98.0% Cr, 98.7% Ni and 86.0% Cd, respectively. BA gave a slightly lower performance with the encapsulation of 94.0% Cr, 88.0 Ni and 74.5% Cd. NAT-K, KASH and BA when mixed with Portland cement played a role in the pozzolanic reaction. Silicate and aluminate phases contained in NAT-K, KASH and BA dissolved and reacted with hydrated lime resulting in a very fine C-S-H binding phase. The zeolitic frameworks of NAT-K and KASH should be partly disturbed and co-exist with the cement hydration and pozzolanic reaction products. The heavy metal encapsulation mechanism thus relied on the remaining NAT-K or KASH and the C-S-H binding phase. Cement paste was highly alkaline and was expected to have negatively charged surfaces that repelled the metal anionic species. According to Mollah's work (Mollah et al., 1992), some Cr ions could substitute the Si^{4+} in a C-S-H structure. In addition, after the pozzolanic reaction, the density of cement mortars blended with 5 wt% NAT-K, KASH or BA was enhanced, which was good for heavy metal encapsulation. The Cd ion adsorption capacities of NAT-K, KASH and BA were comparable to the previous work (Ok et al., 2007), although the used zeolite content was much lower in this work. The zeolite–Portland cement of the Ok et al.'s work adsorbed Cd ion at the same value. This was possibly due to the partly chemical destruction of hydration reaction products and zeolite after being subjected to 400 °C heating. The use of a small amount of NAT-K and KASH produced mortars with improved strength and good heavy metal encapsulation capacity.

4. Conclusions

The conclusions are given as follows:

1) The NAT-K zeolite and KASH zeolite-like material can be produced from lignite BA obtained from the Mae Moh power plant. For NAT-K, the optimum conditions for synthesis were obtained with 6.6 μm BA, pretreatment by iron oxide removal, and refluxing with 7 M KOH at a temperature range of 100–110 °C for 24 h. For KASH, the optimum conditions for synthesis were obtained with 3.0 and 6.6 μm BA, pretreatment by iron oxide removal, and refluxing with 9 M KOH at a temperature range of 100–110 °C for 24 h.
2) Hybridized with NAT-K, the early strength and the density of the cement mortars could be improved. For 5 wt% replacement, the strength and density increased substantially due not only to the pozzolanic effect but also to the microfiller effect. With an increase in the replacement level, the gain in strength was reduced. For 10 wt% NAT-K replacement, the compressive strengths were comparable to normal cement mortar. KASH can replace cement up to 10% with no compressive strength reduction when compared to normal Portland cement mortar.
3) Both NAT-K and KASH can partially replace Portland cement and be used for heavy metal encapsulation. KASH gave a slightly better performance than NAT-K. They can encapsulate approximately 97% Cr, 98% Ni and 84% Cd which is better than BA

Acknowledgments

We wish to thank the National Research University Project under Thailand's Office of the Higher Education Commission and Thailand Research Fund (TRF) under the TRF Senior Research Scholar Contract No. RTA 5480004 for financial supports.

References

Alex, D.E., Dong-ke, Z., 2003. Controlled Release Zeolite Fertilizers: a Value Added Product Produced from Fly Ash. Cooperative Research Centre for Coal in Sustainable Development, Centre for fuel and energy, Curtin University of Technology, Australia.
Atkins, M., Glasser, F.P., Jack, J.J., 1995. Zeolite P in cements: its potential for immobilizing toxic and radioactive waste species. Waste Management 15, 127–135.
Bayat, B., 2002. Comparative study of adsorption properties of Turkish fly ashes. I. The case of nickel (II), copper (II) and zinc (II). Journal of Hazardous Materials 95, 251–273.
Canpolat, F., Yilmaz, M., Kose, M.M., Sumer, M., Yurdusev, M.A., 2004. Use of zeolite, coal bottom ash and fly ash as replacement materials in cement production. Cement & Concrete Research 34, 731–735.
Caputo, D., Liguori, B., Colella, C., 2008. Some advances in understanding the pozzolanic activity of zeolites: the effect of zeolite structure. Cement & Concrete Composites 5, 455–462.
Chareonpanich, M., Jullaphan, O., Tang, C., 2011. Bench-scale synthesis of zeolite A from subbituminous coal ashes with high crystalline silica content. Journal of Cleaner Production 19, 58–63.
Cheriaf, M., Rocha, J.C., Péra, J., 1999. Pozzolanic properties of pulverized coal combustion bottom ash. Cement & Concrete Research 29, 1387–1391.
Chindaprasirt, P., Pimraksa, K., 2008. A study of fly ash–lime granule unfired brick. Powder Technology 182, 33–41.
Gao, L., Cao, Y., Zhou, S.L., Zhuang, T.T., Wang, Y., Zhu, J.H., 2009. Eliminating carcinogenic pollutants in environment: Reducing the tobacco specific nitrosamines level of smoke by zeolite-like calcosilicate. Journal of Hazardous Materials 169, 1034–1039.
Giannetti, B.F., Bonilla, S.H., Almeida, C.M.V.B., 2004. Developing eco-technologies: a possibility to minimize environmental impact in Southern Brazil. Journal of Cleaner Production 12, 36–368.
Hetzer, A., Daughney, C.J., Morgan, H.W., 2006. Cadmium ions biosorption by the thermophilic bacteria Geobacillus stearothermophilus and G. thermocatenulatus. Applied Environmental Microbiology 72, 4020–4027.

Hui, K.S., Chao, C.Y.H., Kot, S.C., 2005. Removal of mixed heavy metal ions in wastewater by zeolite 4A and residual products from recycled coal fly ash. Journal of Hazardous Materials 1-3, 89–101.

Jana, D., 2007. A new look to an old pozzolan clinoptilolite – a promising pozzolan in concrete. In: Proceeding of the 29th Conference on Cement Microscopy, Quebec, Canada.

Jaturapitakkul, C., Cheerarot, R., 2003. Development of bottom ash as pozzolanic material. Journal of Materials in Civil Engineering 15, 48–53.

Jha, V.K., Nagae, M., Matsuda, M., Miyake, M., 2009. Zeolite formation from coal fly ash and heavy metal ion removal characteristics of thus-obtained zeolite X in multi-metal systems. Journal of Environmental Management 90, 2507–2514.

Kadono, T., Tajima, M., Shiomura, T., Imawaka, N., Noda, S., Kubota, T., Okamoto, Y., 2008. Hydrothermal synthesis of giant single crystals of MFI type zeolite: modified bulk material dissolution method. Microporous & Mesoporous Materials 115, 454–460.

Larsen, D., Mann, R., 2005. Origin of high manganese concentrations in coal mine drainage eastern Tennessee. Journal of Geochemical Exploration 86, 143–163.

Mohan, S., Gandhimathi, R., 2009. Removal of heavy metal ions from municipal solid waste leachate using coal fly ash as an adsorbent. Journal of Hazardous Materials 169, 351–359.

Mollah, M.Y.A., Tsai, Y.N., Hess, T.R., Cocke, D.L., 1992. An FTIR, SEM and EDS investigation of solidification/stabilization of chromium using portland cement Type V and Type IP. Journal of Hazardous Materials 30, 273–283.

Noroozifar, M., Khorasani-Motlagh, M., Fard, P.A., 2009. Cyanide uptake from wastewater by modified natrolite zeolite-iron oxyhydroxide system: application of isotherm and kinetic models. Journal of Hazardous Materials 166, 1060–1066.

Ok, Y.S., Yang, J.E., Zhang, Y.S., Kim, S.J., Chung, D.Y., 2007. Heavy metal adsorption by a formulated zeolite-Portland cement mixture. Journal of Hazardous Materials 147, 91–96.

Olmo, I.F., Chacon, E., Irabien, A., 2003. Leaching behavior of lead, chromium (III), and zinc in cement/metal oxide systems. Journal of Environmental Engineering 129, 532–538.

Papandreou, A., Stournaras, C.J., Panias, D., 2007. Copper and cadmium adsorption on pellets made from fired coal fly ash. Journal of Hazardous Materials 148, 538–547.

Pelisser, F., Barcelos, A., Santos, D., Peterson, M., Bernardin, A.M., 2012. Lightweight concrete production with low Portland cement consumption. Journal of Cleaner Production 23, 68–74.

Perraki, T., Kontori, E., Tsivilis, S., Kakali, G., 2010. The effect of zeolite on the properties and hydration of blended cement. Cement & Concrete Composites 32, 128–133.

Perraki, T., Kakali, G., Kontoleon, F., 2003. The effect of natural zeolites on the early hydration of Portland cement. Microporous & Mesoporous Materials 1-3, 205–212.

Pimraksa, K., Setthaya, N., Chindaprasirt, P., 2010. Synthesis of zeolite phases from combustion by-products. Waste Management and Research 28, 1122–1132.

Poona, C.S., Lama, U.L., Koua, S.C., Linb, Z.S., 1999. A study on the hydration rate of natural zeolite blended cement pastes. Construction & Building Materials 13, 427–432.

Quintelas, C., Rocha, Z., Silva, B., Fonseca, B., Figueiredo, H., Tavarea, T., 2009. Removal of Cd (II), Cr (VI), Fe (III) and Ni (II) from aqueous solutions by E. coli biofilm supported on kaolin. Chemical Engineering Journal 149, 319–324.

Rhoades, J.D., 1982. Cation exchange capacity. In: Page, A.L., Miller, R.H., Keeney, D.R. (Eds.), Method of Soil Analysis. American Society Agronomy, Madison, WI, pp. 149–157.

Ríos, C.A., Williams, C.D., 2008. Synthesis of zeolitic materials from natural clinker: a new alternative for recycling coal combustion by-products. Fuel 87, 2482–2492.

Sathonsaowaphak, A., Chindaprasirt, P., Pimraksa, K., 2009. Workability and strength of lignite bottom ash geopolymer mortar. Journal of Hazardous Materials 168, 44–50.

Shi, C., Fernandez-Jimenez, A., 2006. Stabilization/solidification of hazardous and radioactive wastes with alkali-activated cements. Journal of Hazardous Materials B137, 1656–1663.

Singh, B.K., Tomar, R., Tomar, S.S., 2011. Sorption of homologues of radionuclides by synthetic ion exchanger. Microporous & Mesoporous Materials 142, 629–640.

Telukdarie, A., Brouckaert, C., Huang, Y., 2006. A case study on artificial intelligence based cleaner production evaluation system for surface treatment facilities. Journal of Cleaner Production 14, 1622–1634.

Trezza, M.D., 2007. Hydration study of ordinary Portland cement in the presence of zinc ions. Material Research 10, 331–334.

Un, H., 2005. A discussion of the paper “Use of zeolite, coal bottom ash and fly ash as replacement materials in cement production” by F. Canpolat, K. Yilmaz, M.M. Kose, M. Sumer, M.A. Yurdusev, [Cement & Concrete Research, 34(5) (2004) 731–735]. Cement & Concrete Research 35, 1020–1021.

Walex, T.T., Saito, F., Zhang, Q., 2008. The effect of low solid/liquid ratio on hydrothermal synthesis of zeolites from fly ash. Fuel 87, 3194–3199.

Wang, C.F., Li, J.S., Wang, L.J., Sun, X.Y., 2008. Influence of NaOH concentrations on synthesis of pure-form zeolite A from fly ash using two-stage method. Journal of Hazardous Materials 155, 58–64.

Yılmaz, B., Ediz, N., 2008. The use of raw and calcined diatomite in cement production. Cement & Concrete Composites 3, 202–211.

Yilmaz, B., Uçar, A., Öteyaka, B., Uz, V., 2007. Properties of zeolitic tuff (clinoptilolite) blended portland cement. Building & Environment 42, 3808–3815.

High-Calcium Bottom Ash Geopolymer: Sorptivity, Pore Size, and Resistance to Sodium Sulfate Attack

Chaicharn Chotetanorm[1]; Prinya Chindaprasirt[2]; Vanchai Sata[3]; Sumrerng Rukzon[4]; and Apha Sathonsaowaphak[5]

Abstract: The resistance to sulfate attack, compressive strength, sorptivity, and pore size of high-calcium bottom ash geopolymer mortars were studied. Ground lignite bottom ashes (BAs) with median particle sizes of 16, 25, and 32 μm were used. NaOH, sodium silicate, and temperature curing were used to activate the geopolymerization. Results showed that relatively high strengths of 40.0–54.5 MPa were obtained for the high-calcium bottom ash geopolymer mortars. The use of fine BA improved the strength and resistance to sulfate attack of mortars. The good performances were attributable to the high degree of reaction of fine BA and the associated low amount of large pores (0.05–100 μm) compared with those of coarse BA. The incorporation of water improved the workability of mixes, and the compressive strength, sorptivity, and resistance to sulfate attack decreased due to the increase in large pores. **DOI: 10.1061/(ASCE)MT.1943-5533.0000560.** *© 2013 American Society of Civil Engineers.*

CE Database subject headings: Calcium; Sulfates; Pore size distribution; Bottom ash; Compressive strength; Mortars.

Author keywords: Geopolymer; Sodium sulfate resistance; High calcium bottom ash.

Introduction

Portland cement is an energy intensive product because it consumes a large amount of energy. Its production releases approximately 7% of the green house gas produced annually (Malhotra 2002). Efforts have, therefore, been made to reduce the use of portland cement by introducing other supplementary cementitious materials (SCM). Another form of cement that is more environmental-friendly, such as geopolymer, is now receiving more attention (Davidovits 1999; Duxson et al. 2007). The source materials are normally fly ash (Palomo et al. 1999) and metakaolin because they contain large amounts of silica and alumina. The geopolymerization process normally involves the activation of source materials with alkaline solutions such as sodium hydroxide and potassium hydroxide, sodium silicate, and temperature curing (Detphan and Chindaprasirt 2009; Van Jaarsveld et al. 2002).

Bottom ash (BA) is a waste that results from coal burning to produce electricity in power plant. The major output of BA in Thailand is from pulverized coal combustion (PCC) at Mae Moh power plant in the north. The annual output is approximately 0.6 million tons (Wongkeo and Chaipanich 2010) and is disposed at landfills. It has been shown that BA has similar chemical constituents to fly ash, but with different particle sizes and shapes, BA can be used as an SCM to replace part of portland cement (Cheriaf et al. 1999; Jaturapitakkul and Cheerarot 2003). Because its particle size is larger than fly ash, it has to be ground to increase the reactivity. The ground BA has also been successfully used as a source material for making geopolymers (Chindaprasirt et al. 2009; Sathonsaowaphak et al. 2009).

The durability aspect of concrete is an important issue. Reinforced concrete and cementitious composites confront several harmful phenomena such as chloride penetration, carbonation, acid attack, sulfate attack, and the penetration of hazardous liquids or solutions, even by water (Gordon et al. 2011). Sulfate is one of the major problems affecting the performance of concrete. The mechanism of sulfate attack results in expansion and strength reduction (Atahan and Dikme 2011; Lee et al. 2005). Blended cement technology by incorporating SCM in concrete mixes has been selected to mitigate the durability problems of concrete. Most SCM, when incorporated into blended cement concrete to resist sulfate attack, showed satisfactory performance (Bonakdar and Mobasher 2010; Chindaprasirt et al. 2007c). Efforts to study the durability of geopolymer have recently been conducted (Bakharev 2005; Fernandez-Jimenez et al. 2007; Pacheco-Torgal et al. 2012; Thokchom et al. 2010). Thus far, the study has been limited to fly ash and metakaolin geopolymers, and very little work has been done on high calcium BA. The mechanisms of sulfate attack on portland cement and geopolymers are expected to be different because of the large difference in the amount of calcium (Bakharev et al. 2003) and the different chemical roles played by calcium in these systems.

The sorptivity or absorption of water is related to the ability of water or fluid to move into mortar and concrete and is, therefore,

---

[1] Ph.D. Candidate, Dept. of Civil Engineering, Faculty of Engineering, Khon Kaen Univ., Khon Kaen 40002, Thailand. E-mail: 5070400123@stdmail.kku.ac.th

[2] Professor, Sustainable Infrastructure Research and Development Center, Dept. of Civil Engineering, Faculty of Engineering, Khon Kaen Univ., Khon Kaen 40002, Thailand (corresponding author). E-mail: prinya@kku.ac.th

[3] Assistant Professor, Dept. of Civil Engineering, Faculty of Engineering, Khon Kaen Univ., Khon Kaen 40002, Thailand. E-mail: vancsa@kku.ac.th

[4] Assistant Professor, Dept. of Civil Engineering, Faculty of Engineering, Rajamangala Univ. of Technology, Phra Nakhon, Bangkok 10300, Thailand. E-mail: rerng197@rmutp.ac.th

[5] Lecturer, Program of Construction Technology, Faculty of Industrial Technology, Nakhon Ratchasima Rajabhat Univ., Nakhon Ratchasima 30000, Thailand. E-mail: apha_yao@yahoo.com

Note. This manuscript was submitted on January 24, 2012; approved on April 19, 2012; published online on April 23, 2012. Discussion period open until June 1, 2013; separate discussions must be submitted for individual papers. This paper is part of the ***Journal of Materials in Civil Engineering***, Vol. 25, No. 1, January 1, 2013. © ASCE, ISSN 0899-1561/2013/1-105-111/$25.00.

J. Mater. Civ. Eng. 2013.25:105-111.

related to the durability property. Water absorbed in reinforced concrete structures coupled with oxygen may cause steel reinforcements to corrode. Water can go into concrete by means of capillary action of pore systems. Additionally, the resistance to this mechanism is consistent with that of liquid ingress with regard to sulfate and chloride solutions. As expected, the resistance to sorptivity is high when the rate or coefficient of sorptivity is low. The resistance to the sorptivity of concretes is inversely proportioned to the water/binder ratio (Ghrici et al. 2007) and porosity (Gonen and Yazicioglu 2007).

Mercury intrusion porosimetry (MIP) has been widely used to confirm the pore size distribution and porosity of cement paste with other properties; namely, mechanical properties, physical properties, and microstructures (Chindaprasirt et al. 2007b; Poon et al. 2006). The use of MIP has been extended to study the porosity of geopolymers from fly ash, metakaolin, and other alkali activated material (Kong et al. 2007; Zuda et al. 2010). The MIP technique has some limitations due to the ink-bottle effect, however it has been successfully used to compare the pores of similar products (Zuda et al. 2010). Information regarding the MIP of BA geopolymer is crucial to understand its strength and resistance to sulfate and water sorptivity.

Research Significance

High calcium BA geopolymers with various fineness of BA, with and without extra water, were made and tested to assess the effects of BA fineness and water content of geopolymer. The compressive strength, water sorptivity, pore size distribution by MIP, and resistance to sulfate attack are the subjects of this research.

Experimental Details

Materials

The lignite bottom ash was obtained from Mae Moh power station in northern Thailand. To study the effects of BA fineness, three finenesses were used: fine BA (F), medium BA (M) and coarse BA (C), with corresponding median particle sizes of 16, 25, and 32 μm and Blaine finenesses of 5,000, 3,400, and 2,100 cm^2/g, respectively. The X-ray diffraction (XRD) analysis of the BA is given in Fig. 1. The broad hump that showed the amorphous phase of BA was located at the two theta angle at approximately 20–35°, and the peaks of crystal of anorthite, augite, and gehlenite were also observed.

The particle size distributions of fine, medium, and coarse BA are shown in Fig. 2. The chemical composition of BA is shown in Table 1. The SiO$_2$ and Al$_2$O$_3$ contents were reasonably high at 39.3 and 21.3%. Because this bottom ash was from lignite coal, CaO content was high at 16.5%. Sodium silicate solution (NS) with 13.8% Na$_2$O, 32.2% SiO$_2$, and 54.0% H$_2$O, and 10 M NaOH solution (NH) were used as alkaline activators. Local river sand with specific gravity of 2.62 and fineness modulus of 2.85 in saturated surface dry condition was used to make the geopolymer mortars. The gradation of the sand is shown in Fig. 3.

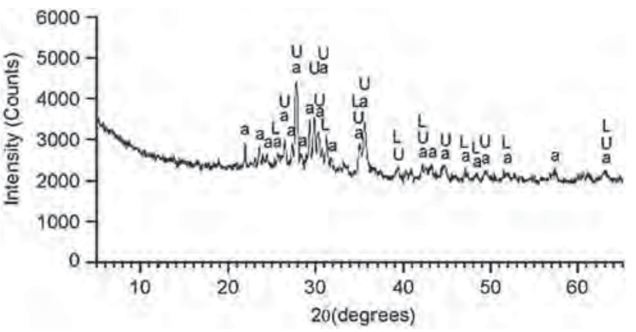

Fig. 1. XRD graph of ground BA

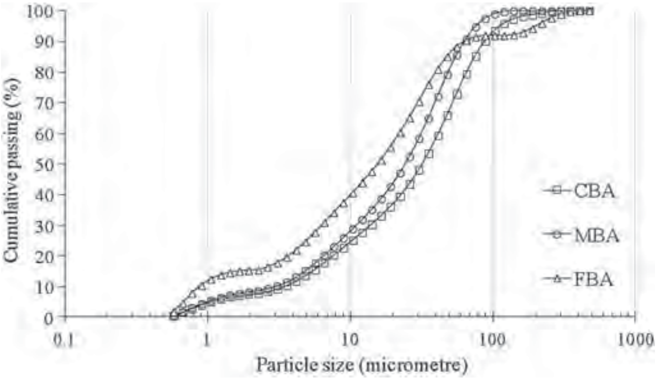

Fig. 2. Gradation curve of each BA fineness

Mix Proportions, Mixing, and Curing

The mix proportions of geopolymer mortars were taken from a previous research study (Sathonsaowaphak et al. 2009) and consisted of a sand/BA ratio of 2.75, liquid alkaline/BA ratio of 0.6, and NS/NH ratio of 1.50. To study the effects of water content, two series of mixes with different water contents were used. For Series A, no extra water was added to the mixes. For Series B, extra water at a water/ash ratio of 0.08 (total liquid/ash ratio of 0.68) was incorporated to the mixes to obtain relatively workable mortars for comparison purposes. The addition of extra water results in dilution of the alkali solutions, and hence, affects the leaching of silica and alumina (Rattanasak and Chindaprasirt 2009). The mix proportions are shown in Table 2.

Mixing was conducted in an air-conditioned room at 25°C to eliminate the effect of temperature variation. The mixing procedure involved mixing of the BA and NH for 5 min. Sand and extra water (if needed) were then incorporated and mixing was conducted for five more minutes. This was followed by the addition of NS with a final mixing of 5 min. The mortar mixtures were then cast into molds, which were wrapped with clingfilm to avoid moisture loss. They were left in the laboratory at 25°C for one hour and then cured at 75°C for 48 h. The specimens were demolded and kept in a controlled room at 23°C and 50% relative humidity until they reached testing age.

For the mixing of paste, the same mixing procedure was used, except sand was not included. The paste mixtures were cast in cylindrical molds of 25 mm in diameter and 50 mm in length, and the same curing regime was used. The paste samples were used to determine the distribution of pore sizes of geopolymer using MIP. The paste samples were used because they gave more accurate results than the mortar samples. Certain differences in pore structure were attributable to interfacial transition zone effects between mortars and pastes. The comparison was, therefore, limited to the same type of materials; i.e., paste has been widely used to study the pore size distribution for cementitious materials (Chindaprasirt et al. 2007b).

Table 1. Composition of High Calcium Lignite BA

Chemical	SiO_2	Al_2O_3	CaO	Fe_2O_3	Na_2O	TiO_2	MgO	K_2O	P_2O_5	SO_3	LOI
Composition (%)	39.3	21.3	16.5	13.5	1.0	0.4	2.6	2.1	0.2	1.5	1.4

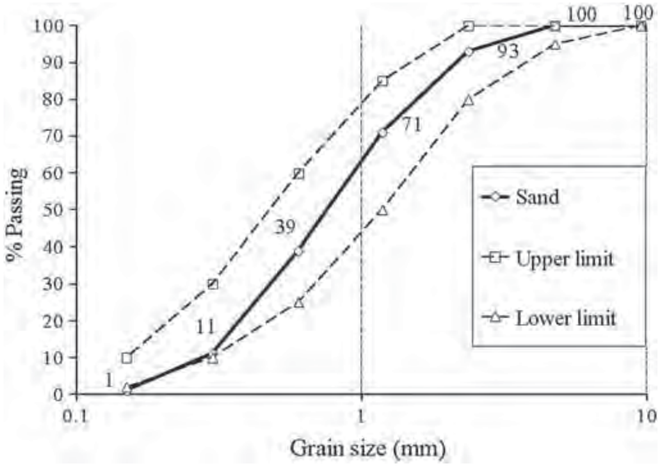

Fig. 3. Gradation curve of sand

Test Methods

Compressive Strength Test

For compressive strength tests (ASTM 2002), 50 × 50 × 50 mm cube specimens were used. The mortars were cast in two layers with tamping. In the final step, specimens were vibrated for 10 s using a vibrating table. The prepared samples were tested for compressive strength at 7, 28, 90, 180, and 360 days. The reported compressive strengths were the average of three samples.

Pore Size

The measurements on intruded volume and pore size distribution of paste were conducted using MIP with the capability of measuring pore size diameter down to 7 nm. The samples were obtained by chiseling from the middle part of the hardened geopolymer paste cylinders and immersing in acetone for 48 h to stop the geopolymerization. After that, the samples were oven-dried at a temperature of 60°C for 24 h. Samples used were 3–6 mm thick and 1–1.5 g. The mercury volume was normalized for each sample weight. The applied pressures were between 9.3 and 206.5 MPa. The mercury contact angle and surface tension were 140° and 0.480 N/m.

Rate of Sorptivity

Mortar discs cut from the parent 100 × 200 mm mortar cylinder were used as samples for the determination of rate of sorptivity (ASTM 2011). The tests were performed at the age of seven days. The side-curved surface of the specimen was sealed with waterproof tape to allow water to penetrate into the specimen from the bottom end. The specimens were placed upright and supported to allow a sufficient gap of 100 mm for water to be absorbed by capillary suction. A 5-mm head of water above the bottom of the specimen was chosen for this investigation. Weights of the specimens before and after immersion were determined after 1, 5, 10, 20, and 30 min and 1, 2, 3, 4, 5, and 6 h of immersion. The weight of water absorbed and the rate of sorptivity were then calculated.

Sulfate Resistance

Mortar bars with dimensions of 25 × 25 × 285 mm were used to test the sulfate resistance (ASTM 2010). They were immersed in 10% sodium sulfate solution after the age of seven days in a 23°C controlled room, and were tested for sulfate-induced expansion and weight change until 360 days of immersed time. The sulfate solution was replaced with fresh solution weekly for the first month and monthly thereafter. The reported results were the average of four samples. The weight changes of the samples were also recorded.

Results and Discussion

Compressive Strength

The compressive strengths of mortars are given in Table 3. It was evident that the strength of geopolymer mortars was affected by the fineness of BA and extra water. Series A mixes with no extra water gave high compressive strengths at 28 days of 40.0–54.5 MPa. The extra water is sometimes needed to improve the workability of the mixes (Sathonsaowaphak et al. 2009). The addition of extra water in a water/ash ratio of 0.08 drastically reduced the compressive strengths to 13.5–22.5 MPa. Although water was needed for the geopolymerization process and workability, the excess water reduced the strength of geopolymer mortars (Chindaprasirt et al. 2007a; Sathonsaowaphak et al. 2009). The leaching of silica and alumina was reduced because extra water diluted the concentration of base solution.

Table 2. Mix Proportions of the Geopolymer Mortars

Mix	Type of BA	BA (g)	NS (g)	NH (g)	Water (g)	Sand (g)
AF	F	100.0	35.8	23.9	0.0	275.0
AM	M	100.0	35.8	23.9	0.0	275.0
AC	C	100.0	35.8	23.9	0.0	275.0
BF	F	100.0	35.8	23.9	8.0	275.0
BM	M	100.0	35.8	23.9	8.0	275.0
BC	C	100.0	35.8	23.9	8.0	275.0

Note: 10 M NH, sand/BA = 2.75, liquid alkaline/BA = 0.597, NS/NH = 1.50.

J. Mater. Civ. Eng. 2013.25:105-111.

Table 3. Compressive Strengths and Rates of Sorptivity of Geopolymer Mortars

Mix	Compressive strength (MPa)					Rate of sorptivity ($\mu m/s^{1/2}$)
	7 days	28 days	90 days	180 days	360 days	7 days
AF	48.5	54.5	51.5	61.5	55.5	6.1
AM	46.0	48.0	46.5	49.5	39.5	7.6
AC	43.0	40.0	32.5	35.0	36.5	11.0
BF	16.0	22.5	22.0	22.5	23.5	14.0
BM	16.0	15.0	15.0	16.5	13.5	16.0
BC	16.5	13.5	13.5	11.5	15.0	40.0

The fineness of BA also contributed to the compressive strength of mortar. For Series A using fine BA (AF mix), the strengths of mortars were highest. The compressive strengths of AF, AM, and AC mixes at 28 days were 54.5, 48.0, and 40.0 MPa, respectively. For Series B, relatively high strengths of the mix using fine BA compared to the mixes using medium and coarse BA were also observed. A similar increase in strengths of geopolymer mortars with the increase in the fineness of BA has been reported (Sathonsaowaphak et al. 2009).

The development of strength was also affected by the ash fineness. For fine BA, the strength developments after seven days of AF and BF mortars were clearly observed. The compressive strengths of AF mortars at 7, 28, 90, 180, and 360 days were 48.5, 54.5, 51.5, 61.5, and 55.5 MPa, respectively. The compressive strengths of BF mortars at the same ages were 16.0, 22.5, 22.0, 22.5, and 23.5 MPa, respectively. For the coarser ashes, the strength developments after seven days of AM, AC, BM, and BC mortars were not observed. The BA with high fineness and high surface area could dissolve more silica and alumina and resulted in the increase in geopolymerization and strength. In addition, a large portion of BA particles were porous and contributed to the low strength of geopolymer mortars (Chindaprasirt et al. 2009). Grinding helped to destroy the pores of BA particles (Sathonsaowaphak et al. 2009) and thus improved the strength of geopolymer mortars. Some losses of strengths of geopolymer concretes were observed at the later age of 365 days. Shrinkage cracking (Wongpa et al. 2010) and sodium and carbon dioxide reaction (Pacheco-Torgal et al. 2007) were proposed as the reasons.

Volume Intrusion of MIP

The results of volume intrusion of the MIP of geopolymer pastes are shown in Fig. 4. The volume intrusion (VI) down to 0.007 μm was dependent on the BA fineness and amount of extra water. In general, the amount of VI increased gradually with the decreasing pore diameter. For fine BA, the increases in VI values were initially lower thanthose of medium BA and coarse BA. The threshold VI values of slightly higher than 0.02 m^3/Mg at a pore diameter of 0.02 μm were quite prominent for both AF and BF pastes. For the medium BA, the threshold values were not as distinct as those of fine BA. They were located at VI of 0.04 m^3/Mg at pore diameter of 0.025 μm and VI of 0.06 m^3/Mg at pore diameter of 0.03 μm for AM and BM pastes, respectively. This indicated that the extra water and the increase in the BA median particle size resulted in the increase in large pores. The results of VI of coarse BA paste clearly reflected this observation. The leaching of alumina and silica was dependent on the contact area of ash particles and base solution (Rattanasak and Chindaprasirt 2009). The fine BA with high surface area eased the dissolution of silica, alumina, and calcium, which resulted in higher geopolymerization (Sathonsaowaphak et al. 2009) and a higher amount of calcium silicate hydrate (C-S-H) (Somna et al. 2011) than those of coarser BA. This produced a denser matrix and higher compressive strength mortars than those with coarser BA and with extra water.

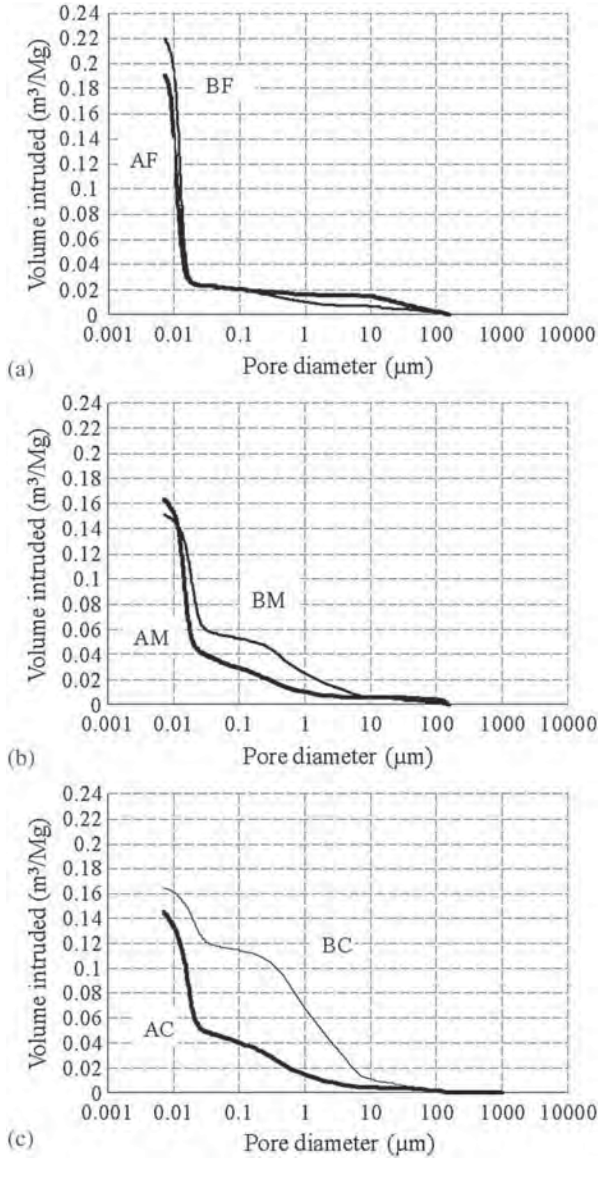

Fig. 4. Intruded volume of MIP of geopolymer pastes: (a) AF and BF pastes; (b) AM and BM pastes; (c) AC and BC pastes

The increase in VI was very high at the approximate pore size of 0.01–0.02 μm. For fine BA, a significantly higher percentage of small pores at approximately 0.01 μm could be observed, compared to that of large pores (larger than 0.02 μm). The high rate of increase was reduced with the addition of extra water and

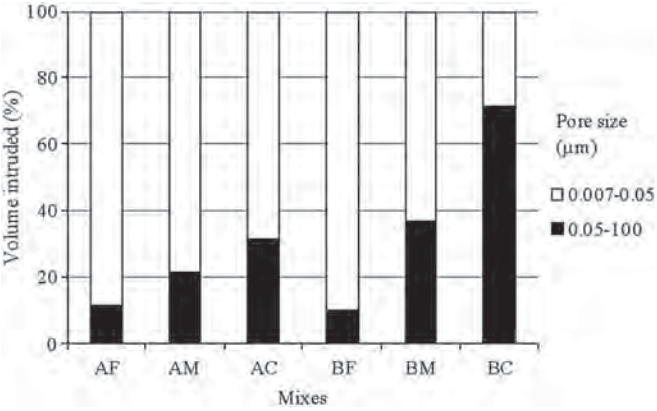

Fig. 5. Percentage of intruded volume of MIP

reduction in fineness of BA. These results suggested an increase in gel pore (approximately 0.01–0.02 μm) and the corresponding increase in gel formation.

To further compare the results, the amount of small pores and large pores were identified, as shown in Fig. 5. The small pores were pores with sizes up to 0.05 μm, which included small capillary pores (Chindaprasirt et al. 2007b). The percentages of VI of small and large pores were clearly affected by the water/ash ratio and fineness of BA. The percentage of VI of large pores between 0.05–100 μm of AF and BF pastes was low at 10%. The percentages of VI increased with the decrease in fineness of BA and with the addition of extra water. The percentages of large pores of AM and AC pastes were 21 and 33%, compared to 37 and 70% of those of BM and BC pastes. The geopolymer porosity was affected by the water/ash ratio (Skvara et al. 2006). The addition of extra water increased the porosity of the geopolymer paste. The incorporation of water effectively improved the workability of geopolymer, with some reductions in strength (Chindaprasirt et al. 2007a). Excess water also diluted the liquid and thus slowed down the dissolution and reaction of geopolymer (Sathonsaowaphak et al. 2009). The increase in porosity and dilution of liquid alkaline activator were the primary reasons for the reduction in strength.

Rate of Sorptivity

The results in Table 3 showed that the rate of sorptivity of mortar decreased with the increase in fineness of BA. The rate of sorptivity of AF, AM, and AC mortars were 6.1, 7.6, and 11.0 $\mu\mathrm{m/s}^{1/2}$, respectively. The sorption versus time$^{1/2}$ curves were linear and very close to the straight line. The relatively low sorptivity indicated that the pores were too small to take up water. The use of fine BA resulted in a dense and strong matrix and the decrease in the rate of sorptivity values, as expected. The obtained rate of sorptivity values were similar to those of portland cement or portland blended cement concrete of 5.0–30.0 $\mu\mathrm{m/s}^{1/2}$ (Ghrici et al. 2007; Gonen and Yazicioglu 2007; Keleştemur and Demirel 2010). The addition of water to improve the workability resulted in mixes with less dense matrices and the rate of sorptivity values increased more than those of Series A. The rate of sorptivity values of BF, BM, and BC mixes were 14.0, 16.0, and 40.0 $\mu\mathrm{m/s}^{1/2}$, respectively. These rate of sorptivity values were approximately 2.5–4 times higher than the corresponding values of Series A. The rate of sorptivity values of BF and BM at 14.0 and 16.0 $\mu\mathrm{m/s}^{1/2}$ were within the normal range of those of portland cement mortar. However, the rate of sorptivity value of BC of 40.0 $\mu\mathrm{m/s}^{1/2}$ was higher than those of portland cement. The high rate of sorptivity of the BC mix corresponded with a large amount of large pores, indicated by the MIP results (Fig. 4).

Sulfate Resistance

The results of mortar bar expansion are given in Fig. 6(a). The expansion of mortar bars was found to depend on the fineness of the BA and the water content of mixture. The expansions of Series B, which contained extra water, were significantly higher than those of Series A. After immersion for 360 days, the expansions of Series B were between 215 and 325 microstrains, whereas those of Series A were between 80 and 160 microstrains. The results correlated with the results of pore size and strength. The mix with extra water content and a large amount of large pores exhibited high expansion and low strength. For the effect of fineness of BA, the expansions were lower with the use of fine BA. For Series A, the expansions after a 360-day immersion were 80, 125, and 160 microstrains for AF, AM, and AC mortars, respectively. For Series B, the trend of the results was similar to the expansions after 360 days of 215, 280, and 325 microstrains for BM, BF, and BC mortars, respectively.

The values of expansion of 215–315 and 230–335 microstrains for Series B mixes after 270 and 360 days of immersion in 10% sulfate solution were still lower than those of mortars made from portland cement replaced with 20–25% fly ash immersed in 5–10% sodium sulfate solution (Chindaprasirt et al. 2007c; Nehdi and Hayek 2005). The expansions of mortars made from portland cement replaced with 20–40% fly ash immersed for 360 days in 5% sodium sulfate solution were between 500 and 750 microstrains (Chindaprasirt et al. 2007c).

The results of the weight change of geopolymer mortar bar immersed in sulfate solution are shown in Fig. 6(b). The weight gains were dependent on the fineness of BA and water content. For Series B mixes with extra water, the weight gains were high at 2–5% and those of Series A mixes were lower than 2% after 180–360 days of

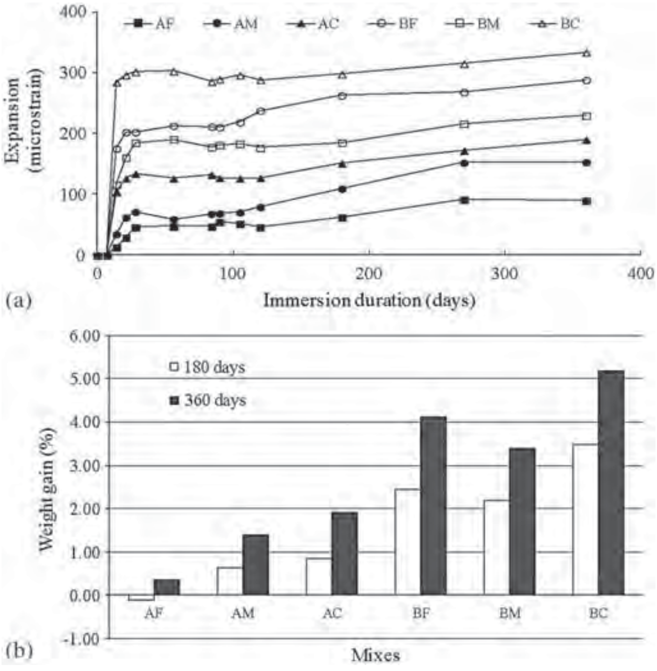

Fig. 6. Change in length and weight of mortar bars in 10% sodium sulfate solution after 180–360 days of immersion: (a) length change; (b) percentages of weight change

immersion. In fact, the initial weight gains of AF and AM mortars were very low, and significant weight gains were obtained after a period of immersion. The weight gain increased with the increasing amount of large pores. For the effect of fineness, the fine BA performed better than the coarse BA. The fine BA geopolymer was denser and contained fewer large pores than the coarse BA geopolymer.

The expansion of high calcium BA geopolymer mortar immersed in sodium sulfate solution was attributable to the formation of ettringite and gypsum crystal (Bakharev 2005; Sata et al. 2012). The high calcium content of BA reacted with sulfate ion and formed the calcium sulfate, which precipitated within the pores of matrix. It was also reported that the calcium reacted and formed C-S-H, and coexisted with the geopolymer gel (Somna et al. 2011). In addition, the sulfate also reacted with other ions such as aluminum and formed ettringite (calcium sulfoaluminate hydrate). The formation of both gypsum crystals and ettringite contributed to the expansion of mortar bars. After immersion in sodium sulfate solution, mortars made from coarse BA and those with extra water with a low degree of geopolymerization and large amount of large pores contained a large amount of ettringite and gypsum, and thus showed large expansion and weight gain. In the study of fly ash geopolymer samples immersed in sodium and magnesium sulfate solutions, the ettringite phase was identified using XRD (Bakharev 2005). Other sulfate products were also likely to be present after the sulfate attack.

Conclusions

Based on the obtained data, the following conclusions were made:

1. The high calcium bottom ash geopolymer with relatively high compressive strengths of 40.0–54.5 MPa at 28 days were obtained with the use of finely ground BA, 10 M NaOH, sodium silicate solution with temperature curing at 75°C for 48 h. The fine BA gave a high compressive strength due to an increase in reactivity through a more increased surface area than medium and coarse BA.
2. The strengths of high calcium bottom ash geopolymer mortar were dependent on BA fineness and the amount of water in the mixes. The addition of extra water at a water/ash ratio of 0.08 significantly improved the workability of mixes. However, the 28-day compressive strengths were significantly reduced to 13.5–22.5 MPa.
3. The threshold values of the intruded volume, pore sizes of paste, and rate of sorptivity of mortar of high calcium bottom ash geopolymer were dependent on the fineness of BA and extra water. The pastes with low percentages of large pores and mortars with low rates of sorptivity were obtained with mixes with no extra water and with fine BA.
4. The resistance to sulfate attack of high calcium bottom ash geopolymer mortar was excellent, because the expansion of mortar bars after immersion in the 10% sodium sulfate solution for 360 days were low. The expansion was primarily related to the formation of ettringite and gypsum.

Acknowledgments

This work was financially supported by the Higher Education Research Promotion and National Research University Project of Thailand, Office of the Higher Education Commission, through the Advanced Functional Materials Cluster of Khon Kaen University and the Thailand Research Fund (TRF) under the TRF Senior Research Scholar, Grant No. RTA5480004.

References

ASTM. (2002). "Standard test method of compressive strength of hydrualic cement mortars (using 2-in. or [50 mm] cube speciments)." C109, West Conshohocken, PA.

ASTM. (2010). "Standard test method for length change of hydraulic-cement mortars exposed to a sulfate solution." C1012, West Conshohocken, PA.

ASTM. (2011). "Standard test method for measurement of rate of absorption of water by hydraulic-cement concretes." C1585, West Conshohocken, PA.

Atahan, H. N., and Dikme, D. (2011). "Use of mineral admixtures for enhanced resistance against sulfate attack." *Constr. Build. Mater.*, 25(8), 3450–3457.

Bakharev, T. (2005). "Durability of geopolymer materials in sodium and magnesium sulfate solutions." *Cem. Concr. Res.*, 35(6), 1233–1246.

Bakharev, T., Sanjayan, J. G., and Cheng, Y. B. (2003). "Resistance of alkali-activated slag concrete to acid attack." *Cem. Concr. Res.*, 33(10), 1607–1611.

Bonakdar, A., and Mobasher, B. (2010). "Multi-parameter study of external sulfate attack in blended cement materials." *Constr. Build. Mater.*, 24(1), 61–70.

Cheriaf, M., Rocha, J. C., and Péra, J. (1999). "Pozzolanic properties of pulverized coal combustion bottom ash." *Cem. Concr. Res.*, 29(9), 1387–1391.

Chindaprasirt, P., Chareerat, T., and Sirivivatnanon, V. (2007a). "Workability and strength of coarse high calcium fly ash geopolymer." *Cem. Concr. Compos.*, 29(3), 224–229.

Chindaprasirt, P., Jaturapitakkul, C., Chalee, W., and Rattanasak, U. (2009). "Comparative study on the characteristics of fly ash and bottom ash geopolymers." *Waste Manage.*, 29(2), 539–543.

Chindaprasirt, P., Jaturapitakkul, C., and Sinsiri, T. (2007b). "Effect of fly ash fineness on microstructure of blended cement paste." *Constr. Build. Mater.*, 21(7), 1534–1541.

Chindaprasirt, P., Kanchanda, P., Sathonsaowaphak, A., and Cao, H. T. (2007c). "Sulfate resistance of blended cements containing fly ash and rice husk ash." *Constr. Build. Mater.*, 21(6), 1356–1361.

Davidovits, J. (1999). "Chemistry of geopolymeric systems, terminology." *Proc., Geopolymer Second Int. Conf., Géopolymère'99*, J. Davidovits, R. Davidovits, and C. James, eds., Geopolymer Institute, Saint-Quentin, France, 9–39.

Detphan, S., and Chindaprasirt, P. (2009). "Preparation of fly ash and rice husk ash geopolymer." *Int. J. Miner. Metall, Mater.*, 16(6), 720–726.

Duxson, P., Provis, J. L., Lukey, G. C., and van Deventer, J. S. J. (2007). "The role of inorganic polymer technology in the development of 'green concrete." *Cem. Concr. Res.*, 37(12), 1590–1597.

Fernandez-Jimenez, A., García-Lodeiro, I., and Palomo, A. (2007). "Durability of alkali-activated fly ash cementitious materials." *J. Mater. Sci.*, 42(9), 3055–3065.

Ghrici, M., Kenai, S., and Said-Mansour, M. (2007). "Mechanical properties and durability of mortar and concrete containing natural pozzolana and limestone blended cements." *Cem. Concr. Compos.*, 29(7), 542–549.

Gonen, T., and Yazicioglu, S. (2007). "The influence of compaction pores on sorptivity and carbonation of concrete." *Constr. Build. Mater.*, 21(5), 1040–1045.

Gordon, L. E., Provis, J. L., and van Deventer, J. S. J. (2011). "Non-traditional ("geopolymer") cements and concretes for construction of large CCS equipment." *Energy Procedia*, 4(0), 2058–2065.

Jaturapitakkul, C., and Cheerarot, R. (2003). "Development of bottom ash as pozzolanic material." *J. Mater. Civ. Eng.*, 15(1), 48–53.

Keleştemur, O., and Demirel, B. (2010). "Corrosion behavior of reinforcing steel embedded in concrete produced with finely ground pumice and silica fume." *Constr. Build. Mater.*, 24(10), 1898–1905.

Kong, D. L. Y., Sanjayan, J. G., and Sagoe-Crentsil, K. (2007). "Comparative performance of geopolymers made with metakaolin and fly ash after exposure to elevated temperatures." *Cem. Concr. Res.*, 37(12), 1583–1589.

J. Mater. Civ. Eng. 2013.25:105-111.

Lee, S. T., Moon, H. Y., and Swamy, R. N. (2005). “Sulfate attack and role of silica fume in resisting strength loss.” *Cem. Concr. Compos.*, 27(1), 65–76.

Malhotra, V. M. (2002). “Introduction: Sustainable development and concrete technology.” *Concr. Int.*, 24, 22.

Nehdi, M., and Hayek, M. (2005). “Behavior of blended cement mortars exposed to sulfate solutions cycling in relative humidity.” *Cem. Concr. Res.*, 35(4), 731–742.

Pacheco-Torgal, F., Abdollahnejad, Z., Camões, A. F., Jamshidi, M., and Ding, Y. (2012). “Durability of alkali-activated binders: A clear advantage over Portland cement or an unproven issue?” *Constr. Build. Mater.*, 30(0), 400–405.

Pacheco-Torgal, F., Castro-Gomes, J., and Jalali, S. (2007). “Investigations about the effect of aggregates on strength and microstructure of geopolymeric mine waste mud binders.” *Cem. Concr. Res.*, 37(6), 933–941.

Palomo, A., Grutzeck, M. W., and Blanco, M. T. (1999). “Alkali-activated fly ashes: A cement for the future.” *Cem. Concr. Res.*, 29(8), 1323–1329.

Poon, C. S., Kou, S. C., and Lam, L. (2006). “Compressive strength, chloride diffusivity and pore structure of high performance metakaolin and silica fume concrete.” *Constr. Build. Mater.*, 20(10), 858–865.

Rattanasak, U., and Chindaprasirt, P. (2009). “Influence of NaOH solution on the synthesis of fly ash geopolymer.” *Miner. Eng.*, 22(12), 1073–1078.

Sata, V., Sathonsaowaphak, A., and Chindaprasirt, P. (2012). “Resistance of lignite bottom ash geopolymer mortar to sulfate and sulfuric acid attack.” *Cem. Concr. Compos.*, 34(5), 700–708.

Sathonsaowaphak, A., Chindaprasirt, P., and Pimraksa, K. (2009). “Workability and strength of lignite bottom ash geopolymer mortar.” *J. Hazard. Mater.*, 168(1), 44–50.

Skvara, F., Kopecky, L., Nemecek, J., and Bittnar, Z. (2006). “Microstructure of geopolymer materials based on fly ash.” *Ceram. Silik.*, 50(4), 208–215.

Somna, K., Jaturapitakkul, C., Kajitvichyanukul, P., and Chindaprasirt, P. (2011). “NaOH-activated ground fly ash geopolymer cured at ambient temperature.” *Fuel*, 90(6), 2118–2124.

Thokchom, S., Ghosh, P., and Ghosh, S. (2010). “Performance of fly ash based geopolymer mortars in sulphate solution.” *J. Eng. Sci. Technol. Rev.*, 3(1), 36–40.

Van Jaarsveld, J. G. S., Van Deventer, J. S. J., and Lukey, G. C. (2002). “The effect of composition and temperature on the properties of fly ash- and kaolinite-based geopolymers.” *Chem. Eng. J.*, 89(1–3), 63–73.

Wongkeo, W., and Chaipanich, A. (2010). “Compressive strength, microstructure and thermal analysis of autoclaved and air cured structural lightweight concrete made with coal bottom ash and silica fume.” *Mater. Sci. Eng. A*, 527(16–17), 3676–3684.

Wongpa, J., Kiattikomol, K., Jaturapitakkul, C., and Chindaprasirt, P. (2010). “Compressive strength, modulus of elasticity, and water permeability of inorganic polymer concrete.” *Mater. Des.*, 31(10), 4748–4754.

Zuda, L., Drchalová, J., Rovnaník, P., Bayer, P., Keršner, Z., and Černý, R. (2010). “Alkali-activated aluminosilicate composite with heat-resistant lightweight aggregates exposed to high temperatures: Mechanical and water transport properties.” *Cem. Concr. Compos.*, 32(2), 157–163.

International Journal of Minerals, Metallurgy and Materials
Volume 20, Number 2, February 2013, Page 214
DOI: 10.1007/s12613-013-0715-6

Properties of high calcium fly ash geopolymer pastes with Portland cement as an additive

*Tanakorn Phoo-ngernkham*1), *Prinya Chindaprasirt*1), *Vanchai Sata*1), *Saengsuree Pangdaeng*1), *and Theerawat Sinsiri*2)

1) Sustainable Infrastructure Research and Development Center, Department of Civil Engineering, Faculty of Engineering, Khon Kaen University, Khon Kaen 40002, Thailand

2) School of Civil Engineering, Institute of Engineering, Suranaree University of Technology, Nakhonratchasima 30000, Thailand

(Received: 21 December 2011; revised: 29 February 2012; accepted: 2 March 2012)

Abstract: The effect of Portland cement (OPC) addition on the properties of high calcium fly ash geopolymer pastes was investigated in the paper. OPC partially replaced fly ash (FA) at the dosages of 0, 5%, 10%, and 15% by mass of binder. Sodium silicate (Na_2SiO_3) and sodium hydroxide (NaOH) solutions were used as the liquid portion in the mixture: NaOH 10 mol/L, Na_2SiO_3/NaOH with a mass ratio of 2.0, and alkaline liquid/binder (L/B) with a mass ratio of 0.6. The curing at 60°C for 24 h was used to accelerate the geopolymerization. The setting time of all fresh pastes, porosity, and compressive strength of the pastes at the stages of 1, 7, 28, and 90 d were tested. The elastic modulus and strain capacity of the pastes at the stage of 7 d were determined. It is revealed that the use of OPC as an additive to replace part of FA results in the decreases in the setting time, porosity, and strain capacity of the paste specimens, while the compressive strength and elastic modulus seem to increase.

Keywords: geopolymers; Portland cement; fly ash; compressive strength; porosity; elastic moduli

1. Introduction

Currently, Portland cement (OPC) is used extensively as a cementitious material for construction and building. However, the process of producing OPC also results in environmental problems and releases a large amount of green house gas [1]. Therefore, the effort focuses on how to replace part of OPC with by-products or natural materials. Recently, a new and more environmental friendly binding material, called geopolymer, was developed [2]. Geopolymer is normally made from a source material containing silica and alumina, and activated with alkali solution.

Fly ash (FA) is a by-product from lignite coal burning from Mae Moh Power Station in northern Thailand. The annual output is approximately 3 million tons. This FA consists mainly of silicon dioxide (SiO_2), aluminum trioxide (Al_2O_3), and calcium oxide (CaO). High CaO is the normal feature of high calcium fly ash. The use of FA as pozzolan in concrete is constantly increasing because it improves the properties of concrete, namely, workability, durability, and long-term strength in hardened concrete [3-4]. It has been also shown that this high calcium fly ash is suitable as a source material for making good geopolymer [5-6]. The high calcium content of fly ash leads to the formation of calcium silicate hydrate which coexists with the aluminosilicate geopolymer products [7-8]. The coexistence of calcium silicate hydrate (C-S-H) phase with the geopolymeric gel has been proved to improve the mechanical properties of final products [9]. In addition, it has been suggested that, for geopolymer containing various Ca compounds, the calcium enters into the geopolymer network, possibly acting as the charge-balancing cation [10].

The reaction of fly ash and alkali solution is an endothermal process and thus requires the extra heat [11-

---

Corresponding author: Prinya Chindaprasirt E-mail: prinya@kku.ac.th

12]. In the production of fly ash geopolymer, a moderate heat is usually incorporated to accelerate the geopolymerization. The reaction of OPC with water is an exothermal process and generates heat. The addition of OPC in a fly ash geopolymer system should be beneficial not only on the mechanical properties but on the setting and reaction of the system. The amount of OPC as an additive should not be large. The heat generated by OPC hydration should assist the geopolymerization process.

This paper studied the properties of geopolymer pastes made from high calcium FA with OPC as an additive. The knowledge would be beneficial to the future applications of geopolymeric materials.

2. Experimental

2.1. Materials

A high calcium fly ash (FA) from Mae Moh Power Plant in northern Thailand and Portland cement Type I (OPC) were used in this study. Sodium hydroxide (NaOH) and sodium silicate (Na_2SiO_3) with 13.89% Na_2O, 32.15% SiO_2, and 46.04% H_2O by mass were used as a liquid portion in the mixture to activate the geopolymerization.

Table 1 shows the chemical composition of FA and OPC. The physical properties of materials are shown in Table 2. The specific gravity of FA and OPC are 2.61 and 3.16, respectively. The median particle sizes of FA and OPC are 8.5 and 14.6 μm with the corresponding Blaine fineness values of 4300 and 3600 cm^2/g, respectively.

2.2. Mix proportion of geopolymer pastes

The mix proportions of geopolymer pastes are shown in Table 3. The control, FA5PC, FA10PC, and FA15PC pastes are geopolymer pastes with 0%, 5%, 10%, and 15% OPC by mass of binder. The constant ratio of liquid alkaline to binder by mass (L/B, 0.60) and the ratio of Na_2SiO_3 to NaOH by mass (2.0) based on the previous research [13] were used for all mixtures. The NaOH and Na_2SiO_3 solutions were first mixed together and used as the liquid solution. FA and OPC were dry and mixed until homogenous. Thereafter, the liquid solution was added, and mixing of pastes was done for 5 min.

Table 1. Chemical composition of materials **wt%**

Materials	SiO_2	Al_2O_3	Fe_2O_3	CaO	MgO	K_2O	Na_2O	SO_3	LOI
FA	29.32	12.96	15.64	25.79	2.94	2.93	2.83	7.29	0.30
OPC	20.80	4.70	3.40	65.30	1.50	0.40	0.10	2.70	0.90

Table 2. Physical properties of materials

Materials	Specific gravity	Median particle size, d_{50} / μm	Blaine fineness / ($cm^2 \cdot g^{-1}$)
FA	2.61	8.5	4300
OPC	3.16	14.6	3600

Table 3. Mix proportions of geopolymer pastes

Mix No.	Symbol	Mix proportion / wt%		SiO_2/Al_2O_3 mole ratio
		FA	OPC	
1	Control	100	0	3.26
2	FA5PC	95	5	3.28
3	FA10PC	90	10	3.30
4	FA15PC	85	15	3.33

2.3. Setting time and compressive strength of geopolymer pastes

After mixing, the setting time of geopolymer pastes were tested in accordance with ASTM C191 [14]. The reported setting times of geopolymer pastes were the average of three samples.

Cube moulds of 50 mm×50 mm×50 mm were used for the compressive strength tests of geopolymer pastes. The specimens were prepared in accordance with ASTM C109 [15]. The moulds were wrapped with vinyl sheets to protect the moisture loss and left standing for 1 h. Then, the specimens were placed in the oven for heat curing at 60°C for 24 h. After the heat curing, the specimens were kept in the laboratory to cool down and demoulded the next day. At last, they were kept in a 23°C control room. The reported compressive strengths of geopolymer pastes are the average of five samples.

2.4. Porosity of geopolymer pastes

Cylindrical specimens with 50 mm in diameter and 100 mm in height were prepared for the porosity measurement of geopolymer paste specimens. The specimens were cured in a 23°C control room and tested after curing time of 1, 7, 28, and 90 d. The porosity was calculated using Eq. (1). Moreover, the water absorption of geopolymer pastes was also tested. The porosity and water absorption were determined as described in ASTM C642 [16]. The methods for measuring porosity and water absorption were used successfully in a number of researches [17-20]. The reported results are the average of three samples.

$$\begin{cases} p = \dfrac{B-A}{B-C} \times 100\% \\ w = \dfrac{B-A}{A} \times 100\% \end{cases} \tag{1}$$

where p is the vacuum saturation porosity; w the vacuum saturation water absorption; A the weight of the oven-dried sample, g; B the weight in air of the saturated sample, g; and C the weight in water of the saturated sample, g.

3. Results and discussion

3.1. Setting time

The setting time of geopolymer pastes at various replacement levels of OPC are shown in Fig. 1. The initial setting time of control, FA5PC, FA10PC, and FA15PC pastes are 30, 27, 20, and 15 min, and the final setting time of these pastes are 58, 47, 38, and 26 min, respectively. The setting time of geopolymer pastes obviously decreased with the increase in the replacement of OPC, indicating the faster activation of the pastes. The addition of calcium in soluble or partly soluble states significantly accelerated the setting and hardening of geopolymer pastes [6, 21]. Readily available free Ca ions from OPC and high-calcium FA also reacted and formed C-S-H and calcium aluminosilicate hydrate (C-A-S-H) [22-23]. The higher Ca content with the reduced amount of SiO_2 and Al_2O_3 of binders led to a higher reaction degree [24]. The faster setting time of FA-OPC paste could be advantages in the repair binding materials or in other conditions where fast setting is required.

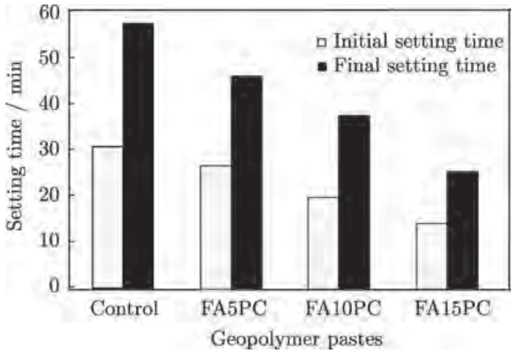

Fig. 1. Setting time of geopolymer pastes.

3.2. Compressive strength

The compressive strengths of geopolymer pastes at various replacement levels of OPC are shown in Fig. 2. The compressive strengths of geopolymer pastes obviously increased with the increase in replacement levels of OPC and curing time. When the content of OPC increased, the compressive strength of geopolymer pastes was significantly improved due to the increased amount of Ca content, which altered the microstructure of geopolymer gels [21, 25]. These results agreed with previous researches [22, 26]. The increase in Ca led to a high compressive strength mix due to the additional formation of C-S-H and C-A-S-H gels, which modified the microstructure of the paste. C-S-H and C-A-S-H within geopolymeric binder could work as a micro-aggregate, thereby enhanced the durability and compressive strength [21, 27]. The reaction with SiO_2 and Al_2O_3 of binder reduced the $Ca(OH)_2$ content of the system, and the pore structure was refined in a similar way as the pozzolanic reaction in the blended cement paste [28]. As shown in Fig. 2, for the low replacement levels of OPC in control and FA5PC mixes, the rates of strength improvement are low after curing for 28 d. However, the rates are high for the high OPC replacement levels in FA10PC and FA15PC mixes. This was associated with the reaction of OPC and pozzolanic reactions to form additional C-S-H and C-A-S-H. The increase in compressive strength at the later stage in this system was very useful, as this could compensate for the possible strength reduction at the later stage often observed [29].

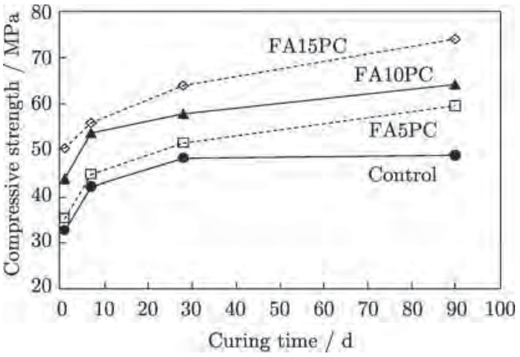

Fig. 2. Compressive strength of geopolymer pastes.

3.3. Porosity and water absorption

The results of porosity and water absorption of geopolymer pastes are shown in Table 4. The porosities at all stages of pastes are lowered with the increases in the replacement level of OPC and curing time. For example, the porosities at 28 d of control, FA5PC, FA10PC, and FA15PC pastes are 14.6%, 13.3%, 12.4%, and 12.0%, respectively, and the porosities of FA10PC pastes at 1, 7, 28, and 90 d are 15.5%, 12.9%, 12.4%, and 12.0%, respectively. The water absorption capacity decreases with the increase in curing time as expected. The water adsorption values were slightly less than the absorptions, as some of pores were not readily accessible. The results corresponded well with the strength behavior. The increase in OPC content led to a higher compressive strength and reduced porosity. The reduced porosity and increased density were the results of pore structure refinement from coarser to finer [30-32].

Table 4. Porosity and water absorption of geopolymer pastes

Mixes	Porosity / %				Water absorption (7 d) / %
	1 d	7 d	28 d	90 d	
Control	18.5	15.2	14.6	14.3	10.2
FA5PC	17.9	14.6	13.3	12.5	9.5
FA10PC	15.5	12.9	12.4	12.0	8.7
FA15PC	13.4	12.6	12.0	11.1	8.5

3.4. Stress-strain and elastic modulus of geopolymer pastes

The relationships between stress and strain of geopolymer pastes curing for 7 d are shown in Table 5 and Fig. 3. The chord modulus was determined as described in ASTM C469 [33]. The values of elastic modulus and compressive strength increased with the OPC replacement levels. The denser and stronger pastes with the addition of OPC resulted in the increase in elastic modulus. The elastic modulus values of normal strength Portland cement pastes were reported to be between 12.5 and 17.5 GPa [34-35], which were similar to that of geopolymer pastes without OPC. The addition of OPC produced additional C-S-H and C-A-S-H within geopolymeric binder and acted as a micro-aggregate, which enhanced the compressive strength [21, 27] and increased the elastic modulus of the pastes. For the strain capacity, the strains at peak stress (strain capacity) were lowered with the increase in the OPC replacement level. The strain capacity at peak stress tended to reduce, whereas the elastic modulus tended to increase with the increase in the OPC content compared to those of the control paste.

Table 5. Strain capacity (ε_p) and elastic modulus (E) of geopolymer pastes curing for 7 d

Mixes	ε_p	E / GPa
Control	0.00302	13.7
FA5PC	0.00247	15.2
FA10PC	0.00238	19.4
FA15PC	0.00230	23.2

Fig. 4 shows the relationship between elastic modulus and compressive strength of geopolymer pastes. The elastic modulus tended to increase linearly with the square root of ultimate compressive strength. The equation predicting this relationship can be written as

$$E = 8.507\sqrt{f_c'} - 41.649 \tag{2}$$

where E stands for the elastic modulus, GPa; and f_c' the ultimate compressive strength, MPa.

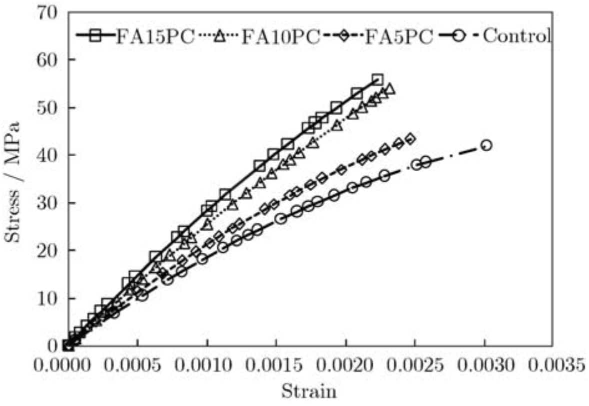

Fig. 3. Relationship between stress and strain of geopolymer pastes.

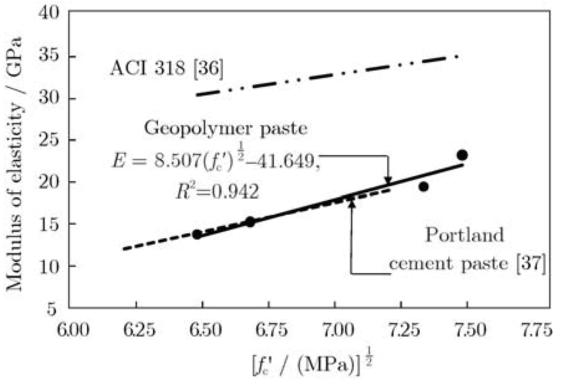

Fig. 4. Relationship between elastic modulus and compressive strength of geopolymer pastes.

As shown in Fig. 4, the elastic modulus values of geopolymer pastes in this study are approximately half of those given by ACI 318 for Portland cement concrete [36], and similar to those of the Portland cement paste with the similar strengths (between 38.5 and 52.2 MPa) [34, 37]. The elastic modulus of inorganic polymer concrete (IPC) depends primarily on the SiO_2/Al_2O_3 mole ratios by mass [38]. In this study, the SiO_2/Al_2O_3 mole ratio of mixes varied in a narrow range between 3.26-3.33, as shown in Table 3, and its effects on the strength and elastic modulus would be small. The influences on the elastic modulus and strength were, therefore, from the addition of OPC. The increased calcium reacted and formed additional C-S-H and C-A-S-H. The results also suggested that the increase in OPC content was very useful in terms of improvement in the stiffness of this inorganic polymer matrix.

3.5. Relationship between compressive strength and porosity of geopolymer pastes

The relationship between compressive strength and porosity of geopolymer pastes is shown in Fig. 5, which can be presented in the form of Eq. (3). The similar relationship between strength and porosity of Portland cement pastes from previous research [39] was also reported for comparison. A slightly lower in the strength and porosity curve obtained from this study could be attributed to the difference in the measuring of porosity. The values obtained from the vacuum saturation porosity, as described in ASTM C642, was slightly lower than that obtained from the mercury intrusion porosimetry (MIP).

$$f'_c = 211.711\exp(-0.103p) \tag{3}$$

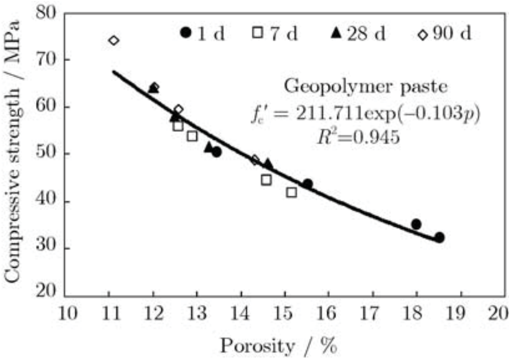

Fig. 5. Relationship between porosity and compressive strength of geopolymer pastes.

The results indicated that increasing the compressive strength of geopolymer pastes corresponded to the reduction in porosity. The addition of OPC resulted in the rich of $Ca(OH)_2$, and increased C-S-H and C-A-S-H phases, which refined the pore structure of geopolymer pastes [40] and increased the compressive strength and elastic modulus of geopolymer pastes.

3.6. SEM analysis

The SEM photos of FA and FA10PC geopolymer pastes are shown in Fig. 6. The FA paste contains a larger number of non-reacted and/or partially reacted fly ash particles embedded in a continuous matrix. For FA10PC paste, a less number of fly ash particles are observed, and the matrix appears denser than that of the FA paste. The use of high calcium fly ash resulted in the formation of C-S-H which co-existed with geopolymer products [7-8]. The incorporation of Portland cement resulted in the less amount of fly ash used and also the formation of additional C-S-H and C-A-S-H, which also would coexist with geopolymer products. This led to the overall increase in the strength of geopolymer products.

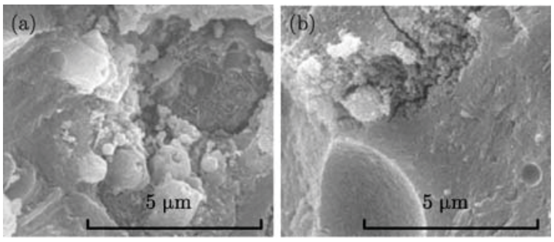

Fig. 6. SEM images of geopolymer pastes: (a) FA; (b) FA10PC.

4. Conclusions

(1) The use of OPC to partially replace FA results in the reduction of setting time due to the increase in calcium content, which accelerates the setting and hardening of geopolymer pastes. The initial and final setting times of geopolymer pastes are between 15-30 min and 26-58 min, respectively.

(2) The incorporation of OPC increases the strength of FA geopolymer mixes due to the formation of additional C-S-H and C-A-S-H gel, which modifies the microstructure and pore of geopolymer pastes. The relatively high compressive strength (curing for 28 d, 64.0 MPa) can be obtained with the replacement of 15wt% OPC.

(3) The incorporation of OPC also increases the elastic modulus and reduces the pore of geopolymer pastes. Additional C-S-H and C-A-S-H are formed and filled the pore to make dense and strong geopolymer pastes.

(4) The strain capacity at peak stress of geopolymer pastes, however, is reduced with the increase in OPC content. The dense and strong pastes are obtained at the compensation of less deformation in terms of strain at peak stress.

Acknowledgements

This work was supported by the Higher Education Research Promotion and National Research University Project of Thailand, the Thailand Research Fund (TRF) under the TRF Senior Research Scholar (No. RTA5480004), and the Royal Golden Jubilee Ph.D. Program (No. PHD/0340/2552).

References

[1] R. McCaffrey, Climate change and the cement industry, *Global Cem. Lime Mag.*, 2002, Environ. Spec. Iss., p. 15.

[2] J. Davidovits, Geopolymers: inorganic polymeric new ma-

terials, *J. Therm. Anal.*, 37(1991), No. 8, p. 1633.

[3] S. Rukzon and P. Chindaprasirt, Mathematical model of strength and porosity of ternary blend Portland rice husk ash and fly ash cement mortar, *Comput. Concr.*, 5(2008), No. 1, p. 1.

[4] I.C. Yeh, Modelling slump of concrete with fly ash and superplasticizer, *Comput. Concr.*, 5(2008), No. 6, p. 559.

[5] P. Chindaprasirt, T. Chareerat, and V. Sirivivatnanon, Workability and strength of coarse high calcium fly ash geopolymer, *Cem. Concr. Compos.*, 29(2007), No. 3, p. 224.

[6] U. Rattanasak, K. Pankhet, and P. Chindaprasirt, Effect of chemical admixtures on properties of high-calcium fly ash geopolymer, *Int. J. Miner. Metall. Mater.*, 18(2011), No. 3, p. 364.

[7] X.L. Guo, H.S. Shi, and W.A. Dick, Compressive strength and microstructural characteristics of Class C fly ash geopolymer, *Cem. Concr. Compos.*, 32(2010), No. 2, p. 142.

[8] K. Somna, C. Jaturapitakkul, P. Kajitvichyanukul, and P. Chindaprasirt, NaOH-activated ground fly ash geopolymer cured at ambient temperature, *Fuel*, 90(2011), No. 6, p. 2118.

[9] J. Temuujin and A. van Riessen, Effect of fly ash preliminary calcination on the properties of geopolymer, *J. Hazard. Mater.*, 164(2009), No. 2-3, p. 634.

[10] J. Tailby and K.J.D. MacKenzie, Structure and mechanical properties of aluminosilicate geopolymer composites with Portland cement and its constituent minerals, *Cem. Concr. Res.*, 40(2010), No. 5, p. 787.

[11] T. Bakharev, Thermal behaviour of geopolymers prepared using class F fly ash and elevated temperature curing, *Cem. Concr. Res.*, 36(2006), p. 1134.

[12] D. Panias, I.P. Giannopoulou, and T. Perraki, Effect of synthesis parameters on the mechanical properties of fly ash-based geopolymers, *Colloids Surf. A*, 301(2007), No. 1-3, p. 246.

[13] A. Sathonsaowaphak, P. Chindaprasirt, and K. Pimraksa, Workability and strength of lignite bottom ash geopolymer mortar, *J. Hazard. Mater.*, 168(2009), No. 1, p. 44.

[14] ASTM C191, *Standard Test Method for Compressive Strength of Cylindrical Concrete Specimens*, Annual Book of ASTM Standard (Vol.04.01), American Society for Testing and Materials, Philadelphia, 2008.

[15] ASTM C109, *Standard Test Method for Compressive Strength of Hydraulic Cement Mortars (Using 2-in or [50 mm] Cube Specimens),* Annual Book of ASTM Standard (Vol.04.01), American Society for Testing and Materials, Philadelphia, 2002.

[16] ASTM C642, *Standard Test Method for Density, Absorption, and Voids in Hardened Concrete*, Annual Book of ASTM Standard (Vol.04.02), American Society for Testing and Materials, Philadelphia, 2006.

[17] P. Chindaprasirt and S. Rukzon, Strength, porosity and corrosion resistance of ternary blend Portland cement, rice husk ash and fly ash mortar, *Constr. Build. Mater.*, 22(2008), No. 8, p. 1601.

[18] T. Gonen and S. Yazicioglu, The influence of compaction pores on sorptivity and carbonation of concrete, *Constr. Build. Mater.*, 21(2007), No. 5, p. 1040.

[19] J.A. Rossignolo and M.V.C. Agnesini, Durability of polymer-modified lightweight aggregate concrete, *Cem. Concr. Compos.*, 26(2004), No. 4, p. 375.

[20] S. Thokchom, P. Ghosh, and S. Ghosh, Effect of water absorption, porosity and sorptivity on durability of geopolymer mortars, *J. Eng. Appl. Sci.*, 4(2009), No. 7, p. 28.

[21] C.K. Yip and J.S.J. van Deventer, Microanalysis of calcium silicate hydrate gel formed within a geopolymeric binder, *J. Mater. Sci.*, 38(2003), No. 18, p. 3851.

[22] I. Garcia-Lodeiro, A. Palomo, A. Fernández-Jiménez, and D.E. MacPhee, Compatibility studies between N-A-S-H and C-A-S-H gels: study in the ternary diagram Na_2O-CaO-Al_2O_3-SiO_2-H_2O, *Cem. Concr. Res.*, 41(2011), No. 9, p. 923.

[23] P.C. Hewlett, *Cement Admixtures: Use and Applications*, Longman, Essex, 1988, p. 3.

[24] P. Duxson, G.C. Lukey, and J.S.J. Van De Venter, Geopolymer, Green Chemistry and Sustainable Development Solutions, [in] *Proceedings of the World Congress of Geopolymer 2005, St Quentin,* 2006, p. 180.

[25] K. Dombrowski, A. Buchwald, and M. Weil, The influence of calcium content on the structure and thermal performance of fly ash based geopolymers, *J. Mater. Sci.*, 42(2007), No. 9, p. 3033.

[26] X.L. Guo, H.S. Shi, L.M. Chen, and W.A. Dick, Alkali-activated complex binders from Class C fly ash and Ca-containing admixtures, *J. Hazard. Mater.*, 173(2010), No. 1-3, p. 480.

[27] C.K. Yip, G.C. Lukey, and J.S.J. Van Deventer, The coexistence of geopolymeric gel and calcium silicate hydrate at the early stage of alkaline activation, *Cem. Concr. Res.*, 35(2005), No. 9, p. 1688.

[28] W. Kroehong, T. Sinsiri, C. Jaturapitakkul, and P. Chindaprasirt, Effect of palm oil fuel ash fineness on the microstructure of blended cement paste, *Constr. Build. Mater.*, 25(2011), No. 11, p. 4095.

[29] J. Wongpa, K. Kiattikomol, C. Jaturapitakkul, and P. Chindaprasirt, Compressive strength, modulus of elasticity, and water permeability of inorganic polymer concrete, *Mater. Des.*, 31(2010), No. 10, p. 4748.

[30] S. Astutiningsih and Y. Liu, Geopolymersation of Australian Slag with Effective Dissolution by the Alkaline, [in] *Proceedings of the World Congress of Geopolymer 2005, St Quentin,* 2005, p. 69.

[31] D. Dutta, S. Thokchom, P. Ghosh, and S. Ghosh, Effect of silica fume additions on porosity of fly ash geopolymers, *J. Eng. Appl. Sci.*, 5(2010), No. 10, p. 74.

[32] I. García Lodeiro, A. Fernández-Jimenez, A. Palomo, and

D.E. Macphee, Effect on fresh C-S-H gels of the simultaneous addition of alkali and aluminium, *Cem. Concr. Res.*, 40(2010), No. 1, p. 27.

[33] ASTM C469, *Standard Test Method for Static Modulus of Elasticity and Poisson's Ratio of Concrete in Compression*, Annual Book of ASTM Standard (Vol.02.01), American Society for Testing and Materials, Philadelphia, 2002.

[34] D.J. Cook and P. Chindaprasirt, A mathematical model for the prediction of damage in concrete, *Cem. Concr. Res.*, 11(1981), No. 4, p. 581.

[35] R.F. Feldman and C.Y. Huang, Properties of Portland cement-silica fume pastes II: mechanical properties, *Cem. Concr. Res.*, 15(1985), No. 6, p. 943.

[36] ACI Standard 318, *Building Code Requirements for Structural Concrete (ACI 318-08) and Commentary,* American Concrete Institute Committee, Farmington Hills, 2008, p. 456.

[37] P. Chindaprasirt, *Influence of Load History on the Properties of Concrete,* [Dissertation], The University of New South Wales, Sydney, 1980.

[38] P. Duxson, J.L. Provis, G.C. Lukey, and J.S.J. van Deventer, The role of inorganic polymer technology in the development of "green concrete", *Cem. Concr. Res.*, 37(2007), No. 12, p. 1590.

[39] R.L. Day and B.K. Marsh, Measurement of porosity in blended cement pastes, *Cem. Concr. Res.*, 18(1988), No. 1, p. 63.

[40] F. Škvára, L. Kopecký, J. Němeček, and Z. Bittnar, Microstructure of geopolymer materials based on fly ash, *Ceram. Silik*, 50(2006), No. 4, p. 208.

Construction and Building Materials 42 (2013) 33–39

Contents lists available at SciVerse ScienceDirect

Construction and Building Materials

journal homepage: www.elsevier.com/locate/conbuildmat

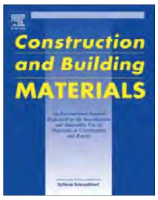

Properties of pervious geopolymer concrete using recycled aggregates

Vanchai Sata [*], Ampol Wongsa, Prinya Chindaprasirt

Sustainable Infrastructure Research and Development Center, Department of Civil Engineering, Faculty of Engineering, Khon Kaen University, Khon Kaen 40002, Thailand

HIGHLIGHTS

- ▶ Recycled aggregates (RAs) were used to make pervious geopolymer concrete (PGC).
- ▶ PGCs were prepared from high-calcium fly ash geopolymer binder and two different types of RA.
- ▶ Mechanical properties, total void ratio, and water permeability were tested.
- ▶ These RA could be used as coarse aggregates to produce PGC with acceptable properties.

ARTICLE INFO

Article history:
Received 19 October 2012
Received in revised form 27 December 2012
Accepted 27 December 2012

Keywords:
Recycled aggregate
Geopolymer
Pervious concrete
High-calcium
Fly ash

ABSTRACT

In this paper, the use of recycled aggregates (RAs) for making pervious geopolymer concrete (PGC) was studied. PGCs were prepared from high-calcium fly ash (FA), sodium silicate (Na_2SiO_3) solution, sodium hydroxide (NaOH) solution, and two different types of RA viz., crushed structural concrete member (RC) and crushed clay brick (RB). The results were also compared with those of natural coarse aggregate (NA). Compressive strength, splitting tensile strength, total void ratio, and water permeability coefficient of the PGCs were determined. The results indicate that both RC and RB can be used as recycled coarse aggregates for making PGC with acceptable properties.

1. Introduction

Pervious concrete is a special concrete that contains continuous voids and possesses high water permeability compared to normal concrete. It has been developed as an environmentally friendly material for use in water purification, permeable pavement, acoustic absorption, thermal insulation, and other applications in civil engineering and architecture [1–3]. Generally, the sizes of connected pore in pervious concrete range from 2 to 8 mm in diameter with void content between 15% and 35% and compressive strength between 2.8 and 28.0 MPa [4]. Typically, pervious concrete consists of binder, coarse aggregates, water, and admixture.

It is generally known that cement manufacturing is an energy intensive process and releases a large amount of green house gas to the atmosphere. The cement industry contributes about 7% by weight of the total carbon dioxide emissions [5]. Therefore, the use of supplementary materials to partially replace Portland cement and alternative cementing materials should be developed in order to reduce the use of Portland cement [6–8]. Geopolymer binder is one such alternative cement which is synthesized by mixing aluminosilicate material and high alkali solutions [9]. It utilizes by-products such as fly ash or metakaolin as aluminosilicate source to react with high alkali solutions of sodium or potassium based. Fly ash geopolymers have been studied by several researchers and were found to have high early strength, high later age strength, and excellent resistance to sulfate and acid attack [9–12].

In addition, the use of waste such as recycled aggregate in concrete is beneficial for the environment. The use of these materials can reduce wastes to landfill and reduce consumption of natural material resources. The studies with respect to the applicability of recycled aggregate in concrete have been conducted around the world [13–16]. However, most researchers have focused on the mechanical properties of recycled aggregate as a test element and its application in normal cement concrete. The study on the use of recycled aggregate in pervious concrete especially that made with fly ash geopolymer binder is now at the very beginning.

The strength and void ratio of pervious geopolymer concrete were studied with high-calcium fly ash as a source material [17]. Pervious fly ash geopolymer concretes (PGCs) were prepared with Na_2SiO_3 and NaOH solutions, and natural coarse aggregate with FA

---

[*] Corresponding author. Tel.: +66 4320 2846x127; fax: +66 4320 2846x102.
E-mail address: vancsa@kku.ac.th (V. Sata).

0950-0618/$ - see front matter Crown Copyright © 2013 Published by Elsevier Ltd. All rights reserved.
http://dx.doi.org/10.1016/j.conbuildmat.2012.12.046

to coarse aggregate ratio of 1:8 by weight and constant Na_2SiO_3/NaOH ratio of 0.50. The results indicate that the high-calcium fly ash geopolymer binder could be used to produce pervious concrete with satisfactory mechanical properties. In this study, recycled coarse aggregates from crushed structural concrete members and crushed clay bricks were used to replace natural coarse aggregate for PGC. The effects of NaOH concentrations on the properties of PGC were evaluated. The results were also compared with PGC containing natural coarse aggregate.

2. Materials and methods

2.1. Materials

High-calcium fly ash (FA) was procured from Mae Moh Electricity Power Station in northern Thailand. The FA had a median particle size of 50 μm, a Blaine fineness of 2250 cm^2/g, and 45% (by weight) retained on 45 μm sieve. SiO_2, Al_2O_3, and Fe_2O_3 made up 71.7% of the FA whereas the CaO content was 19.4%. It can be classified as Class C pozzolan according to ASTM C618 [18]. Three concentrations of sodium hydroxide solution (NaOH) at 10, 15, and 20 M, and a commercial grade sodium silicate solution (Na_2SiO_3) with 15.32% Na_2O, 32.87% SiO_2 and 51.81% water were used. The NaOH solution was prepared by dissolving NaOH pellets in distilled water. For example, 10 M NaOH was obtained from 400 gm of NaOH pellets and 1 l of distilled water. Sodium silicate solution was used without any modification.

Three types of single-size coarse aggregates with 4.5–9.5 mm diameter were used in this study. The first was natural coarse aggregate from crushed limestone (NA), the second was a recycled aggregate from crushed structural concrete (RC) obtained from the strength test in laboratory, and the last was a recycled aggregate from crushed broken clay brick obtained from construction site (RB). RC was from the concretes with compressive strengths of 30–40 MPa and RB was from local clay bricks with compressive strengths of 5.0–9.0 MPa. Fig. 1 shows the coarse aggregates used in this study and their properties are shown in Table 1. The specific gravity (SG) of NA was 2.72 and the dry-rodded density was 1550 kg/m^3. The SG slightly RC was slightly lower at 2.53 as it contained NA and some adhered mortar. The SG of RB was significantly lower at 2.02 reflecting the different material from NA and RB altogether. The dry-rodded density of RC and RB were lower than that of NA while the water absorptions were higher as expected. The mortar content of RC was 65%. The Los Angeles abrasion loss of NA, RC, and RB were 30.2%, 43.3%, and 42.4%, respectively. The high water absorption and high Los Angeles abrasion loss of RC and RB were due to the residues of cement mortar attached on aggregate surface and the high porosity of the recycled aggregate [16,19].

(a) NA

(b) RC

(c) RB

Fig. 1. Comparison of coarse aggregates.

2.2. Mix proportions, mixing, casting, and curing

All pervious geopolymer concretes (PGCs) were produced with FA to coarse aggregate ratio of 1–8 by weight. The Na_2SiO_3/NaOH and alkali liquid (LA)/FA ratios were kept constant at 0.50 and 0.45, respectively. The typical mixture consisted of 221 kg/m^3 FA, 33 kg/m^3 Na_2SiO_3, 66 kg/m^3 NaOH, and 1768 kg/m^3 of coarse aggregate. The parameters of this study were the types of coarse aggregates (NA, RC, and RB) and the NaOH concentrations (10, 15, and 20 M). The mix proportions of PGC are shown in Table 2. The symbol RC10 means the PGC with RC as coarse aggregate and 10 M NaOH.

The mixing of PGC was done in an air conditioned room at 25 °C. FA and NaOH were mixed in a pan-type mixer for 5 min. Coarse aggregate was then added and mixed for 4 min. Finally, Na_2SiO_3 solution was added and mixed for another minute. The total mixing time was 10 min.

After mixing, PGC were cast in 100 × 200 mm cylindrical molds and compacted on a vibrating table. The specimens were immediately wrapped with vinyl sheet to protect from moisture loss and kept in the controlled 25 °C room for 1 h. After that, they were placed in an oven for heat curing at 60 °C for 48 h. After the heat curing, the specimens were put in the laboratory to cool down and demoulded the next day. The specimens were then wrapped with vinyl sheet and stored in the controlled room at 23 ± 2 °C and 50% RH until the testing age. Fig. 2 shows the specimens of PGC containing NA, RC, and RB.

2.3. Testing methods

The compressive and splitting tensile strengths of PGC were determined at the age of 7 days in accordance with ASTM C39 [20] and ASTM C496 [21]. The results were presented as the average value of three specimens.

The total void ratio and water permeability coefficient of PGC were tested using 100 × 200 mm cylindrical specimen. The total void ratio was calculated using Eq. (1) [22] and the reported values were the average of three specimens

$$V = \left(1 - \frac{(W_2 - W_1)}{\rho_w \mathrm{Vol}}\right) \times 100 \tag{1}$$

where V is the total void ratio (%), W_1 is the weight of specimen under water (g), W_2 is the saturated weight of specimen (g), ρ_w is the density of water (g/cm^3), and Vol is the volume of specimen (cm^3).

After the total void ratio test, the specimen was placed in the water permeability test set-up as shown in Fig. 3. The water permeability coefficient of PGC was tested using the constant head method and carried out when a steady state flow was reached. The coefficients of water permeability (k) were the averages of three specimens and calculated following Darcy's law [4,23,24] as shown in following equation:

$$k = \frac{QL}{HAt} \tag{2}$$

where k is the coefficient of water permeability (cm/s), Q is the quantity of water collected (cm^3) over time t (s), L is the length of specimen (cm), H is the water head (cm), and A is the cross sectional area of specimen (cm^2).

3. Results and discussions

3.1. Density, compressive strength, and splitting tensile strength

The results of density, compressive strength, and splitting tensile strength tests of PGC are shown in Table. 3. The densities of PGCs were between 1420 and 1840 kg/m^3 which were lower than that of the conventional concrete (about 2400 kg/m^3) due to the high void of pervious concrete. The NaOH concentration had no effect on the density of PGC. For example, the densities of RC10, RC15, and RC20 concretes were 1720, 1710, and 1730 kg/m^3,

Table 1
Properties of coarse aggregates (NA, RC, and RB).

Aggregates	Specific gravity	Dry-rodded density (kg/m^3)	Absorption (%)	Los Angeles abrasion loss (%)
NA	2.72	1590	0.21	30.2
RC	2.53	1340	4.58	43.3
RB	2.02	950	16.2	42.5

Table 2
Mix proportions of pervious geopolymer concretes (PGCs).

Mixes	Mix proportion (kg/m^3)							
	FA	Na_2SiO_3	NaOH (10 M)	NaOH (15 M)	NaOH (20 M)	Coarse aggregates		
						NA	RC	RB
NA10	221	33	66	–	–	1768	–	–
NA15	221	33	–	66	–	1768	–	–
NA20	221	33	–	–	66	1768	–	–
RC10	221	33	66	–	–	–	1768	–
RC15	221	33	–	66	–	–	1768	–
RC20	221	33	–	–	66	–	1768	–
RB10	221	33	66	–	–	–	–	1768
RB15	221	33	–	66	–	–	–	1768
RB20	221	33	–	–	66	–	–	1768

Note: Na_2SiO_3/NaOH = 0.50.

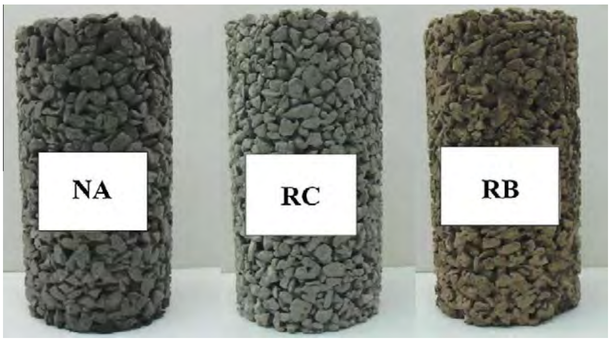

Fig. 2. Specimens of PGC containing NA, RC, and RB after demoulding.

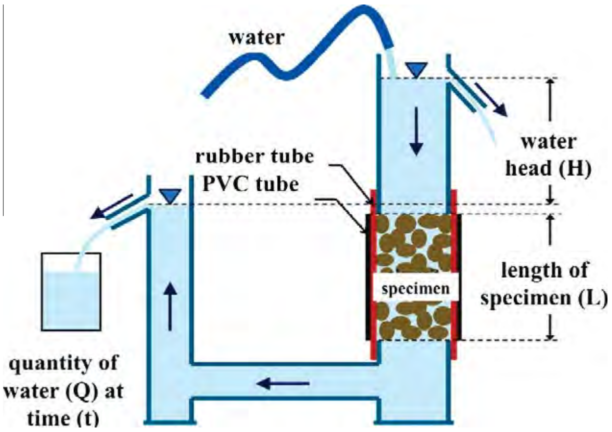

Fig. 3. Test set-up of water permeability.

respectively. The density of PGC containing RB as coarse aggregate was lowest with the average value of 1480 kg/m^3, while the densities of PGCs containing NA, and RC were higher at 1800 and 1720 kg/m^3. The dry-rodded density of aggregate and the density of PGC containing NA, RC, and RB were plotted in Fig. 4. As expected, the density of PGC increased as the dry-rodded density of aggregate increased. The relationship was a linear correlation with high R^2 value of 0.93 as shown in Eq. (3). This equation gives a prediction of the density of PGC based on a known dry-rodded density of aggregate

$$D = 0.51(D_r) + 1010 \tag{3}$$

where D is the density of pervious concrete (kg/m^3) and D_r is the dry-rodded density of aggregate (kg/m^3).

The compressive strengths of PGC containing NA were between 11.9 and 13.6 MPa and similar to the PGC containing a slightly larger aggregate with similar alkali liquid to fly ash ratio [17]. The use of recycled aggregate reduced the compressive strengths of PGC. The compressive strengths of PGC containing RC and RB were between 7.0–10.3, and 2.9–6.6 MPa, respectively. The highest compressive strength of 13.6 MPa occurred with NA10 and NA15 concretes, while the RB10 concrete showed the lowest compressive strength of 2.9 MPa. However, their compressive strengths were within the typical strength distribution reported [4].

At the same NaOH concentration, the compressive strengths of PGC containing NA were higher than those of RC and RB. For example, the compressive strength of NA15 was 13.6 MPa, while those of RC15 and RB15 were 10.0 and 4.0 MPa, respectively. The reduction in strength was due to the weakness of the attached mortar in recycled aggregate [25]. In addition, the low dry-rodded density and abrasion resistance of RC and RB also contributed to the low compressive strength [26]. The compressive strength of PGC was plotted as a function of dry-rodded density of aggregate as shown in Fig. 4. By linear regression, the empirical relationship with R^2 of 0.87 was derived as

$$f'_c = 0.0132(D_r) - 8.19 \tag{4}$$

where f'_c is the compressive strength of PGC (MPa) and D_r is the dry-rodded density of aggregate (kg/m^3).

The results also indicated that the optimum NaOH concentration to produce good strength PGC was 15–20 M. Since the formation of gel depended on the concentration of alkali OH ion, the low NaOH concentration resulted in a weak chemical reaction and slightly decreased compressive strength. The compressive strength increased with an increase in NaOH concentration mainly through the leaching of silica and alumina with high NaOH concentration

Table 3
Density, compressive strength, and splitting tensile strength of PGC at the age of 7 days.

Mixes	Density (kg/m^3)	Compressive strength (MPa)	Splitting tensile strength (MPa)
NA10	1840	13.6	1.6
NA15	1760	13.6	1.8
NA20	1810	11.9	1.5
RC10	1730	7.0	1.3
RC15	1710	10.0	1.4
RC20	1720	10.3	1.5
RB10	1420	2.9	0.4
RB15	1510	4.0	0.7
RB20	1520	6.6	0.9

[27]. However, an increase in alkali concentration enhanced strength development of geopolymer, but excess hydroxide ion concentration caused aluminosilicate gel precipitation at early stage and resulted also in low strength geopolymer [28,29]. The reduction of strength due to the increased in NaOH concentration from 15 M to 20 M could be observed in the NA aggregate. Similar to conventional concrete, the compressive strength of PGC improved when the density increased as shown in Fig. 5. The relationship between density and compressive strength of PGC was linear with R^2 equal to 0.84 and the function can be written as

$$f'_c = 0.0245(D) - 31.97 \qquad (5)$$

where f'_c is the compressive strength (MPa) and D is the density of PGC (kg/m^3).

The splitting tensile strength of PGC ranged from 0.4 to 1.8 MPa. The results followed the same trend as those of the compressive strength. The splitting tensile strength values of PGC containing NA aggregate were higher than those of RC and RB aggregates. NA15 concrete gave the maximum splitting tensile strength of 1.8 MPa while RB10 concrete gave the lowest strength of 0.4 MPa. The average ratio of splitting tensile to compressive strengths of PGC was 14.4% which was slightly higher than 8–14% for conventional concrete and Portland cement concrete containing recycled aggregate [16,30,31] as shown in Fig. 6. This was due to the denser and stronger interfacial transition zone between aggregates and geopolymer binder compared with that of cement binder as a result of the use of soluble silicate [32].

The relationship between compressive strength and splitting tensile strength of PGC compared with the value suggested by ACI 318 [33] is shown in Fig. 7. The results showed that as compressive strength increased, the splitting tensile strength also increased. The splitting tensile strengths of PGC were slightly lower than that predicted by ACI 318 [33]. Eq. (6) was used for prediction the splitting tensile strength of PGC

$$f_{st} = 0.44(f'_c)^{0.50} \qquad (6)$$

where f_{st} is the splitting tensile strength (MPa) and f'_c is the compressive strength of PGC (MPa).

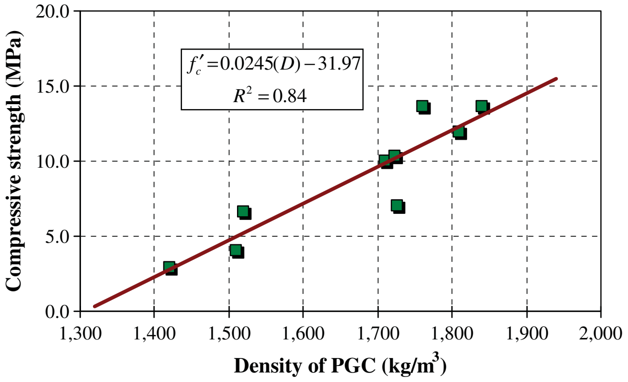

Fig. 5. Relationship between compressive strength at the age of 7 days and density of PGC.

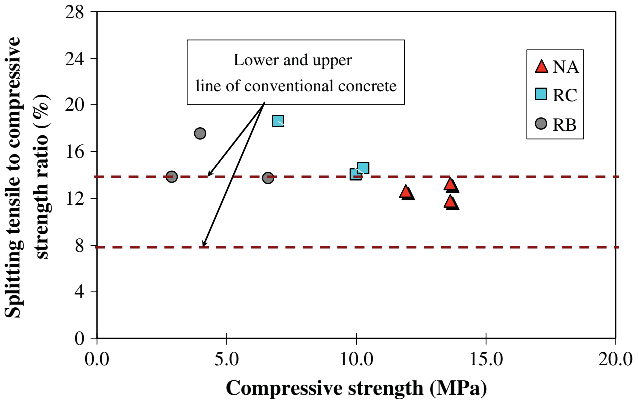

Fig. 6. Splitting tensile to compressive strength ratios and compressive strength of PGC at the age of 7 days.

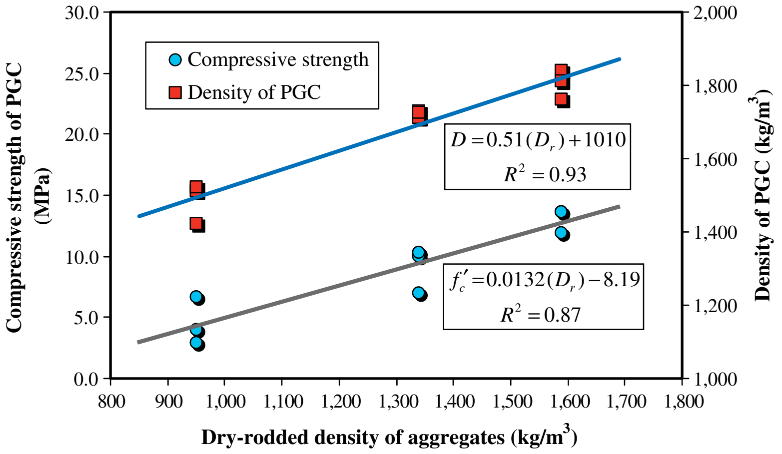

Fig. 4. Relationship between compressive strength at the age of 7 days, density of PGC and dry-rodded density of aggregates.

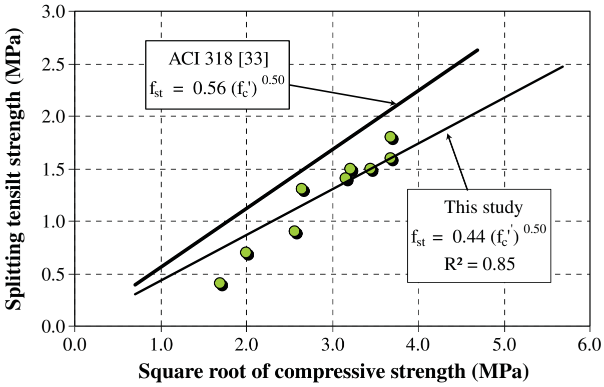

Fig. 7. Relationship between compressive strength and splitting tensile strength of PGC at the age of 7 days.

3.2. Fracture surfaces

Fig. 8 compares the PGC failure patterns of various aggregates and Figs. 9–11 show the fracture surfaces of PGC specimens after splitting tensile test. The majority of failure of PGC with NA aggregate occurred at the interface between geopolymer paste and aggregate. However, for RC aggregate, the fractures were at the attached mortar. As compare to normal aggregate and geopolymer paste, the poor quality due to its high porosity of the attached mortar had created the weak zones in PGC. When the PGC approached the ultimate load, the cracks passed though these zones instead of paste and coarse aggregate [25,34]. The failure surface of PGC containing RB showed fracture through the recycled aggregate particles indicating that RB aggregate was the weakest point. The RC and RB aggregate particles were not strong as suggested by their high Los Angeles abrasion losses (43.2% and 42.5%).

3.3. Total void ratio and water permeability coefficient

Table 4 shows the results of total void ratios and water permeability coefficient of PGC. The total void ratios of all PGC varied between 21.7% and 27.4% which were typical values of ACI 522 (15–35%). It was reported that PGCs with high total void ratios of 28.7–30.4% were successfully made with the use of a relatively large coarse aggregate of 12.5–20.0 mm [17]. The total void ratios of PGC containing NA slightly increased with the increasing NaOH concentrations. They were 24.2%, 25.3%, and 27.4% for NA10, NA15, and NA20 concretes, respectively. The use of RC in PGC at various NaOH concentrations showed nearly the same total void ratios of 26.8%, 26.9%, and 26.4% for RC10, RC15, and RC20, respectively. In the case of using RB in PGC, the total void ratios ranged from 21.7% to 23.7% which were lower than those of NA and RC. It could, therefore, be concluded that the total void ratios of the PGC with different NaOH concentrations but the same aggregate and geopolymer paste content were not very different.

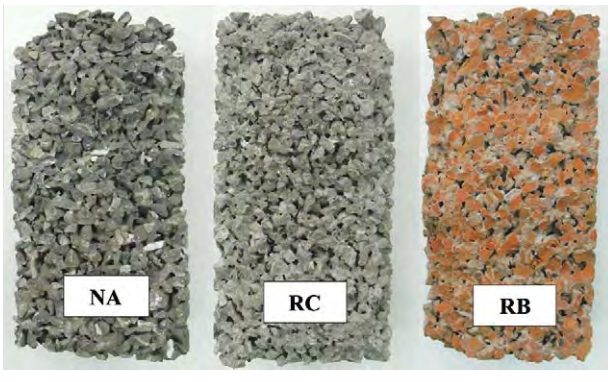

Fig. 8. Failure surface of PGC by splitting tensile strength.

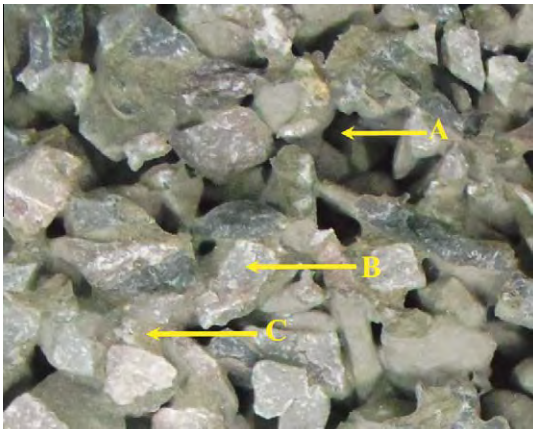

Fig. 9. Fracture surface of PGC containing NA; (A) void; (B) failure at bond; and (C) geopolymer paste.

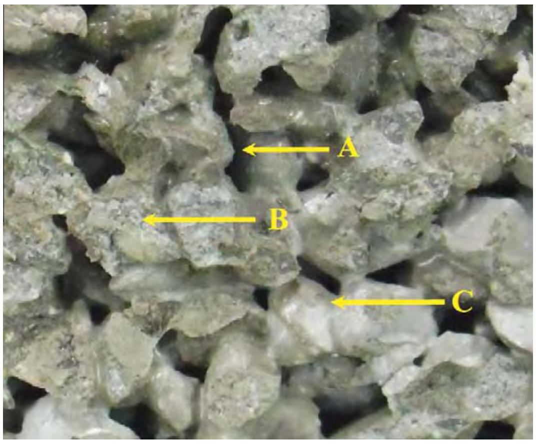

Fig. 10. Fracture surface of PGC containing RC; (A) void; (B) fractured RC at attached mortar; and (C) geopolymer paste.

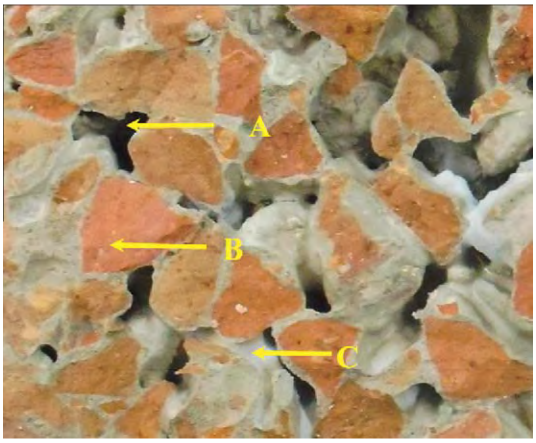

Fig. 11. Fracture surface of PGC containing RB; (A) void; (B) fractured RB; and (C) geopolymer paste.

With regard to the water permeability coefficient of PGC, the trend of the results was similar to that of the total void ratio. The low values of water permeability coefficients of 0.71–1.2 cm/s

Table 4
Total void ratio and water permeability coefficient of PGC at the age of 7 days.

Mixes	Total void ratio (%)	Water permeability coefficient (cm/s)
NA10	24.2	1.25
NA15	25.3	1.18
NA20	27.4	1.71
RC10	26.8	1.56
RC15	26.9	1.46
RC20	26.4	1.47
RB10	23.7	1.12
RB15	21.7	0.71
RB20	22.4	0.80

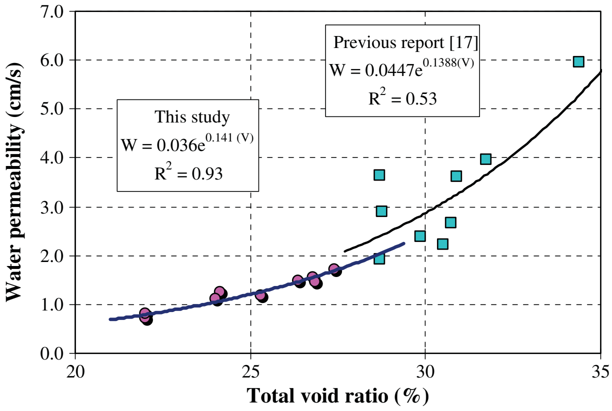

Fig. 12. Relationship between water permeability coefficient and total void ratio of PGC.

were achieved with PGC using RB aggregate. Also, the water permeability coefficient values of PGC with the same aggregate varied in a narrow range with different NaOH concentrations. Thus, the relationship between water permeability coefficient and total void ratio of all PGCs could be fitted as Eq. (7) as shown in Fig. 12. The R^2 value of 0.93 indicated a relatively strong relation between water permeability coefficient and total void ratio

$$k = 0.036e^{0.141(V)} \tag{7}$$

where k is coefficient of water permeability coefficient (cm/s) and V is total void ratio (%).

Similar trend of results was reported by the previous work [17] as shown in Fig. 12. The permeability of PGC increased exponentially with the void content similar to normal Portland cement pervious concrete [23].

4. Conclusions

The recycled aggregate from crushed structural concrete member (RC) and crushed clay bricks (RB) could be used as coarse aggregates for making pervious geopolymer concrete (PGC) using high-calcium fly ash as a source material. PGCs containing RC and RB gave lower compressive strengths than those containing natural aggregate (NA). However, the obtained compressive strengths of 2.9–10.3 MPa were within the typical strength distribution reported [4]. The relationships of density and compressive strength, splitting tensile and compressive strength, and total void ratio and water permeability coefficient in pervious high-calcium fly ash geopolymer concrete incorporating recycled coarse aggregates were similar to those of conventional pervious concrete. The total void ratio and water permeability coefficient of the PGCs with different NaOH concentrations but the same aggregate and geopolymer paste content were not very different. For the effect of NaOH concentrations, the high concentration 15–20 M NaOH gave PGC with higher strength than the low concentration 10 M NaOH.

The overall results indicate that it is feasible to use RC and RB as recycled coarse aggregates with high-calcium fly ash geopolymer binder for making pervious concrete with acceptable properties. However, the using RC and RB resulted in significant losses in strength as compared to a NA pervious concrete.

Acknowledgements

This work was supported by the Higher Education Research Promotion and National Research University Project of Thailand, Office of the Higher Education Commission, through the Advanced Functional Materials Cluster of Khon Kaen University. The authors also would like to acknowledge the support of the Thailand Research Fund (TRF) under TRF New Researcher Scholar Contact No. MRG5480004 and TRF Senior Research Scholar Grant No. RTA5480004.

References

[1] Kim HK, Lee HK. Acoustic absorption modeling of porous concrete considering the gradation and shape of aggregate and void ratio. J Sound Vib 2010;329(7):866–79.
[2] Chindaprasirt P, Hatanaka S, Chareerat T, Mishima N, Yuasa Y. Cement paste characteristics and porous concrete properties. Constr Build Mater 2008;22(5):894–901.
[3] Kevern JT, Schaefer VR, Wang K. Evaluation of pervious concrete workability using gyratory compaction. J Mater Civil Eng 2009;12(12):764–70.
[4] ACI committee 522, Pervious concrete, Report no. 522R-10, American Concrete Institute, Detroit, USA; 2010. p. 38.
[5] Ali MB, Saidur R, Hossain MS. A review on emission analysis in cement industries. Renew Sust Energy Rev 2011;15(5):2252–61.
[6] Slanička Š. The influence of fly ash fineness on the strength of concrete. Cem Concr Res 1991;21(2–3):285–96.
[7] Sata V, Jaturapitakkul C, Rattanashotinunt C. Compressive strength and heat evolution of concretes containing palm oil fuel ash. J Mater Civil Eng 2010;22(10):1033–8.
[8] Chindaprasirt P, Homwuttiwong S, Sirivivatnanon V. Influence of fly ash fineness on strength, drying shrinkage and sulfate resistance of blended cement mortar. Cem Concr Res 2004;34(7):1087–92.
[9] Davidovits J. Geopolymer: inorganic polymeric new materials. J Therm Anal 1991;37:1633–56.
[10] Temuujin J, Minjigmaa A, Lee M, Chen-Tan N, van Riessen A. Characteristic of class F fly ash geopolymer pastes immersed in acid and alkalie solutions. Cem Concr Compos 2011;33(10):1086–91.
[11] Sata V, Sathonsaowaphak A, Chindaprasirt P. Resistance of lignite bottom ash geopolymer mortar to sulfate and sulfuric acid attack. Cem Concr Compos 2012;34(5):700–8.
[12] Chindaprasirt P, Chareerat T, Sirivivatnanon V. Workability and strength of coarse high calcium fly ash geopolymer. Cem Concr Compos 2007;29(3):224–9.
[13] Poon CS, Shui ZH, Lam L. Effect of microstructure of ITZ on compressive strength of concrete prepared with recycled aggregates. Constr Build Mater 2004;18(6):461–8.
[14] Etxeberria M, Marí A, Vázquez E. Recycled aggregate concrete as structural material. Mater Struct 2007;40(5):529–41.
[15] Limbachiya M, Meddah MS, Ouchagour Y. Use of recycled concrete aggregate in fly-ash concrete. Constr Build Mater 2012;27(1):439–49.
[16] Tangchirapat W, Buranasing R, Jaturapitakkul C, Chindaprasirt P. Influence of rice husk–bark ash on mechanical properties of concrete containing high amount of recycled aggregates. Constr Build Mater 2008;22(8):1812–9.
[17] Tho-in T, Sata V, Chindaprasirt P, Jaturapitakkul C. Pervious high-calcium fly ash geopolymer concrete. Constr Build Mater 2012;30:366–71.
[18] American Society for Testing and Materials (ASTMs) C 618-03. Standard test method for coal fly ash and raw or calcined natural pozzolan for use in, concrete; 2003.
[19] de Juan MS, Gutiérrez PA. Study on the influence of attached mortar content on the properties of recycled concrete aggregate. Constr Build Mater 2009;23(2):872–7.
[20] American Society for Testing and Materials (ASTMs) C 39/C 39M-01. Standard test method for compressive strength of cylindrical concrete specimens; 2003.
[21] American Society for Testing and Materials (ASTMs) C 496-96. Standard test method for splitting tensile strength of cylindrical concrete specimens; 2003.
[22] Park AB, Tia M. An experimental study on the water-purification properties of porous concrete. Cem Concr Res 2004;34:177–84.
[23] Neithalath N, Sumanasooriya MS, Deo O. Characterizing pore volume, sizes, and connectivity in pervious concretes for permeability prediction. Mater Character 2010;61:802–13.
[24] Japan Concrete Institute. In: Proceedings of the JCI symposium on design, construction and recent applications of porous, concrete; 2004. p. 1–10.

[25] Etxeberria M, Vázquez E, Marí A, Barra M. Influence of amount of recycled coarse aggregates and production process on properties of recycled aggregate concrete. Cem Concr Res 2007;37(5):735–42.
[26] Tu T-Y, Chen Y-Y, Hwang C-L. Properties of HPC with recycled aggregates. Cem Concr Res 2006;36(5):943–50.
[27] Chindaprasirt P, Jaturapitakkul C, Chalee W, Rattanasak U. Comparative study on the characteristics of fly ash and bottom ash geopolymers. Waste Manage 2009;29(2):539–43.
[28] Somna K, Jaturapitakkul C, Kajitvichyanukul P, Chindaprasirt P. NaOH-activated ground fly ash geopolymer cured at ambient temperature. Fuel 2011;90:2118–24.
[29] Lee WK, van Deventer JSJ. The effects of inorganic salt contamination on the strength and durability of geopolymer. Colloids Surf A 2002;211(2–3):115–26.
[30] Sagoe-Crentsil KK, Brown T, Taylor AH. Performance of concrete made with commercially produced coarse recycled concrete aggregate. Cem Concr Res 2001;31(5):707–12.
[31] Mindess S, Young JF, Darwin D. Concrete. 2nd ed. Prentice Hall; 2003.
[32] Sarker P. Bond strength of reinforcing steel embedded in fly ash-based geopolymer concrete. Mater Struct 2011;44(5):1021–30.
[33] ACI committee 318. Building code requirements for structural concrete (ACI 318-99) and commentary (ACI 318R-99). American Concrete Institute, Detroit, USA1999; p. 391.
[34] Kwan WH, Ramli M, Kam KJ, Sulieman MZ. Influence of the amount of recycled coarse aggregate in concrete design and durability properties. Constr Build Mater 2012;26(1):565–73.

Advanced Powder Technology 24 (2013) 703–707

Contents lists available at SciVerse ScienceDirect

Advanced Powder Technology

journal homepage: www.elsevier.com/locate/apt

Original Research Paper

Role of microwave radiation in curing the fly ash geopolymer

Prinya Chindaprasirt [a], Ubolluk Rattanasak [b,*], Sompop Taebuanhuad [b]

[a] Sustainable Infrastructure Research and Development Center, Department of Civil Engineering, Faculty of Engineering, Khon Kaen University, Khon Kaen 40002, Thailand
[b] Department of Chemistry and Center for Innovation in Chemistry, Faculty of Science, Burapha University, Chonburi 20131, Thailand

ARTICLE INFO

Article history:
Received 14 August 2012
Received in revised form 19 November 2012
Accepted 27 December 2012
Available online 10 January 2013

Keywords:
Geopolymer
Microwave radiation
Microstructure
Compressive strength

ABSTRACT

Fly ash geopolymer requires rather long heat curing to obtain reasonable strength development at an early age. However, the long heat curing period limits the application of the fly ash geopolymer. High strength development and a reduction in heat curing duration have been considered for energy saving. Therefore, this research proposed a process using 90-W microwave radiation for 5 min followed by conventional heat curing for high-calcium fly ash geopolymer. Results showed that the compressive strengths of geopolymer with microwave radiation followed by conventional heat curing were comparable to those of the control cured at 65 °C for 24 h. Microwave radiation gave the enhanced densification. In addition, SEM images showed that the gels formed on the fly ash particles owing to the promoted dissolution of amorphous phases from fly ash. This method accelerated the geopolymerization and gave the high compressive strength comparable to the conventional curing.

1. Introduction

Coal-fired power plants currently produce 40% of the global electricity for households and industries. Besides generating power energy, coal wastes, i.e. fly ash and bottom ash are obtained and utilized related to the environmental aspect [1,2]. In addition to the use of fly ash to partially replace Portland cement, the high content fly ash usage has been introduced and termed "geopolymer" which is a low heat cured alumino-silicate material [3]. Owing to the endothermic reaction, heat curing at 65 °C was employed in order to gain high early strength of lignite fly ash geopolymers with good physical and mechanical properties [4,5]. However, the 24-h or longer heat curing periods limit the application of geopolymer. Although the room temperature curing has been considered for energy saving, the prolonged curing duration was required to obtain reasonable strength for lignite fly ash geopolymer [6].

Heat curing has been applied to construction materials especially for the precast concrete to improve the strength development process. This concrete attains sufficient strength in short curing time, so the moulds can be reused, and the final products can be rapidly delivered to the site [7]. For the conventional heating technique, heat is distributed in the specimen from the exterior to the interior leading to the non-uniform and long heating period to attain the required temperature. In contrast, the microwave technique allows a uniform and fast heating due to the interaction between the polar molecules and microwave electric fields [7–11]. Application of microwave to the fresh concrete results in removal of water, collapse of capillary pore and densification of sample. However, microwave radiation is mostly used in concrete curing and the radiation period is usually long (more than 1 h with high wattage) [7,8]. This could limit the use of microwave curing due to the energy cost.

Therefore, this research proposed the process to reduce the microwave curing duration and energy using the short-time microwave radiation in addition to the convention heat curing for the fly ash geopolymer. Microwave radiation could play the role in the geopolymer formation and strength enhancement. Additionally, this method could shorten the curing time of geopolymer, accelerate the geopolymerization and give the high compressive strength at an early age compared to the conventional curing.

2. Experimental procedure

2.1. Materials

Coal fly ash from Mae Moh power plant in the north of Thailand was used as raw material. This fly ash was generated from the pulverized coal combustion process (1200 °C) using lignite coal as the feed. The properties of this fly ash are tabulated in Table 1. In addition to Al_2O_3 and SiO_2, this fly ash had high contents of CaO and magnetite (Fe_3O_4). Sodium hydroxide pellet (NaOH) dissolved in the deionized water to obtain 10 M NaOH solution, and sodium silicate solution (Na_2SiO_3) with SiO_2:Na_2O mass ratio of 3.2 was also used. The viscosities of 10 M NaOH and Na_2SiO_3 were 9.3, and 60.6 cps (centipoises), respectively. The graded river sand with fineness

---

* Corresponding author. Tel.: +66 38 103066; fax: +66 38 393494.
E-mail address: ubolluk@buu.ac.th (U. Rattanasak).

0921-8831/$ - see front matter © 2012 The Society of Powder Technology Japan. Published by Elsevier B.V. and The Society of Powder Technology Japan. All rights reserved.
http://dx.doi.org/10.1016/j.apt.2012.12.005

Table 1
Properties of fly ash.

Chemical composition (wt%)	SiO_2	39.2
	Al_2O_3	19.7
	CaO	16.9
	Fe_3O_4	12.1
	SO_3	2.8
	Others	9.3
Median particle size (μm)		19.0

modulus of 2.8 and specific gravity of 2.65 was employed to prepare the mortar specimen for strength test.

2.2. Geopolymer preparation

To prepare the liquor, 10 M NaOH and Na_2SiO_3 were mixed in a container with the Na_2SiO_3/NaOH mass ratio of 1.5. The liquor was then added to the fly ash in a pan mixer and the paste was thoroughly mixed. The fly ash-to-liquor mass ratio of 1.86 (fly ash = 65 wt% and liquor = 35 wt%). The paste was continuously mixed for 5 min and then cast into 50-mm cubic acrylic mould (1-cm thickness). The paste specimens were vibrated for 10 s and covered with cling film to avoid the moisture evaporation during the heat curing.

For geopolymer mortar preparation, sand was added to the paste mixture with the sand-to-fly ash mass ratio of 1.5 and mixed for another 2 min. The mixture was then cast into 50-mm cubic acrylic mould. The curing condition was the same as for the paste preparation. Compressive strength test was performed on the geopolymer mortars.

2.3. Microwave and conventional curing temperature profile

In this study, the 2.45-GHz household microwave and the conventional oven were employed. Owing to preliminary results, 90- and 180-W microwave power levels were applied on the geopolymer mortars for 3, 5 and 10 min to obtain the temperature profile at the middle of the samples. Higher wattage resulted in rapid evaporation in short time, heat evolution and cracks on the surface of specimens. Result is reported as an average of five samples.

In addition, the effect of microwave and conventional curing on the compressive strength of geopolymer mortar was evaluated. 90-W microwave curing for 5 min was selected in addition to the convention heat curing at 65 °C for 3, 6 and 12 h. After heat curing, specimens were cooled down and cured continuously at 25 °C. The compressive strength was tested at the age of 7 days. The reported results were the averages of five samples. Table 2 shows the curing conditions. Curing at 65 °C for 24 h (system 1) was the control.

2.4. XRD, SEM and degree of reaction

Geopolymer paste was prepared for the testing of XRD, SEM and degree of reaction. 90-W microwave radiation for 5 min in addition to the conventional heat curing at 65 °C for 3, 6 and 12 h was used. XRD and SEM analyses were performed on the hardened samples. In addition, degree of reaction was determined both on geopolymer paste and fly ash by identification of unreacted fly ash in specimen using the dissolution of the powdery sample in 2 M HCl and 5 wt% Na_2CO_3 [12–14]. The hardened geopolymer pastes were ground to obtain particles that passed a 150-μm sieve. A 100-mL beaker filled with powdered samples (5 g) and 2 M HCl (30 mL) was placed in a 60 °C water bath and stirred for 20 min to accelerate the dissolution. Solid phase was then filtered using a vacuum filter. The remaining solid was washed with warm water thrice to completely remove HCl. Acetone was applied in the last filtration to remove water before drying at 70 °C for 2 h. Degree of reaction was calculated using Eq. (1). The degree of reaction of the fly ash particles was also determined and assigned as “blank.” All the results were subtracted with blank to obtain the corrected degree of reaction. The reported results were the averages of three samples.

$$\text{Degree of reaction} = \frac{m_{\text{sample}} - m_{\text{residue}}}{m_{\text{sample}}} \times 100 \tag{1}$$

where m_{sample} is the weight of powdery sample (g) and m_{residue} is the weight of dried residue (g).

3. Results and discussion

3.1. Temperature profile of microwave curing

The temperature profiles of the 50-mm cube geopolymer mortar are reported in Fig. 1. Application of 90- and 180-W microwave power levels generated high temperature in the specimen in a short period of time. At 5 min microwave radiation, 90- and 180-W gave slightly different temperatures. For 10-min microwave radiation, the temperature difference was noticeable. Increase in the microwave radiation time led to high temperature, however, longer radiation time and increase in wattage resulted in rapid evaporation, high heat evolution and sequential cracks on the surface of specimens owing to the energy beyond the requirement for water removal in materials [15]. For this reason, 90-W microwave radiation for 5 min was selected for further study.

3.2. Effect of microwave and conventional curing on the compressive strength

To study the effect of curing conditions on the properties of geopolymer mortars, the compressive strength was primarily focused in this section. Table 3 presents the strengths of the specimens

Table 2
Curing conditions of geopolymer.

System	Curing conditions	Note
1	65 °C oven curing for 1, 3, 6, 12 and 24 h	65 °C oven curing
2	65 °C oven curing for 1, 3, 6, 12 and 24 h → 90 W MW curing for 3 min	65 °C oven curing before MW radiation
3	90 W MW curing for 3 min	MW radiation only
4	90 W MW curing for 5 min	MW radiation only
5	90 W MW curing for 10 min	MW radiation only
6	90 W MW curing for 3 min → 65 °C oven curing for 1, 3, 6, 12 and 24 h	MW radiation before 65 °C oven curing
7	90 W MW curing for 5 min → 65 °C oven curing for 1, 3, 6 and 12 h	MW radiation before 65 °C oven curing
8	90 W MW curing for 10 min → 65 °C oven curing for 1, 3, 6 and 12 h	MW radiation before 65 °C oven curing
9	25 °C curing for 7 and 28 days (room temp., RT)	No heat curing

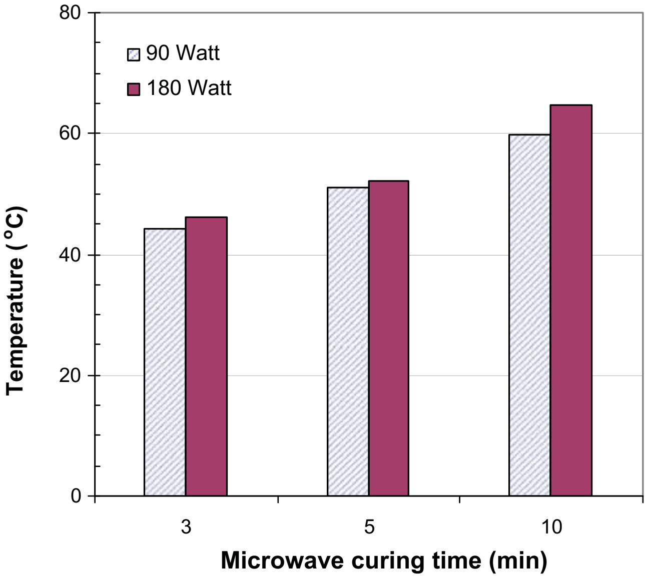

Fig. 1. Temperature profile of geopolymer mortar.

Table 3
Compressive strengths of geopolymer mortars at various curing conditions.

System	Curing conditions	Compressive strength (MPa)						
		Additional curing time in 65 °C oven					RT	
		1 h	3 h	6 h	12 h	24 h	7 d	28 d
1	65 °C	13.0	15.7	22.2	21.2	***32.7***[a]		
2	65 °C → 90 W (3 min)	9.9	16.6	25.2	23.9	***32.4***		
3	90 W (3 min)						9.4	
4	90 W (5 min)						16.2	
5	90 W (10 min)						17.4	
6	90 W (3 min) → 65 °C	12.9	17.4	21.2	29.0	***33.8***	–	
7	90 W (5 min) → 65 °C	21.9	29.2	***35.5***	***42.5***			
8	90 W (10 min) → 65 °C	20.0	27.4	***34.6***	***41.4***			
9	25 °C (RT)						20.0	***35.8***

Bolditalic values = strengths equal to or higher than that of the control.
[a] Comparative strength (control).

cured with microwave radiation, heat curing and room temperature curing. Curing at 65 °C for 24 h (system 1) was the control and the strength result of this condition was compared to the others. The control had the compressive strength of 32.7 MPa. The strength of system 2 with the same heat curing time was similar at 32.4 MPa. From this result, it could be noted that the additional microwave radiation after the normal heat curing did not improve the strength of geopolymer. This was due to the complete geopolymerization after the optimum duration of heat curing. With no heat curing or room temperature curing (system 9), the specimens gained the strength with age and the strengths at 7 and 28 days were 20.0 and 35.8 MPa respectively. Without heat curing, the strength development of the fly ash geopolymer mortar was extremely slow. The heat curing contributed to the strength of geopolymer at the early age. However, the use of only microwave radiations for 3–10 min (systems 3–5) gave the samples with strength up to 28–50% of the control strength.

The use of microwave radiation followed by conventional heat curing provided the high strength gain of geopolymer as shown in systems 6–8. The optimum time of microwave radiation shortened the required time of conventional heat curing. For 3 min of 90-W radiation, the additional heating of 12 h slightly increased the strength of the geopolymer mortar to 29.0 MPa compared to 21.2 MPa of that with 6-h heat curing alone. To obtain the strength of over 32.7 MPa (control), the additional heat curing time of 24 h was still required owing to the low accelerated temperature of the microwave radiation (3 min of 90-W).

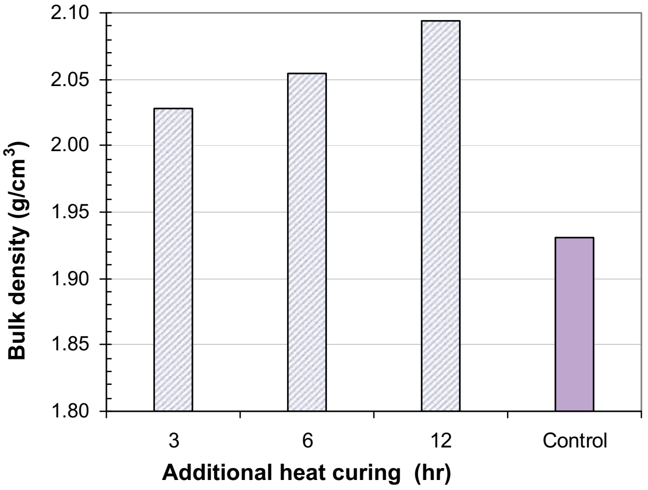

Fig. 2. Bulk density of geopolymer mortars with 90 W microwave radiation for 5 min.

However, for the microwave radiation of 5–10 min, only 6-h additional heat curing was needed to obtain the strength equivalent to the control. Extension of radiation time to more than 10 min could increase the accelerated temperature beyond 65 °C and risked getting close to the boiling temperature of water. This resulted in rapid water evaporation, high pressure and subsequent cracks in sample.

The results of bulk densities of the geopolymer mortar (systems 6–8) are presented in Fig. 2. The microwave radiation enhanced the densification compared with those entirely cured with conventional heat curing. This result implied that the microwave radiation overcame the activation energy of geopolymerization. The microwave effect, in the presence of an external electric field, resulted in the densification of the matrices. In contrast to the conventional heating, the preferential interaction of the microwaves gave lower porosity leading to the accelerated densification [16]. High compressive strengths of the samples were, thus, achieved.

3.3. XRD patterns of microwave radiation cured geopolymers

Fig. 3 shows the X-ray diffraction (XRD) patterns of geopolymer pastes under microwave radiation followed by the conventional heat curing for 3, 6 and 12 h. The results of original fly ash and the 24-h heat cured sample (control) are also presented. Numerous peaks of crystalline quartz (SiO_2), calcium sulfate ($CaSO_4$) and calcium oxide (CaO) of this high calcium fly ash were identified. In addition, the XRD pattern of fly ash showed many sharp peaks owing to the crystalline phases in the sample.

For geopolymer pastes, the product was semi-crystalline with a high amount of amorphous gel as indicated by the broad hump and some sharp peaks of crystallinity. The broad hump of these pastes appeared at 22–38°, indicating the highly disorder silicate glass phase in geopolymer [17]. The calcium silicate compounds from the reaction between high calcium fly ash, silica and silicate solution were also detected. In addition, samples with microwave radiation exhibited the sharp peaks of crystalline phases with high degree of amorphous phase of the semi-crystalline geopolymer.

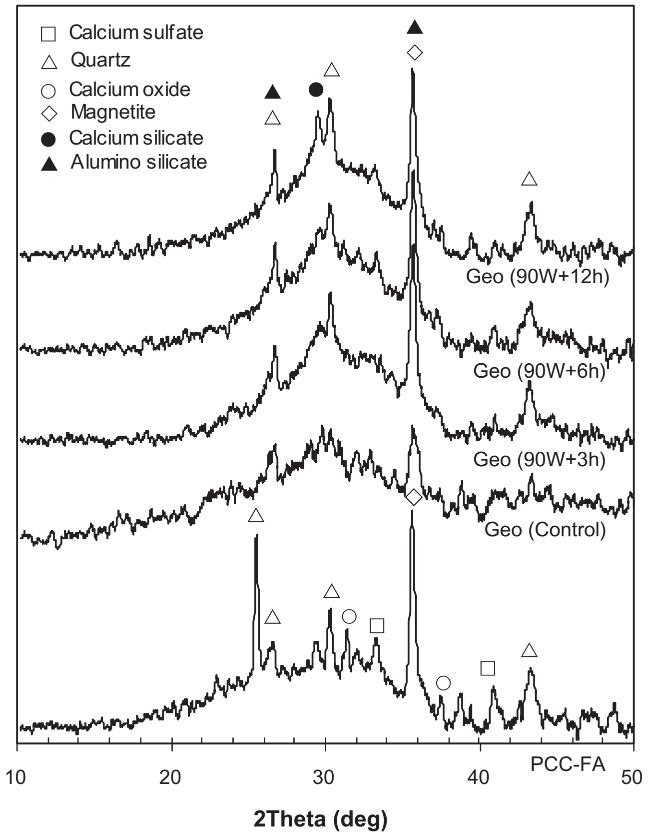

Fig. 3. XRD patterns of geopolymer pastes with microwave radiation and additional 65 °C heat curing.

Quartz and alumino-silicate compounds had an effect on both the physical and mechanical properties of the geopolymer. The presence of some of these crystalline products in geopolymer resulted in an increase in the compressive strength [18].

In addition, the dissolution of SiO_2 and Al_2O_3, especially from the glassy phase, was enhanced by the partial microwave radiation at the early stage of reaction [19]. Therefore, microwave radiation promoted the dissolution of Si and Al species from fly ash owing to the rapid heating up of an aqueous solution. Furthermore, the active water with hydrogen bond breaking under microwave radiation could independently attack Si–O and Al–O bonds leading to the enhancement of the dissolution of glassy phase of fly ash particles [19].

3.4. Microstructural study

Fig. 4 exhibits the SEM images of the geopolymer with partial microwave radiation (Fig. 4a–c) and the control sample with the heat curing for 24 h (Fig. 4d). The unreacted spherical fly ash, partially reacted grains of fly ash particles, and a continuous mass of geopolymer products were recognized. Gel formation on fly ash particles showed the dissolution of glassy phase in the alkaline solution. With microwave radiation as shown in Fig. 4a–c, a large number of gels was formed on the fly ash particles owing to the promoted dissolution of Si and Al species from fly ash with microwave radiation [19]. It was found that the prolonged radiation significantly retarded the nucleation of alumino-silicate gel [11,19]. Prolonged microwave radiation was thus not recommended. Increase in additional heat curing provided more reaction products on the fly ash particles. For the control sample, the partially reacted grains of fly ash particles were also observed. The gradual dissolution of the glassy phase of fly ash particles resulted in the normal formation of gel. The early-stage microwave radiation followed by the conventional heating effectively contributed to the geopolymerization of fly ash. Cracks and occupied fly ash pores were also found in the continuous mass of geopolymer products. Cracks were due to the moisture removal during heat curing.

The mechanism of microwave radiation in geopolymer curing could be explained as follows. Microwave radiation prior to conventional heat curing affected the strength gain of geopolymer. Early-stage of microwave radiation contributed to the gel formation of geopolymer. Applying the microwave to fresh sample promoted the dissolution of Si and Al species from fly ash owing to the rapid heating up of the aqueous solution. It stimulated the breaking of hydrogen bonds in water molecules. Gel formation on fly ash particles, as observed by SEM analysis, showed the

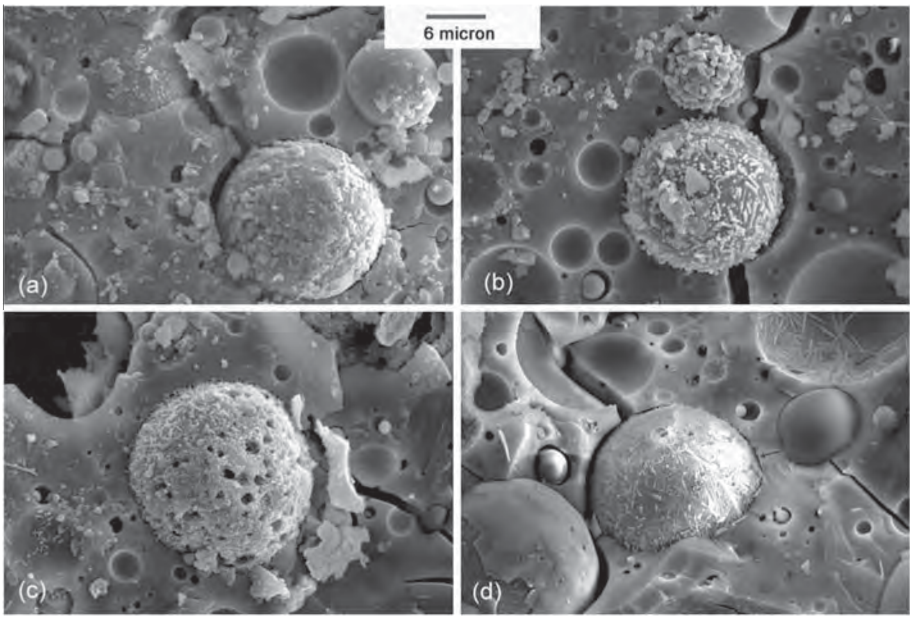

Fig. 4. Microstructure of geopolymer pastes with microwave radiation and additional 65 °C heat curing; (a) 3 h, (b) 6 h, (c) 12 h, and (d) Control.

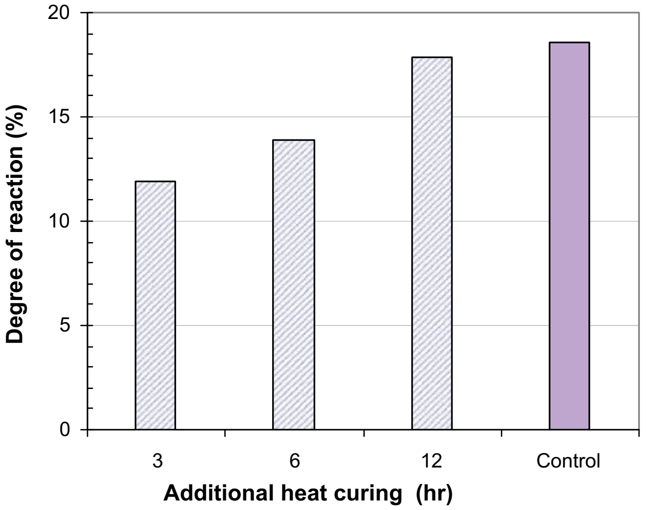

Fig. 5. Degree of reaction of fly ash geopolymer with microwave radiation.

dissolution of glassy phase in the alkaline solution. Higher densification of matrices compared with those cured in the electric oven could be obtained. Additional heat curing provided the additional reaction products. Therefore, the early-stage microwave radiation followed by the conventional heating effectively enhanced the geopolymerization. The main advantages are the reduction in curing time and energy and hence the associated reduced cost.

3.5. Degree of reaction

The degrees of reaction of geopolymer pastes with microwave radiation are presented in Fig. 5. With partial microwave radiation and heat curing for 3, 6, and 12 h, the degrees of reaction were 11.9%, 13.9% and 17.9%, respectively compared to 18.6% degree of reaction of the control. The control with entire 24-h heat curing had similar degree of reaction to that with microwave radiation and 12-h conventional curing. The results suggested that the time for normal curing could be reduced by half using the radiation. The results conformed to the results of the SEM and the strengths.

4. Conclusions

Microwave radiation effectively enhanced the geopolymerization and compressive strength of fly ah geopolymer. The microwave radiation followed by conventional heat curing reduced the heat curing time and energy. The 90-W microwave radiation for 5 min followed by 6-h at 65 °C additional heat curing produced geopolymer mortar with strength comparable to that of the control (24-h at 65 °C). The microwave radiation resulted in the densification of the matrices and increase in the bulk density of the samples. The mechanism of strength enhancement could be explained as follows.

1. Early-stage of microwave radiation promoted the dissolution of Si and Al species and enhanced the gel formation of geopolymer and stimulated the breaking of hydrogen bonds in water molecules.
2. Gel formation on fly ash particles resulted in higher densification of matrices.
3. The additional conventional heat curing provided the additional formation of reaction products.

Therefore, the early-stage microwave radiation followed by the conventional heating effectively contributed to the geopolymerization of fly ash geopolymer.

Acknowledgements

The authors gratefully acknowledge the financial support from the Higher Education Research Promotion, and National Research University Project of Thailand, Office of the Higher Education Commission, through the Advanced Functional Materials Cluster of Khon Kaen University and the Thailand Research Fund (TRF) under TRF Senior Research Scholar Contract No. RTA5480004. Appreciation is also extended to the Center for Innovation in Chemistry (PERCH-CIC).

References

[1] H. Tanaka, A. Fujii, Effect of stirring on the dissolution of coal fly ash and synthesis of pure-form Na–A and -X zeolites by two-step process, Adv. Powder Technol. 20 (2009) 473–479.
[2] H. Kazemian, Z. Naghdali, T. Ghaffari Kashani, F. Farhadi, Conversion of high silicon fly ash to Na–P1 zeolite: alkaline fusion followed by hydrothermal crystallization, Adv. Powder Technol. 21 (2010) 279–283.
[3] J. Davidovit, Geopolymer: inorganic polymeric new materials, J. Therm. Anal. 37 (1991) 1633–1656.
[4] U. Rattanasak, P. Chindaprasirt, Influence of NaOH solution on the synthesis of fly ash geopolymer, Miner. Eng. 22 (2009) 1073–1078.
[5] U. Rattanasak, K. Pankhet, P. Chindaprasirt, Effect of chemical admixtures on properties of high-calcium fly ash geopolymer, Int. J. Miner. Metall. Mater. 18 (2011) 364–369.
[6] K. Somna, C. Jaturapitakkul, P. Kajitvichyanukul, P. Chindaprasirt, NaOH-activated ground fly ash geopolymer cured at ambient temperature, Fuel 90 (2011) 2118–2124.
[7] C.K.Y. Leung, T. Pheerapha, Very high early strength of microwave cured concrete, Cem. Concr. Res. 25 (1995) 136–146.
[8] R.H. Haddad, I.L. Al-Qadi, Characterization of Portland cement concrete using electromagnetic waves over the microwave frequencies, Cem. Concr. Res. 28 (1998) 1379–1391.
[9] H. Tanaka, A. Fujii, S. Fujimoto, Y. Tanaka, Microwave-assisted two-step process for the synthesis of a single-phase Na–A zeolite from coal fly ash, Adv. Powder Technol. 19 (2008) 83–94.
[10] K. Fukui, K. Kanayama, T. Yamamoto, H. Yoshida, Effects of microwave irradiation on the crystalline phase of zeolite synthesized from fly ash by hydrothermal treatment, Adv. Powder Technol. 18 (2007) 381–393.
[11] K. Fukui, K. Arai, K. Kanayama, H. Yoshida, Phillipsite synthesis from fly ash prepared by hydrothermal treatment with microwave heating, Adv. Powder Technol. 17 (2006) 369–382.
[12] P. Termkhajornkit, T. Nawa, M. Nakai, T. Saito, Effect of fly ash on autogenous shrinkage, Cem. Concr. Res. 35 (2005) 473–482.
[13] P. Chindaprasirt, C. Jaturapitakkul, W. Chalee, U. Rattanasak, Comparative study on the characteristics of fly ash and bottom ash geopolymers, Waste Manage. 29 (2009) 539–543.
[14] P. Chindaprasirt, U. Rattanasak, C. Jaturapitakkul, Utilization of fly ash blends from pulverized coal and fluidized bed combustions in geopolymeric materials, Cem. Concr. Compos. 33 (2011) 55–61.
[15] E. Bescher, M. Sambol, E.K. Rice, J.D. Mackenzie, Determination of water-to-cement ratio in freshly mixed rapid-setting calcium sulfoaluminate concrete using 2.45 GHz microwave radiation, Cem. Concr. Res. 34 (2004) 807–812.
[16] T. Ebadzadeh, M.H. Sarrafi, E. Salahi, Microwave-assisted synthesis and sintering of mullite, Ceram. Int. 35 (2009) 3175–3179.
[17] P. Chindaprasirt, U. Rattanasak, Utilization of blended fluidized bed combustion (FBC) ash and pulverized coal combustion (PCC) fly ash in geopolymer, Waste Manage. 30 (2010) 667–672.
[18] E. Alvarez-Ayuso, X. Querol, F. Plana, A. Alastuey, N. Moreno, M. Izquierdo, Environmental, physical and structural characterisation of geopolymer matrixs synthesized from coal (co-)combustion fly ashes, J. Hazard. Mater. 154 (2008) 175–183.
[19] M. Inada, H. Tsujimoto, Y. Eguchi, N. Enomoto, J. Hojo, Microwave-assisted zeolite synthesis from coal fly ash in hydrothermal process, Fuel 84 (2005) 1482–1486.

Materials and Structures
DOI 10.1617/s11527-012-9907-1

ORIGINAL ARTICLE

Resistance to acid and sulfate solutions of microwave-assisted high calcium fly ash geopolymer

Prinya Chindaprasirt · Ubolluk Rattanasak · Sompop Taebuanhuad

Received: 19 March 2012 / Accepted: 27 June 2012

Abstract In this paper, 90-W microwave radiation for 5 min plus a shortened heat curing period was applied to cure the fresh geopolymer paste. Results showed that microwave radiation contributed to the dissolution of fly ash in the alkaline solution. Numerous gel formations were observed in microscopic scale. This resulted in a dense composite and strong bonding between the fly ash and the geopolymer matrix leading to high strength gain compared to those of the control pastes cured at 65 °C for 24 h. In addition, resistances to the sulfuric acid and sulfate attacks of the microwave geopolymer were superior to that of the control as indicated by the relatively low strength loss. The microwave radiation also helped the geopolymer attaining thermal stability as the dense matrices were obtained.

Keywords Geopolymer · Microwave · Radiation · Fly ash · Durability

1 Introduction

Recently, fly ash geopolymer is becoming a well known binding material. The pulverized combustion coal (PCC) fly ash contains both the amorphous and semi-crystalline silica and alumina. In an alkaline solution, they can be effectively converted to alumino-silicate material or geopolymer [1–4]. Fly ash composes of crystalline phases such as quartz and mullite in the interior and a glassy phase of silica and alumina at the surface layer [5]. This glassy phase plays an important role in geopolymer formation due to the high solubility in the alkaline solution. Room temperature (RT) curing can be employed, however the strength development is slow and prolonged curing is normally required to obtain reasonable strength [6]. Owing to the endothermic reaction of fly ash geopolymer, the heat curing of 60–90 °C for 24–48 h is usually employed in order to obtain the high early strength with good physical and mechanical properties [6–8]. However, the heat curing for 24–48 h is the major set back of the synthesis of the fly ash geopolymer.

Heat curing has been applied in concrete, especially for the precast concrete, to improve the strength in short curing time [9]. At present, a microwave radiation technique is utilized in the synthesis of zeolite and in the curing of concrete resulting in the shortening of heating process [9–11]. Microwave energy is directly transferred through the material and allows a fast and uniform heating due to the

---

P. Chindaprasirt
Sustainable Infrastructure Research and Development Center, Department of Civil Engineering, Faculty of Engineering, Khon Kaen University, Khon Kaen 40002, Thailand

U. Rattanasak (✉) · S. Taebuanhuad
Department of Chemistry and Center for Innovation in Chemistry, Faculty of Science, Burapha University, Chonburi 20131, Thailand
e-mail: ubolluk@buu.ac.th

interaction between the microwave electric fields and the polar molecules. Removal of water in the fresh concrete, collapse of capillary pore and densification of sample are achieved with microwave application [9, 10]. Improved microstructure can be obtained at an early age. Short-time curing process is preferred to reduce the energy consumption.

This paper presents the effect of microwave radiation on the strength and resistance to acid and sulfate solutions of fly ash geopolymer. In addition to the convention heat, microwave radiation was applied to accelerate the geopolymer formation. This method could shorten the curing time and provide a strong and durable geopolymer.

2 Experimental program

2.1 Materials and specimen preparation

Lignite coal fly ash from the pulverized coal combustion process (1200 °C) of an electric power plant in northern Thailand was used as raw material. The oxide compositions and particle size of this fly ash are tabulated in Table 1. The majority of fly ash compositions composed of Al_2O_3, SiO_2, CaO and magnetite (Fe_3O_4). 10 M sodium hydroxide (NaOH) solution was prepared by dissolving NaOH pellets in the distilled water [3]. Sodium silicate solution (Na_2SiO_3) with SiO_2-to-Na_2O weight ratio of 3.2 was also used. For mortar specimens for strength test, the graded river sand with fineness modulus of 2.8 and specific gravity of 2.65 was employed.

Table 1 Properties of fly ash

Chemical composition (wt%)	
SiO_2	39.2
Al_2O_3	19.7
CaO	16.9
Fe_3O_4	12.1
SO_3	2.9
K_2O	2.8
MgO	1.7
Na_2O	1.7
Others	1.9
Loss on ignition (%)	1.1
Median particle size (μm)	19.0

The geopolymer was prepared by mixing fly ash with the 10 M NaOH and Na_2SiO_3 solutions in a pan mixer. The mass ratio of Na_2SiO_3/10 M NaOH of 1.5 was used based on the previous research [3, 8]. The mass fraction of fly ash in the mixture was controlled at 0.65 (65 parts of fly ash and 35 parts of mixing solution). The paste was continuously mixed for 5 min and then cast into 50 mm cubic acrylic mould. The specimens were vibrated for 10 s to remove the air bubbles and then covered with cling film to avoid the moisture evaporation during the heat curing.

In the case of geopolymer mortar, sand was added to the paste mixture with the sand-to-fly ash mass ratio of 1.5 and mixed for another 2 min. The procedures for casting, vibration and curing of specimens were the same as those of paste. Compressive strength test was performed on the geopolymer mortars at the age of 7 days. The reported results were the average of five samples.

2.2 Microwave and conventional heat curing

In this study, microwave energy was generated by the household microwave oven with frequency of 2.45 GHz. In addition, the conventional oven was employed. From preliminary test, it was found that 90 W microwave power level applied to the geopolymer pastes for 5 min increased the specimen temperature to 60–65 °C. Higher watts and longer time microwave radiation resulted in high temperature, rapid evaporation, and crack formation on the surfaces of specimens. The specimens were then applied with the convention heat curing at 65 °C for 3, 6 and 12 h. These conditions were selected to compare with the control specimens with heat curing at 65 °C for 24 h. After heat curing, specimens were cooled down and cured in a controlled room at 25 °C.

2.3 XRD, SEM, TGA and durability test (acid and salt resistances)

Geopolymer paste was prepared for the testing of X-ray diffraction (XRD), scanning electron microscopy (SEM) and thermogravimetry (TGA) analyses. The specimens were broken into small sizes for XRD, SEM and TGA analyses. For the SEM analysis, small sample pieces were gold coated for the investigation of the microstructure. For the durability test; after 7 days of curing, the geopolymer mortars were then

Table 2 Compressive strengths of geopolymer mortars at various curing conditions

Sys.	Curing conditions	Compressive strength (MPa)					
		Curing time in oven at 65 °C				25 °C (RT)	
		3 h	6 h	12 h	24 h	7 days	28 days
1	65 °C				32.7[a]		
2	90 W (5 min) + 65 °C	29.2	35.5	42.5			
3	25 °C (RT)					20.0	35.8

[a] Control strength

immersed in 3%volH_2SO_4 and 5%wt$MgSO_4$ solutions. After immersion of 90 and 180 days, the strength tests were performed. Acid and sulfate resistances were expressed in the terms of strength loss. The reported results were the average of five samples.

3 Results and discussion

3.1 Compressive strength

The compressive strengths of geopolymer with 90-W microwave radiation and heat curing compared to those of normal heat curing and RT curing are shown in Table 2.

The control geopolymer was the mix with 65 °C curing for 24 h (system 1) and had the compressive strength of 32.7 MPa. The strength of system 1 was comparable to 35.8 MPa of the mix cured at RT (25 °C) for 28 days (system 3). Therefore, heat curing was preferable in terms of short curing time. System 2 was the mix with 90 W microwave radiation for 5 min incorporated with the conventional heat curing. The system 2 with 6 h heat curing produced the compressive strength of 35.5 MPa which was slightly higher than that of the control. The microwave radiation shortened the required time of heat curing and enhanced the strength development of the geopolymer paste. The presence of an electric field in microwave resulted in a lower porosity and the densification of the matrices [11].

3.2 Durability

The durability of geopolymer was presented in term of the strength after immersion for 3 and 6 months in the 3%volH_2SO_4 (pH = 0.85) and 5%wt$MgSO_4$ (pH = 9.85) compared with the control as shown in Figs. 1 and 2. H_2SO_4 acid is a strong acid and readily attacks calcium compound and other calcareous materials in

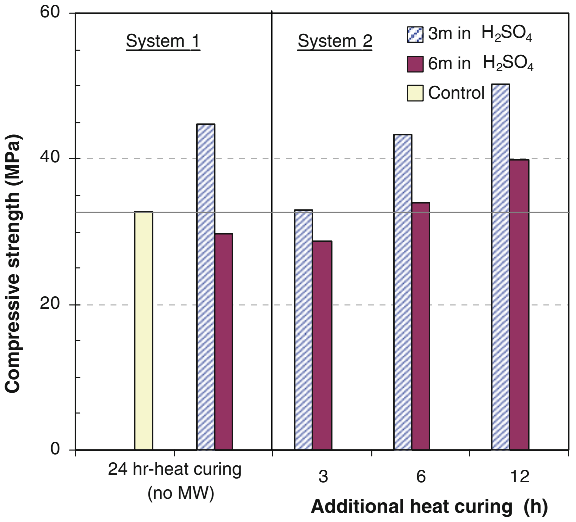

Fig. 1 Compressive strength of geopolymers under H_2SO_4 attack

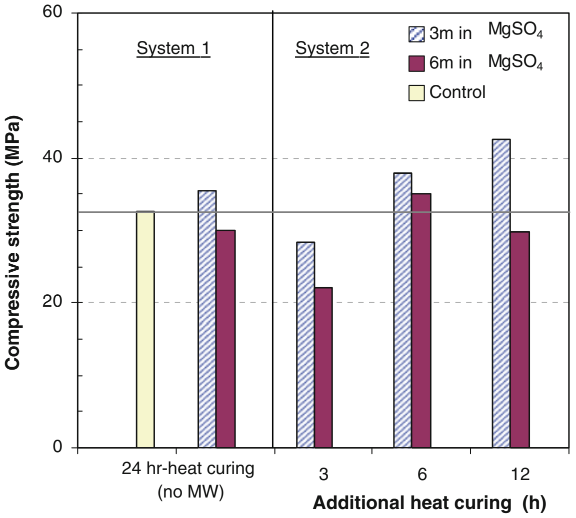

Fig. 2 Compressive strength of geopolymers under $MgSO_4$ attack

concrete. Owing to the microwave radiation, a dense matrix was achieved leading to a low leaching of calcium compounds by acid and a low strength loss. In the presence of moisture, the compressive strength of geopolymer developed with time due to additional pozzolanic reaction of high calcium fly ash. The compressive strengths after immersion in the H_2SO_4 for 3 months were all higher than that of the control. However, the strengths significantly decreased after 6 months immersion in the acid.

The reactions of geopolymer paste in H_2SO_4 solution consisted of the reaction between $Ca(OH)_2$ and H_2SO_4, and resulted in $CaSO_4$ which was easily leached out from the matrix (Eq. 1). The use of high calcium fly ash led to $Ca(OH)_2$ formation within geopolymer matrix and was identified from the XRD pattern. Internal $CaSO_4$ further reacted with aluminium compound in the fly ash leading to the formation of calcium sulfoaluminate or ettringite (Eq. 2). This ettringite caused the expansion, cracking and a loss of strength in the geopolymer. In addition, the calcium silicate hydrate (CSH) also reacted with H_2SO_4 and formed calcium sulfate and amorphous silica gel [12] which were easily destroyed by external physical forces (Eq. 3). These compounds and products were presented as indicated by the results of the XRD patterns.

$$Ca(OH)_2\ (s) + H_2SO_4\ (aq) \rightarrow CaSO_4 \cdot 2H_2O\ (s) \tag{1}$$

$$3CaO\ (s) + Al_2O_3\ (s) + 3CaSO_4\ (s) + 32H_2O\ (l) \rightarrow Ca_6Al_2(SO_4)_3(OH)_{12}{\cdot}26H_2O\ (s) \tag{2}$$

$$3CaO \cdot SiO_2\ (s) + 3H_2SO_4\ (aq) + 3H_2O\ (l) \rightarrow 3CaSO_4 \cdot 2H_2O\ (s) + SiO_2\ (s) \tag{3}$$

The alumino-silicate network in geopolymer could also be attacked by hydrogen ions (H^+) from H_2SO_4 acid ionization. H^+ ruptured the alumino-silicate network at aluminium sites (–Al–O–Si–O–) and yielded silicic acid ($Si(OH)_4$) and aluminium ions (Al^{3+}) [13]. The breaking of oxy-aluminium bridge (–Al···O–Si–O) rendered the geopolymer paste susceptible to acid attack.

After immersion in the $MgSO_4$ solution, the compressive strengths of all geopolymer mortars were lower than those immersed in the H_2SO_4 solution for the same period. For the 6-month immersion in the $MgSO_4$ solution, only the samples with microwave radiation and 6-h heat curing gave the strength higher than that of the control. White substance on the surface of the samples was observed. The XRD pattern of this white substance is presented in Fig. 3 and indicated the presence of the magnesium hydroxide ($Mg(OH)_2$), silica (SiO_2), calcium magnesium silicate (Ca–Mg–Si–O) and magnesium silicate (Mg–Si–O) compounds.

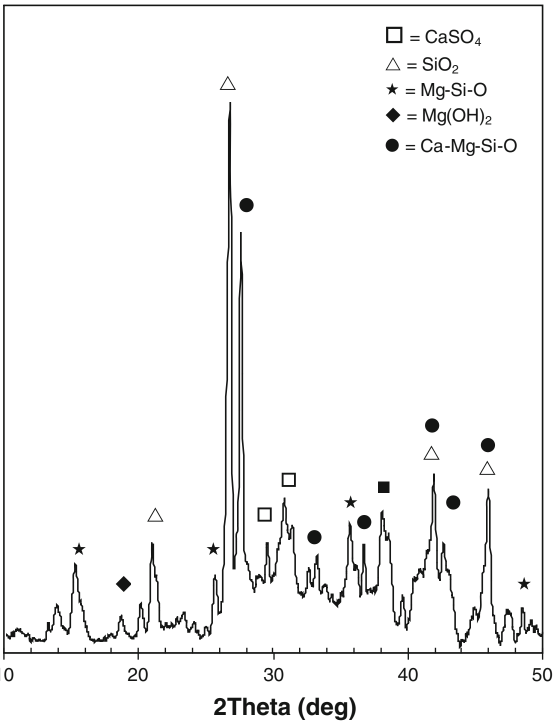

Fig. 3 XRD pattern of white substance after immersion in $MgSO_4$ solution

The reaction between Mg^{2+} ion, sulfate ion and hydroxyl ion (OH^-) from $Ca(OH)_2$ and NaOH in geopolymer matrix yielded the $Mg(OH)_2$ and calcium sulfate in the form of gypsum ($CaSO_4{\cdot}2H_2O$) as presented in Eq. 4 [12]. $Mg(OH)_2$ and gypsum are insoluble compound leading to the deposition on the material surface.

$$Mg^{2+}\ (aq) + SO_4^{2-}\ (aq) + Ca(OH)_2\ (s) + H_2O\ (l) \rightarrow Mg(OH)_2\ (s) + CaSO_4 \cdot 2H_2O\ (s) \tag{4}$$

In addition, decomposition of CSH phase also took place and resulted in the formation of amorphous hydrous silica (SiO_2) as shown in Eq. 5 [12].

$$3Mg^{2+}\ (aq) + 3SO_4^{2-}\ (aq) + 3CaO \cdot SiO_2\ (s) + 9H_2O\ (l) \rightarrow 3Mg(OH)_2\ (s) + 3[CaSO_4 \cdot 2H_2O]\ (s) + SiO_2\ (s) \quad (5)$$

The degradation of CSH phase in the present of $MgSO_4$ is significant faster and more thorough than that with other sulfate compounds. This was due to the low pH (~ 10.5) of saturated solution, which is too low to maintain the stability of CSH [12].

Concurrently, additional amount of gypsum, $Mg(OH)_2$ and magnesium silicate hydrate were also formed as shown in Eq. 6. The hydrated magnesium silicate possessed no binding capacity [12, 14]. The immersion in $MgSO_4$ solution, therefore, resulted in the deterioration of materials and lowered the compressive strength.

$$6Mg^{2+}\ (aq) + 6SO_4^{2-}\ (aq) + 2[3CaO \cdot SiO_2]\ (s) + 17H_2O\ (l) \rightarrow 3MgO \cdot 2SiO_2 \cdot 2H_2O\ (s) + 6[CaSO_4 \cdot 2H_2O]\ (s) + 3Mg(OH)_2\ (s) \quad (6)$$

In addition, sulfate ions (SO_4^{2-}) from $MgSO_4$ solution were strongly absorbed on surface of aluminosilicate owing to the strong interaction between SO_4^{2-} ions and aluminol edge site (Al–OH) on the surface of solid [15]. The SO_4^{2-} replaced –OH edge group, which was attached to Al ion leading to a high void ratio [15]. This replacement corresponded to the increased pores observed on geopolymer surface, and also affected the compressive strength of geopolymer.

3.3 Effect of microwave radiation on the geopolymer properties

XRD patterns of geopolymer pastes and fly ash are presented in Fig. 4. There were numerous sharp peaks of crystalline quartz (SiO_2), alumina (Al_2O_3), calcium sulfate ($CaSO_4$) and calcium oxide (CaO) identified in this fly ash. The crystalline phases appeared mainly in the core, whereas a glassy phase occupies the fly ash surface [5]. This glassy phase could be dissolved in alkaline solution forming geopolymer gel over the fly ash particles [3, 7]. In case of geopolymer pastes, the semi-crystalline gel was detected as indicated by both broad hump and some sharp peaks. The 22–38° 2θ broad hump of these pastes indicated the highly disorder glass phase in geopolymer [16]. In addition, new compounds of alumino-silicate (Al–Si–O) and calcium silicate (Ca–Si–O) were also detected. The Ca–Si–O was the same product of the hydration of Portland cement. This was produced by the reaction between high calcium fly ash and NaOH/sodium silicate solutions. The crystalline quartz remained in the geopolymer paste owing to its low reactivity compared with the glassy phase on the fly ash particles [5].

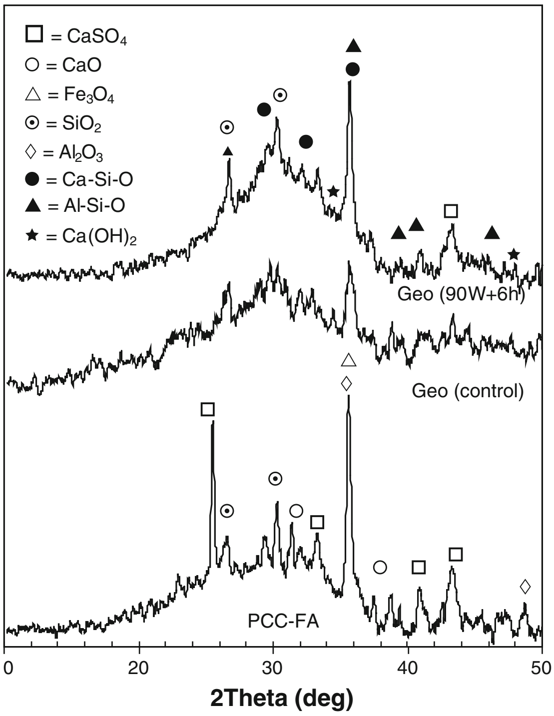

Fig. 4 Typical XRD patterns of geopolymer pastes and fly ash

Moreover, the samples with microwave radiation exhibited the sharp peaks of crystalline phases and the increase in height of hump peak compared with the control confirming the semi-crystalline geopolymer. The quartz, calcium- and alumino-silicate compounds had significant effects on the physical properties of the geopolymer. The presence of some of these crystalline products in geopolymer also enhanced the compressive strength [16].

Figure 5 shows the microstructure of the geopolymer with microwave radiation and the control. Partially reacted fly ash embedded in continuous mass of geopolymer products was readily observed. The gel formation on the fly ash surface confirmed the dissolution of the glassy phase in the alkaline solution and deposited on the fly ash surface [5]. Numerous gel formations occurred with microwave radiation. Microwave radiation promoted the dissolution of Si

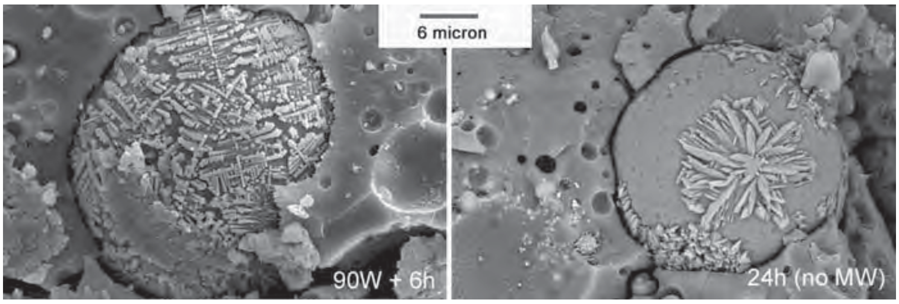

Fig. 5 Microstructure of geopolymer pastes

and Al species from the fly ash particles. In addition to the microwave energy, the additional heat curing contributed to more gel formation on the fly ash particles. With only heat curing, the gradual dissolution of the glassy phase on fly ash surface took place and led to less surface reaction compared with that with radiation. Cracks from the moisture removal during heat curing, voids and occupied fly ash pores were also detected in the geopolymer matrices.

Microwave radiation enhanced the dissolution rate at the early stage of geopolymerization compared with the conventional heat curing. It resulted in the rapid heating up of an aqueous alkaline solution by microwave energy, and the glassy SiO_2 and Al_2O_3 phases were easily leached out. In addition, the hydrogen bond between water molecules was broken under the microwave radiation and resulted in single water molecule. This molecule would consequently attack the Si–O and Al–O bonds of fly ash [5].

Thermogravimetric analysis (TGA) and differential thermogravimetry (DTG) were used to determine the geopolymer's thermal stability and its fraction of volatile components by monitoring the weight change during heating of specimen. Figure 6 shows the TGA/DTG curves of fly ash and geopolymer pastes. Fly ash lost the weight at approximately 100, 400 and 700 °C owing to the evaporation of water, and decompositions of magnesite ($MgCO_3$) and calcium sulfate ($CaSO_4$) into CaO and SO_3, respectively.

For microwave radiation, a dense and strong sample was obtained as indicated by the low weight loss at high temperature compared with that of the control. Both the radiation and control geopolymers had a considerable weight loss at high temperature. This is probably due to the use of the alkaline solutions in the geopolymer mixture [16]. The geopolymer was, therefore, relatively stable at high temperature and microwave radiation contributed to the dimensional stability of the geopolymer.

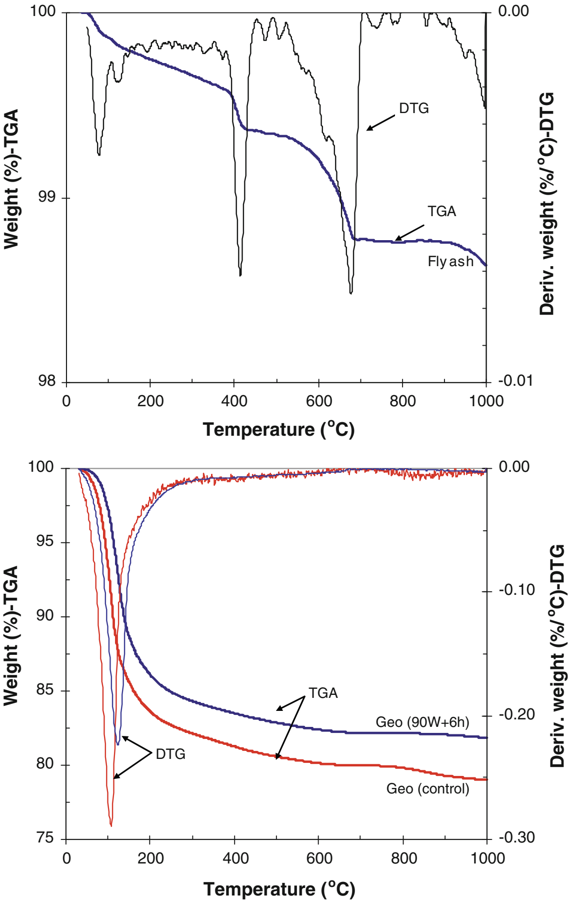

Fig. 6 TGA/DTG curves of geopolymer pastes

4 Conclusions

Microwave radiation and additional heat curing of geopolymer contributed to the dissolution of the glassy phase on fly ash surface in alkaline solution. The microwave radiation shortened the required time of heat curing and enhanced the geopolymerization. A dense sample was achieved leading to a low strength loss under the acid and sulfate attacks compared with that of the control. However, gypsum, $Mg(OH)_2$, SiO_2, and magnesium silicate hydrate were formed and deposited onto the geopolymer surface during sulfate immersion. This caused the deterioration of materials and reflected in compressive strength loss. Numerous gel formations occurred with microwave radiation due to the promoted dissolution of Si and Al species from the fly ash surface. The geopolymer with microwave radiation possessed a dense sample with strong bonding leading to the dimensional stability of geopolymer.

Acknowledgments The authors gratefully acknowledge the financial support from the Higher Education Research Promotion, and National Research University Project of Thailand, Office of the Higher Education Commission, through the Advanced Functional Materials Cluster of Khon Kaen University and the Thailand Research Fund (TRF) under TRF Senior Research Scholar contract no. RTA5480004. Appreciation is also extended to the Center for Innovation in Chemistry (PERCH-CIC).

References

1. Davidovits J (1991) Geopolymer: inorganic polymeric new materials. J Therm Anal 137(8):1633–1656
2. Van Jaarsveld JGS, Van Deventer JSJ (1999) Effect of the alkali metal activator on the properties of fly ash-based geopolymers. Ind Eng Chem Res 8(10):3932–3941
3. Rattanasak U, Chindaprasirt P (2009) Influence of NaOH solution on the synthesis of fly ash geopolymer. Miner Eng 22(12):1073–1078
4. Chindaprasirt P, Rattanasak U, Jaturapitakkul C (2011) Utilization of fly ash blends from pulverized coal and fluidized bed combustions in geopolymeric materials. Cem Concr Compost 33(1):55–61
5. Inada M, Tsujimoto H, Eguchi Y, Enomoto N, Hojo J (2005) Microwave-assisted zeolite synthesis from coal fly ash in hydrothermal process. Fuel 84(12–13):1482–1486
6. Somna K, Jaturapitakkul C, Kajitvichyanukul P, Chindaprasirt P (2011) NaOH-activated ground fly ash geopolymer cured at ambient temperature. Fuel 90(6):2118–2124
7. Chindaprasirt P, Jaturapitakkul C, Chalee W, Rattanasak U (2009) Comparative study on the characteristics of fly ash and bottom ash geopolymers. Waste Manage 29(2):539–543
8. Rattanasak U, Pankhet K, Chindaprasirt P (2011) Effect of chemical admixtures on properties of high-calcium fly ash geopolymer. Int J Miner Metall Mater 18(3):364–369
9. Leung CKY, Pheerapha T (1995) Very high early strength of microwave cured concrete. Cem Concr Res 25(1):136–146
10. Haddad RH, Al-Qadi IL (1998) Characterization of Portland cement concrete using electromagnetic waves over the microwave frequencies. Cem Concr Res 28(10):1379–1391
11. Ebadzadeh T, Sarrafi MH, Salahi E (2009) Microwave-assisted synthesis and sintering of mullite. Ceram Int 35(8):3175–3179
12. Skalny J, Marchand J, Odler I (2002) Sulfate attack on concrete. Spon Press, London
13. Wilson AD, Nicholson JW (1993) Acid–base cements: their biomedical and industrial applications (chemistry of solid state materials). Cambridge University Press, New York
14. Rattanasak U, Chindaprasirt P, Suwanvitaya P (2010) Development of high volume rice husk ash alumino-silicate composite. Int J Miner Metall Mater 17(5):654–659
15. Sridharan A, Rao SM, Gajarajan VS (1990) Effect of sulfate contamination on the volume change behaviour of bentonite. In: Physico-chemical aspects of soils and related materials. ASTM STP 1095, pp 60–68
16. Chindaprasirt P, Rattanasak U (2010) Utilization of blended fluidized bed combustion (FBC) ash and pulverized coal combustion (PCC) fly ash in geopolymer. Waste Manage 30(4):667–672

International Journal of Minerals, Metallurgy and Materials
Volume 20, Number 5, May 2013, Page 462
DOI: 10.1007/s12613-013-0752-1

Cellular lightweight concrete containing high-calcium fly ash and natural zeolite

Khamphee Jitchaiyaphum$^{1)}$, *Theerawat Sinsiri*$^{1)}$, *Chai Jaturapitakkul*$^{2)}$, *and Prinya Chindaprasirt*$^{3)}$

1) School of Civil Engineering, Institute of Engineering, Suranaree University of Technology, Nakhon Ratchasima 30000, Thailand

2) Department of Civil Engineering, Faculty of Engineering, King Mongkut's University of Technology Thonburi, Bangkok 10140, Thailand

3) Sustainable Infrastructure Research and Development Center, Department of Civil Engineering, Faculty of Engineering, Khon Kaen University, Khon Kaen 40002, Thailand

(Received: 12 July 2012; revised: 3 October 2012; accepted: 10 October 2012)

Abstract: Cellular lightweight concrete (CLC) with the controlled density of approximately 800 kg/m^3 was made from a preformed foam, Type-I Portland cement (OPC), fly ash (FA), or natural zeolite (NZ), and its compressive strength, setting time, water absorption, and microstructure of were tested. High-calcium FA and NZ with the median particle sizes of 14.52 and 7.72 μm, respectively, were used to partially replace OPC at 0, 10wt%, 20wt%, and 30wt% of the binder (OPC and pozzolan admixture). A water-to-binder mass ratio (W/B) of 0.5 was used for all mixes. The testing results indicated that CLC containing 10wt% NZ had the highest compressive strength. The replacement of OPC with NZ decreased the total porosity and air void size but increased the capillary porosity of the CLC. The incorporation of a suitable amount of NZ decreased the setting time, total porosity, and pore size of the paste compared with the findings with the same amount of FA. The total porosity and cumulative pore volume decreased, whereas the gel and capillary pores increased as a result of adding both pozzolans at all replacement levels. The water absorption increased as the capillary porosity increased; this effect depended on the volume of air entrained and the type or amount of pozzolan.

Keywords: lightweight concrete; fly ash; zeolites; compressive strength; microstructure; water absorption

1. Introduction

Lightweight concrete has been widely used in wall panels, masonry blocks, roof decks, and precast concrete units in many building applications. There are many advantageous qualities of lightweight concrete, such as its low density, low thermal conductivity, reduction of dead load, fast building rate, and low haulage cost [1]. The air voids needed to produce lightweight concrete can be obtained using expanded lightweight aggregate materials, such as perlite, blast furnace slag, volcanic ash, and coal bottom ash. The air voids can also be formed in cement paste by adding the prepared foam to the unhardened mixture. Cellular lightweight concrete (CLC) is a well-known low-density product that contains blends of Portland cement, silica, pozzolan, and lime as well as a homogeneous void or cellular structure attained with gas-forming chemicals or foaming agents. Autoclave curing is usually employed for CLC that contains binder ingredients other than, or in addition to, Portland cement [2]. Density control is achieved by substituting macroscopic air cells for all or part of the fine aggregate. Normal-weight coarse aggregates are not usually used, but lightweight aggregates, both fine and coarse, are often found in CLC [3]. After molding, the concrete hardens under normal atmospheric conditions [4].

Since CLC is a porous material with a homogeneous cellular structure, it possesses a number of attractive characteristics, such as good thermal and acoustic insulation, satisfactory workability, and self-flowing properties. Its good thermal and acoustic performance makes it a natural choice as a building construction material. Although

---

Corresponding author: Theerawat Sinsiri E-mail: sinsiri@sut.ac.th

its mechanical properties are low compared with those of normal concrete, CLC products are used in many applications, such as partition walls and load-bearing walls in low-rise residential buildings [5−6].

Fly ash (FA) is a by-product from the combustion of pulverized coal in power plants. More than 3.5 million tons of coal fly ash is produced in Thailand annually. Using FA as a replacement ingredient in cement is currently a common practice in Thailand because FA improves the properties of concrete and reduces its cost. The high content of amorphous silica, alumina (which comprises more than 70wt%), and fine spherical particles (15 μm in diameter on average) in FA are the primary reasons for its high pozzolanic index. Many researchers have already examined the influence of FA on the properties of concrete, such as compressive strength, sulfate resistance, and durability [7].

Natural zeolite (NZ), a volcanic or volcanogenic sediment material, has a three-dimensional structure, and it is classified as a hydrated aluminosilicate of alkali and alkaline earth cations with uniform pores, grooves, and pits. NZs possess special properties, such as ion exchange, molecular sieves, large surface areas, and catalytic activity, which make this material preferable for large-scale industrial applications[1]. Approximately 40 NZs have been identified over the last 200 years. The most common NZs are analcime, chabazite, clinoptilolite, mordenite, and phillipsite. Based on the recorded production and production estimates, the worldwide production of NZ is approximately 3-4 million tons per year[1].

The current research presents the test results and evaluations of incorporating FA and NZ into preformed foam CLC as a replacement for Portland cement. This information is essential for its wider application to other construction materials.

2. Experimental

2.1. Materials

Type-I Portland cement (OPC), foaming agent, water, FA, and NZ were the materials used. The specific gravities of OPC, FA, and NZ were measured in accordance with ASTM C 188-95(2003) [8], and their particle sizes were measured using laser particle size analysis. These data are provided in Table 1. A scanning electron microscopy (SEM) photo of an OPC particle is shown in Fig. 1(a). FA was obtained from a silo at the Mae Moh Power Plant in northern Thailand. Its SEM photo, which is shown in Fig. 1(b), reveals the spherical shape of the particles. NZ was a clinoptilolite ($(Na,K,Ca)_6(Si,Al)_{36}O_{72}\cdot 20H_2O$). An SEM photo of NZ, which is shown in Fig. 1(c), demonstrates its irregular and crushed-shape particles. Other researchers have also reported similar observations [9]. The chemical compositions of these three materials are listed in Table 2. The foaming agent was synthetic. Fig. 2 shows the particle size distributions obtained using the Malvern Mastersizer Instrument. The particle size of FA is similar to that of cement, whereas that of NZ is smaller.

Table 1. Physical properties of the material

Sample	Specific gravity	Median particle size, d_{50} / μm	Blaine fineness / $(cm^2\cdot g^{-1})$
OPC	3.15	14.12	3600
FA	2.02	14.52	4300
NZ	2.09	7.72	11300

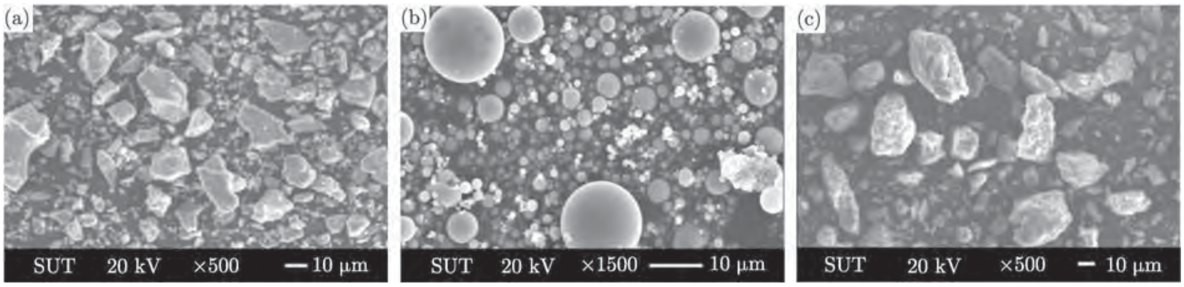

Fig. 1. SEM images of OPC (a), FA (b), and NZ (c).

Table 2. Chemical compositions of OPC, FA, and NZ wt%

Ingredient	SiO_2	Al_2O_3	Fe_2O_3	CaO	MgO	Na_2O	K_2O	SO_3	LOI	$SiO_2 + Al_2O_3 + Fe_2O_3$
OPC	19.85	4.49	3.56	66.96	1.36	—	0.34	2.46	0.98	—
FA	43.87	26.33	10.81	12.69	1.23	—	1.10	2.74	1.23	81.01
NZ	75.32	10.28	2.66	3.95	1.20	0.89	4.29	—	1.41	88.26

Note: LOI—loss on ignition.

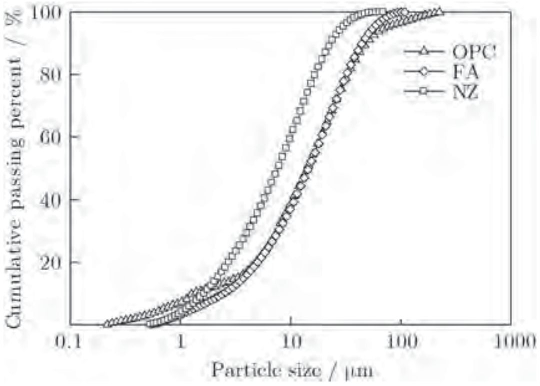

Fig. 2. Material particle size distribution.

2.2. Mix proportions

This experiment studied the effect of the filler contents on the density, setting time, water absorption, and compressive strength of CLC. The OPC was replaced with FA and NZ at levels of 0-30wt%. The mixes were labeled CON, FA10, FA20, FA30, NZ10, NZ20, and NZ30. For example, FA10 denotes the mix with 10wt% FA, and CON denotes the control mix (CLC with only OPC). The mass ratio of water to binder (W/B) of 0.5 was used for all mixtures. The foam required for a CLC density of 800-850 kg/m^3 was obtained per ASTM C 796-04[3]. The concrete mix proportions are provided in Table 3.

Table 3. Mix proportion of CLC

Mix No.	Symbol	Pozzolan replacement / wt%	Mix proportion / (kg·m^{-3})					W/B
			Binder			Foaming agent	Water	
			Cement	FA	NZ			
1	CON	0	665.0	—	—	0.772	332	0.5
2	FA10	10	598.5	66.5	—	0.759	332	0.5
3	FA20	20	532.0	133.0	—	0.746	332	0.5
4	FA30	30	465.5	199.5	—	0.733	332	0.5
5	NZ10	10	598.5	—	66.5	0.760	332	0.5
6	NZ20	20	532.0	—	133.0	0.748	332	0.5
7	NZ30	30	465.5	—	199.5	0.737	332	0.5

The foaming agent was diluted with water at a mass ratio of 1:40. Next, the liquid was pressurized with air at 6 kg/cm^2 and aerated to a density of 45 kg/m^3. OPC and FA (or NZ) were thoroughly mixed using a horizontal mixer. The foaming agent was added and mixed until a uniform paste was obtained. This process usually required approximately 3 min. The samples were poured into molds, and an external vibrator was applied to facilitate compaction. The CLCs were removed from the molds after 24 h, wrapped with a plastic film and placed in a moist room at (23±2)°C. A set of 100 mm×100 mm×100 mm specimens was used for the strength and porosity tests.

2.3. Compressive strength test

A compressive strength test was conducted at 3, 14, 28, and 60 d in accordance with BS 1881-116 [10]. The results are presented as the averages of three samples.

2.4. Concrete porosity determination

The pore-size measurements of the hardened CLC were determined using mercury intrusion porosimetry (MIP) with a pressure capacity of 228 MPa. The Washburn equation was used to determine pressure [11]. After curing for 3, 14, 28, and 60 d, the samples were obtained by carefully breaking the cube specimens with a chisel. The representative samples of 5 to 10-mm pieces, weighing between 2 and 3 g, were removed from the middle of each specimen. To stop the hydration reaction, the samples were submerged directly into liquid nitrogen for 5 min and vacuumed at a pressure of 0.5 Pa at –40°C for 48 h. This method has been previously used to stop the hydration reaction of cement paste [12-14]. A constant contact angle of 140° and a constant mercury surface tension of 480×10^{-3}J·m^{-2} were used to calculate the pore size.

2.5. X-ray diffraction (XRD)

Dried FA and NZ sample powders were sifted through a No. 100 sieve (150 μm openings). A sample of powder weighing approximately 1 g was used for XRD analysis. The XRD scans were performed for 2θ between 10° and 65° with an increment of 0.02°/step at a scan speed of 0.5 s/step. A quantitative XRD analysis determined the amorphous FA and NZ phases using Bruker's TOPAS software.

3. Results and discussion

3.1. Material properties

The chemical compositions of OPC, FA, and NZ are provided in Table 2. The main chemical component of FA is SiO_2, which accounts for 43.87wt% of its mass. As prescribed by ASTM C 618-03 [15], this sample is a Class F fly ash because the sum of SiO_2, Al_2O_3, and Fe_2O_3 is higher than 70wt%, and the LOI and SO_3 content do not exceed 6% and 5wt%, respectively. NZ has a high SiO_2 content of 75.32wt% and an LOI of 1.41%. The total content of SiO_2, Al_2O_3, and Fe_2O_3 in the NZ is 88.26wt%, which is more than the minimum requirement (70wt%) specified by

ASTM C 618-03 [15] for natural pozzolans.

The XRD patterns of FA and NZ shown in Fig. 3 indicate that the former powder consists primarily of crystalline phases of quartz; for NZ, the common zeolite mineral clinoptilolite is the major crystalline phase, and quartz is contained as a minor phase. Uzal and Turanlı [9] reported a similar result. A quantitative XRD analysis reveals that the contents of amorphous phases in FA and NZ are 78.8wt% and 20.5wt%, respectively. Moreover, the crystalline phase consists of 85wt% quartz and 15wt% mullite for FA and 22wt% quartz and 78wt% clinoptilolite for NZ.

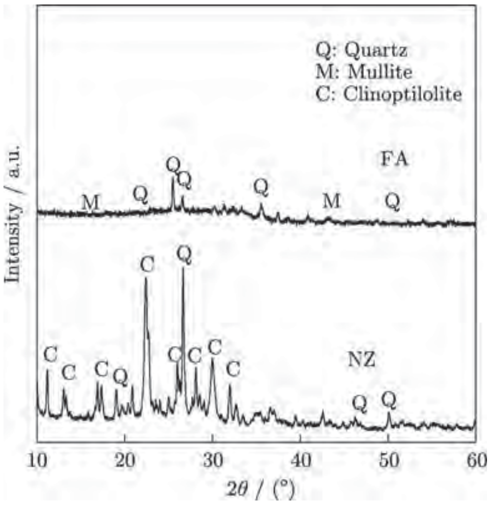

Fig. 3. XRD patterns of FA and NZ.

3.2. Setting time

The initial and final setting times of CLCs containing FA and NZ are presented in Fig. 4. It shows that the setting times prolong as the content of FA or NZ increases. The initial setting times of FA and NZ pastes increase from 5.2 to 14.45 h and from 5.2 to 12.15 h, respectively, whereas the final setting times increase from 13.1 to 23.5 h and from 13.1 to 19.95 h, respectively. The increase of pozzolan content reduces the cement content in the mix. As a result, a delay in the setting time of the cementitious system is due primary to a lower proportion of cement in the blended system. The setting times of the paste that contained NZ are slightly shorter than those of the paste contained FA because the former is a pozzolan with a Blaine fineness of 11300 cm^2/g, whereas the latter has a fineness of only 4300 cm^2/g. The fine pozzolan with a high surface area produces a greater pozzolanic reaction than the coarser pozzolan [16-17].

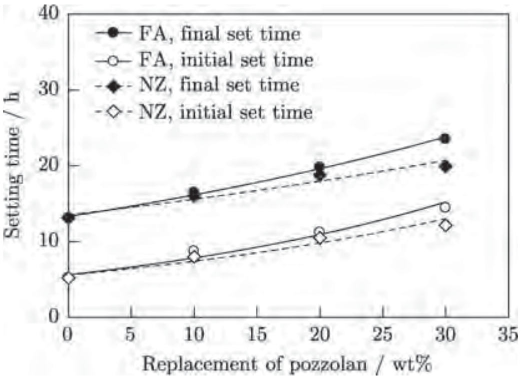

Fig. 4. Effect of FA and NZ on the setting time of CLC.

3.3. Compressive strength

Table 4 shows the compressive and relative strengths of CON. The compressive strengths of the control mix at 3, 14, 28, and 60 d are 1.81, 2.70, 3.05, and 3.15 MPa, respectively. The compressive strengths of the CLC increase with increasing the curing time due to the hydration reaction that increases the calcium silicate hydrate (C–S–H) product [18]. At 3 d the compressive strength of CLC containing 10wt% FA is slightly higher than that of the control mix at the same time point. This result is due to the proper amount of FA content, which affects the pozzolanic reaction rate and better dispersion and improves the compressive strength of the paste [7, 19-20]. The compressive strengths of CLC containing 20wt% or 30wt% FA are lower than that of the control mix. This result is due to the low OPC content that have been observed in other research [21]. In addition, the compressive strengths of FA30 at 14, 28, and 60 d are lower than those of the other mixes due to the greater amount of FA. FA is a pozzolan, and its pozzolanic reaction is slow compared with that of OPC; thus, the rate of strength development is also slow [19, 22].

Table 4. Compressive strength of CLCs containing OPC, FA, and NZ

Mix No.	Symbol	Compressive strength / MPa				Relative strength to CON / %			
		3 d	14 d	28 d	60 d	3 d	14 d	28 d	60 d
1	CON	1.81	2.70	3.05	3.15	100	100	100	100
2	FA10	1.95	3.17	3.45	3.65	108	117	113	116
3	FA20	1.65	2.75	3.10	3.30	91	102	102	105
4	FA30	1.27	2.15	2.42	2.58	70	80	79	82
5	NZ10	2.19	3.72	4.27	4.51	121	138	140	143
6	NZ20	1.92	3.18	3.66	3.91	106	118	120	124
7	NZ30	0.85	1.56	2.05	2.25	47	58	67	71

The compressive strengths of NZ30 at 3, 14, 28, and 60 d are 0.85, 1.56, 2.05, and 2.25 MPa, respectively. The strengths are weaker than those of the OPC due to the high NZ content and the slower pozzolanic reaction rate of zeolite, which do not significantly contribute to compressive strength [23]. The compressive strengths of NZ10 and NZ20 at 3, 14, 28, and 60 d are 2.19, 3.72, 4.27, and 4.51, and 1.92, 3.18, 3.66, and 3.91 MPa, respectively. These strengths are higher than those of CON at the same time point. The high SiO_2 content (75.32wt%) and NZ fineness (median particle size = 7.72 μm) improve the reaction with $Ca(OH)_2$ to produce an additional calcium silicate hydrate (C–S–H), which improves the compressive strength [1, 24−25].

At the replacement levels of 10wt% and 20wt%, the compressive strengths of CLC containing NZ are higher than those of CLC containing FA, as shown in Table 4. This finding is due to the high purity level (up to 90wt%) of NZ and the high SiO_2 content compared with those of FA. According to Ref. [25], the 28-d strength of zeolite concrete with a replacement level of 15wt% (the optimum) is also 23wt% higher than that of the control mix. As a result, the strength of hardened concrete is improved by incorporating a proper amount of zeolite [1, 16, 19, 26-27]. The optimum replacement level of NZ or FA is 10wt%. For a higher replacement level of 20wt%, the strengths of CLC are slightly reduced compared with those at the optimum replacement level of 10wt%; however, these strengths are still higher than those of the control mix. Replacing cement with FA or NZ affects the compressive strength because the compressive strength significantly increases with time but decreases with increasing the replacement level. Three factors can explain the increased compressive strength of CLC: hydration reaction, filler effect, and pozzolanic reaction. Hydration reaction is directly related to the cement amount in the mix. The filler effect involves the nucleation and packing effects, which depend on the material fineness. The nucleation effect occurs when small particles are dispersed into the cement paste and act as nucleation sites that enhance cement hydration, whereas the packing effect is the result of small particles that fill the voids of the paste [28-30]. Therefore, CLC with pozzolans of high fineness results in a more homogeneous and denser matrix, which increases the compressive strength of the paste.

3.4. Water absorption

The results of CLC water absorption at 28 d are presented in Fig. 5. The water absorption of CON is 30.0wt% at 28 d, whereas those of FA10, FA20, and FA30 are 30.6wt%, 32.5wt%, and 35.3wt%, respectively. The water absorption of CLC containing FA increases as the FA content increases. Kunhanandan Nambiar and Ramamurthy [31] reported similar results when they used Class F fly ash to replace sand at the sand-to-FA ratio of 0-100wt% to obtain foam concrete with the water absorption of 23wt%-30wt%.

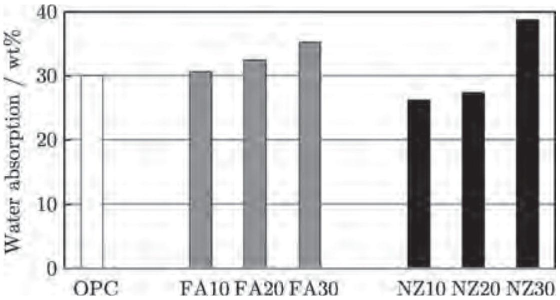

Fig. 5. Water absorption of CLC at 28 d.

The water absorptions of NZ10 and NZ20 are 26.3wt% and 27.3wt%, respectively. These figures are lower than those of CON. This finding is due to the amount of pore bubbles from the foam, which is slightly reduced with the addition of NZ. However, the water absorption of NZ30 is higher (38.8wt%). Other researchers have made similar observations regarding water absorption [25, 32]. This finding is related to the porosity results: a small increase in capillary pores in CLC hence causes a small increase of water absorption.

Fig. 5 shows that the water absorption of CLC containing NZ is more effective than CLC with FA at replacement levels of 0-20wt%. The water absorption of CLC containing 30wt% FA is slightly lower than that containing 30wt% NZ. It is observed that replacing cement with pozzolan in CLC results in the increase of large capillary pores. The result shows that large capillary pores of FA10 and FA20 are higher than those of NZ10, NZ20, and CON. Therefore, an increase of large capillary pores in CLC could influence their water absorption.

3.5. Microstructure of CLC

3.5.1. Porosity of CLC

The porosity results of all CLCs at 28 and 60 d are presented in Table 5 and Fig. 6. The porosity system consists of four types of pores: gel pores or small pores, less than 10 nm; medium capillary pores, 10 to 50 nm; large capillary pores, 50 to 10000 nm; and air void or extra large pores, larger than 10000 nm. Large capillary pores and extra large pores are influential on strength and permeability characteristics, whereas small pores and medium capillary pores are influential on drying shrinkage and creep [33−34]. The total porosities of the control mix, FA10, FA20, and FA30 at 28 d are 52.27%, 48.56%, 50.78%, and 59.32%, respectively. Incorporating 10wt% and 20wt% FA results in the CLCs with reduced total porosity. This result is due to the gradual filling of large pores from factors, such as the hydration reaction, the dispersing effect, the packing effect, and the pozzolanic reaction of FA particles. Small and spherical FA particles fill air voids and decrease the porosity [28, 30]. At 30wt% FA, the total porosity significantly increases, primarily due to the packing effect of FA particles filling the air bubbles, which increases the capillary porosity of CLC. Note that the total porosity and capillary porosity of the CLCs increase, whereas the compressive strength and extra large pores decrease. Other investigations have reported similar findings [7]. The porosity of CLC containing FA at 60 d has a similar trend to that at 28 d.

Table 5. Porosity of CLCs containing OPC, FA, and NZ

Mix No.	Symbol	Porosity at 28 d / %					Porosity at 60 d / %				
		Small	Medium capillary	Large capillary	Extra large	Total	Small	Medium capillary	Large capillary	Extra large	Total
1	CON	0.05	2.84	26.72	22.66	52.27	0.05	2.15	26.93	22.51	51.64
2	FA10	0.28	1.94	38.62	7.72	48.56	0.35	1.86	36.80	7.71	46.72
3	FA20	0.19	2.93	40.51	7.15	50.78	0.20	2.42	40.37	7.56	50.55
4	FA30	0.24	4.39	47.70	6.99	59.32	0.25	3.96	47.67	6.73	58.61
5	NZ10	0.20	4.29	33.88	4.69	43.06	0.21	3.77	31.72	4.55	40.25
6	NZ20	0.38	4.72	34.37	5.34	44.81	0.31	4.40	34.11	5.13	43.95
7	NZ30	0.30	9.26	50.60	9.55	69.71	0.31	7.90	50.49	9.13	67.83

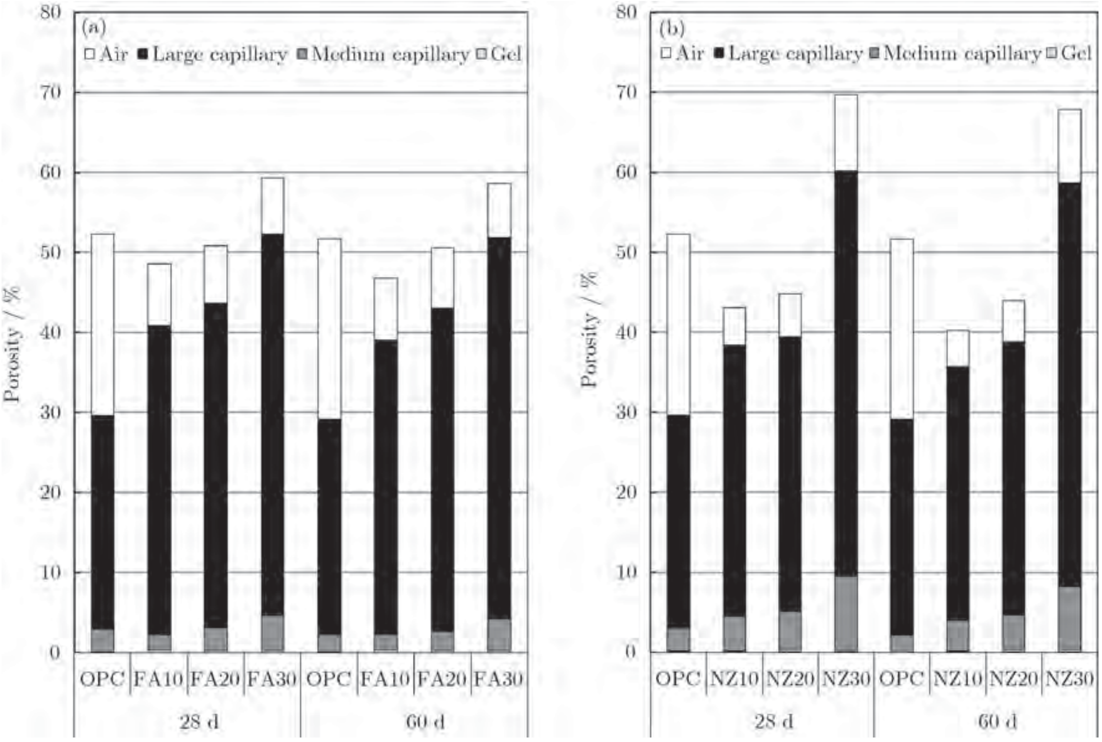

Fig. 6. CLC porosity with admixtures FA (a) and NZ (b).

As shown in Fig. 6, the total porosity of CLCs containing NZ10 and NZ20 are smaller than that of OPC concrete at all replacement levels and times. It is because NZ is more effective at reducing pore size due to a better dispersing effect, packing effect, and pozzolanic reaction of finer NZ particles. The small NZ particles fill the pores and decrease the porosity [9, 27].

Compared with FA, high-fineness NZ has a faster pozzolanic reaction and a better filler effect at reducing the voids of CLC. However, a considerable decrease in the total porosity of NZ10 occur 28 d later, primarily due to the decrease in large capillary pores. This decrease might be associated with the pore system becoming denser as a result of the additional formation and growth of the pozzolanic reaction products [9, 27].

The 10wt% incorporation of pozzolanic materials decreases the total porosity due to the filling effect and pore refinement. The total porosity of OPC concrete is 52.27%, whereas those of FA10 and NZ10 are 48.56% and 43.06%, respectively. The total porosity of NZ10 is reduced more than that of FA10 due to its finer particles. The increase in pozzolan content to 20% and 30% increases the total porosity. The reduced OPC content and hydration products offset the filling effect. The extra large pores of CLCs containing pozzolans are reduced, whereas the small pores, medium capillary pores, and large capillary pores increase. The filling effect reduces extra large pores and increases small pores, medium capillary pores, and large capillary pores. All pores other than small pores increase significantly for 30% pozzolans. Again, this result is due to the reduced amounts of OPC and hydration products. Other investigations also reported similar findings [7]. The pores exhibit a similar trend at 60 d compared with that at 28 d.

As shown in Table 5 and Fig. 6, the incorporation of higher CLC replacement levels of both FA and NZ results in greater gel porosity compared with that of the control mix at all times. CLC with NZ exhibits increased gel porosity, which suggests that CLC with NZ is more effective than that with FA, and this is due to the better dispersion, packing effect and pozzolanic reaction in the blended cement paste. Other researchers have reported similar results [7, 16].

3.5.2. Effects of FA and NZ on the pore size distribution of CLC

The cumulative pore volumes of CLCs with FA and NZ are shown in Figs. 7 and 8. The cumulative pore volumes of the control mix at 28 and 60 d are 0.454 and 0.452 mL/g, respectively. These values decrease with curing time due to the hydration reactions and the increase of the C–S–H product [14, 23].

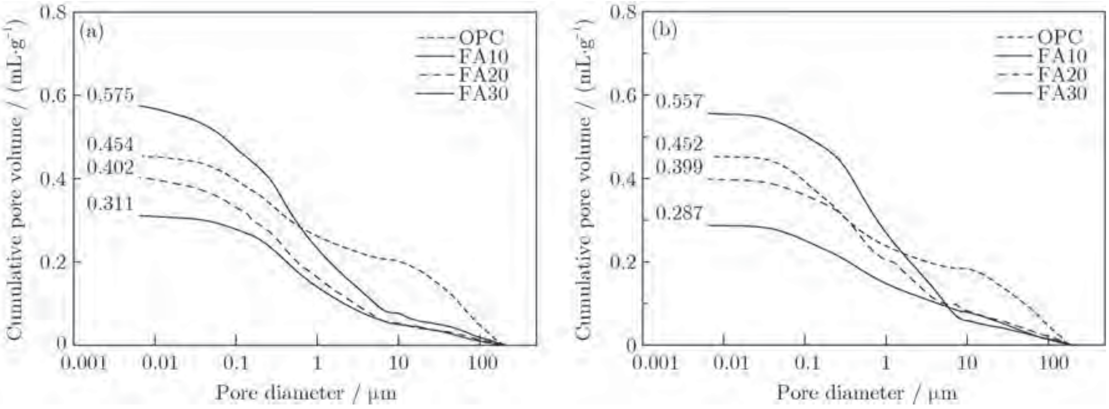

Fig. 7. Relationship of cumulative pore volume and pore diameter of CLC containing FA: (a) 28 d; (b) 60 d.

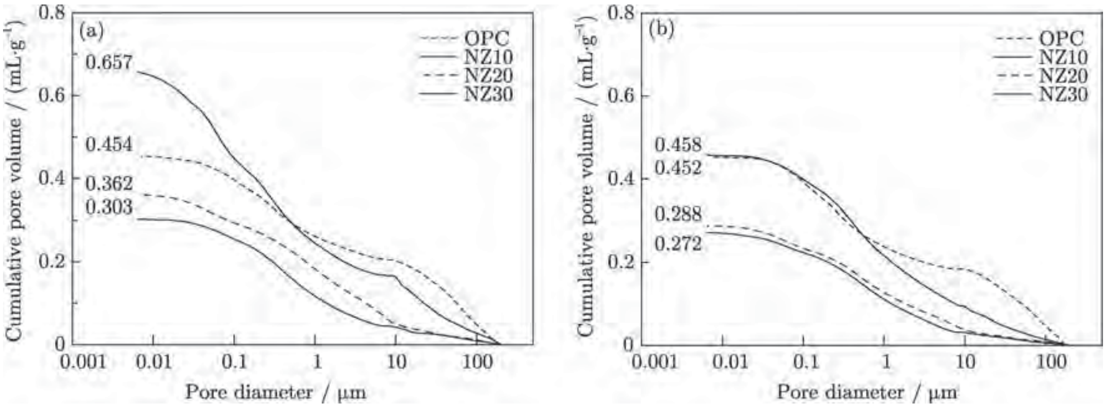

Fig. 8. Relationship of cumulative pore volume and pore diameter of CLC containing NZ: (a) 28 d; (b) 60 d.

As shown in Fig. 7, the cumulative pore volumes of CLC containing 10wt% FA are 0.311 mL/g at 28 d and 0.287 mL/g at 60 d. These figures are lower than those of the control mix and CLC containing 20wt% or 30wt% FA. As shown in Fig. 8, the cumulative pore volumes of CLC containing 10wt% NZ are 0.303 mL/g at 28 d and 0.272 mL/g at 60 d. FA and NZ are effective pozzolans with successful pozzolanic reactions. Incorporating a proper amount of pozzolan fills voids, reduces porosity, and increases the density of the paste [14, 16]. The SiO_2 and Al_2O_3 in pozzolanic materials react with $Ca(OH)_2$ to produce C–S–H and C–A–H, which results in a reduction of $Ca(OH)_2$ content by pozzolanic reaction [23, 27]. The results also reveal that the cumulative pore volumes of concretes containing NZ are smaller than those containing FA. This finding suggests that NZ is slightly more effective than

FA at reducing porosity.

3.5.3. SEM observations

The morphologies of the fractured surfaces of CLCs at 28 d are shown in Figs. 9 and 10. The pores of the control mix are clearly shaded circles of various sizes with relatively smooth surfaces. The pore sizes vary from less than 50 μm to 600 μm. Another researcher reported a similar observation [32].

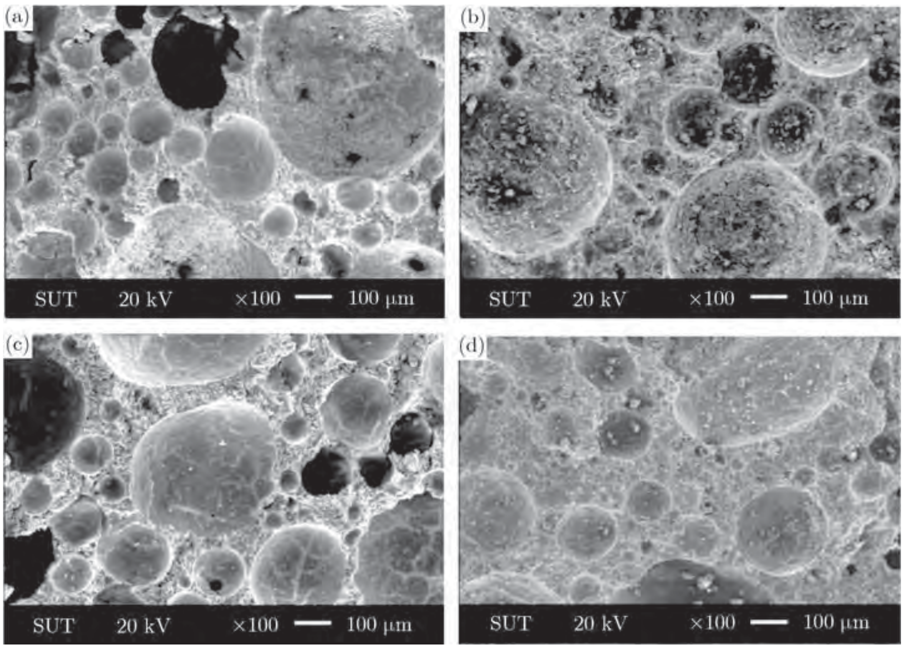

Fig. 9. SEM images of the fractured surfaces of CLCs containing FA at 28 d: (a) OPC; (b) FA10; (c) FA20; (d) FA30.

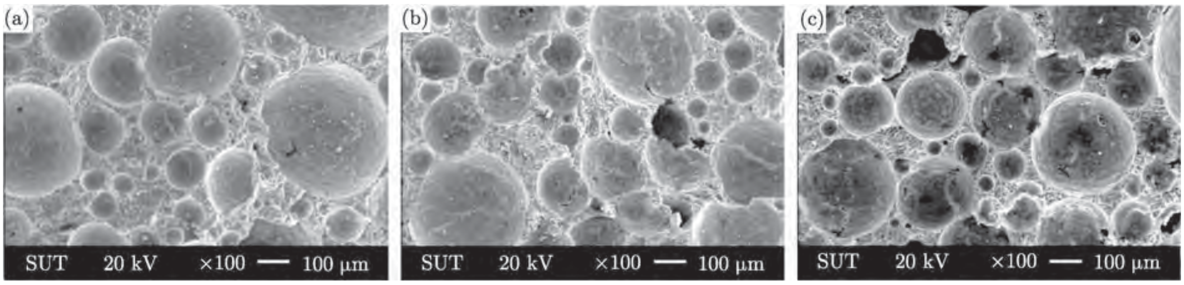

Fig. 10. SEM images of the fractured surfaces of CLCs containing NZ at 28 d: (a) NZ10; (b) NZ20; (c) NZ30.

Figs. 9(b)-9(d) display the SEM images of CLCs containing 10wt%, 20wt%, and 30wt% FA, respectively, which have completely different microstructures from the control mix (Fig. 9(a)). Clearly, the pores are more uniform than those of the control mix because FA facilitates the distribution of air voids by preventing them from merging and overlapping [35]. The pore sizes of these CLCs range from less than 50 μm to 400 μm. In addition, the pore size decreases as the FA replacement level increases [14]. Furthermore, some microcracks are detected at the pore surfaces (Figs. 9(c) and 9(d)). Drying shrinkage and mechanical stresses that occurred during sample preparation probably induce these features.

Figs. 10(a)-10(c) display the SEM images captured from CLCs containing 10wt%, 20wt%, and 30wt% NZ, respectively. Clearly, these pore sizes are slightly more uniform than those of CLCs containing FA. The pore sizes range from less than 50 μm to 300 μm. Fig. 10(a) shows that there are several closed pores, which demonstrates that CLC with 10wt% NZ have low water absorption [36]. In addition, the pore size decreases as the NZ replacement level increases (Fig. 10(c)).

SEM observations reveal that the pores of CLCs containing NZ are denser than those of CLCs containing FA at the same replacement level (excluding the 30wt% replacement level) and control mix. This effect is due to cement hydration and pozzolanic reactions [14, 26]. Numerous large pores are observed with 30wt% pozzolan replacement, which reflects the high total porosity and low strength of these CLCs, due primarily to their low OPC content and reduced hydration products.

4. Conclusions

CLCs with OPC partially replaced by FA or NZ with a density of approximately 800 kg/m^3 can be produced with relatively good compressive strength. NZ is slightly more reactive than FA and enhances the strength of CLC. The optimum replacement level for both FA and NZ is 10wt%, which, compared with CON, results in the 28-d compressive strength increasing by 113% and 140%, respectively. A replacement level of 20wt% results in decreased strength; however, these CLCs are still stronger than the control mix.

CLCs containing NZ set slightly faster than those containing FA. This finding is due to the high fineness of NZ, which also has a higher surface area and a greater pozzolanic reaction. The increase in pozzolans also prolongs the setting time of CLCs with NZ compared with the control mix due to the lower content of OPC.

The capillary porosity of CLCs containing FA and NZ increases as the replacement level of both types of pozzolans increases. Moreover, water absorption is primarily related to capillary porosity. The water absorption increases as the capillary porosity increases, which decreases the compressive strength.

The reduction of air voids in CLCs with density control is due to replacing OPC with pozzolans. The pozzolans cause a filler effect and refine the pore-size structure of the paste. This effect changes larger pores into smaller ones. Thus, the total porosity and cumulative pore volumes of CLCs containing FA and NZ are less than those of OPC.

Acknowledgements

The authors acknowledge the financial support of the Rajamangala University of Technology Isan, Thailand, for a grant originating from the Strategic Scholarships for Frontier Research Network, which supports the Joint Ph.D. Program and Thai doctoral degree. Thanks are also extended to the Thailand Research Fund (TRF) for financial support originating from the TRF Senior Research Scholarship (No. RTA5480004), as well as the TRF New Researcher Scholarship (No. MRG5280178).

References

[1] C. Karakurt, H. Kurama, and İ.B. Topçu, Utilization of natural zeolite in aerated concrete production, *Cem. Concr. Compos.*, 32(2010), No.1, p. 1.

[2] ACI Committee 116, *Cement and Concrete Terminology (ACI 116R-00)*, ACI Manual of Concrete Practice, 2000.

[3] ASTM C796-04, *Standard Test Method for Foaming Agents for Use in Producing Cellular Concrete Using Preformed Foam*, Annual Book of ASTM Standards, 2004.

[4] A. Just and B. Middendorf, Microstructure of high-strength foam concrete, *Mater. Charact.*, 60(2009), No. 7, p. 741.

[5] P.J. Tikalsky, J. Pospisil and W. MacDonald, A method for assessment of the freeze-thaw resistance of preformed foam cellular concrete, *Cem. Concr. Res.*, 34(2004), No. 5, p. 889.

[6] E.K. Kunhanandan Nambiar and K. Ramamurthy, Models relating mixture composition to the density and strength of foam concrete using response surface methodology, *Cem. Concr. Compos.*, 28(2006), No. 9, p. 752.

[7] P. Chindaprasirt, C. Jaturapitakkul, and T. Sinsiri, Effect of fly ash fineness on compressive strength and pore size of blended cement paste, *Cem. Concr. Compos.*, 27(2005), No. 4, p. 425.

[8] ASTM C188-95, *Standard Test Method for Density of Hydraulic Cement*, Annual Book of ASTM Standards, Vol. 04.01, 2003.

[9] B. Uzal and L. Turanl Blended cements containing high volume of natural zeolites: properties, hydration and paste microstructure, *Cem. Concr. Compos.*, 34(2012), No. 1, p. 101.

[10] BS 1881-116, *Method of Determination of Compressive Strength of Concrete Cubes,* British Standards Institute, 1983.

[11] E.W. Washburn, Note on a method of determining the distribution of pore sizes in a porous material, *PNAS*, 7(1921), No. 4, p. 115.

[12] C. Gallé, Effect of drying on cement-based materials pore structure as identified by mercury intrusion porosimetry: a comparative study between oven-, vacuum-, and freeze-drying, *Cem. Concr. Res.*, 31(2001), No. 10, p. 1467.

[13] L. Konecny and S.J. Naqvi, The effect of different drying techniques on the pore size distribution of blended cement mortars, *Cem. Concr. Res.*, 23(1993), No. 5, p. 1223.

[14] P. Chindaprasirt, C. Jaturapitakkul, and T. Sinsiri, Effect of fly ash fineness on microstructure of blended cement paste, *Constr. Build. Mater.*, 21(2007), No. 7, p. 1534.

[15] ASTM C618, *Standard Specification for Coal Fly Ash and Raw or Calcined Natural Pozzolan for Use as a Mineral Admixture in Concrete*, Annual book of ASTM Standards, Vol. 04.02, 2003.

[16] W. Kroehong, T. Sinsiri, C. Jaturapitakkul, and P. Chindaprasirt, Effect of palm oil fuel ash fineness on the microstructure of blended cement paste, *Constr. Build. Mater.*, 25(2011), No. 11, p. 4095.

[17] F. Canpolat, K. Yılmaz, M.M. Köse, M. Sümer, and M.A. Yurdusev, Use of zeolite, coal bottom ash and fly ash as replacement materials in cement production, *Cem. Concr. Res.*, 34(2004), No. 5, p. 731.

[18] K.L. Scrivener and A. Nonat, Hydration of cementitious materials, present and future, *Cem. Concr. Res.*,

41(2011), No. 7, p. 651.

[19] W. Wongkeo and A. Chaipanich, Compressive strength, microstructure and thermal analysis of autoclaved and air cured structural lightweight concrete made with coal bottom ash and silica fume, *Mater. Sci. Eng. A*, 527(2010), No. 16-17, p. 3676.

[20] E.K. Kunhanandan Nambiar and K. Ramamurthy, Influence of filler type on the properties of foam concrete, *Cem. Concr. Compos.*, 28(2006), No. 5, p. 475.

[21] S. Kolias and C. Georgiou, The effect of paste volume and of water content on the strength and water absorption of concrete, *Cem. Concr. Compos.*, 27(2005), No. 2, p. 211.

[22] T. Nochaiya, W. Wongkeo, and A. Chaipanich, Utilization of fly ash with silica fume and properties of Portland cement-fly ash-silica fume concrete, *Fuel*, 89(2010), No. 3, p. 768.

[23] C.S. Poon, L. Lam, S.C. Kou, and Z.S. Lin, A study on the hydration rate of natural zeolite blended cement pastes, *Constr. Build. Mater.*, 13(1999), No. 8, p. 427.

[24] T. Perraki, E. Kontori, S. Tsivilis, and G. Kakali, The effect of zeolite on the properties and hydration of blended cements, *Cem. Concr. Compos.*, 32(2010), No. 2, p. 128.

[25] B. Ahmadi and M. Shekarchi, Use of natural zeolite as a supplementary cementitious material, *Cem. Concr. Compos.*, 32(2010), No. 2, p. 134.

[26] B. Yılmaz, A. Uçar, B. Öteyaka, and V. Uz, Properties of zeolitic tuff (clinoptilolite) blended portland cement, *Build. Environ.*, 42(2007), No. 11, p. 3808.

[27] C. Bilim, Properties of cement mortars containing clinoptilolite as a supplementary cementitious material, *Constr. Build. Mater.*, 25(2011), No. 8, p. 3175.

[28] M. Cyr, P. Lawrence, and E. Ringot, Efficiency of mineral admixtures in mortars: quantification of the physical and chemical effects of fine admixtures in relation with compressive strength, *Cem. Concr. Res.*, 36(2006), No. 2, p. 264.

[29] M.K. Gopalan, Nucleation and pozzolanic factors in strength development of class fly ash concrete, *ACI Mater. J.*, 90(1993), No. 2, p. 117.

[30] D.G. Montgomery, D.C. Hughes, and R.I.T. Williams, Fly ash in concrete: a microstructure study, *Cem. Concr. Res.*, 11(1981), No. 4, p. 591.

[31] E.K. Kunhanandan Nambiar, K. Ramamurthy, Sorption characteristics of foam concrete, *Cem. Concr. Res.*, 37(2007), No. 9, p. 1341.

[32] P. Chindaprasirt and U. Rattanasak, Shrinkage behavior of structural foam lightweight concrete containing glycol compounds and fly ash, *Mater. Des.*, 32(2011), No. 2, p. 723.

[33] P.K. Mehta, Studies on blended Portland cements containing Santorin earth, *Cem. Concr. Res.*, 11(1981), No. 4, p. 507.

[34] J.M. Khatib and S. Wild, Pore size distribution of metakaolin paste, *Cem. Concr. Res.*, 26(1996), No. 10, p. 1545.

[35] E.K. Kunhanandan Nambiar and K. Ramamurthy, Air-void characterisation of foam concrete, *Cem. Concr. Res.*, 37(2007), No. 2, p. 211.

[36] K.S. Wang, I.J. Chiou, C.H. Chen, and D. Wang, Lightweight properties and pore structure of foamed material made from sewage sludge ash, *Constr. Build. Mater.*, 19(2005), No. 8, p. 627.

Japanese Journal of Applied Physics **52** (2013) 06GF05 **REGULAR PAPER**
http://dx.doi.org/**10.7567/JJAP.52.06GF05**

Dielectric Responses and Electrical Properties of $CaCu_3Ti_{4-x}V_xO_{12}$ Ceramics Prepared by a Simple Poly(ethylene glycol) Sol–Gel Route

Nuchjarin Sangwong[1], Prasit Thongbai[2]*, Teerapon Yamwong[3], Santi Maensiri[4], and Prinya Chindaprasirt[5]

[1] *Materials Science and Nanotechnology Program, Faculty of Science, Khon Kaen University, Khon Kaen 40002, Thailand*
[2] *Department of Physics, Faculty of Science, Khon Kaen University, Khon Kaen 40002, Thailand*
[3] *National Metal and Materials Technology Center (MTEC), Thailand Science Park, Pathumthani 12120, Thailand*
[4] *School of Physics, Institute of Science, Suranaree University, Nakhon Ratchasima 30000, Thailand*
[5] *Sustainable Infrastructure Research and Development Center, Department of Civil Engineering, Faculty of Engineering, Khon Kaen University, Khon Kaen 40002, Thailand*
E-mail: pthongbai@kku.ac.th; prasitphysics@hotmail.com

Received November 29, 2012; accepted February 26, 2013; published online June 20, 2013

Nanocrystalline $CaCu_3Ti_{4-x}V_xO_{12}$ ($x = 0$, 0.025, and 0.05) powders with particle sizes of 100–200 nm were successfully synthesized using a poly(ethylene glycol) solution. All the ceramic samples exhibited the pure $CaCu_3Ti_4O_{12}$ phase. The grain size of $CaCu_3Ti_{4-x}V_xO_{12}$ ceramics increased slightly as V doping ion concentration increased; whereas, the dielectric permittivity of the ceramics decreased slightly. The nonlinear current–voltage properties of $CaCu_3Ti_4O_{12}$ ceramics were improved significantly by substitution of V ions. Impedance spectroscopy analysis and investigation of non-ohmic electrical properties revealed that the electrical resistance of the grain boundary and breakdown electric field strength were markedly increased by substitution of V ions; whereas, electrostatic potential barrier height at grain boundaries decreased slightly.

1. Introduction

Recently, dielectric materials with high values of dielectric permittivity (ε') have been playing an important role in microelectronic devices such as multilayered ceramic capacitors (MLCCs). Many researchers have investigated the dielectric and electrical properties of perovskite oxides and related oxide ceramics to improve the dielectric properties of high-permittivity materials.[1–14] Among them, $CaCu_3Ti_4O_{12}$ (CCTO) and related oxides (such as $Na_{1/2}Bi_{1/2}Cu_3Ti_4O_{12}$, $Na_{1/2}La_{1/2}Cu_3Ti_4O_{12}$, $Na_{1/2}Y_{1/2}Cu_3Ti_4O_{12}$, and $Y_{2/3}Cu_3Ti_4O_{12}$) have gained considerable interest both scientifically and technologically. Interestingly, these ceramics can exhibits values of ε' in the range of 10^3–10^5 at room temperature.[3,5,9,10,15–25]

To date, many investigations have been carried out to understand the physical mechanism(s) related to the apparent giant dielectric response in CCTO ceramics.[3,5,9,10,17,20] However, the origin of giant dielectric properties is still unclear. Both the intrinsic and extrinsic effects were proposed to underlie the unusually high ε' values of CCTO ceramics and single crystals. For the intrinsic effect, different models have been proposed to explain the giant dielectric response such as the mixed-valent structure model,[10,20] polaron relaxation model,[26] and nanoscale disorder model.[27,28] For the extrinsic effect, it is widely believed that the origin of the giant dielectric response in the CCTO ceramics is attributed to the internal barrier layer capacitor (IBLC) effect.[5,9,15–19,22,24] The giant dielectric response in CCTO is mainly caused by the polarization at grain boundary (GB) regions, which is well known as the "Maxwell–Wagner polarization".[5,29] Moreover, it was also found that this polarization can be introduced at other interfaces, both inside and outside the ceramics, such as internal domain boundaries (DBs)[30] and at the sample-electrode interface.[9,31,32]

It is interesting that CCTO and related oxide ceramics can also exhibit nonlinear current–voltage behavior.[5,16,17,19,22,24,33–36] This is because of the existence of intrinsic potential barriers at the GBs, i.e., the Schottky effect.[37,38] Therefore, it is possible that CCTO ceramics have the potential for varistor and gas sensor applications.[5]

To improve dielectric properties and to clarify the giant dielectric response in CCTO ceramics, substitution of metal ions into Ca^{2+}, Cu^{2+}, and Ti^{4+} sites for CCTO ceramics has been extensively investigated.[9,18,19,21,24,36,39–44] All doping ions have significant effects on ε', $\tan\delta$, electrical conductivity of GBs (σ_{gb}), as well as activation energy required for conduction at GBs and inside the grains. Moreover, doping ions also show a great effect on the nonlinear current density–electric field (J–E) characteristics of CCTO ceramics. For example, it was found that substitution of 2.0 wt% vanadium (V) can reduce the resistance of GB (R_{gb}) with a slight increase in the capacitance of GBs (C_{gb}).[45] Sen et al.[46] reported that ε' of CCTO ceramics was decreased by substitution of V ions. Ramajo et al.[36] found that addition of VO_2 into $CaCu_3Ti_4O_{12}/CaTiO_3$ composite ceramics can decrease ε', especially at high frequencies. A large decrease in ε' at high frequencies may be due to the effect of V doping on dielectric relaxation. It was also found that the nonlinear electrical properties of $CaCu_3Ti_4O_{12}/CaTiO_3$ ceramics can be improved significantly. According to the IBLC model,[29] the dielectric response in ceramics is closely related to the electrical response at GBs. Therefore, systematic investigation of the giant dielectric and electrical properties of CCTO-based ceramics is therefore important.

In general, the conventional solid state reaction method is selected to prepare CCTO using $CaCO_3$, CuO, and TiO_2 as the starting raw materials. This method requires high sintering temperatures and long reaction times to produce the pure CCTO phase. In contrast to the SSR method, synthesis of CCTO from chemical solutions usually offers the possibilities of close stoichiometric control and low-temperature chemical reactions.[15] Thus, preparation of CCTO ceramics using chemical solutions is therefore important.

In this work, the dielectric and electrical properties of $CaCu_3Ti_{4-x}V_xO_{12}$ ($x = 0$, 0.025, and 0.05) ceramics were systematically investigated at different temperatures. The phase formation and microstructure of the sintered ceramics were characterized. The effects of V doping ions on the giant dielectric properties and electrical response at GBs are discussed on the basis of the results of impedance spectroscopy analysis and measurement of current–voltage at various temperatures.

2. Experimental Procedure

A poly(ethylene glycol) (PEG) solution route was used to prepare $CaCu_3Ti_{4-x}V_xO_{12}$ powders, where $x = 0$, 0.025, and 0.05 (abbreviated as CCTO, CCTVO-1, and CCTVO-2 samples, respectively). The starting raw materials were $Ca(NO_3)_2{\cdot}4H_2O$ (99%, Sigma-Aldrich), $Cu(NO_3)_2{\cdot}4H_2O$ (99.5%, Carlo Erba), $C_{16}H_{28}O_6Ti$ (75 wt% in isopropanol, Sigma-Aldrich), ethanol, and PEG. Firstly, stoichiometric amounts of $Ca(NO_3)_2{\cdot}4H_2O$ and $Cu(NO_3)_2{\cdot}4H_2O$ were dissolved in the solution of PEG (2.5 wt%) in ethanol with constant stirring at room temperature. Secondly, $C_{16}H_{28}O_6Ti$ solution was dropped slowly into the metal ion solution mentioned above with constant stirring. Immediately, a clean and transparent solution was obtained. Thirdly, the mixed solution was dried at 623 K for 30 min. The resulting dried porous precursors were ground and calcined at 1073 K for 3 h. The obtained $CaCu_3Ti_{4-x}V_xO_{12}$ powders were ground and pressed into pellets of 9.5 mm diameter and ~1–2 mm thickness by uniaxial compression at 200 MPa. Finally, these pellets were sintered in air at 1333 K for 1 h.

Scanning electron microscopy (SEM; LEO 1450VP) and X-ray diffraction (XRD; Philips PW3040) techniques were used to examine the microstructure and to characterize the phase formation of the sintered $CaCu_3Ti_{4-x}V_xO_{12}$ ceramics, respectively. Nanoparticles of $CaCu_3Ti_{4-x}V_xO_{12}$ powders were observed by transmission electron microscopy (TEM; FEI Tecnai G^2). Au electrodes were sputtered on the polished-face of each pellet at a current of 25 mA for 8 min using a Polaron SC500 sputter coating unit. The capacitance and dissipation factor (or $\tan\delta$) of the samples were measured using an Agilent 4294A Precision Impedance analyzer over the frequency range from 10^2 to 10^7 Hz at an oscillation voltage of 500 mV. The measurements were performed over the temperature range of 203–423 K. All temperature steps were kept constant with an accuracy of ±1 K. Current–voltage measurements were measured in the temperature range of 313–353 K using a high-voltage measurement unit (Keithley 247). The breakdown electric field (E_b) was obtained at the current density of 1 $mA{\cdot}cm^{-2}$. Nonlinear coefficient (α) was calculated in the range of 1–10 $mA{\cdot}cm^{-2}$.

The complex impedance Z^* was calculated from the relation,

$$\varepsilon^* = \varepsilon' - i\varepsilon'' = \frac{1}{i\omega C_0 Z^*} = \frac{1}{i\omega C_0(Z' - iZ'')}, \quad (1)$$

where ε' and ε'' are, respectively, the real (dielectric constant) and imaginary parts (dielectric loss) of the complex permittivity ε^*. Z' and Z'' are the real and imaginary parts of Z^*, respectively. ω is the angular frequency ($\omega = 2\pi f$) and $i = \sqrt{-1}$. $C_0 = \varepsilon_0 S/d$ is the empty cell capacitance, where S is the sample area, d is the sample thickness, and ε_0 is the permittivity of free space, $\varepsilon_0 = 8.854 \times 10^{-12}$ F/m.

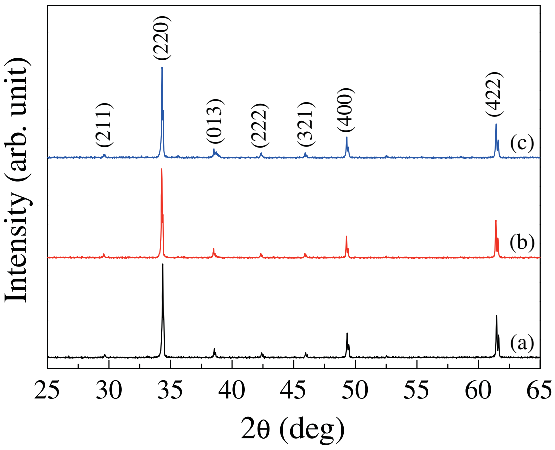

Fig. 1. (Color online) XRD patterns of (a) CCTO, (b) CCTVO-1, and (c) CCTVO-3 ceramic samples.

3. Results and Discussion

Figure 1 shows the XRD patterns of the CCTO and V-doped CCTO ceramics sintered at 1333 K for 1 h. All diffraction peaks for all of the samples confirm the formation of the $CaCu_3Ti_4O_{12}$ phase (JCPDS 75-2188) without any possible impurities such as CuO, TiO_2, or $CaTiO_3$. The lattice parameters (a) of the sintered ceramics were calculated by Cohen's least mean square method. The a values of the CCTO, CCTVO-1, and CCTVO-2 samples were found to be 7.389(9), 7.389(1), and 7.394(6) Å, respectively. These values are comparable to those reported in the literature[1,16] and JCPDS 75-2188 for 7.391 Å.

SEM images of the surface morphologies of the CCTO and V-doped CCTO ceramics are shown in Fig. 2. The microstructures of the CCTO ceramic sample consist of grains, GBs, and pores. The grain sizes of the CCTO ceramic sample are about 1–2 µm, as shown in Fig. 2(a). The mean grain size of the CCTVO-1 ceramic samples tends to increase slightly, as shown in Fig. 2(b). The largest grain of this sample was found to be ~5 µm in size. Figures 2(c) and 2(d) show the surface morphologies of the CCTVO-2 ceramic sample at different regions. The largest grain of the CCTVO-2 ceramic sample was found to be ~10 µm in size. These results mean that substitution of V ions can increase the sintering rate of CCTO ceramics. The grain growth mechanism in a ceramic is usually driven by GB mobility. For CCTO ceramics, the liquid phase sintering mechanism is likely to be the main factor for increasing the grain growth rate.[19] The presence of the liquid phase during heating and sintering processes can increase the diffusion rate of ions across GBs. For V-doped CCTO ceramics, it is likely that the related V phase may act as a liquid phase during heating and sintering processes. The effect of V doping on microstructural changes of ceramics is usually observed in a V-doped ZnO system. It is caused by the relatively low melting points of V and the related second phase.[47] Note that a large number of pores are observed in the microstructures of all ceramic samples, especially for the CCTO sample. The porosity of CCTO ceramics tends to

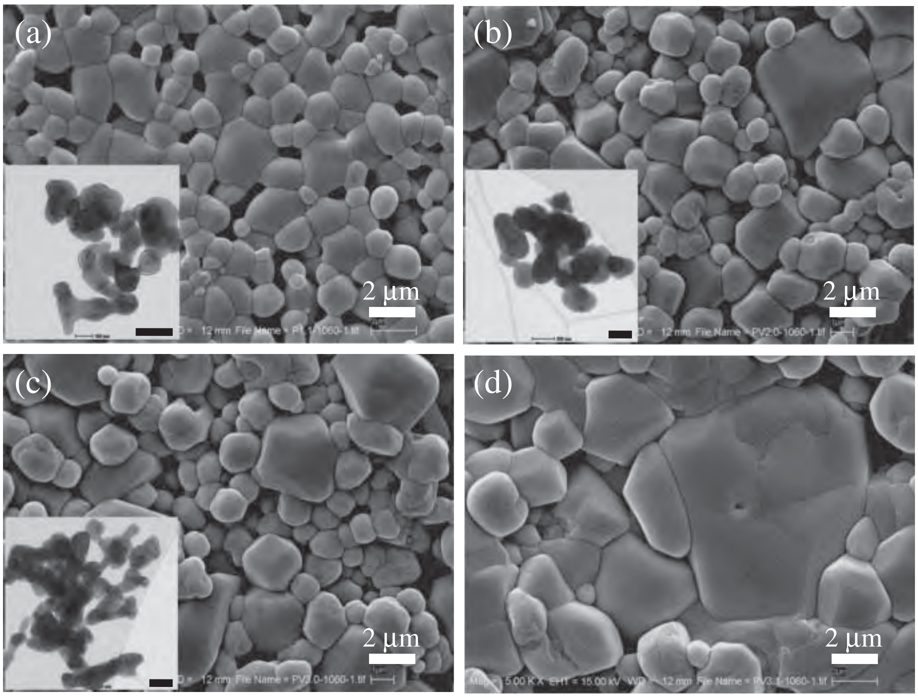

Fig. 2. SEM images of surface morphologies of (a) CCTO, (b) CCTVO-1, and (c, d) CCTVO-2 ceramic samples. Insets of figures (a–c) show their TEM images, revealing nanoparticles of the CCTO, CCTVO-1, and CCTVO-2 samples, respectively; each scale bar is 200 nm.

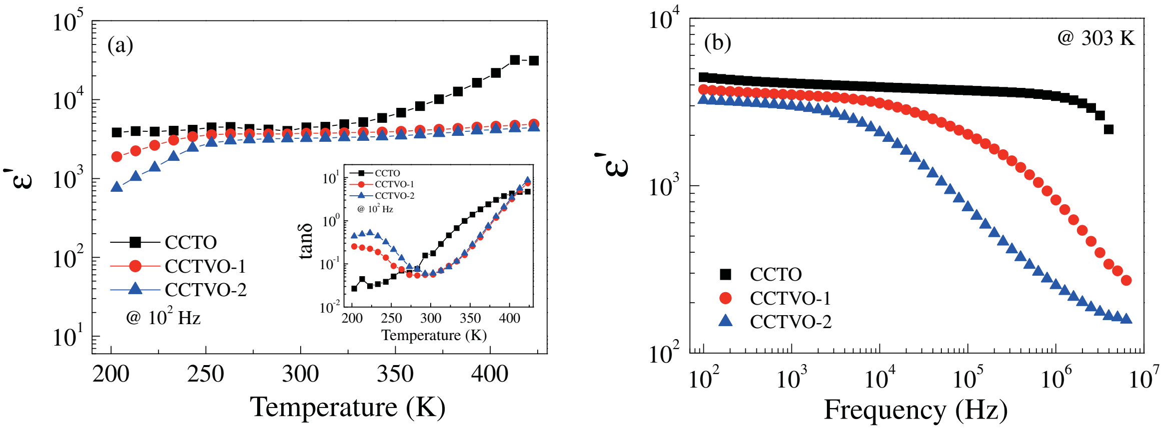

Fig. 3. (Color online) (a) ε' of CCTO and V-doped CCTO ceramic samples as a function of temperature; the inset shows the temperature dependence of $\tan\delta$ at a frequency of 10^2 Hz. (b) Frequency dependence of ε' at 303 K in CCTO and V-doped CCTO ceramic samples.

decrease with increasing V doping content. This result indicates that the CCTO ceramic sample sintered at 1333 K for 1 h has a low relative density. The insets of Figs. 2(a)–2(c) show the nanoparticles of the CCTO, CCTVO-1, and CCTVO-2 powders, respectively. The particle sizes of all samples are in the range of 100–200 nm.

Figure 3(a) shows the temperature dependence of ε' at 10^2 Hz for the CCTO and V-doped CCTO ceramics. Obviously, ε' in the temperature range of 203–423 K of CCTO ceramics decreases slightly with increasing V doping concentration. At high temperatures, ε' of the CCTO ceramic sample significantly increased compared with those observed in the CCTVO-1 and CCTVO-2 ceramic samples. The inset of Fig. 3(a) shows the temperature dependence of $\tan\delta$ at a frequency of 10^2 Hz. At a temperature of $\sim$300 K, $\tan\delta$ was decreased by substitution of V ions. However, at low temperatures below 270 K, $\tan\delta$ increased with increasing V concentration. The apparent $\tan\delta$ peaks in the CCTVO-1 and CCTVO-2 samples at a low temperature are attributed to the dielectric relaxation process related to the decrease in their ε' with increasing temperature. Figure 3(b) shows the frequency dependence of ε' at 303 K for the CCTO and V-doped CCTO ceramic samples. Obviously, substitution of V into CCTO ceramics has a remarkable influence on the dielectric relaxation behavior. The step like decrease in ε' of V-doped CCTO ceramics shifts to a low-frequency range as V concentration increased. It is important to note that the relationship between the dielectric response and microstructure of V-doped CCTO ceramics is very unique. This is because the dielectric response in CCTO ceramics is usually enhanced as grain size increased or vice versa.[9,15,19,22–24,37,41,42] Recently,

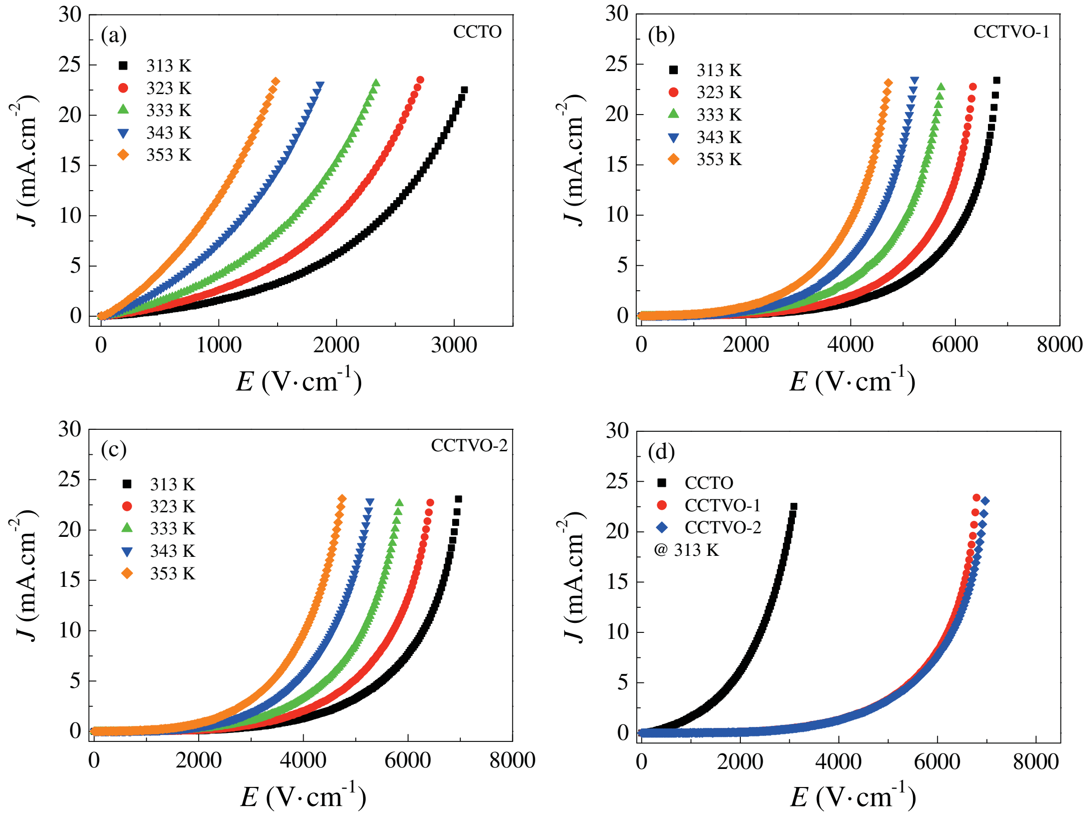

Fig. 4. (Color online) Temperature dependence of non-ohmic properties of (a) CCTO, (b) CCTVO-1, and (c) CCTVO-3 ceramic samples. (d) Non-ohmic characteristics (J vs E) of all samples at temperature of 313 K.

Schmidt et al.[48] have studied the effects of sintering temperature on the IBLC structure in CCTO ceramics. They found that the ε' of a CCTO ceramic is dependent on its C_{gb} and independent of mean grain size. Thus, the decrease in ε' observed in V-doped CCTO ceramics may be caused by the decrease in C_{gb}. Substitution of V ions to CCTO ceramics may have an effect on the electrical response of GBs. Investigation of electrical responses at GBs of CCTO ceramics is therefore important.

To study the physical nature of electrical transport at the GBs of CCTO ceramics, non-ohmic characteristics were investigated at various temperatures. The nonlinear J–E strength of the CCTO, CCTVO-1, and CCTVO-2 samples are shown in Figs. 4(a)–4(c), respectively. The J–E curves of all the samples show non-ohmic characteristics. It was observed that E_b decreases with increasing temperature, and non-ohmic J–E characteristic tends to become ohmic characteristic in nature as temperature increases. This behavior indicates the effect of temperature on the Schottky barrier.[38] It is likely that the electrical response of GBs in CCTO ceramics may be related to the existence of Schottky barriers at the GBs. Figure 4(d) shows the J–E curves of all samples at 313 K, showing the influence of V doping ions on the nonlinear electrical properties, indicating the effect of V on the intrinsic electrical properties of GBs. E_b of the CCTO ceramics was increased by substitution of V ions. The values of E_b were determined to be 781, 3731, and 3800 $\mathrm{V{\cdot}cm^{-1}}$ for the CCTO, CCTVO-1, and CCTVO-2 ceramic samples, respectively, and those values of α were 2.00, 4.41, and 4.42, respectively. These results are similar to those of the VO_2-added $CaCu_3Ti_4O_{12}/CaTiO_3$ composite ceramics.[36] This means that substitution of V can change the intrinsic electrical properties of CCTO ceramics.

To understand the electrical properties of GBs, the total resistance of GBs is estimated by impedance spectroscopy, which is a powerful tool in separating the grain and the GB effects.[29] In general, the resistances of grains (R_g) and GB (R_{gb}) of CCTO ceramics can be calculated from the diameters of two semicircular arcs of the Z^* plot that appeared in the high- and low-frequency ranges, respectively.[29,48] At higher than room temperature, only the large semicircular arc in the low-frequency range is generally observed over the measured frequency range. R_g can be estimated from a nonzero intercept on the Z' axis at high frequencies.[29] We found that the large semicircular arcs of all the samples cannot be observed at room temperature. Thus, Z^* plots for CCTO and V-doped CCTO ceramics must be replotted in a high-temperature range. As shown in Fig. 5, the large semicircular arcs of all the samples can be observed at a temperature of 393 K. Substitution of V can increase the total R_{gb} of CCTO ceramics. It is likely that R_{gb} of the CCTVO-2 sample is larger than that of the CCTVO-1 sample. This result is consistent with the slight increase in E_b of the CCTVO-2 sample compared with the CCTVO-1 sample, as shown in Fig. 4(d).

To deepen the understanding on the intrinsic electrical properties of GBs, the potential barrier height existing at GBs for all ceramic samples should be calculated. The electrical response of GBs in CCTO polycrystalline ceramics is closely related to the existence of Schottky barriers at the GBs.[5,37,38]

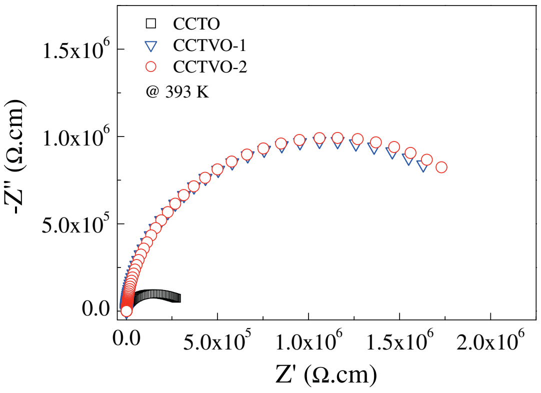

Fig. 5. (Color online) Impedance complex plane (Z^*) plots for CCTO and V-doped CCTO ceramics at temperature of 393 K.

Therefore, electrical conduction in the prebreakdown region is dominated by the Schottky emission. As a result, the relationship between J and E is as follows:[17,38,41,42]

$$J = AT^2 \exp\left(\frac{\beta E^{1/2} - \Phi_B}{k_B T}\right), \tag{2}$$

$$\ln J = \frac{\beta E^{1/2}}{k_B T} + \left[\ln(AT^2) - \frac{\Phi_B}{k_B T}\right], \tag{3}$$

where Φ_B is the height of electrostatic potential barrier at the GBs, E is the electric field, β is a constant related to the potential barrier width, and A is the Richardson constant. To calculate Φ_B, the last term on the right hand side of Eq. (3) is expressed as

$$\ln J_0 = \ln(AT^2) - \frac{\Phi_B}{k_B T}. \tag{4}$$

Equation (3) is therefore expressed as

$$\ln J = J_0 + \frac{\beta E^{1/2}}{k_B T}. \tag{5}$$

From Eq. (5), ln J_0 in the temperature range from 313 to 353 K of all samples can be calculated from the plots of ln J vs $E^{1/2}$ by the linear fitting of the slope. ln J_0 can be obtained at $E = 0$. Figures 6(a) and 6(b) show the fitted linear relationship between ln J and $E^{1/2}$. Using the relationship in Eq. (4), the Φ_B values of the CCTO and V-doped CCTO ceramics were calculated from the slopes of the plots of ln J_0 vs $1000/T$. As shown in Fig. 7, good linear fitting results are achieved and found to be 0.562, 0.551, and 0.437 eV for the CCTO, CCTVO-1, and CCTVO-2 ceramic samples, respectively. The overall electrical and dielectric properties of the V-doped CCTO ceramics are very similar to those observed in the La-doped CCTO ceramics.[42] The ε' and Φ_B of CCTO ceramics decreased with increasing doping concentration (i.e., La or V); whereas, E_b increased. For the TiO_2/CCTO composite system,[17] it was found that Φ_B is independent of the amount of TiO_2; on the other hand, R_{gb} increased slightly. The increase in R_{gb} of the TiO_2/CCTO ceramics was suggested to be caused by the increase in the thickness of GB. Note that Φ_B decreased after doping CCTO with V; whereas, the R_{gb} values of the CCTVO-1 and CCTVO-2 samples at 393 K are nearly the same. However, this behavior is difficult to describe well. The electrical resistance of GBs may not be dependent only on potential barrier height. Other factors may have an effect on electrical resistance such as segregations of impurities related to the liquid phase sintering process. However, the presence of a small amount of liquid films on the GBs is difficult to observe. This extrinsic factor may have an influence on the electrical properties of the CCTVO-1 and CCTVO-2 ceramic samples. According to previous works,[15,33,34,37,38,41,49] the relationship between the Schottky effect at GBs and dielectric properties can be well explained and easy to understand. However, in some cases as well as the results presented in this work,[35,36,42] this relationship is not easily established.

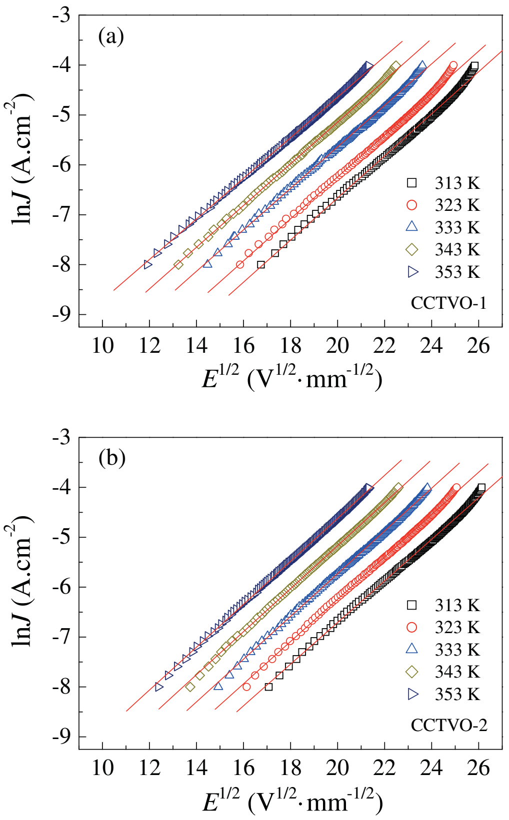

Fig. 6. (Color online) Plots of ln J vs $E^{1/2}$ for (a) CCTVO-1 and (b) CCTVO-2 ceramic samples.

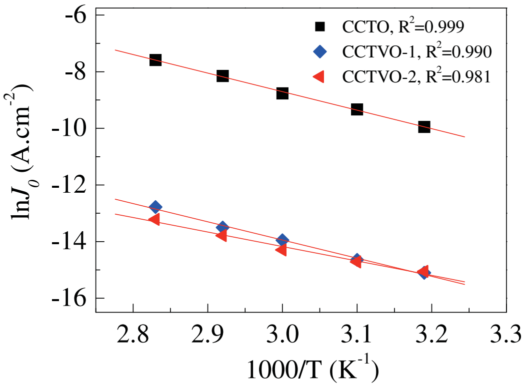

Fig. 7. (Color online) Plots of ln J_0 vs $1000/T$ for $CaCu_3Ti_{4-x}V_xO_{12}$ ceramic samples; the solid lines are fitted results obtained using Eq. (4).

4. Conclusions

In conclusion, we have successfully prepared nanocrystalline $CaCu_3Ti_{4-x}V_xO_{12}$ ($x = 0$, 0.025, and 0.05) powders with particle sizes of 100–200 nm. It was found that the grain size of CCTO ceramics increased slightly as V doping ion concentration increased. ε' decreased slightly as V concentration increased. Substitution of V can improve the non-ohmic properties of CCTO ceramics. By impedance spectroscopy analysis and investigation of non-ohmic properties at different temperatures, it was shown that R_{gb} and E_b were significantly increased by substitution of V ions, whereas, electrostatic potential barrier height at grain boundaries decreased slightly.

Acknowledgments

This work was financially supported by the Higher Education Research Promotion and National Research University Project of Thailand, Office of the Higher Education Commission, through the Advanced Functional Materials Cluster of Khon Kaen University and the Thailand Research Fund (TRF) under the TRF Senior Research Scholar Contract No. RTA5480004.

---

1) M. A. Subramanian, D. Li, N. Duan, B. A. Reisner, and A. W. Sleight: J. Solid State Chem. **151** (2000) 323.
2) C. Pecharromán, F. Esteban-Betegón, J. F. Bartolomé, S. López-Esteban, and J. S. Moya: Adv. Mater. **13** (2001) 1541.
3) C. C. Homes, T. Vogt, S. M. Shapiro, S. Wakimoto, and A. P. Ramirez: Science **293** (2001) 673.
4) J. Wu, C. W. Nan, Y. Lin, and Y. Deng: Phys. Rev. Lett. **89** (2002) 217601.
5) S. Y. Chung, I. D. Kim, and S. J. L. Kang: Nat. Mater. **3** (2004) 774.
6) Y. J. Yamashita and Y. Hosono: Jpn. J. Appl. Phys. **43** (2004) 6679.
7) X. Q. Liu, S. Y. Wu, X. M. Chen, and H. Y. Zhu: J. Appl. Phys. **104** (2008) 054114.
8) S. Tangwancharoen, P. Thongbai, T. Yamwong, and S. Maensiri: Mater. Chem. Phys. **115** (2009) 585.
9) P. Lunkenheimer, S. Krohns, S. Riegg, S. G. Ebbinghaus, A. Reller, and A. Loidl: Eur. Phys. J. Spec. Top. **180** (2009) 61.
10) Y. Wang, L. Ni, and X. M. Chen: J. Mater. Sci.: Mater. Electron. **22** (2011) 345.
11) B. W. Jia, X. Q. Liu, and X. M. Chen: J. Appl. Phys. **110** (2011) 064110.
12) T. Hoshina, T. Furuta, T. Yamazaki, H. Takeda, and T. Tsurumi: Jpn. J. Appl. Phys. **51** (2012) 09LC04.
13) S. Tsukada and Y. Akishige: Jpn. J. Appl. Phys. **51** (2012) 09LC01.
14) K. Mimura, K. Kato, H. Imai, S. Wada, H. Haneda, and M. Kuwabara: Jpn. J. Appl. Phys. **51** (2012) 09LC03.
15) L. Liu, H. Fan, P. Fang, and X. Chen: Mater. Res. Bull. **43** (2008) 1800.
16) S. Vangchangyia, E. Swatsitang, P. Thongbai, S. Pinitsoontorn, T. Yamwong, S. Maensiri, V. Amornkitbamrung, and P. Chindaprasirt: J. Am. Ceram. Soc. **95** (2012) 1497.
17) Y. H. Lin, J. Cai, M. Li, C. W. Nan, and J. He: J. Appl. Phys. **103** (2008) 074111.
18) R. Kashyap, O. P. Thakur, and R. P. Tandon: Ceram. Int. **38** (2012) 3029.
19) P. Thongbai, J. Jumpatam, T. Yamwong, and S. Maensiri: J. Eur. Ceram. Soc. **32** (2012) 2423.
20) L. Ni and X. M. Chen: Appl. Phys. Lett. **91** (2007) 122905.
21) S. Kwon, C. C. Huang, E. A. Patterson, D. P. Cann, E. F. Alberta, S. Kwon, and W. S. Hackenberger: Mater. Lett. **62** (2008) 633.
22) P. Thongbai, B. Putasaeng, T. Yamwong, and S. Maensiri: J. Mater. Sci.: Mater. Electron. **23** (2012) 795.
23) S. Kwon and D. P. Cann: J. Mater. Sci. **44** (2009) 4117.
24) P. Thongbai, B. Putasaeng, T. Yamwong, and S. Maensiri: Mater. Res. Bull. **47** (2012) 2257.
25) R. Kumar, M. Zulfequar, V. N. Singh, J. S. Tawale, and T. D. Senguttuvan: J. Alloys Compd. **541** (2012) 428.
26) C. C. Wang and L. W. Zhang: Appl. Phys. Lett. **90** (2007) 142905.
27) Y. Zhu, J. C. Zheng, L. Wu, A. I. Frenkel, J. Hanson, P. Northrup, and W. Ku: Phys. Rev. Lett. **99** (2007) 037602.
28) J. C. Zheng, A. I. Frenkel, L. Wu, J. Hanson, W. Ku, E. S. Bozin, S. J. L. Billinge, and Y. Zhu: Phys. Rev. B **81** (2010) 144203.
29) D. C. Sinclair, T. B. Adams, F. D. Morrison, and A. R. West: Appl. Phys. Lett. **80** (2002) 2153.
30) T. T. Fang and C. P. Liu: Chem. Mater. **17** (2005) 5167.
31) P. Lunkenheimer, R. Fichtl, S. G. Ebbinghaus, and A. Loidl: Phys. Rev. B **70** (2004) 172102.
32) M. Li, D. C. Sinclair, and A. R. West: J. Appl. Phys. **109** (2011) 084106.
33) P. Thongbai, T. Yamwong, and S. Maensiri: Mater. Res. Bull. **47** (2012) 432.
34) J. Jumpatam, P. Thongbai, B. Kongsook, T. Yamwong, and S. Maensiri: Mater. Lett. **76** (2012) 40.
35) M. A. Ramírez, P. R. Bueno, J. A. Varela, and E. Longo: Appl. Phys. Lett. **89** (2006) 212102.
36) L. Ramajo, R. Parra, J. A. Varela, M. M. Reboredo, M. A. Ramirex, and M. S. Castro: J. Alloys Compd. **497** (2010) 349.
37) T. B. Adams, D. C. Sinclair, and A. R. West: Phys. Rev. B **73** (2006) 094124.
38) A. A. Felix, M. O. Orlandi, and J. A. Varela: Solid State Commun. **151** (2011) 1377.
39) L. Ni and X. M. Chen: J. Am. Ceram. Soc. **93** (2010) 184.
40) M. Li, G. Cai, D. F. Zhang, W. Y. Wang, W. J. Wang, and X. L. Chen: J. Appl. Phys. **104** (2008) 074107.
41) J. Cai, Y. H. Lin, B. Cheng, C. W. Nan, J. He, Y. Wu, and X. Chen: Appl. Phys. Lett. **91** (2007) 252905.
42) B. Cheng, Y. H. Lin, J. Yuan, J. Cai, C. W. Nan, X. Xiao, and J. He: J. Appl. Phys. **106** (2009) 034111.
43) L. Zhang, Y. Wu, X. Guo, Z. Wang, and Y. Zou: J. Mater. Sci.: Mater. Electron. **23** (2012) 865.
44) A. K. Rai, N. K. Singh, S. K. Acharya, L. Singh, and K. D. Mandal: Mater. Sci. Eng. B **177** (2012) 1213.
45) D. Capsoni, M. Binia, V. Massarotti, G. Chiodelli, M. C. Mozzatic, and C. B. Azzoni: J. Solid State Chem. **177** (2004) 4494.
46) A. Sen, U. N. Maiti, R. Thapa, and K. K. Chattopadhyay: Appl. Phys. A **104** (2011) 1105.
47) J. K. Tsai and T. B. Wu: J. Appl. Phys. **76** (1994) 4817.
48) R. Schmidt, M. C. Stennett, N. C. Hyatt, J. Pokorny, J. Prado-Gonjal, M. Li, and D. C. Sinclair: J. Eur. Ceram. Soc. **32** (2012) 3313.
49) J. Jumpatam, B. Putasaeng, T. Yamwong, P. Thongbai, and S. Maensiri: Ceram. Int. **39** (2013) 1057.

Cement & Concrete Composites 41 (2013) 24–28

Contents lists available at SciVerse ScienceDirect

Cement & Concrete Composites

journal homepage: www.elsevier.com/locate/cemconcomp

Controlling ettringite formation in FBC fly ash geopolymer concrete

Prinya Chindaprasirt [a], Siwanant Thaiwitcharoen [b], Supranee Kaewpirom [b], Ubolluk Rattanasak [b,*]

[a] Sustainable Infrastructure Research and Development Center, Department of Civil Engineering, Faculty of Engineering, Khon Kaen University, Khon Kaen 40002, Thailand
[b] Department of Chemistry and Center of Excellence for Innovation in Chemistry, Faculty of Science, Burapha University, Chonburi 20131, Thailand

ARTICLE INFO

Article history:
Received 25 August 2011
Received in revised form 17 April 2013
Accepted 24 April 2013
Available online 3 May 2013

Keywords:
Geopolymer
Fluidized bed coal combustion
Ettringite formation
$Al(OH)_3$

ABSTRACT

Fluidized bed coal combstion (FBC) is extensively used in small self-generation power plants. The fly ash obtained from this FBC process contains high quantity of calcium and sulfate compounds which hinders its use in the construction industry. In addition, its reactivity is low and additional source material or additive is, therefore, needed to increase the reaction. This research studied the use of $Al(OH)_3$ and high concentrations of NaOH to control ettringite formation in the FBC fly ash geopolymer. Two replacement levels of 2.5 wt.% and 5.0 wt.% of $Al(OH)_3$ and three NaOH concentrations of 10, 12 and 15 M were used in the study. Results indicated that the NaOH concentration affected the ettringite formation and strength of the FBC geopolymer. No ettringite was formed at high NaOH concentration of 15 M which helped the dissolution of calcium sulfate and formed the additional calcium hydroxide. The subsequent pozzolanic reaction led to strength gain of the geopolymer. For 15 M NaOH, the addition of 2.5 wt.% $Al(OH)_3$ promoted the reaction and formed a dense matrix of alumino silicate compound. Relatively high 7-day compressive strength of 30 MPa was obtained.

1. Introduction

Fluidized bed combustion (FBC) is an efficient and environmentally-friendly technique for coal combustion process. This FBC technology is growing particularly in small enterprises due to the reduction of SO_2 and NO_x gasses released in flue gas [1]. Generally, the bed is operated at 800–900 °C, the low temperature prohibited the formation of nitrogen oxides (NOx) from the combustion air. The FBC system also permits the removal of sulfur dioxide (SO_2) from the combustion of high-sulfur fuels by the addition of sulfur absorbents such as limestone in the bed. A wide range of fuels including high-ash or high-moisture content fuels could be handled and efficiently burnt using the FBC process. The fly ash from fluidized bed combustion (FBC) contains high amount of $CaSO_4$ and CaO due to the use of lime for the SO_2 capture. These compounds hindered the use of FBC fly ash in construction since concrete with high $CaSO_4$ is prone to unsoundness [2]. Substantial amount of FBC fly ash is, therefore, disposed at landfill sites and thus needed to be utilized.

Ettringite formation, after the concrete had hardened, can promote concrete deterioration [3]. Ettringite is basically a hydrated sulfate of calcium and aluminum ($Ca_6Al_2(SO_4)_3(OH)_{12}{\cdot}26H_2O$) and exists in various forms, particularly as parallel needles of differing sizes in pores [4]. Ettringite is formed from the reaction between the anhydrite ($CaSO_4$) and residual dehydroxylated mineral (alumino-silicate) found in coal. This growth can lead to a deleterious effect on the mechanical properties of the material. For the FCB fly ash where sufficient $CaSO_4$ and alumino-silicate are present, its utilization as binder can lead to the formation of ettringite within the solidified matrix resulting in a significant structural problem. The needle-like crystals of ettringite growth exerts substantial internal stresses resulting in microcracking, swelling, and eventual failure [5]. However, in environments of high alkali hydroxide concentration, the formation of ettringite can be deterred [6].

Many researches indicate that the FBC-fly ash can be used as a source material for making geopolymer [7–9]. The geopolymer is an alumino-silicate compound prepared by incorporating high alkaline and sodium silicate solutions under low heat curing. This alumino-silicate cementitious compound possesses good mechanical properties viz., high compressive strength and stability at temperature up to 1400 °C [10].

Addition of alumina in geopolymer system resulted in increased aluminate ($Al(OH)_4^-$) species leading to a faster rate of condensation [11]. In the presence of sufficient quantity of calcium, calcium alumino-silicate hydrate (C–A–S–H) is formed [12,13]. FBC fly ash contains significant amount of calcium and sulfate, it is expected that addition of the alumina results in the formation of both C–A–S–H and ettringite. Formation of ettringite plays an important role in the FBC fly ash geopolymer system.

Since the calcium compounds ($CaSO_4$ and CaO) in FBC fly ash could result in the formation of ettringite in the geopolymer, this research attempted to control the formation of the ettringite by

---

[*] Corresponding author. Tel.: +66 38 103066; fax: +66 38 393494.
E-mail address: ubolluk@buu.ac.th (U. Rattanasak).

0958-9465/$ - see front matter © 2013 Elsevier Ltd. All rights reserved.
http://dx.doi.org/10.1016/j.cemconcomp.2013.04.009

preparing the FBC-fly ash geopolymer with various NaOH concentrations and addition of $Al(OH)_3$. $Al(OH)_3$ is commercially available and when dissolved it produces strong alkali solution forming aluminate ion, $Al(OH)_4^-$. This ion can react with silica to form additional alumino-silicate compound, and it reacts with calcium compounds present in FBC fly ash to form calcium aluminate hydrate (C–A–H). This would result in the geopolymer formation with strength gain and good physical properties.

2. Experimental procedure

2.1. Materials

FBC-fly ash obtained from a small power plant in Thailand was used as a source material for geopolymer synthesis. Typical chemical composition of this FBC fly ash determined by X-ray fluorescence (XRF) is shown in Table 1. The major compounds were lime (CaO), quartz (SiO_2), alumina (Al_2O_3) and anhydrite ($CaSO_4$). The FBC-fly ash contained high CaO content of 42.2% due to the addition of lime to extract sulfate oxides. This fly ash had the particle size (D_{50}) of 24 μm with a specific gravity of 2.34. The FBC-fly ash reactivity was low and the glassy phase content was also low owing to the low burning temperature of 900 °C. Aluminum hydroxide ($Al(OH)_3$) was also used as the additional source of aluminum compound for making geopolymer. Sodium hydroxide (NaOH) pellets were dissolved with distilled water to provide the NaOH solutions of 10, 12 and 15 M concentrations. The sodium silicate solution (Na_2SiO_3) with 9% Na_2O and 30% SiO_2 by weight was used as the external source of SiO_2. River sand with specific gravity of 2.65 and fineness modulus of 2.8 was employed to prepare the mortar for strength test in accordance with ASTM C109.

2.2. Geopolymer preparation

The effect of NaOH concentration on the ettringite formation was studied by varying the NaOH concentration. For preliminary study, 15 M NaOH was selected to prepare the $Al(OH)_3$-FBC fly ash blend geopolymer as it was reported that there was no ettringite formation [5]. 2.5 wt.% and 5.0 wt.% $Al(OH)_3$ were incorporated to make the FBC fly ash geopolymer [14]. The Na_2SiO_3-to-NaOH mass ratio of 2 was used for the study. The NaOH and Na_2SiO_3 were thoroughly mixed together and then added to the powdery raw material. Owing to the high water absorption of the sample, the high powder-to-liquid mass ratio of 1.5 was used. The mix proportion is tabulated in Table 2. The mixture was continuously mixed in a pan mixer for 2 min before casting in 5-cm cubic acrylic mold and vibrated for 10 s to remove the air bubbles. The specimens were then covered with clingfilm and cured at 60 °C for 24 h.

For the geopolymer mortar strength test, sand was added to the paste mixture with the sand to powder ratio of 2:1 (by weight) and mixed for another 2 min. Casting and curing condition were similar to the paste preparation. Compressive strength test was performed at the ages of 7, 30 and 90 days. The results were reported as the average of three samples.

Table 1
Chemical composition and LOI of FBC fly ash.

Chemical composition	(wt.%)
SiO_2	21.0
Al_2O_3	8.1
Fe_2O_3	6.9
CaO	42.2
SiO_3	14.8
Other oxides	6.0
Loss on ignition (LOI)	1.0

2.3. Geopolymer testing

The geopolymer pastes were prepared for the XRD, TGA and SEM analyses. In addition, the degree of reaction was determined both on geopolymer and starting materials. This method was based on the dissolution of the powdery sample in 2 M HCl and 3 wt.% Na_2CO_3 [14–16]. 2 M HCl was used to dissolve CaO and MgO from the hydrated product, and 3 wt.% Na_2CO_3 was then employed to dissolve SiO_2, Al_2O_3, and Fe_2O_3. The remaining portion was the unreacted fly ash residue. The degree of reaction was calculated from the following equation:

$$\text{Degree of reaction} = \frac{m_{\text{sample}} - m_{\text{residue}}}{m_{\text{sample}}} \times 100 \tag{1}$$

where m_{sample} is the weight of powdery sample (g); m_{residue} the weight of dried residue (g).

The degree of reaction of the "blank" (raw materials before mixing with alkali solutions) was also determined. The degree of reaction of blank was then subtracted from those of geopolymers to obtain the corrected degree of reaction. The results were reported as an average of three samples.

3. Results and discussion

3.1. Morphological study of geopolymer pastes

The effect of NaOH concentration on ettringite formation was presented in XRD pattern as shown in Fig. 1. The XRD of FBC fly ash showed numerous sharp peaks of crystalline phases. Calcium and silica were the main compounds detected in the ash. Low reactive FBC fly ash could be converted to a more amorphous material by the geopolymerization process. The broad peaks and peak shift were found with the geopolymer pastes at 24–38° 2θ, indicating that the geopolymerization reaction resulted in the highly disorder material in the form of amorphous gel with some crystalline products [7,8]. This corresponded to the detection of aluminosilicate in the geopolymer matrix. New compounds of ettringite, calcium-silicate, and calcium-alumino-silicate were also formed. Ettringite was found quite readily in the sample with NaOH concentration of 10 M at 41° and 43° 2θ. Less ettringite was formed for the concentration of 12 M NaOH with the presence of peak at only 43° 2θ. For the highest concentration of 15 M NaOH, ettringite could not be detected and the peaks at 41° and 43° 2θ disappeared. It was previously reported that difficulty of ettringite formation was found in the presence of high alkali hydroxide concentration [6]. The high NaOH concentration could reduce the amount of gypsum in the FBC fly ash system resulting in the gypsum dissolution via the double decomposition reaction as shown in Eq. (2)[17].

$$CaSO_4 \cdot 2H_2O(s) + NaOH(aq) \rightarrow 4Ca(OH)_2(s) + Na_2SO_4(aq) \tag{2}$$

Sodium hydroxide, thus, promoted gypsum dissolution and the formation of calcium hydroxide. As gypsum dissolved in the NaOH solution, the concentration of both calcium and sulfate ions increased leading to the precipitation of calcium hydroxide ($Ksp = 7.9 \times 10^{-6}$). Therefore the amount of calcium hydroxide formed could limit the ettringite formations and thus allowing the formation of other phases [17].

From the result, 15 M NaOH was selected as the alkali solution to prepare the $Al(OH)_3$-FBC fly ash blend geopolymer. $Al(OH)_3$ was then incorporated to the FBC fly ash geopolymer. Two dosages of 2.5% and 5.0% of $Al(OH)_3$ by weight were blended with FBC fly ash and used as the source materials for making geopolymer. The results of XRD pattern of blend geopolymer pastes are shown in Fig. 1. The incorporation of $Al(OH)_3$ resulted in the formation of the alumino-silicate compound at 34° 2θ. At high $Al(OH)_3$ content

Table 2
Mix proportion of geopolymers (g).

Sample	% $Al(OH)_3$	Fly ash	$Al(OH)_3$	Na_2SiO_3	NaOH	NaOH concentration (M)
100FBC	0	40	–	40	20	10/12/15
2.5Al	2.5	39	1	40	20	15
5Al	5	38	2	40	20	15

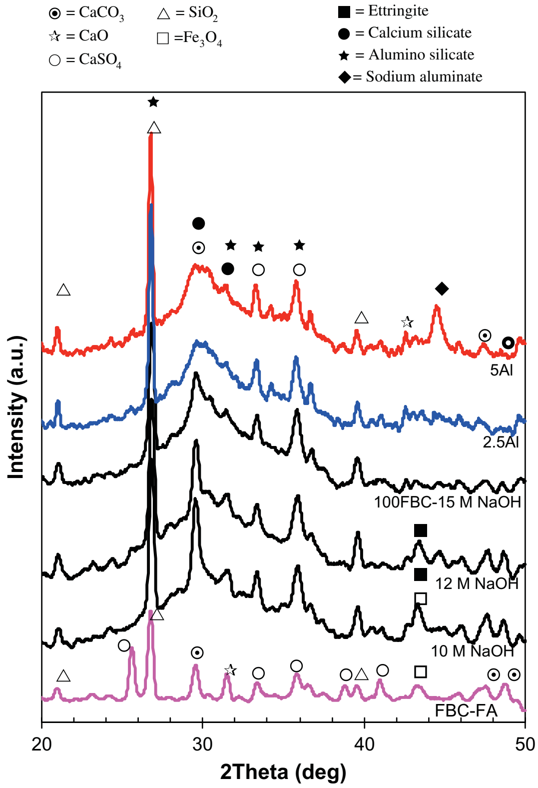

Fig. 1. XRD pattern of as-received FBC, FBC geopolymers and blend geopolymers prepared with 15 M NaOH.

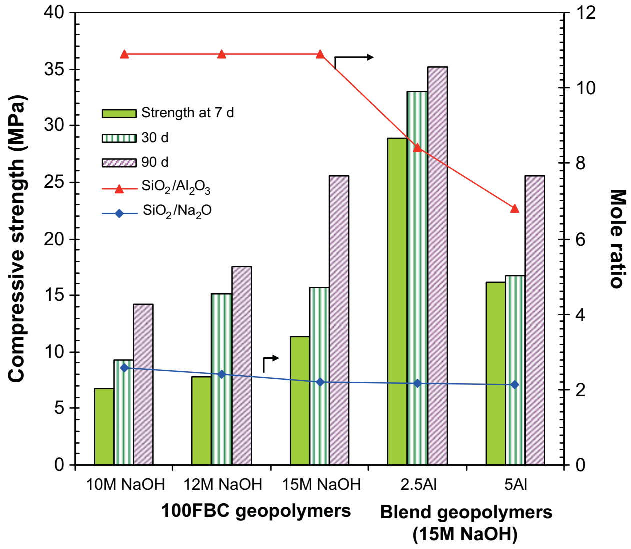

Fig. 2. Compressive strength of geopolymers.

of 5 wt.%, sodium-aluminate compound was detected in the composite with a prominent peak at 44.5° 2θ. With high alkaline concentration, this compound could subsequently convert to zeolite as an intermediate phase and could weaken the geopolymer.

3.2. Compressive strength of geopolymer mortars

The results of compressive strength of FBC fly ash geopolymer mortar are presented in Fig. 2. The 7-day strengths of FBC fly ash geopolymers were low at 7, 8 and 12 MPa for the mixes with 10, 12 and 15 M NaOH, respectively. This was due to the low reactive amorphous phase and high crystallinity of the as-received starting material. The compressive strength increased with the curing age owing to the high calcium content of FBC fly ash and the formation of calcium silicate hydrate (C–S–H) in the composite. In addition to alumino silicate compound, C–S–H was another significant factor enhancing the strength of FBC fly ash geopolymer. The leaching of minerals such as silicon and aluminum ions occurred when fly ash came into contact with NaOH and sodium silicate solutions [16] leading to the formation of calcium silicate and alumino-silicate gels. The calcium silicate hydrate (C–S–H) co-existed with the geopolymer products [18,19] and helped to develop the strength of geopolymer as a function of time. The increase in the NaOH concentration led to the higher strength gain since high NaOH concentration could better leach out the Si^{4+} and Al^{3+} ions resulting in the better formation of geopolymer gel [20]. The highest concentration of 15 M NaOH resulted with the geopolymer having a 90-day compressive strength of 26.0 MPa. In addition, the change in the NaOH concentration affected the SiO_2/Na_2O ratio. The increase in the NaOH concentration resulted in low SiO_2/Na_2O ratio and led to the formation of solid sodium silicate compound which was a weak compound and contributed to a relatively low strength matrix [14].

Compressive strengths of $Al(OH)_3$-FBC blend geopolymer prepared with 15 M NaOH are also presented in Fig. 2. Addition of 2.5 wt.% of $Al(OH)_3$ enhanced the strength of the geopolymer owing to the increase in the alumina which led to the reduction of the SiO_2/Al_2O_3 mole ratio. The higher Si/Al ratio gave geopolymer with a relatively low strength [21]. For the incorporation of 2.5 wt.% of $Al(OH)_3$, the strength of geopolymer at 90 days was thus increased to 36 MPa. The aluminum ion from $Al(OH)_3$ reacted with silicon ion to form the additional alumino-silicate gel. However, the incorporation of the high amount $Al(OH)_3$ of 5 wt.% resulted in the reduction of the strength of the geopolymer and the strengths were similar to the geopolymer without $Al(OH)_3$. The excess aluminum ion reacted with NaOH solution and formed the sodium aluminate compound as detected in the XRD pattern and it seems that this lowered the geopolymer strength.

3.3. Microstructural study

The results of microstructure study of FBC fly ash and geopolymers are shown in Fig. 3. The composite consisted of the unreacted fly ash particles, geopolymer matrix and other compounds. The needle-like ettringite was found in FBC fly ash geopolymer prepared with 12 M NaOH and less (Fig. 3a) and was in accordance with the XRD result. Ettringite was observed in crack and void of the geopolymer matrix. It could be converted to calcium aluminate monosulfate in the presence of moisture and high content of

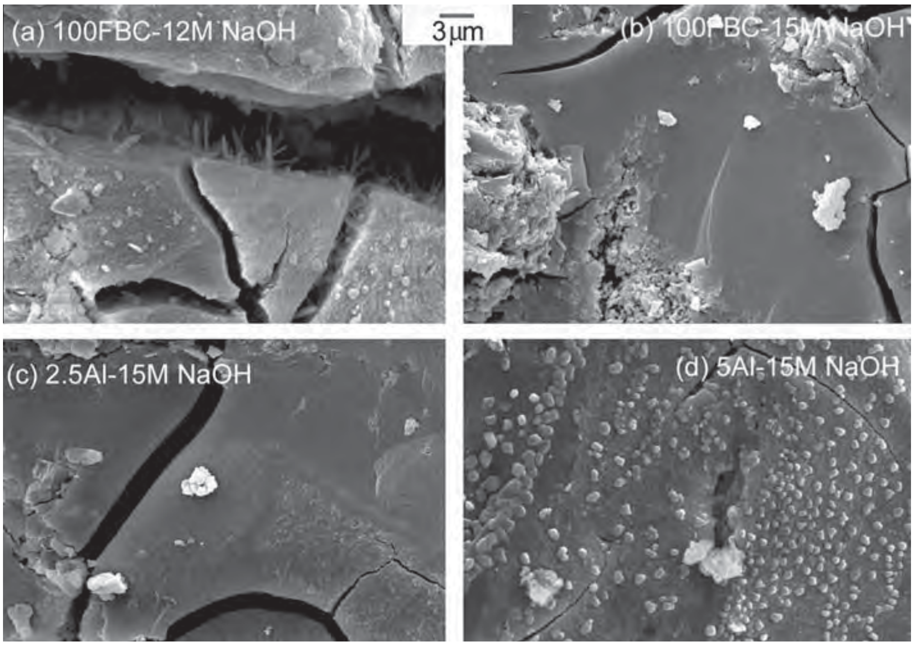

Fig. 3. SEM micrographs of geopolymer pastes at the age of 90 days.

calcium sulfate in the matrix. For the FBC fly ash geopolymer prepared with 15 M NaOH, no ettringite formation was observed (Fig. 3b). As mentioned, the high NaOH concentration helped the dissolution of calcium sulfate and formed calcium hydroxide. The pozzolanic reaction could subsequently carry out through the reaction between this calcium hydroxide and silica and alumina from the FBC fly ash particles resulting in more C–S–H in the matrix. With 2.5% $Al(OH)_3$, the prepared sample with 15 M NaOH also showed the dense and homogeneous matrix with no sign of ettringite formed in the cracks and voids (Fig. 3c). For the incorporation of 5 wt.% of $Al(OH)_3$ with 15 M NaOH, the matrix consisted of sodium silicate (Fig. 3d) and excess gibbsite ($Al(OH)_3$) with a small amount of cross linked geopolymer leading to a lower strength matrix [14]. Sodium aluminate zeolite could be found as indicated by the XRD peak at 44.5° 2θ.

3.4. Degree of reaction

Fig. 4 shows the degree of reaction of blend geopolymer pastes prepared with 15 M NaOH. The test was based on the dissolution of product, the remaining unreacted fly ash was determined. The FBC fly ash geopolymer has the degree of reaction of 21.9%. With $Al(OH)_3$ content of 2.5%, more products were formed in the composite leading to less unreacted material remaining in the sample. For the high dosage of 5% of $Al(OH)_3$, excess $Al(OH)_3$ was available and was difficult to be dissolved in chemical reagents. The degrees of reaction were 24.3% and 23.7% respectively for the samples with 2.5% and 5.0% $Al(OH)_3$. The high degree of reaction of the geopolymer with 2.5% $Al(OH)_3$ agreed with the results of strength in Fig. 4. The optimum $Al(OH)_3$ content was, therefore, 2.5% by weight of the powder and this mix gave a dense matrix with high degree of reaction and high strength.

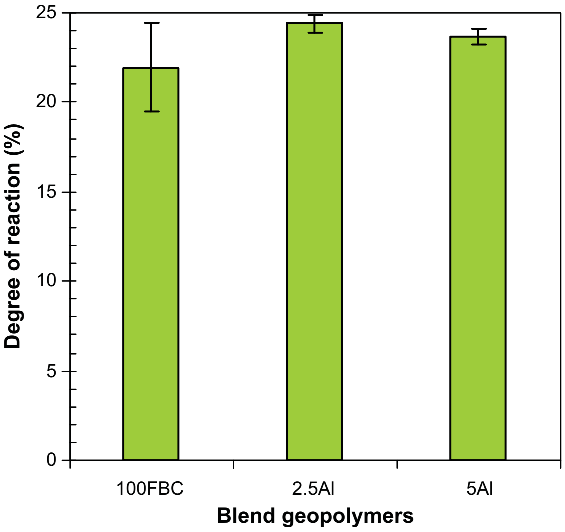

Fig. 4. Degree of reaction of geopolymer pastes at 90 days.

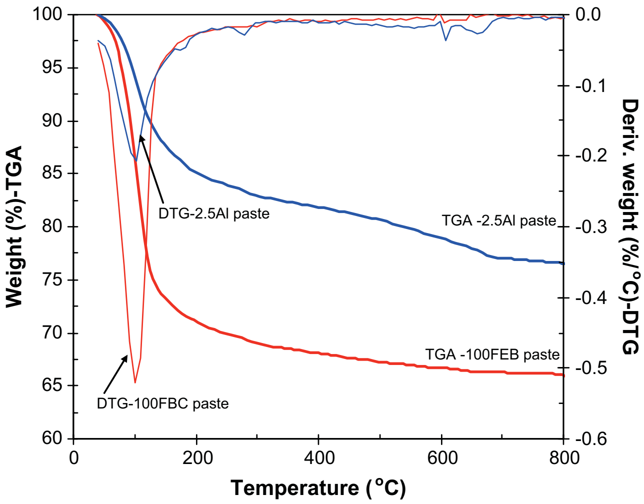

Fig. 5. TGA/DTG curves of geopolymer pastes at 90 days.

3.5. Thermal stability of geopolymers

Thermal stability of geopolymer pastes was measured by thermogravimetric analysis (TGA) and differential thermogravimetry (DTG), results are shown in Fig. 5. TGA/DTG monitored the weight change during heating of specimen. FBC geopolymer showed higher weight loss than the 2.5Al blend geopolymer. This was due to the reaction between free lime in FBC fly ash and $Al(OH)_3$ in base condition forming the more binding materials (i.e. aluminosilicate and calcium aluminate compounds) in matrix. Weight loss was found at 100 °C owing to the evaporation of water. Two peaks at 300 and 580 °C, respectively, presented the starting and finishing dehydroxylation of $Al(OH)_3$. Less decomposition of $Ca(OH)_2$ at 400 °C indicated that calcium compound reacted with aluminate ion and resulted in more complex compounds, i.e. calcium aluminate and alumino silicate compounds.

4. Conclusions

Based on the results of this study, the following conclusions could be drawn.

The concentration of NaOH affected the ettringite formation in FBC fly ash geopolymer. For NaOH concentration of 10 M and 12 M NaOH, the ettringite was detected in cracks and voids of the geopolymer matrix. With NaOH concentration of 15 M, the dissolution of calcium sulfate was facilitated resulting in the formation of calcium hydroxide. This resulted in the pozzolanic reaction and led to strength gain of the geopolymer. The incorporation of 2.5 wt.% of $Al(OH)_3$ in FBC fly ash geopolymer promoted the reaction and provided dense and homogeneous matrix with the formation of additional alumino-silicate compound. However, the high dosage of 5 wt.% of $Al(OH)_3$ resulted in excess $Al(OH)_3$ and formed sodium aluminate which weakened the geopolymer. FBC fly ash utilization in geopolymer offers a new effective method to recycle FBC fly ash and an alternative cementitious material for non-structural member which does not require high strength products such as pavement, block and wall panel.

Acknowledgements

This work was supported by the Higher Education Research Promotion and National Research University Project of Thailand, Office of the Higher Education Commission, through the Advanced Functional Materials Cluster of Khon Kaen University and the Thailand Research Fund (TRF) under TRF Senior Research Scholar Contract No. RTA5480004. Appreciation is also extended to the Center of Excellence for Innovation in Chemistry (PERCH-CIC), Office of the Higher Education Commission, Ministry of Education.

References

[1] Basu P. Combustion of coal in circulating fluidized-bed boilers: a review. Chem Eng Sci 1999;54(22):5547–57.

[2] Glinicki MA, Zieliński M. The effluence of CFBC-fly ash addition on the phase composition of air-entrained concrete. B Pol Acad Sci 2008;56(1):45–52.

[3] Havlica J, Brandstetr J, Odler I. Possibilities of utilizing solid residues from pressured fluidized bed coal combustion (PSBC) for the production of blended cements. Cem Concr Res 1998;28(2):299–307.

[4] Stark J, Bollman K. Delayed ettringite formation in concrete. In: Proc. Nordic Concrete Research Meeting. Reykjavik, Iceland; 1999. p. 4–28.

[5] Sheetz BE, Kwan SPIs. Control of ettringite swelling. Ashlines 2003;4(1):1–10.

[6] Brown PW, Bothe JV. The stability of ettringite. Adv Cem Res 1993;5(18):47–63.

[7] Chindaprasirt P, Rattanasak U, Jaturapitakkul C. Utilization of fly ash blends from pulverized coal and fluidized bed combustions in geopolymeric materials. Cem Concr Compos 2011;33(1):55–60.

[8] Chindaprasirt P, Rattanasak U. Utilization of blended fluidized bed combustion (FBC) ash and pulverized coal combustion (PCC) fly ash in geopolymer. Waste Manage 2010;30(4):667–72.

[9] Xu H, Li H, Shen L, Zhang M, Zhai J. Low-reactive circulating fluidized bed combustion (CFBC) fly ashes as source material for geopolymer synthesis. Waste Manage 2010;30(1):57–62.

[10] Hussain M, Varley RJ, Cheng YB, Mathys Z, Simon GP. Synthesis and thermal behavior of inorganic–organic hybrid geopolymer composites. J Appl Polym Sci 2005;96(1):112–21.

[11] Steveson M, Sagoe-Crentsil K. Relationships between composition, structure and strength of inorganic polymers. J Mater Sci 2005;40(8):2023–36.

[12] Garcia-Lodeiro I, Palomo A, Fernández-Jiménez A, MacPhee DE. Compatibility studies between N–A–S–H and C–A–S–H gels: Study in the ternary diagram $Na_2O–CaO–Al_2O_3–SiO_2–H_2O$. Cem Concr Res 2011;41(9):923–31.

[13] Hong SY, Glasser FB. Alkali sorption by C–S–H and C–A–S–H gels: Part II. Role of alumina. Cem Concr Res 2002;32(7):1101–11.

[14] Rattanasak U, Chindaprasirt P, Suwanvitaya P. Development of high volume rice husk ash alumino silicate composites. Int J Miner Metall Mater 2010;17(3):654–9.

[15] Termkhajornkit P, Nawa T, Nakai M, Saito T. Effect of fly ash on autogenous shrinkage. Cem Concr Res 2005;35(3):473–82.

[16] Chindaprasirt P, Jaturapitakkul C, Chalee W, Rattanasak U. Comparative study on the characteristics of fly ash and bottom ash geopolymers. Waste Manage 2009;29(2):539–43.

[17] Clark BA, Brown PW. Formation of ettringite from monosubstituted calcium sulfoaluminate hydrate and gypsum. J Am Ceram Soc 1999;82(10):2900–5.

[18] Xiaolu G, Huisheng S, Warren AD. Compressive strength and microstructural characteristics of class C fly ash geopolymer. Cem Concr Compos 2010;32(2):142–7.

[19] Somna K, Jaturapitakkul C, Kajitvichyanukul P, Chindaprasirt P. NaOH-activated ground fly ash geopolymer cured at ambient temperature. Fuel 2011;90(1–2):2118–24.

[20] Rattanasak U, Chindaprasirt P. Influence of NaOH solution on the synthesis of fly ash geopolymer. Miner Eng 2009;22(12):1073–8.

[21] Fletcher RA, Mackenzie KJD, Nicholson CL, Shimada S. The composition range of aluminosilicate geopolymers. J Eur Ceram Soc 2005;25(9):1471–7.

Construction and Building Materials 47 (2013) 896–901

Contents lists available at SciVerse ScienceDirect

Construction and Building Materials

journal homepage: www.elsevier.com/locate/conbuildmat

Pressed lightweight concrete containing calcined diatomite aggregate

Patcharapol Posi [a], Surasit Lertnimoolchai [b], Vanchai Sata [a], Prinya Chindaprasirt [a,*]

[a] *Sustainable Infrastructure Research and Development Center, Department of Civil Engineering, Faculty of Engineering, Khon Kaen University, Khon Kaen 40002, Thailand*
[b] *Concrete Precision Unit, Udornthani 41000, Thailand*

HIGHLIGHTS

- Coarse diatomite aggregate calcined at 1000 °C contributed to high strength.
- Fine diatomite aggregate calcined at 600 °C also gave high strength.
- Pressed lightweight concrete gave 28-day compressive strengths of 7–12 MPa.
- Concretes with unit weight of 1000–1200 kg/m^3 were obtained.

ARTICLE INFO

Article history:
Received 24 January 2013
Received in revised form 3 May 2013
Accepted 5 May 2013

Keywords:
Pressed lightweight concrete
Lightweight aggregate
Diatomite
Compressive strength
Density

ABSTRACT

Diatomite in its natural form possesses low reactivity and is a weak material. Calcination rids of the burnable elements and enhances the properties of diatomite. This research studies the properties of pressed lightweight concrete containing calcined diatomite aggregate. The diatomite was crushed and classified as fine, medium and coarse aggregates and then calcined at 400–1000 °C for 4 h. The pressed lightweight concretes with 28-day compressive strength of 7.8–12.9 MPa, density of 1000–1200 kg/m^3, porosity of 58–61%, water absorption of 61–72% and thermal conductivity of 0.15–0.19 W/mK were obtained. The light weight and high strength blocks were obtained with the use coarse diatomite aggregate obtained from high calcined temperature of 1000 °C and the use of fine diatomite aggregate obtained from calcination temperature of 600 °C. At the high temperature of 1000 °C, the coarse aggregate was stable and strong and this contributed to the strength of the pressed lightweight concrete. At the calcination temperature of 600 °C, the fine diatiomite aggregate was reactive. Calcined diatomite is a suitable lightweight aggregate for making pressed lightweight concrete blocks.

1. Introduction

Lightweight concrete is concrete with density less than normal concrete and not exceeds 1840 kg/m^3 [1].The production of lightweight aggregate concrete has been expanding. It includes no-fines concrete of low density of 400–1200 kg/m^3 for block production and of 1000–1840 kg/m^3 for structural concrete. The types of lightweight concrete are related to the availability of lightweight aggregate [2]. By the methods of production, lightweight concretes are classified into three types (a) lightweight concrete with porous lightweight aggregate of low apparent specific gravity (b) lightweight concrete with large voids within the concrete or mortar mass (c) lightweight concrete with no fine aggregate [3].The use of lightweight concrete blocks and structure lightweight concrete in construction can reduce the cost of construction as lightweight concrete reduce the dead load, cross sectional area, and amount of reinforcement of concrete structure.

Lightweight aggregate concrete (LWAC) has been the subject of investigations for many years [4,5]. They are mostly used for masonry wall as well as structural concrete because of the high strength to weight ratio, low coefficient of thermal conductivity and good sound insulation characteristic due to air voids in the lightweight aggregate [6]. Lightweight aggregate (LWA) are from either natural source such as perlite, diatomite, and pumice or from manufacturing such as expanded clay, expanded shale and sintered fly ash.

Diatoms were unicellular algae and probably the most widespread group of plants on the earth. There are more than twenty-five thousand species of diatoms with no two having the same morphology [7]. When the diatoms died, the tiny shells sunk, and over the centuries and formed thick layers. Eventually these deposits were fossilized and compressed into a soft, chalky rock that is now called diatomaceous earth [8]. Diatomaceous earth or diatomite is light in weight due to its cellular structure and high porosity [9] and possesses low thermal conductivity, but it is a rather soft material with low reactivity [10]. The uncalcined lightweight diatomite aggregate was used in making light weight

---

[*] Corresponding author.
E-mail address: prinya@kku.ac.th (P. Chindaprasirt).

0950-0618/$ - see front matter © 2013 Elsevier Ltd. All rights reserved.
http://dx.doi.org/10.1016/j.conbuildmat.2013.05.094

concrete with reasonable strength of 2.5–8 MPa with unit weight of 900–1190 kg/m^3 [11]. Calcination of fine diatomite at 700 °C results in dehydroxylation of clay minerals and enhances its pozzolanic reactivity [9]. Thus, this research explores the use of diatomite in making lightweight aggregate by improving its properties with calcination at different temperatures. The effect of aggregate gradations on the properties of lightweight concrete was also studied. The pressed lightweight concrete blocks containing calcined diatomite should be suitable for use in masonry wall. In addition, the knowledge obtained should also be useful for the future study for its use in structural lightweight concrete as specified in ACI 213 [11].

2. Experimental program

2.1. Materials

Materials used in this research consisted of Type I Ordinary Portland Cement (OPC) and diatomite (DE) from Lampang province in the north of Thailand. Diatomite was crushed and calcined at 400, 600, 800, and 1000 °C for 4 h [9] and then classified as fine aggregate (FA), medium aggregate (MA) and coarse aggregate (CA) with particle sizes ranging between 0.001–1.18, 1.18–4.75, 4.75–12.5 mm, respectively as shown in Fig. 1. Chemical composition and mineralogical composition of as-received DE were determined using X-ray fluorescence (XRF) and X-ray diffraction (XRD), respectively. The differential thermal analysis (DTA) and thermal gravitation analysis (TGA) were performed on DE to investigate its physical and chemical changes during heating. The physical properties of materials are shown in Table 1 and the chemical compositions of DE are shown in Table 2. The increase in fineness modulus resulted in increase in the water absorption and decrease in bulk density of DE. The water absorption of FA, MA, and CA were 61%, 102%, and 112% and bulk densities were 600, 425, and 417 kg/m^3, respectively. The sum of SiO_2, Al_2O_3, and Fe_2O_3 of diatomite aggregate increased with the increase in calcined temperature. This was due to the reduction in the loss on ignition (LOI) of DE with the increase in calcined temperature. The loss on ignition (LOI) of uncalcined DE (UC) was 9.1% which was below 10.0% as described in ASTM C 618 [12] for class N pozzolan. The LOIs of DE calcined at 400, 600, 800, and 1000 °C reduced to 7.0%, 4.5%, 1.0% and 0.60%, respectively. The reduction in the burnable elements improved the chemical composition of DE.

2.2. Mix proportion

2.2.1. Effect of calcined temperature

The FA, MA were calcined at 600 °C to obtain the pozzolanic property of DE [13] and CA was calcined at 400, 600, 800, and 1000 °C (CA400, CA600, CA800, and CA1000) to study the effect of the calcined temperatures on the coarse aggregate.

Fig. 1. Coarse, medium and fine DE aggregates.

Table 1
Physical properties of materials.

Materials	OPC	FA	MA	CA
Specific gravity	3.16	1.85	2.27	2.45
Median particle size (μm)	14.6	–	–	–
Particle size (mm)	–	0.001–1.18	1.18–4.75	4.75–12.5
Fineness modulus	–	1.33	4.02	5.75
Density (kg/m^3)	1440	600	425	417
Water absorption (%)	–	61	102	112

Table 2
Chemical composition of DE (by weight).

Chemical compositions (%)	Calcined temperature				
	Uncalcined	400 °C	600 °C	800 °C	1000 °C
SiO_2	74.30	76.09	78.40	78.29	79.86
Al_2O_3	8.07	7.98	8.18	9.43	9.01
Fe_2O_3	5.35	5.46	5.19	7.08	6.29
CaO	0.48	0.43	0.47	0.54	0.51
K_2O	1.76	1.89	1.99	2.21	2.28
TiO_2	0.11	0.43	0.51	0.51	0.56
Na_2O	0.15	0.13	0.12	0.17	0.16
P_2O_5	0.11	0.08	0.09	0.11	0.10
BaO	0.04	0.04	0.04	0.04	0.04
MgO	0.47	0.43	0.47	0.56	0.47
LOI	9.10	7.00	4.50	1.00	0.60

2.2.2. Effect of aggregate gradation

To study the effect of aggregate gradation, the FA and MA portions were varied and the CA portion was kept constant at 30%. The effect of the change in the small aggregate portion is larger than that of the large portion [14]. A total of three aggregate gradations with FA:MA:CA ratios of 0:70:30, 30:40:30, and 70:0:30 (0FA, 30FA, and 70FA) were used.

2.3. Details of mixing

All mixtures were made with water to cement ratio (W/C) of 2.0 by mass and diatomite to cement ratio (D/C) of 1.8 by mass. OPC and DE were firstly mixed until the mixture was homogenous which took approximately 1½ min. Afterward, water was added and the mixing was done for another 1½ min. The 50 × 50 × 50 mm cubes were made with a pressed machine with the pressure of 0.85 MPa. The pressing technique with small pressure was adopted as it simulated the manufacturing of concrete blocks without the need to use a large number of molds which requires assembling and cleaning of molds as well as demolding. The specimens were then covered with damp cloth and plastic sheet to prevent moisture loss in a controlled 25 °C room. At the age of 28 days, they were tested for density, compressive strength, water absorption and thermal conductivity. Samples of pressed lightweight concrete for testing are shown in Fig. 2.

2.4. Details of test

2.4.1. Density and compressive strength

The density was determined as described in ASTM C 138 [15]. The density was measured at the ages of 28 days using the compressive strength specimens. After the density determination, the cube specimens were tested to determine the compressive strength in accordance with ASTM C109 [16]. The reported compressive strengths were the average of three samples.

2.4.2. Porosity and water absorption

The cube specimens were tested for porosity and water absorption at the age of 28 days in accordance with ASTM C 642 [17]. The porosity was calculated using Eq. (1) and Eq. (2) was used for the calculation of water absorption.

$$\text{Porosity } (\%) = [(C - A)/(C - D)] * 100 \tag{1}$$

$$\text{Absorption } (\%) = [(B - A)/A] * 100 \tag{2}$$

where A = mass of oven – dry sample in air (g); B = mass of surface – dry sample in air after immersion (g), C = mass of surface – dry sample in air after immersion and boiling (g), and D = apparent mass of sample in water after immersion and boiling (g)

2.4.3. Thermal conductivity

The cube specimens were tested to determine the thermal conductivity at the age of 28 days in accordance with ASTM D 5930 [18].

3. Results and discussion

3.1. Scanning electron microscopy

The results of SEM of DE are shown in Fig. 3. The DE consisted of cylindrical shape particles approximately 10 μm in diameter and 30 μm in length with square cellular structure. The surface consisting of micro-pores made DE very porous and low in density [9,19].

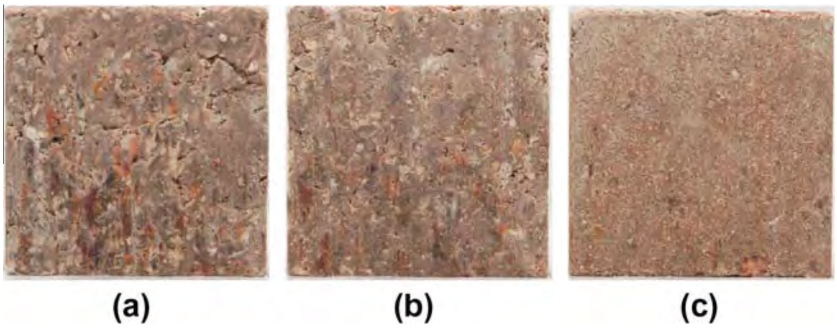

Fig. 2. Pressed lightweight concretes (a) 0FA, (b) 30FA, and (c) 70FA.

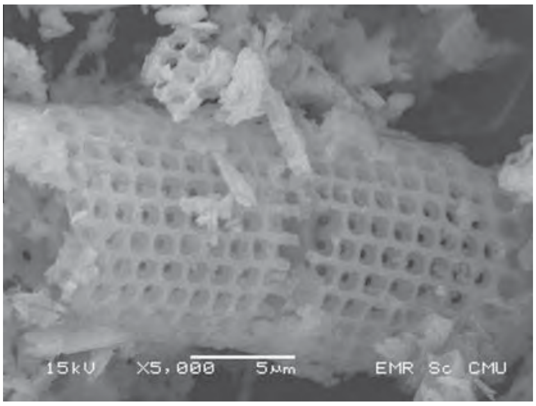

Fig. 3. SEM photomicrographs of diatomite.

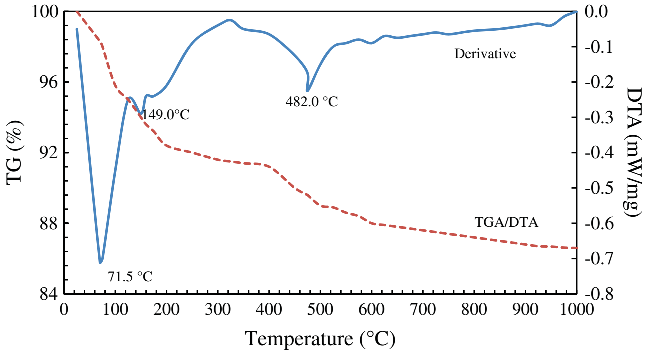

Fig. 4. DTA and TG curves of diatomite.

3.2. Differential thermal analysis (DTA) and thermal gravitation analysis (TGA)

The results of DTA and TGA of diatomite are shown in Fig. 4. The endothermic peaks associated with the loss of adsorbed water on particle surfaces of diatomite were observed at 71.5 °C and 149.0 °C. The other peak at 482.0 °C ascribed the dehydroxylation of clay minerals containing in DE [9]. This, therefore, indicated that the optimum calcined temperature for reactive diatomite should not be higher than 500 °C.

3.3. Mineralogical and morphological composition using XRD

The XRD results of DE are shown in Fig. 5. The DE contained mainly quartz, kaolinite and nontronite. Calcination at 400 °C reduced the peaks of kaolinite and nontronite. At higher temperature of 600 °C, kaolinite and nontronite peaks disappeared. This corresponded to the dehydroxylation of kaolinite. When clay mineral (kaolinite) was calcined at this temperature, it thus became active [13]. This was confirmed by the disappearance of main peaks of kaolinite at 12.5°, 24.8° and 61.8° 2θ. At 800 °C, small amounts of hematite and magnesium aluminum silicate were observed. At 1000 °C, the magnesium aluminum silicate peak disappeared as confirmed by the disappearance of main peaks at 19.8° and 25.8° 2θ. The peaks of mullite at 33.2° and 35.2° 2θ were observed at this high calcined temperature.

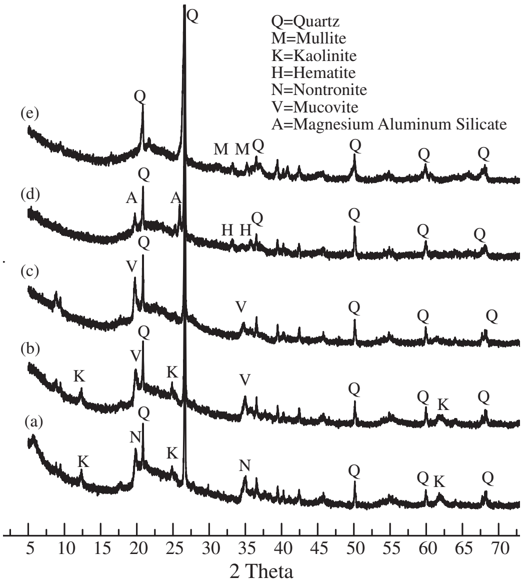

Fig. 5. XRD patterns of DE (a) UC, (b) 400 °C, (c) 600 °C, (d) 800 °C, and (e) 1000 °C.

3.4. Compressive strength

The results of compressive strength of lightweight concrete containing calcined DE pressed cube are shown in Fig. 6. The compressive strength tended to increase slightly with the increasing calcination temperature of CA up to 800 °C and increased significantly when calcined at 1000 °C. For example, the 28-day compressive strengths of series 70FA mixes with 25, 400, 600, 800, and 1000 °C calcined CA were 8.1, 8.0, 8.6, 8.8, and 12.9 MPa, respectively. At calcination temperature below 500 °C (Fig. 4), the kaolinite (clay) in the uncalcined DE (UC) and CA400 was unstable and could swell when mixed with water [20]. A number of researches suggested the calcined temperatures between 600 and 800 °C as optimum calcined temperature for the pozzolanic property of DE

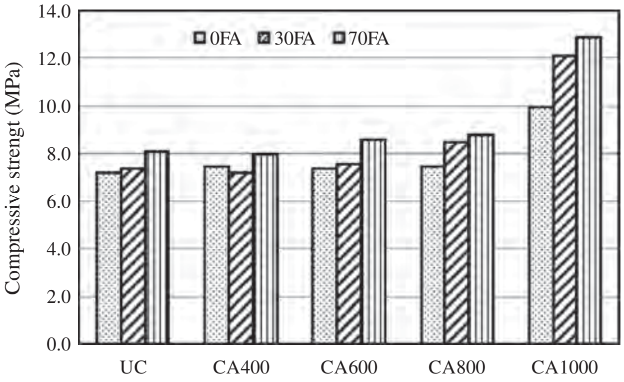

Fig. 6. Compressive strength at 28 days lightweight concrete.

[9,19,21]. The CA1000 mix showed the highest compressive strength due to the appearance of mullite which was stable and strong mineral.

With regards to aggregate sizes, the mixes with a high amount of FA showed high compressive strength compared to those with the low amount of FA. For example, the 28-day compressive strengths of series 0FA, 30FA, and 70FA of CA1000 mixes were 10.0, 12.1, and 12.9 MPa, respectively. The use of FA aggregate with high surface area resulted in the better bonding of matrix and aggregate than that of CA and led to an increase in strength [22]. Furthermore, the FA was calcined at 600 °C and thus possessed pozzolanic property which also contributed to the strength development of the lightweight concrete.

3.5. Density

The results of the density of lightweight concretes with calcined diatomite are shown in Fig. 7. The increased in calcined temperature resulted in DE with a slightly reduced density compared with that of the uncalcined DE, due to the calcination of burnable elements [9]. For example, the density of lightweight concretes with UC, CA400, CA600, CA800, and CA1000 of 30FA series were 1313, 1219, 1169, 1222, and 1139 kg/m^3, respectively. The density also increased with the increasing amount of FA due to the relatively high densities of FA of 600 k/m^3 compared with the lower values of MA and CA of 425 and 417 k/m^3, respectively (Table 1). The densities of series 0FA, 30FA, and 70FA mixes with CA1000 were 1070, 1139, and 1238 kg/m^3, respectively. For 70FA series, the high amount of FA filled the space in the matrices and made concrete more compact and stronger than those using low amount of FA.

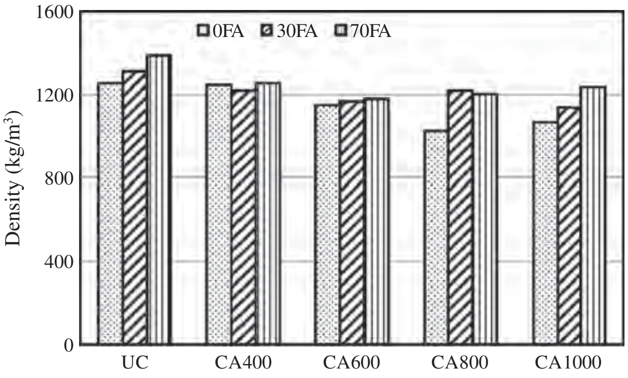

Fig. 7. Density of lightweight concrete at 28 days.

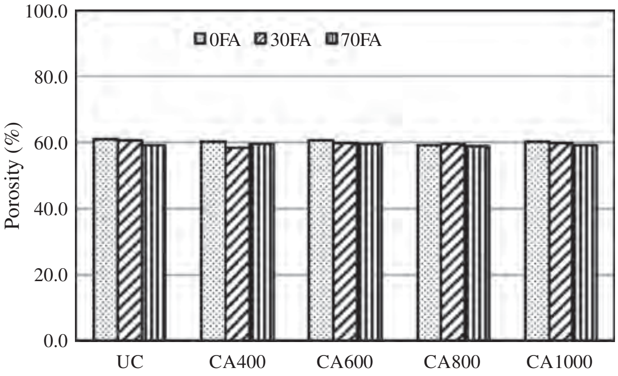

Fig. 8. Porosity at 28 days of lightweight concrete.

3.6. Porosity and water absorption

The results of porosity are shown in Fig. 8. The porosities at the age of 28 days were not very different and were between 59.0% and 61.2%. The results, however, indicated that the porosities slightly decreased with the increase in the amount of FA. For example, the porosities at 28 days of series 0FA, 30FA, and 70FA of CA1000 mixes were 60.30%, 60.12%, and 59.42%, respectively. The results of water absorption were similar to those of porosity as shown in Fig. 9. There was an indication that the water absorption values reduced with the increase in the amount of FA. The water absorption at 28 days of CA800 mixes of series 0FA, 30FA, and 70FA were 67.46, 66.73, and 66.06%, respectively. This was due to the increase in the surface area and reduction in the porosity of the concrete containing high amount of FA.

3.7. Thermal conductivity

The results of the thermal conductivity of lightweight concretes are shown in Fig. 10. The thermal conductivity slightly decreased with the increasing calcined temperature of DE. For example, the thermal conductivity of the concretes with UC, CA400, CA600, CA800, and CA1000 of series 0FA were 0.184, 0.157, 0.145, 0.130, and 0.151 W/mK, respectively. The reduction was due to the ridding of water molecule and other burnable minerals in aggregate with high calcination temperature [9]. In addition, the increase in calcined temperature of DE resulted in a decrease in density of pressed lightweight concrete and also a decrease in thermal conductivity. The reduction in the thermal conductivity is rather attractive thermal property on this lightweight concrete. For the calcinations at high temperatures of CA600, CA800, and CA1000 mixes, there was an indication that the thermal conductivity increased with the increasing amount of FA.

The thermal conductivity values of series 0FA, 30FA, and 70FA mixes with CA800 were 0.130, 0.148, and 0.159 W/mK, respectively. The thermal conductivity increased with the increasing of FA due to the increases in the filling of voids of small aggregate and the increase in the bonding of the small aggregate and the matrix due to increased surface area and pozzolanic property of the aggregate.

3.8. Relationship of compressive strength, thermal conductivity, density, and calcined temperature

The relationship between compressive strength and calcined temperature of lightweight concrete was presented by Eq. (3) and shown Fig. 11. The compressive strength increased with the increasing calcined temperature [9,19].

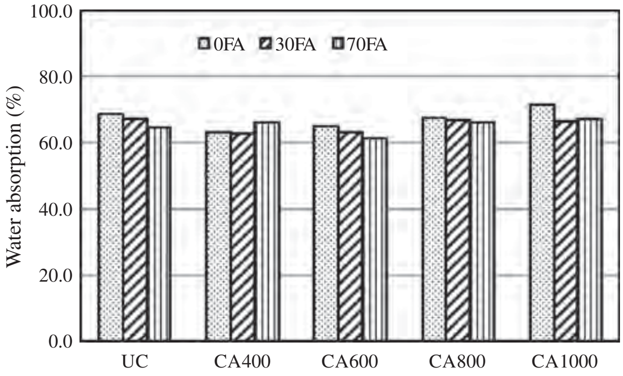

Fig. 9. Water absorption at 28 days of lightweight concrete.

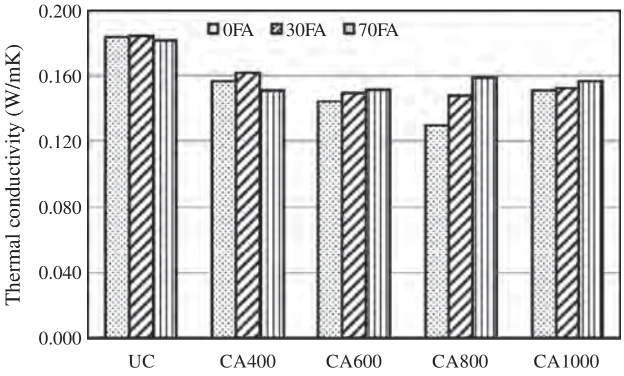

Fig. 10. Thermal conductivity at 28 days of lightweight concrete.

$$f_c' = (1\times10^{-0.5})T^2 - 0.0067T + 7.7068 \tag{3}$$

where f_c' is compressive strength (MPa) and T is the calcined temperature of DE (°C).

The relationship between density and thermal conductivity was linearly described by Eq. (4) and is shown in Fig. 12. The thermal conductivity increased with the increasing density [23,24] as the thermal conductivity depends on the density of concrete [25]. The increases in density of pressed lightweight concrete resulted in dense and packed structure and likewise an increase in the thermal conductivity. The values of thermal conductivity were between 0.130 and 0.184 W/mK with the corresponding densities between 1000 and 1200 kg/m^3 and were similar to the previously published results of 0.2–0.3 W/mK for low-strength lightweight DE concrete for thermal insulation [14].

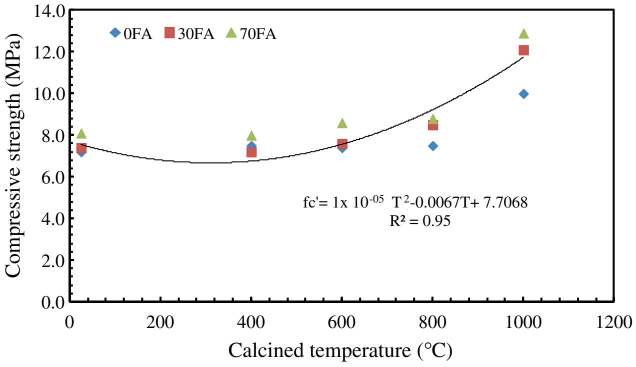

Fig. 11. Relationship of compressive strength and calcined temperature of lightweight concrete.

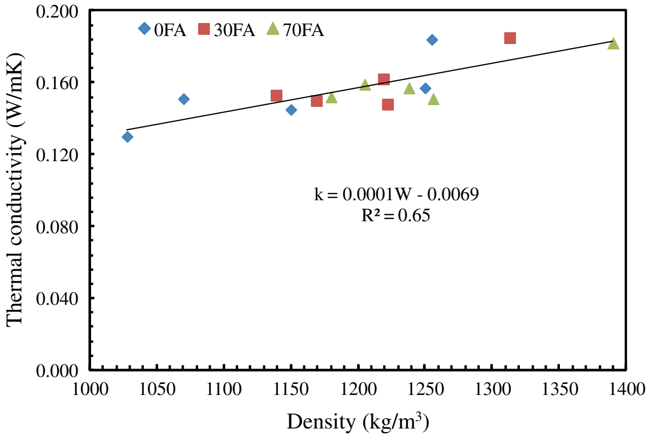

Fig. 12. Relationship between thermal conductivity and density of lightweight concrete.

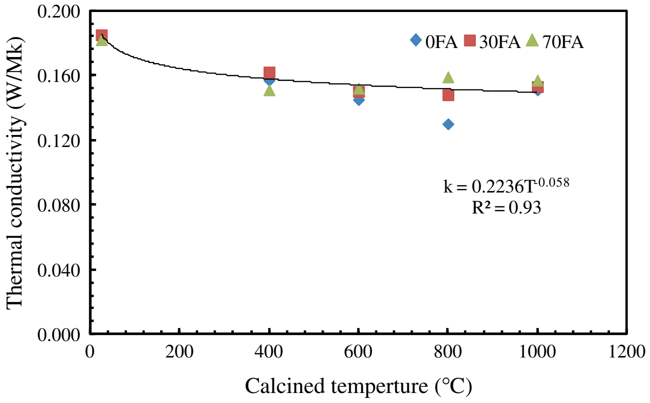

Fig. 13. Relationship between thermal conductivity and calcined temperature of DE.

$$k = 0.0001W - 0.0069 \tag{4}$$

where k is thermal conductivity (W/mK) and W is Density of lightweight concrete (kg/m^3).

In addition, the relationship of thermal conductivity and calcined temperature of DE was obtained from Eq. (5) and shown in Fig. 13.

$$k = 0.2236T^{-0.058} \tag{5}$$

where k is thermal conductivity (W/mK) and T is the calcined temperature of CA (°C).

It was demonstrated that DE could be used to make pressed lightweight concrete with densities of 1000–1200 kg/m^3 and reasonably high strengths of 7.8–12.9 MPa.

4. Conclusion

Based on the obtained data, the following conclusions can be draw.

(1) DTA and TG curves of DE indicated that the optimum calcined temperature for reactive diatomite should not be less than 500 °C which was consistent with XRD results of DE calcined at 600 °C where the kaolinite and nontronite peaks disappeared. At 1000 °C, the appearance of peak of mullite which was stable and strong indicated the strong aggregate.

(2) The use of calcined DE aggregate increased compressive strength, and reduced density, and thermal conductivity compared to those with uncalcined DE. The porosity and water absorption of concrete were less affected and the results of concrete with various calcined temperatures were similar.
(3) The calcined temperatures should be 600 °C for fine and medium aggregate to obtain the pozzolanic property; and 1000 °C for coarse aggregate to obtain good strength.
(4) The use of calcined DE is considered very attractive as the improvement in strength, density and thermal conductivity are very important.

Acknowledgement

This work was supported by the Higher Education Research Promotion and National Research University Project of Thailand, Office of the Higher Education Commission, through the Advanced Functional Materials Cluster of Khon Kaen University AFM-2553-Ph.d-01, and the Thailand Research Fund (TRF) under the TRF Senior Research Scholar, Grant No. RTA5480004.

References

[1] ASTM C330-89. Specification for lightweight aggregates for structural concrete, vol. 04.02. Annual Book of ASTM Standard; 1989.
[2] Chandra SBL. Lightweight aggregate concrete: science, technology and application. Norwich, New York (USA): William Andrew Publishing; 2002.
[3] Neville AM. Concrete technology. New York (USA): Longman; 1987.
[4] Chen B, Liu J. Experimental application of mineral admixtures in lightweight concrete with high strength and workability. Constr Build Mater 2008;22(6):1108–13.
[5] Kayali O, Haque MN, Zhu B. Some characteristics of high strength fiber reinforced lightweight aggregate concrete. Cement Concr Compos 2003;25(2):207–13.
[6] Demirdag S, Ugur I, Sarac S. The effects of cement/fly ash ratios on the volcanic slag aggregate lightweight concrete masonry units. Constr Build Mater 2008;22(8):1730–5.
[7] Round FE, Crawford RM, Mann DG. The diatoms: biology and morphology of the genera. Cambridge University Press; Cambridge: 1990.
[8] Korunic Z. Diatomaceous earths, a group of natural insecticides. J Stored Prod Res 1998;34:87–97.
[9] Pimraksa K, Chindaprasirt P. Lightweight bricks made of diatomaceous earth, lime and gypsum. Ceram Int 2009;35(1):471–8.
[10] Degirmenci N, Yilmaz A. Use of diatomite as partial replacement for Portland cement in cement mortars. Constr Build Mater 2009;23(1):284–8.
[11] ACI 213. Guide for structural lightweight-aggregate concrete. American Concrete Institute; 2003.
[12] ASTM C 618. Standard specification for coal fly ash and raw or calcined natural pozzolan for use in concrete, vol. 04.01. Annual Book of ASTM Standard; 2012.
[13] Baronio G, Binda L. Study of the pozzolanicity of some bricks and clays. Constr Build Mater 1997;11(1):41–6.
[14] Ünal O, Uygunoğlu T, Yildiz A. Investigation of properties of low-strength lightweight concrete for thermal insulation. Build Environ 2007;42(2):584–90.
[15] ASTM C138. Standard test of method for unit weight of mortar, vol. 04.01. Annual Book of ASTM Standard; 2009.
[16] ASTM C109. Standard test method of compressive strength of hydraulic cement mortars (using 2-in. or [50 mm] cube specimens), vol. 04.01. Annual Book of ASTM Standard; 2002.
[17] ASTM C642. Standard test method for density, absorption, and voids in hardened concrete, vol. 04.02. Annual Book of ASTM Standard. 2006
[18] ASTM D5930. Standard test method for thermal conductivity of plastics by means of a transient line-source technique, vol. 04.01. Annual Book of ASTM Standard; 2009
[19] Pimraksa K, Chindaprasirt P, Rungchet A, Sagoe-Crentsil K, Sato T. Lightweight geopolymer made of highly porous siliceous materials with various Na_2O/Al_2O_3 and SiO_2/Al_2O_3 ratios. Mater Sci Eng, A 2011;528(21):6616–23.
[20] Charles C, Diane H, McGeary D. Physical geology. Eleventh edition. New York (USA): McGraw-Hill Publish; 2007.
[21] Yılmaz B, Ediz N. The use of raw and calcined diatomite in cement production. Cement Concr Compos 2008;30(3):202–11.
[22] Husem M. The effects of bond strengths between lightweight and ordinary aggregate-mortar, aggregate-cement paste on the mechanical properties of concrete. Mater Sci Eng, A 2003;363(1–2):152–8.
[23] Uysal H, Demirboğa R, Şahin R, Gül R. The effects of different cement dosages, slumps, and pumice aggregate ratios on the thermal conductivity and density of concrete. Cem Concr Res 2004;34(5):845–8.
[24] Topçu İB, Uygunoğlu T. Properties of autoclaved lightweight aggregate concrete. Build Environ 2007;42(12):4108–16.
[25] Kim K-H, Jeon S-E, Kim J-K, Yang S. An experimental study on thermal conductivity of concrete. Cem Concr Res 2003;33(3):363–71.

International Journal of Minerals, Metallurgy and Materials
Volume 20, Number 8, August 2013, Page 1
DOI: 10.1007/s12613-013-0000-0

Strength, porosity, and chloride resistance of mortar using the combination of two kinds of pozzolanic materials

Sumrerng Rukzon 1) *and Prinya Chindaprasirt* 2)

1) Department of Civil Engineering, Faculty of Engineering, Rajamangala University of Technology Phra Nakhon, Bangkok 10800, Thailand

2) Sustainable Infrastructure Research and Development Center, Department of Civil Engineering, Faculty of Engineering, Khon Kaen University, Khon Kaen 40002, Thailand

(Received: 29 September 2012; revised: 30 December 2012; accepted: 3 January 2013)

Abstract: This article presents a study on the resistance to chloride penetration, corrosion, porosity, and strength of mortar containing fine fly ash (FA), ground rice husk-bark ash (RB), and ground bagasse ash (BA). Ordinary Portland cement (CT) was blended with a single pozzolan and two pozzolans. Strength, porosity, rapid chloride penetration, immersion, and corrosion tests were performed to characterize the mortar. Test results showed that the use of ternary blends of CT, FA, and RB or BA decreased the porosity of the mortar, as compared with binary blended mortar containing CT and RB or BA. The resistance to chloride penetration of the mortar improved substantially with partial replacement of CT with FA, RB, and BA. The use of ternary blends of CT, FA and RB or BA produced the mortars with good strength and resistance to chloride penetration. The resistance to chloride penetration was higher with an increase in the replacement level due to the reduced calcium hydroxide.

Keywords: mortar; pozzolanic materials; strength; porosity; chloride penetration; agricultural wastes

1. Introduction

Nowadays, researchers are interested in the properties of waste materials from industrial and agricultural production because the waste materials can substitute for some part of cement in order to reduce the amount of cement usage. Several attractive waste materials, such as fly ash, rice husk ash, palm oil fuel ash, and bagasse ash are considered for producing concrete [1-5]. These materials are pozzolanic materials containing silica and/or alumina compounds, which can develop additional pozzolanic reaction. Therefore, it is possible to have an appropriate mix proportion between cement and pozzolanic materials for producing good and strong concrete compared with normal concrete [6]. In addition, the pozzolanic materials can further contribute to the increase in durability of concrete.

In Thailand, industrial and agricultural by-products are used as fuel sources for the generation of power in industrial plants. Residues from the process are waste ashes, such as fly ash, rice husk-bark ash, bagasse ash, and palm oil fuel ash. These ashes cause unpleasant environment for nearby communities. This problem can be solved by adding value to the waste ashes and reuse them. Fly ash is the most used pozzolanic material in the construction industry. The other pozzolans are now receiving more attention, and the studies of the properties of these pozzolans are needed. The purpose of this research is to study and develop the waste ashes for use as pozzolans. The information is critical for the construction industry to accept and utilize these new pozzolans. Besides, the pollution and environmental problems will be alleviated.

2. Experimental

2.1. Materials

Portland cement type I (CT), fly ash (from Mae Moh power plant in Thailand), bagasse ash (from a sugar mill), rice husk-bark ash (from a small power plant), and type-F superplasticizer (SP) were the materials used in this research. Graded river sand passing through a standard sieve

---

Corresponding author: Sumrerng Rukzon E-mail: rerng197@rmutp.ac.th, sumrerng.r@rmutp.ac.th

with the fineness modulus of 2.85 and the density of 2.65 g/cm^3 was used as a fine aggregate. Fine fly ash (FA) was obtained from the classification of original fly ash with 3% retained on the sieve No. 325 (opening 45 µm). Bagasse ash (BA) and rice husk-bark ash (RB) were ground by a ball mill until 3% weight retained on the sieve No. 325.

The physical properties of the pozzolans are given in Table 1. The Blaine finenesses of CT, BA, RB, and FA were 3600, 12500, 12000, and 5800 cm^2/g, respectively. The densities of CT, BA, RB, and FA were 3.14, 2.24, 2.25, and 2.46 g/cm^3, respectively. The median particle sizes of the material used from the finest to the coarsest are given as follows: FA 16 µm, RB 19.5 µm, BA 16.4 µm, and CT 16 µm. The chemical constituents of the pozzolans are given in Table 2. In addition, the SEM images of the materials are shown in Fig. 1.

Table 1. Physical properties of CT, FA, RB, and BA

Raw materials	Median particle size, d_{50} / µm	Retained on sieve No.325 / wt%	Density / (g·cm^{-3})	Blaine fineness / (cm^2·g^{-1})
CT	21	—	3.14	3600
FA	16	3	2.46	5800
RB	19.5	3	2.25	12000
BA	16.4	3	2.24	12500

Table 2. Compositions of CT, FA, RB, and BA wt%

Raw materials	CaO	SiO_2	Al_2O_3	Fe_2O_3	MgO	K_2O	SO_3	LOI	SiO_2+ Al_2O_3+ Fe_2O_3
CT	54.98	25.1	5.5	5.9	3.4	0.5	4.7	0.9	—
FA	11.57	45.1	17.2	13.4	6.8	1.8	2.2	2.5	75.7
RB	5.5	76.3	1.6	1.5	0.01	3.9	0.9	8.24	79.4
BA	8.5	64.7	4.8	3.2	0.01	2	0.9	17.5	72.7

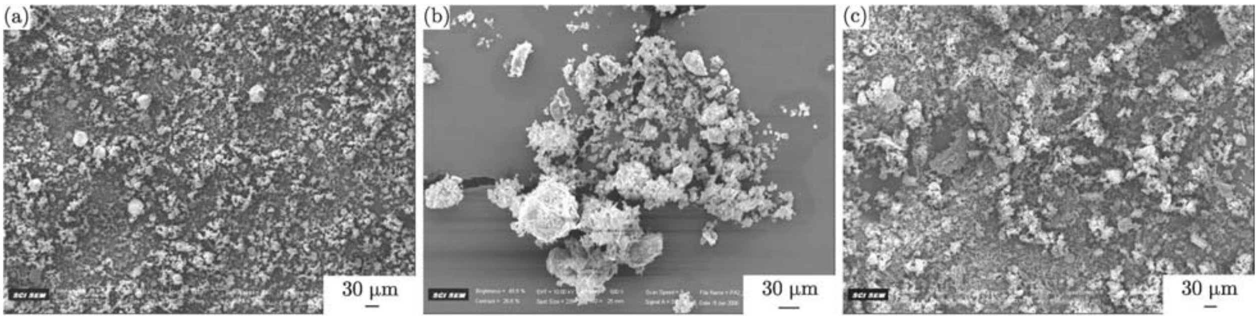

Fig. 1. SEM images of (a) fine FA, (b) ground rice husk-bark ash (RB), and (c) ground bagasse ash (BA).

2.2. Mix proportions and curing

Ordinary Portland cement (CT) was partially replaced with 0-40% of pozzolans. In addition to a single pozzolan, a blend of equal weight portion of FA and RB (FARB) and a blend of equal weight portion of FA and BA (FABA) were also used. Sand-to-binder ratios of 2.75 by weight and water to binder ratio (W/B) of 0.5 were used. SP was incorporated in order to obtain mortar mixes with a similar flow of 110% ± 5% in accordance with ASTM C109 [7]. The cast specimens were covered with polyurethane sheet and damped cloth and placed in a (23 ± 2)°C chamber. They were demolded at the age of 1 d and cured in water at (23 ± 20)°C. The mortar mix proportions are given in Table 3.

2.3. Compressive strength

The 50 mm cube specimens were prepared in accord-

Table 3. Mortar mix proportions

Mix symbol	CT	FA	RB	BA
CT	100	—	—	—
20FA	80	20	—	—
40FA	60	40	—	—
20RB	80	—	20	—
40RB	60	—	40	—
20BA	80	—	—	20
40BA	60	—	—	40
20FARB	80	10	10	—
40FARB	60	20	20	—
20FABA	80	10	—	10
40FABA	60	20	—	20

ance with ASTM C109 [7]. They were tested at the ages of 7, 28, and 90 d. The reported results are the average of three samples.

2.4. Porosity test

The porosity tests were tested at the ages of 7, 28, and 90 d in accordance with ASTM C39 [8] using cylindrical specimens with 100 mm in diameter and 200 mm in height. The cylindrical specimens were cured in water for 7, 28, and 90 d and were cut into 50 mm thick slices discarding the two ends. Then, they were dried at (100 ± 5)°C until their weights were constant. They were placed in the desiccators under vacuum for 3 h before they were immersed in the de-aired distilled water in order to obtain the saturated concrete samples. The porosity is calculated by the following equation:

$$p = \frac{W_\mathrm{a} - W_\mathrm{d}}{W_\mathrm{a} - W_\mathrm{w}} \times 100\% \qquad (1)$$

where p is the effective porosity, W_a is the saturated specimen weight in air (g), W_d is the dried specimen weight after 24 h in the oven at (100 ± 5)°C (g), and W_w is the specimen weight in water (g). The reported results are the average of two samples.

2.5. Rapid test on resistance to chloride penetration

The ϕ 100 mm × 200 mm cylinders were prepared in accordance with ASTM C39 [8]. They were tested at the age of 28 d. After being cured in water until the age of 27 d, they were cut into 50 mm thick slices with the 50 mm ends discarded. The 50 mm slices were epoxy-coated around the cylinder.

2.5.1. Rapid chloride penetration test

The epoxy-coated specimens were conditioned and tested at the age of 28 d for rapid chloride penetration test (RCPT) in accordance with the method described in ASTM C1202 [9]. The reported results are the average of two samples.

2.5.2. Immersion test

To confirm the results, actual chloride penetration of mortar immersed in NaCl solution was performed. The test set-up was similar to that described in RTA T263 [10] with the exception that ϕ100 mm × 50 mm cylinder and 3% NaCl solution were used. Chloride penetration fronts into mortar specimens were determined using 0.1 mol/L $AgNO_3$ solution [11]. The ϕ100 mm × 50 mm slices were epoxy-coated at the top as well as around the cylindrical slice. The specimens were immersed at the age of 28 d and kept immersed for 30 d.

2.6. Accelerated corrosion test with impressed voltage

The mortar prisms of dimensions 40 mm × 40 mm × 160 mm with embedded steel of 9 mm in diameter and 195 mm in length were used for this test (anode). The steel was secured such that it protruded from the top surface of the prisms by 15.5 mm, thus provided a sufficient mortar cover of 15.5 mm at the bottom and the side of the prism, as shown in Fig. 2. The mortar prisms were subjected to the accelerated corrosion test with impressed voltage using a 5% NaCl solution and a constant voltage of 12 V dc (cathode). The condition of concrete was monitored visually at the interval of 4 h, and the time of initiation of first crack was recorded. This is used as a measurement of the specimen's relative resistance against chloride attack and reinforcement corrosion [12-13].

Fig. 2. Accelerated corrosion test with impressed voltage.

3. Results

3.1. SP requirement of mortar

The test result of the amount of SP required for the mortar component is shown in Table 4. The use of FA reduced the SP requirement as the FA particles were spherical and exerted the ball bearing effect to produce mortar with improved workability. The RB mortar required more SP than CT mortar because of the high fineness and porosity of RB. The SP required for CT, 20RB and 40RB mortars were 0.22%, 0.28%, and 2.5%. Similar increases in the water requirement and/or SP content of RB mortars were reported [14-15]. The increase in the SP requirement was partly due to the high loss of ignition of 8.24% for RB. For the BA, the amount of SP required further increased to 1.2% for the 20BA mortar and 3.8% for the 40BA mortar. The increase in SP requirement was due to the increase in loss on ignition (LOI) as the loss on ignition (LOI) of BA was rather high at 17.5%. For the ternary blended system (TBS), the SP requirements were intermediate between those of single pozzolan mortar (binary blended system, BBS). The SP requirements of FA + RB mortars were between those of FA and RB mortars, and the SP requirements of FA + BA mortars were between those of FA and

Table 4. Compressive strength of mortars

Mix	SP / %	Compressive strength / MPa — Normalized / %		
		7 d	28 d	90 d
CT	0.22	42.9 — 100	45.3 — 100	48.8 — 100
20FA	0.14	37.6 — 88	41.9 — 92	47.4 — 97
40FA	0.10	36.0 — 84	40.7 — 90	46.5 — 95
20RB	0.28	36.6 — 85	40.4 — 89	44.8 — 92
40RB	2.50	35.3 — 82	39.5 — 87	43.5 — 89
20BA	1.20	35.5 — 83	38.9 — 86	42.9 — 88
40BA	3.80	32.2 — 75	38.1 — 84	41.6 — 85
20FARB	0.24	38.1 — 89	41.4 — 91	46.3 — 95
40FARB	1.40	37.6 — 88	40.7 — 90	45.5 — 90
20FABA	0.72	36.1 — 84	41.0 — 91	46.1 — 94
40FABA	2.10	35.2 — 88	39.7 — 91	45.5 — 93

BA mortars.

3.2. Compressive strength

The results of compressive strengths and their percentages are shown in Table 4. The strength of the CT mortar at 7, 28, and 90 d were 42.9, 45.3, and 48.8 MPa, respectively. The strength of FA, RB, and BA mortars tested at 7 d were 83%-88% of that of CT mortar at the same age. At 28 and 90 d, they were 86%-92% and 88%-97%, respectively. The slight increase in the percentage strength was due to the pozzolanic reaction, which contributed to the strength development at the later age. The FA, RB, and BA could be used as pozzolanic materials because their strength indices or strength percentages were higher than 75% as required by ASTM C618 [16].

For the ternary blended mortars (two pozzolans), the test results showed good trend of strength development in comparison with the binary blended (single pozzolan). For example, the normalized 7-d strength of 40FARB mortar was 88%, higher than 84% of 40FA mortar and 82% of 40RB mortar. The normalized 7-d strength of 40FABA mortar was 84%, higher than 75% of 40RB mortar. The use of the ternary blended system (TBS) improved the strength development of mortar through the synergic effect of two pozzolans [17-19].

3.3. Porosity

The porosity percentage in this topic was examined by the division basis of a vacuum pump, as in previous researches [3, 13]. The values of porosity at 7, 28, and 90 d were calculated by Eq. (1), as shown in Fig. 3. The porosity reduced with curing time, which was as expected due to the addition hydration and pozolanic reaction. The incorporation of pozzolans increased the porosity of mortars, and the increase was more with the increase in the replacement level. At the same replacement level, the increase in porosity was the largest with the use of BA, and this was followed by RB and FA. The incorporation of fly ash increased the total porosity of the paste with pore refinement [20]. Similar increase in the porosity of pastes with the use of pozzolans was also reported in Refs. [3, 13]. The RB and BA were very fine pozzolans with some pores remained in the particles [1, 3]. Their uses, therefore, resulted in the increase in the porosity of mortars. The large increase in porosity of BA mortar was due to the large content of loss on ignition (LOI), which consisted of numerous pores in the remainder of the unburnt or not completely burnt portions.

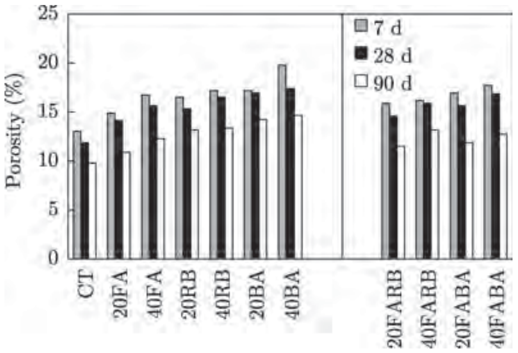

Fig. 3. Porosity of mortars.

For the ternary blended system or TBS (two pozzolans), the porosity of mortars also increased compared with the control mortar. However, the porosity of TBS mortars was significantly lower than that of the corresponding mortar mixed with a single pozzolan (RB or BA) especially at the later age of 90 d. For example, the porosity of 20FARB at 90 d was 11.25%, as compared with 10.5% of 20FA mortar and 13.0% of 20RB mortar. Also, the porosity of 20FABA at 90 d was 11.5%, as compared with 14.0% of 20BA. The reduction in porosity was a result of the FA inclusion and its synergy effect with the other pozzolan. The use of TBS slightly increased the porosity of mortars and possibly led to the strength reduction [20-21]. Khatib and Mangat [22] reported that if the porosity is increased, the strength will be generally decreased. However, the increase in porosity was accompanied with pore refinement, which could offset the strength reduction and enhance the durability of the mortar. The porosities in this study were in the range of 9.8%-19.8%, and the strengths were between 32.2 and 48.8 MPa.

3.4. Chloride resistance

Three kinds of test methods for resistance to chloride were studied to compare and reinforce the finding.

3.4.1. Rapid chloride penetration test (RCPT)

The rapid chloride penetration test (RCPT) as per ASTM C1202 [9] was conducted for the mortar samples at the age of 28 d. Fig. 4 shows the test specimens' preparation and the test device installation. Normally, the test used electric current and may cause the heat problem especially with mortar specimens with rather high coulomb passed [23]. In this research, the mortar strengths were reasonably high (32.2-42.9 MPa), and the developed heat was acceptable.

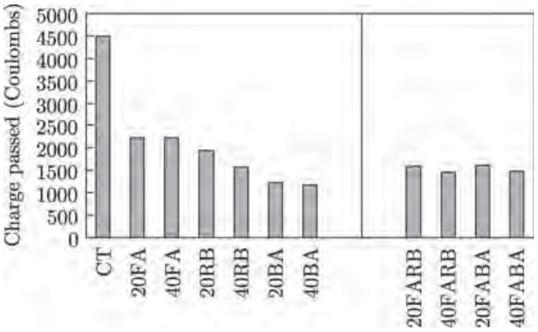

Fig. 4. Rapid chloride penetration test (RCPT) results.

The test results of RCPT are shown in Fig. 4. The chloride penetration was significantly reduced when the pozzolanic materials were used to partially substitute Portland cement. Similar finding was also reported by other researchers [3, 19, 23]. The main composition of RB and BA was SiO_2 [15, 24]. The product derived from the pozzolanic reaction between $Ca(OH)_2$and SiO_2 was calcium silicate hydrate (CSH) [25], which reduced the total $Ca(OH)_2$ in the system and increased the mortar durability. The chloride penetration of CT mortar was 4500 C. The chloride penetration of 20FA and 40FA mortar reduced to 2235 and 2230 C. The incorporation of pozzolans, such as fly ash, reduced the $Ca(OH)_2$ in the system and enhanced the resistance to chloride penetration [23, 26-27]. The use of 20% and 40% RB reduced the chloride penetration of mortars compared with those FA mortars. The chloride penetrations of 20RB and 40RB mortars were 1950 and 1560 C. The chloride penetrations of 20BA and 40BA mortars were the lowest at 1230 and 1180 C. The increases in the resistance to chloride penetration were due to low calcium oxide and high SiO_2 contents of both RB and BA, resulting in increased CSH and reduced calcium in the system. The incorporation of pozzolans resulted in CSH gel with reduced calcium to silicate ratio (C/S ratio) and increased the durability of mortar [28].

For the ternary blended system (TBS), the results, as shown in Fig. 4, indicated that the chloride penetrations of the TBS mortars were also significantly reduced, as compared with that of the CT mortar. The chloride penetrations of the TBS mortars were only 1460-1620 C, which were lower than those of FA mortars and the 20RB mortar.

3.4.2. Immersion test

The results of the chloride depth test are shown in Fig. 5. The results conformed with the RCPT ones and the difference was the order of magnitude. The chloride depth of CT mortar was 18.5 mm and reduced to 17.5 and 16.0 mm with the incorporation of 20% and 40% of FA. The chloride depths of 20RB and 40RB mortars were 17.5 and 15.5 mm and were comparable to those of FA mortars. The incorporation of BA significantly reduced the chloride depth of the mortars and suggested that the most effective pozzolanic material for the chloride resistance was BA.

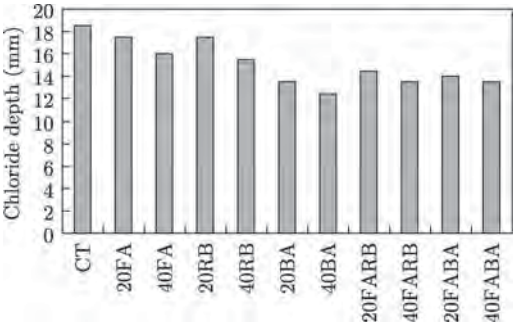

Fig. 5. Chloride depth by immersion test.

For the ternary blended system (TBS), the chloride depths were generally reduced compared with the binary blended system (BBS) mortars. The chloride depths of the TBS mortars were 13.5-14.5 mm, which were only slightly higher than the lowest values of BA mortars of 12.5-13.5 mm. This again confirmed the synergy effect of the fine pozzolans in the ternary system [17, 23].

3.5. Time to the first crack

The test results of time to the first crack of mortars are shown in the Fig. 6. The time to the first crack of CT mortar was 72 h and increased with the incorporation and amount of pozzolan. The times to the first crack of 20FA and 40FA increased slightly to 84 and 90 h compared with that of the control mortar. The times to the first crack of 20RB and 40RB increased further to 98 and 110 h. The times to the first crack of 20BA and 40BA mortars were the highest at 122 and 130 h. The results clearly showed that the incorporation of pozzolans effectively increased the resistance to chloride attack as indicated by the increased time to the first crack. For the binary blended system (BBS), the incorporation of BA was most effective and followed in turn by RB and FA.

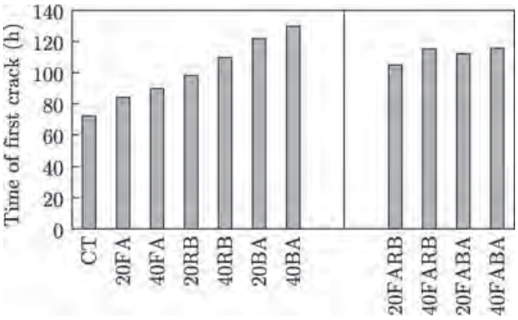

Fig. 6. Time of the first crack of mortars.

For the ternary blended system (TBS), the times to the first crack of the TBS mortars were significantly longer than that of the CT mortars. The times to the first crack of 20FARB, 20FABA, 40FARB, and 40 FABA mortars were 105-116 h compared with 72 h of the CT mortar. The times to the first crack of 20FARB and 40FARB mortars were relatively high and comparable to those of 20RB and 40RB mortars. The times to the first crack of 20FABA and 40 FABA were slightly lower than those of 20BA and 40 BA. The pozzolanic reaction enhanced the durability of pastes through the reduction in pore size and the cavities [29]. The small particles of pozzolan also acted as the nucleation sites for accelerating the hydration reaction in the cement plate [30]. The results confirmed the synergic effect of the two pozzolans system [17]. Fig. 7 shows the mortar prism after the test of time to the first crack.

Fig. 7. Samples after the test of time to the first crack.

All test results confirm the finding that the waste ashes derived from the industrial and agricultural production, namely, fly ash, rice husk-bark ash, and bagasse ash are effective pozzolanic materials and suitable for use as supplementary cementitious materials. The use of the ternary blended system (TBS) with FA blended with RB or BA is very attractive. The results suggested a better performance of the ternary blend compared with the binary blend considering strength, porosity, and resistance to chloride penetration.

In summary, the use of the ternary blended system (TBS) improved the strength development of mortars through the synergic effect of two pozzolans. This is due to the better dispersion and filler effect of the finer fly ash despite the higher pozzolanic activity. This makes the mortar denser and, hence, better resistant to the ingression of chloride. The incorporation of fly ash adds additional dispersing effect of cement grains as well as the other fine pozzolan particles. The use of fly ash reduced the SP requirement as the fly ash particles were spherical and exerted the ball bearing effect to produce mortars with improved durability. In addition, the high SiO_2 contents of both rice husk-bark ash and bagasse ash result in increased CSH and reduced $Ca(OH)_2$ in the system. The product derived from the pozzolanic reaction between $Ca(OH)_2$and SiO_2 was CSH, which reduced the total $Ca(OH)_2$ in the system and increased the mortar durability.

4. Conclusions

From the test, it can be concluded that FA, RB, and BA can be used as pozzolans to replace part of Portland cement in making mortars with relatively high strength and good resistance to chloride penetration. Test results also indicate that the use of the blend of pozzolans in the equal portion of BA and FA, and RB and FA also effectively improves the mortar in terms of strength and resistance to chloride penetration. The improvement is due to the dispersing effect of fly ash and the synergic effect of the blend of fine pozzolans.

Acknowledgements

This work was financially supported by the Office of the National Research Council of Thailand (NRCT), Higher Education Research Promotion and National Research University Project of Thailand, Office of the Higher Education Commission, through the Advanced Functional Materials Cluster of Khon Kaen University and the Thailand Research Fund (TRF) under the TRF Senior Research Scholar Contract No. RTA5480004 and Rajamangala University of Technology Phra Nakhon (RMUTP).

References

[1] S. Rukzon and P. Chindaprasirt, Strength and carbonation model of rice husk ash cement mortar with different fineness, *J. Mater. Civ. Eng.*, 22(2010), No. 3, p. 253.

[2] P. Chindaprasirt, C. Chotetanorm, and S. Rukzon, Use of palm oil fuel ash to improve chloride and corrosion re-

sistance of high-strength and high-workability concrete, *J. Mater. Civ. Eng.*, 23(2011), p. 499.

[3] S. Rukzon and P. Chindaprasirt, Utilization of bagasse ash in high-strength concrete, *Mater. Des.*, 34(2012), p. 45.

[4] S. Rukzon, P. Chindaprasirt, and R. Mahachai, Effect of grinding on chemical and physical properties of rice husk ash, *Int. J. Miner., Metall. Mater.*, 16(2009), No. 2, p. 242.

[5] S. Rukzon and P. Chindaprasirt, Strength and chloride resistance of blended Portland cement mortar containing palm oil fuel ash and fly ash, *Int. J. Miner., Metall. Mater.*, 16(2009), No. 4, p. 475.

[6] H.Y. Moon., H.S. Kim, and D.H. Choi, Relationship between average pore diameter and chloride diffusivity in various concretes, *Constr. Build. Mater.*, 20(2006), No. 9, p. 725.

[7] ASTM C109, *Standard Test Method for Compressive Strength of Hydraulic Cement Mortars* (*Using* 2-*in or* [50 *mm*] *Cube Specimens*).

[8] ASTM C39, *Standard Test Method for Compressive Strength of Cylindrical Concrete Specimens.*

[9] ASTM C1202, *Standard Test Method for Electrical Indication of Concrete's Ability to Resist Chloride Ion Penetration.*

[10] Test Method RTA T362, *Interim Test for Verification of Curing Regime - Sorptivity*, Road and Traffic Authority, 2001, p. 3.

[11] N. Otsuki, S. Nagataki, and K. Nakashita, Evaluation of $AgNO_3$ solution spray method for measurement of chloride penetration into hardened cementitious matrix materials, *Constr. Build. Mater.*, 7(1993), No. 4, p.195.

[12] V. Saraswathy and H.W. Song, Corrosion performance of rice husk ash blended concrete, *Constr. Build. Mater.*, 21(2007), No. 8, p. 1779.

[13] P. Chindaprasirt and S. Rukzon, Strength, porosity and corrosion resistance of ternary blend Portland cement, rice husk ash and fly ash mortar, *Constr. Build. Mater.*, 22(2008), No. 8, p. 1601.

[14] A. Sathonsaowaphak, P. Chindaprasirt, and K. Pimraksa, Workability and strength of lignite bottom ash geopolymer mortar, *J. Harzad. Mater.*, 168(2009), No. 1, p. 44.

[15] V. Sata, C. Jaturapitakkul, and K. Kiattikomol, Utilization of palm oil fuel ash in high-strength concrete, *J. Mater. Civ. Eng.*, 16(2004), No. 6, p. 623.

[16] ASTM C618, *Standard Test Method for Compressive Strength of Cylindrical Concrete Specimens.*

[17] G.C. Isaia, A.L. Gastaldini, and R. Moraes, Physical and pozzolanic action of mineral additions on the mechanical strength of high-performance concrete, *Cem. Concr. Compos.*, 25(2003), No. 1, p. 69.

[18] S. Rukzon and P. Chindaprasirt, Use of disposed waste ash from landfills to replace Portland cement, *Waste Manage. Res.*, 27(2009), No. 6, p. 588.

[19] S. Rukzon and P. Chindaprasirt, Strength and chloride penetration of Portland cement mortar containing palm oil fuel ash and ground river sand, *Comput. Concr.*, 6(2009), No. 5, p. 391.

[20] P. Chindaprasirt., C. Jaturapitakkul, and T. Sinsiri, Effect of fly ash fineness on compressive strength and pore size of blended cement paste, *Cem. Concr. Compos.*, 27(2005), No. 4, p. 425.

[21] M.I. Khan., C.J. Lynsdale, and P. Waldron, Porosity and strength of PFA/SF/OPC ternary blended paste, *Cem. Concr. Res.,* 30(2000), No. 8, p. 1225.

[22] J.M. Khatib and P.S. Mangat, Porosity of cement paste cured at 45 ° C as a function of location relative to casting position, *Cem. Concr. Compos.*, 25(2003), No. 1, p. 97.

[23] P. Chindaprasirt., S. Rukzon, and V. Sirivivatnanon, Resistance to chloride penetration of blended Portland cement mortar containing palm oil fuel ash, rice husk ash and fly ash, *Const. Build. Mater.*, 22(2008), No. 5, p. 932.

[24] K. Ganesan., K. Rajagopal, and K. Thangavel, Evaluation of bagasse ash as supplementary cementitious material, *Cem. Concr. Compos.*, 29(2007), No. 6, p. 515.

[25] A.M. Neville, *Properties of Concrete*, 4th Ed., Longman Group UK Limited, Malaysia, 1995.

[26] F.G. Leng, N.Q. Feng, and X.Y. Lu, An experimental study on the properties of resistance to diffusion of chloride ions of fly ash and blast furnace slag concrete, *Cem. Concr. Res.*, 30(2000), No. 6, p. 989.

[27] X. He, Y. Chen, B. Ma, Y. Li, H. Zhang, and W. Zhang, Studies on small ionic diffusivity concrete, [in] *Proceedings of the International Workshop on Sustainable Development and Concrete Technology*, Beijing, 2004, p. 319.

[28] C.J. Shi and J.A. Stegemann, Acid corrosion resistance of different cementing materials, *Cem. Concr. Res.*, 30(2000), No. 5, p. 803.

[29] M.H. Zhang and V.M. Malhotra, High-performance concrete incorporating rice husk ash as a supplementary cementing material, *ACI Mater. J.*, 93(1996), No. 6, p. 629.

[30] P.K. Mehta, Studies on the mechanisms by which condensed silica fume improves the properties of concrete: durability aspects, [in] *Proceedings of International Workshop on Condensed Silica Fume in Concrete*, Ottawa, 1987, p. 17.

Ferroelectrics, 451:84–89, 2013

ISSN: 0015-0193 print / 1563-5112 online
DOI: 10.1080/00150193.2013.839223

Investigation on the Dielectric Properties of 0–3 Lead Zirconate Titanate-Geopolymer Composites

SAMPAWAN KANTAKAM,[1] KEDSARIN PIMRAKSA,[2] ATHIPONG NGAMJARUROJANA,[1] PRINYA CHINDAPRASIRT,[3] AND ARNON CHAIPANICH[1,*]

[1]Advanced Cement-Based Materials Research Unit, Department of Physics and Materials Science, Faculty of Science, Chiang Mai University, Chiang Mai 50200, Thailand
[2]Department of Industrial Chemistry, Faculty of Science, Chiang Mai University, Chiang Mai 50200, Thailand
[3]Sustainable Infrastructure Research and Development Center, Department of Civil Engineering, Faculty of Engineering, Khon Kaen University, Khon Kaen 40002, Thailand

Lead zirconate titanate (PZT)-fly ash geopolymer pastes composites of 0–3 connectivity were fabricated using 30–50% by volume. The mineralogical compositions of fly ash geopolymer materials were investigated using X-ray diffraction (XRD). The 10 mol sodium hydroxide solution and sodium silicate solution at a sodium silicate-to-sodium hydroxide ratio of 0.67 were used to prepare geopolymer pastes. The pastes were cured at 60°C for 2 days. The results showed that the dielectric constant of PZT-fly ash geopolymer pastes composites decreased with increasing PZT content at 1 KHz. The dielectric properties of PZT-fly ash geopolymer pastes composites were also found to depend on the frequency.

Keywords Dielectric properties; PZT; fly ash geopolymer; composite

1. Introduction

The use of a structural material for electronics enables a structure to provide electronic functions, thereby making the structure multifunctional and smart [1]. Ferroelectric materials are the active components in a wide variety of piezoelectric devices used in the biomedical, military, aerospace and electronics industries [2]. An important piezoelectric material is lead zirconate titanate (PZT) due to its advantageous properties and well-characterized behavior [3]. Cement-based piezoelectric composite has good compatibility with civil engineering's main structural material [4]. The advantage of using composites such as the cement-based piezoelectric composites are a better match to the host, concrete, than normal piezoelectric ceramic or other types of piezoelectric composites. In 2002, PZT-cement composites of 0–3 connectivity were fabricated using the mixture and spread normally [5]. PZT-cement composites are able to solve problems that cannot be matched.

Received December 11, 2012; in final form March 14, 2013.
*Corresponding author. E-mail: arnonchaipanich@gmail.com

Current global warming and climate change affecting the world is one of the most important issues that were raised. CO_2 release from industries is the main cause of global warming. Cement industry is a major contributor to CO_2 emissions and therefore should be improved by the reduction of the consumption of Portland cement. In the past few years, cement mixed with cement or pozzolanic materials are widely used in cement and concrete construction by replacing part of the cement. Because fly ash (FA) has been widely used to replace cement with silica fume (SF) and other natural pozzolanic materials require less water or can be used to great success [6]. On one hand, fly ash has been recognized as an important construction material since it benefits the environment and the interests of the engineering [7].

Fly ash is the fine portion of coal combustion by-products produced at power-generating stations and collected from flue gases by electrostatic precipitators [8]. In Thailand, the annual output of lignite fly ash from Mae Moh Power Station is around 3.0 million tons. Approximately 1.8 million tons are used as pozzolanic materials in the concrete industry. The level of fly ash replacement is normally restricted to less than 30% of Portland cement. Around 1.2 million tons are left over and discarded at landfill sites [9]. This lignite fly ash contains a reasonable amount of silica and alumina and can be used as a source material for making geopolymers [9–11]. Other materials containing high amount of silica and/or alumina such as metakaolin [12], bottom ash [13], and rice husk ash [14] are also suitable for being used as source materials for making geopolymers.

Aluminosilicate inorganic polymers, also called geopolymers [15]. The materials formed under high alkali conditions from aluminosilicate solid and alkali silicate solutions [15]. The geopolymer is a type of cross-linked long-chain inorganic polymer material between tetrahedral [AlO_4] and [SiO_4] units, built in three-dimensional structures. The linkages of [AlO_4] and [SiO_4] units require charge balancing from alkali ions such as Li^+, Na^+, and K^+. The mechanism of the existence of alkali ions in the molecular structure of geopolymer materials is not clearly understood at present. Usually, the accustomed viewpoint is that alkali metal ions play a charge-balancing role or are actively bonded to the matrix. Hence, the typical geopolymer composition is usually expressed as $nM_2O\cdot Al_2O_3\cdot xSiO_2\cdot yH_2O$ (M is an alkali metal element such as Li, Na, or K) [16]. Geopolymer fabrication is one of the efficient methods to form the fast inorganic ionic conductor owing to free sintering and low cost. Hydroxide and water molecules in a geopolymer material are the most important factor influencing the dielectric property and their electrical conductivity at room temperature [16]. Free alkali metal ions are also expected to play an important role in the electrical properties of geopolymer materials. Therefore, this investigation aimed at studying the dielectric properties in a frequency range of 1–100 kHz of PZT-fly ash geopolymer pastes composites.

2. Experimental

Lignite high calcium fly ash from Mae Moh Power Plant in the North of Thailand was used for this study. Its particle size distribution, chemical and mineralogical compositions were investigated. Sodium silicate to sodium hydroxide ratio of 0.67 and 10 mol NaOH solution were used as alkali solutions.

Lead zirconate titanate, $Pb(Zr_{0.52}Ti_{0.48})O_3$. PZT solid solutions were pressed with an applied pressure using uniaxial press and sintered at 1200°C for 2 h. PZT ceramic median particles size of 425 μm were used in this investigation [17].

The compositions of fly ash geopolymer pastes representing as SiO_2/Al_2O_3, Na_2O/SiO_2, Na_2O/Al_2O_3, and H_2O/Na_2O ratios are shown in the ratio of liquid alkali

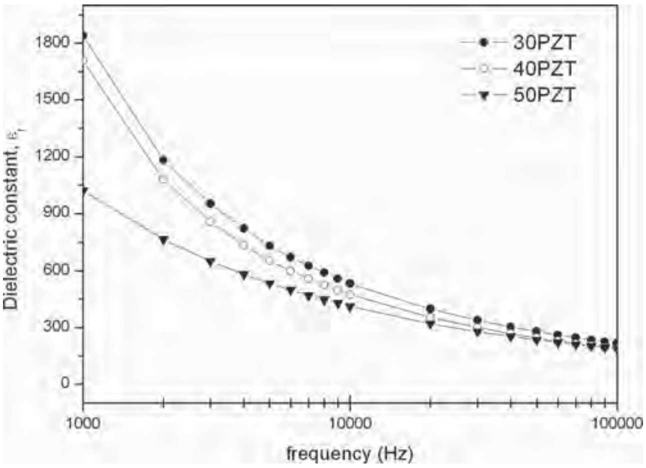

Figure 1. Dielectric constant of PZT-FA geopolymer composites at frequency for 1–100 kHz.

solution to fly ash(L/A) of 0.4. The 0–3 composites were produced by first mixing fly ash (FA) and PZT ceramic using PZT at 30%, 40% and 50% by vol. The NaOH solution was then added to the mixture and mixed for 5 min and the sodium silicate solution was added to the mixture and mixed for another 5 min and the sodium silicate to sodium hydroxide ratio of 0.67 were used. After mixing, the alkali activated fly ash paste was cast in a 15-mm-diameter and 2-mm-thick plastic mould. The cast samples were left standing in the 25°C control room for 1 h. It was then sealed to avoid the loss of water and put to cure in a controlled chamber at 60°C for 48 h. The surfaces of the specimens were coated with silver paint for dielectric property measurements.

The mineralogical and phase compositions of fly ashes and geopolymer specimens were investigated using X-ray diffraction (Philips PW 1792) using Ni-filtered Cuk radiation. Thereafter, the composites were coated silver paint. The capacitance and dielectric loss tangent were measured with a LCZ-meter (Hewlett Packard, model 4276A) under stress free at room temperature (25°C) with frequency of 100–100000 Hz. The dielectric constant was then calculated from a parallel plate capacitor equation, e.g. $\varepsilon_r = \mathrm{Cd}/\varepsilon_0\mathrm{A}$, where C is the capacitance of the sample, d and A are the thickness and the area of the electrode, respectively, and ε_0 is the dielectric permittivity of vacuum [18].

3. Results and Discussion

The dielectric properties, e.g. dielectric constant, ε_r and dielectric loss, tanδ, of the PZT-FA geopolymer composites (PZT-FA geopolymer 30/70, 40/60 and 50/50 vol%) were measured and plotted versus the frequency at room temperature, as shown in Figures 1 and 2, it can be seen that the dielectric constant and the dielectric loss decreases sharply with increasing frequency. The dielectric constant values of the composites are significantly higher at low frequency. With increasing frequency, some polarizations, especially interfacial polarizations cannot follow the change of electric field because of the long time for the construction of space charge polarization. Therefore, the dielectric constant of the composites is lower at high frequency [19]. Dielectric constant, ε_r value of 30% PZT composite is 1840 at 1 kHz

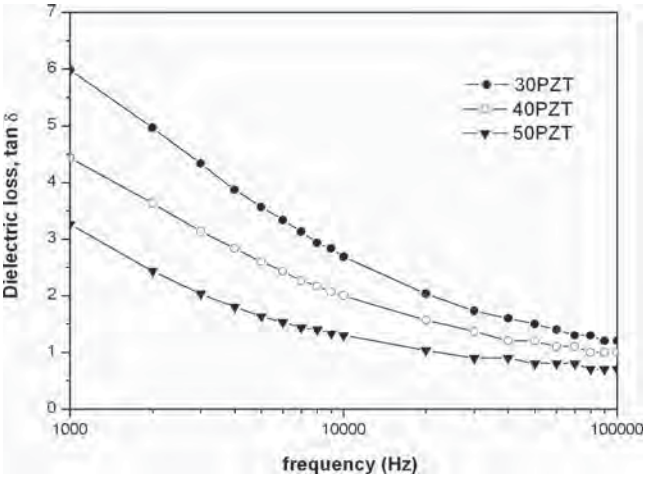

Figure 2. Dielectric loss of PZT-FA geopolymer composites at frequency for 1–100 Hz.

and 188 at 100 kHz (Fig. 1). Dielectric loss, *tanδ* value of 30% PZT composite is 5.9 at 1 kHz and 1.2 at 100 kHz (Fig. 2).

The variation of dielectric properties, e.g. the dielectric constant, ε_r and dielectric loss, *tanδ* as a function of content of PZT has been studied at the frequency of 1 kHz and the results are plotted in Figure 3, it can be seen that there is roughly nonlinear decrease of the dielectric constant values of the composites as a function of the PZT content where ε_r value of 1834.2 (30% PZT), 1706.2 (40% PZT) and 1017.6 (50% PZT). From the previous studies the dielectric constants at 1 kHz of geopolymer pastes and PZT are found to be $\approx 1 \times 10^5$ and $\approx 1 \times 10^3$, respectively [4, 20]. The dielectric loss was found to reduce with increasing PZT content where *tanδ* value = 5.9, 4.3 and 3.2 for 30%, 40% and 50% PZT, respectively.

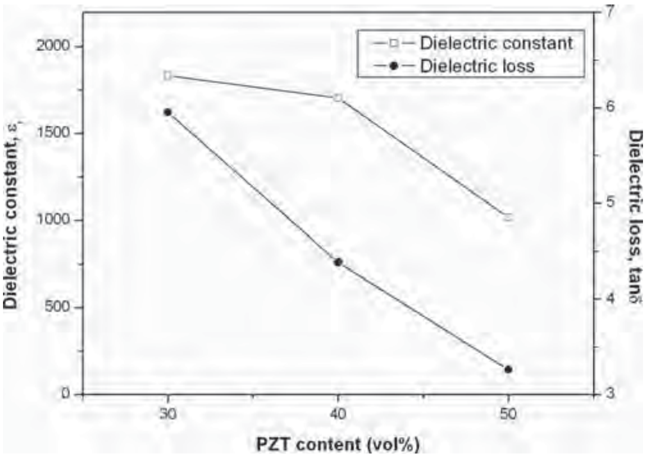

Figure 3. Effect of PZT content on dielectric constant and dielectric loss of PZT-FA geopolymer composites at frequency for 1 kHz.

4. Conclusion

0–3 PZT-FA geopolymer composites (PZT percentages of 30, 40, and 50 by volume) were prepared using PZT ceramic and FA geopolymer paste. Both the ε_r and *tanδ* decreases with increasing frequencies from 1–100 kHz. At 1 kHz, ε_r value can be seen to decrease from 1834.2 to 1017.6 (30% to 50% PZT) and tanδ value reduced from 5.9 to 3.2 (30% to 50% PZT). The dielectric constant decreases with increasing content of PZT in PZT-FA geopolymer composites system.

Acknowledgments

The authors are grateful to members of staff at the Electroceramics Research Laboratory, Faculty of science, and Chiang Mai University for the research facilities made possible for this research work. The authors would like to express their gratitude for TRF Functional Materials Research Grant awarded to Assistant Prof. Dr. Arnon Chaipanich by the Thailand Research Fund (TRF). The authors are also grateful to the Thailand Research Fund (TRF) for the TRF Senior Research Scholar Contract No. RTA5480004 awarded to Professor Dr. Prinya Chindaprasirt.

References

1. D. D. L. Chung, Piezoresistive cement-based materials for strain sensing, *J. Intel. Mat. Syst. Str.* **13**(9), 599–609 (2002).
2. J. L. Jones, M. Hoffman, and S. C. Vogel, Ferroelastic domain switching in lead zirconate titanate measured by in situ neutron diffraction, *Mech. of Mat.* **39**, 283–290 (2007).
3. J. M. Calderon-Moreno, Stress induced domain switching of PZT in compression tests, *Mats. Sci. Eng. A.* **315**, 227–230 (2001).
4. A. Chaipanich, Dielectric and piezoelectric properties of PZT–cement composites, *Current. Appl. Phys.* **7**, 537–539 (2007).
5. Z. Li, D. Zhang, and K. Wu, Cement-based 0–3 piezoelectric composites, *J.Am. Ceram. Soc.* **85**, 305–313 (2002).
6. W. Wongkeo, P. Thongsanitgarn, and A. Chaipanich, Compressive strength and drying shrinkage of fly ash-bottom ash-silica fume multi-blended cement mortars, *Mater. Design.* **36**, 655–662 (2012).
7. A. Chaipanich, T. Nochaiya, W. Wongkeo, and P. Torkittikul, Compressive strength and microstructure of carbon nanotubes–fly ash cement composites, *Mats. Sci. Eng. A.* **527**, 1063–1067 (2010).
8. B. W. Jo, S. K. Park, and J. B. Park, Properties of concrete made with alkali-activated fly ash lightweight Aggregate (AFLA), *Cem. Concr. Compos.* **29**, 128 (2007).
9. P. Chindaprasirt, C. Jaturapitakkul, W. Chalee, and U. Rattanasak, Comparative study on the characteristics of fly ash and bottom ash geopolymers, *Waste Manage.* **29**, 539 (2007).
10. P. Chindaprasirt, T. Chareerat, and V. Sirivivatnanon, Workability and strength of coarse high calcium fly ash geopolymer, *Cem. Concr. Compos.* **29**, 224 (2007).
11. U. Rattanasak and P. Chindaprasirt, Influence of NaOH solution on the synthesis of fly ash geopolymer, *Miner. Eng.* **22**, 1073 (2009).
12. P. De Silva, K. Sagoe-Crenstil, and V. Sirivivatnanon, Kinetics of geopolymerization: Role of Al_2O_3 and SiO_2, *Cem. Concr. Res.* **37**, 512 (2007).
13. A. Sathonsaowaphak, P. Chindaprasirt, and K. Pimraksa, Workability and strength of lignite high bottom ash geopolymer mortar, *J. Hazard. Mater.* **168**, 44 (2009).
14. S. Detphan and P. Chindaprasirt, Preparation of fly ash and rice husk ash geopolymer, *Int. J. Miner. Metall. Mater.* **16**, 720 (2009).

15. K. J. D. Mackenzie and M. J. Bolton, Electrical and mechanical properties of aluminosilicate inorganic polymer composites with carbon nanotubes, *J. Mater. Sci.* **44**, 2851 (2009).
16. X. M. Cui, G. J. Zheng, Y. C. Han, F. Su, and J. Zhou, A study on electrical conductivity of chemosynthetic Al2O_3-2SiO_2 geopolymer materials, *J. Power Sources.* **184**, 652 (2008).
17. R. Rianyoi, R. Potong, A. Ngamjarurojana, and A. Chaipanich, Influence of barium titanate content and particle size on electromechanical coupling coefficient of lead-free piezoelectric ceramic-Portland cement composites, *Ceram Inter.* **39**, S47–S51 (2013).
18. R. Yimnirun, S. Wongsaenmai, A. Ngamjarurojana, and S. Ananta, Effects of uniaxial stress on dielectric properties of ferroelectric ceramics, *Current. Appl. Phys.* **6**, 520–524 (2006).
19. X. Cheng, S. Huang, J. Chang, and Z. Li, *J. Appl. Phy.* **101**, 094110 (2007).
20. S. Hanjitsuwan, P. Chindaprasirt, and K. Pimraksa, Electrical conductivity and dielectric property of fly ash geopolymer pastes, *Int. J. Miner. Metall. Mater.* **10**, 94 (2011).

J Therm Anal Calorim (2013) 113:1079–1090
DOI 10.1007/s10973-013-3017-3

Thermogravimetry of ternary cement blends

Effect of different curing methods

**Watcharapong Wongkeo · Pailyn Thongsanitgarn ·
Prinya Chindaprasirt · Arnon Chaipanich**

Received: 28 September 2012 / Accepted: 25 January 2013 / Published online: 17 April 2013

Abstract This study reports the microstructure characteristic and compressive strength of multi-blended cement under different curing methods. Fly ash, ground bottom ash, and undensified silica fume were used to replace part of cement at 50 % by mass. Mortar and paste specimens were cured in air at ambient temperature, water at 25, 40, and 60 °C and sealed with plastic sheeting for 28 days. In addition, these specimens were cured in an autoclave for 6, 9, and 12 h. Results indicated that the compressive strength of multi-blended mixes containing silica fume 10 % by mass cured with plastic sealed and cured in water at 25 and 40 °C was similar to or higher than the corresponding Portland cement control at 28 day. Moreover, the mixes containing silica fume 10 % by mass cured in water at 60 °C had higher compressive strength than Portland cement control. X-ray diffraction and thermogravimetry results confirmed that there was increased pozzolanic reaction with increasing silica fume content which relates to the increasing in strength. For autoclaved curing, the compressive strength of multi-blended cement specimens with silica fume (total of 50 % replacement) was noticeably higher than control Portland cement mix and was highest when autoclaving time was 9 h. X-ray diffraction results showed the pattern of 0.9, 1.1, and 1.4 nm tobermorite crystalline phases as the main product of this curing. Thermogravimetry results showed dehydration of 1.4 nm tobermorite and 1.1 nm tobermorite at about 80–90 and 135–150 °C, respectively. Tobermorite (also shown by scanning electron microscope) thereby as a result lead to significant compressive strength improvement in the short time of autoclaved curing.

Keywords Blended cement · Fly ash · Bottom ash · Silica fume · Microstructure · Compressive strength

Introduction

The production of Portland cement is one of major contributor to CO_2 emission which implicated to global warming and climate change hence it should be improved and reduced. The reduction of cement consumption by mean of using Portland cement replacement materials has been widely investigated. Pozzolanic materials such as fly ash (FA), granulated blast furnace slag (GGBS), silica fume (SF), and other natural pozzolan materials are widely used to replace part of Portland cement as blended cement. Many researchers have studied high-volume fly ash (HVFA) as a Portland cement replacement (binary blended cement) in mortar or concrete but only a few studies have been carried out to determine properties of multi-blended cement at high level (volume) content. In commercial practice, the dosage of FA is limited to 15–20 % by mass of the total cementitious material while HVFA generally has 50 % or more of FA by mass of the cementitious material [1]. However, the strengths of HVFA concrete are lower than that of only Portland cement concrete (PC) at early age [2–6].

SF is widely used as a pozzolanic materials in blended cement or as a mineral admixture in high strength concrete (HSC) due to its high reactivity thus can give strength at early age compared with FA or other mineral admixtures.

W. Wongkeo · P. Thongsanitgarn · A. Chaipanich (✉)
Advanced Cement-Based Materials Research Unit,
Department of Physics and Materials, Faculty of Science,
Chiang Mai University, Chiang Mai 50200, Thailand
e-mail: arnon@chiangmai.ac.th

P. Chindaprasirt
Sustainable Infrastructure Research and Development Center,
Department of Civil Engineering, Faculty of Engineering,
Khon Kaen University, Khon Kaen 40002, Thailand

SF particle is the nano size range (≈ 100 nm) and contained more than 85 % of SiO_2 in amorphous form. Previous studies [7–10] reported that the utilization of nano size range material as cement replacement or admixture materials have been found to improve physical and mechanical properties of Portland cement, especially blended cement with pozzolanic materials. However, the usage of SF is limited due to its tendency to agglomerate and the high water demand [11]. Thus, mix designs involving high-volume SF also use high level water reducers or superplasticizers. The incorporations of FA and SF have been found to offer enhanced properties of blended cement concrete than FA or SF concrete alone. Nassif et al. [12] studied the effect of pozzolanic materials and curing methods on the elastic modulus of high performance concrete (HPC) using FA, SF, and GGBS as pozzolanic materials in blended cement. It is found that concrete incorporating FA and SF can improve slump of concrete when compared to concrete containing SF only. Guneyisi et al. [13] reported that the compressive strength of ternary (PC + FA + SF) blended cement was higher than that of binary (PC + FA) blended cement at the same replacement level. In addition, Barbhuiya et al. [14] investigated the properties of FA concrete modified with hydrated lime and SF. The FA concrete incorporating SF improved the early strength of concrete. Nochaiya et al. [15] studied the utilization of FA with SF and properties of Portland cement–fly ash–silica fume concrete. It is also reported that the utilization of SF with FA was found to increase the compressive strength of concrete at early ages (pre 28 days).

Bottom ash (BA) is another by-product of thermoelectric power plants occurring at the same time as FA. It consists of chemical composition similar to FA. However, the utilization of BA in the substitution of Portland cement is limited due to its high particle size and porous particle, compared to FA. However, BA can be used to replace part of cement by reducing the particle size. Cheriaf et al. [16] studied the pozzolanic properties of BA by varying the time of grinding. It was found that the pozzolanic activity of BA increased with increased time of grinding and strength can be improved. Wongkeo and Chaipanich [17] studied the use of ground BA and SF to produce the bottom ash lightweight concrete (BLWC). It was found that the properties of BLWC improved when SF was added to the mix.

Curing of cement, mortar or concrete specimens is very important for their strength and durability development. Curing is a process to keep their specimens saturated or to prevent loss of moisture that is essential for the hydration of cement. The rate and degree of hydration, strength gain, and other properties depend on the curing process. Nowadays, curing is more important for concrete that contains mineral admixtures than for normal concrete [18]. Curing at ambient temperature can be divided into two groups: (1) water curing and (2) sealed curing. Water curing is better than sealed curing, particularly important when using low w/c ratio concrete ($w/c < 0.40$) [19]. In addition, the rate of hydration of cement increased with increasing curing temperature, especially at lower degree of hydration [20]. In practice, concrete is mostly cured by covering it with wet burlap, waterproof paper, or plastic sheeting. Autoclaved is synonymous of high-pressure steam curing. The curing temperature of this curing exceeds 100 °C. Normally, the range of curing temperature used in autoclaving is 160–210 °C (320–410 °F) at steam pressure of 6–20 atm [19]. The chemistry of hydration changes under these conditions have substantially different properties from products cured below 100 °C. In the absence of reactive silica (PC only) the α-C_2SH phase is formed whereas tobermorite ($C_5S_6H_5$) phase is formed on continued heating in the presence of reactive silica [21]. The change of hydration product has lead to strength gain and properties development in the short time of curing. Thus, the used of suitable curing method can improve strength and properties of blended cement at early age.

This paper reports the effect of curing methods on the compressive strength and characteristic of blends cement mortar containing FA, ground bottom ash (BA), and SF. Curing methods such as air cured at ambient temperature, sealed cured with plastic sheeting, water cured at 25, 40, and 60 °C, and high-pressure steam curing (autoclaved) were used in this study.

Experimental

Materials

Ordinary Portland cement type 1 (PC) was used in the binder phase of this study. FA and BA obtained from Mae Moh power plant in Lampang, Thailand and undensified SF grade 920-U produced by Elkem were used as supplementary materials. The chemical compositions and physical properties of raw materials (PC, FA, BA, and SF powder) are given in Table 1. River sand with specific gravity of 2.65 was used as fine aggregate of mortar. Napthalene based superplasticizer from Sika (Thailand) Limited was used in this study.

Samples preparation and test methods

The selective dissolution method with 1 % HF (hydrofluoric acid) solution was used to determine the amorphous

Table 1 Chemical compositions and physical properties of materials used in this research

	PC	FA	BA	SF
Chemical composition/%				
SiO_2	20.64	45.37	47.592	93.549
Al_2O_3	4.848	20.65	19.1	0.556
CaO	63.62	10.43	10.16	1.128
Fe_2O_3	3.17	12.31	14.34	0.172
MgO	1.137	2.127	1.477	0.747
Na_2O	0.51	1.331	1.084	0.137
K_2O	0.812	1.496	1.213	1.047
P_2O_5	0.32	0.245	0.164	0.531
TiO_2	0.213	0.517	0.311	0.002
SO_3	2.753	2.526	2.436	1.006
Loss on ignition	2.076	3.002	2.124	1.16
Specific gravity	3.15	2.10	2.70	2.20
Average particle size/µm	8.31	5.22	7.81	0.1

phase of FA, BA, and SF powder. The procedure was followed and applied by Fernandez-Jimenez et al. [22]. 1 g of each powder was added to a plastic beaker containing 100 mL of 1 % HF. The mix was stirred using magnetic stirrer for 6 h at ambient temperature and then filtered using filter paper. The filter paper and the insoluble residue was oven-dried at 105 °C for 24 h. The amorphous phase was determined by subtracting the final from the initial mass.

In this study, FA, BA, and SF were used to replace part of PC. The replacement levels of FA were 30, 40, 45, and 50 % while those of BA were 10, 15, and 20 % by mass of binder. SF was used to replace PC at 5 and 10 % by mass. The mix proportions and mix design are summarized in Table 2. The seven mortar mixes were designed having a constant water/binder ratio of 0.485 and flow of mortar of 110 ± 5 mm. The mortar mixes were mixed and then cast into 50 × 50 × 50 mm molds and compacted using a vibrating table. The mortar specimens were stored in molds for 24 h and then demolded. All the mortar specimens were cured in air at ambient temperature (at 26–30 °C and relative humidity 50–65), water at 25, 40, and 60 °C and sealed with plastic sheeting for 28 days. For autoclaved curing, the mortar specimens were autoclaved at 130 °C and under pressure 20 psi for 6, 9, and 12 h. After the end of autoclaved curing periods for 6, 9, and 12 h, all of the samples were left in a autoclaved chamber for cooling period of 12 h before compressive strength, XRD, and TG tests. The compressive strength was tested using tecnotest compression testing machines. Moreover, the identification phases of the samples was investigated using X-ray diffractometer (XRD; PHILIPS X'Pert MPD) and thermogravimetry using the Mettler Toledo TG/SDTA 851e (inert atmosphere 180 with N_2 flow of 30 mL min^{-1}, heating rate 10 °C min^{-1}, analysis range 30–800 °C). For XRD and TG testing, samples were immersed in acetone after reaching the required curing age to stop hydration process before characterization tests. For autoclaved curing, the samples were immersed in acetone after the end of cooling period for 12 h. The 28 days of hydration were selected to identify phases using XRD and TG technique. This is due to the hydration process that would have mostly occurred by 28 days and the standard test age used to determine the relative strength of concrete in practice.

Table 3 Percentage of insoluble and soluble phase of pozolanic materials after treated with 1 % HF solution

Raw materials	Insoluble residue/%	Soluble phase/%
FA	37.00	63.00
BA	47.36	52.64
SF	25.94	74.06

Table 2 Mix proportion of blended cement mortar

Materials	Mix						
	100PC	50FA	45FA5SF	40FA10SF	30FA 20BA	30FA15BA5SF	30FA10BA10SF
OPC/kg m^{-3}	538	269	269	269	269	269	269
FA/kg m^{-3}	–	269	242	215	161	161	161
SF/kg m^{-3}	–	–	27	54	–	27	54
BA/kg m^{-3}	–	–	–	–	108	81	54
Aggregate/kg m^{-3}	1,480	1,420	1,420	1,420	1,436	1,430	1,428
Water/kg m^{-3}	261	261	261	261	261	261	261
SP/%	0.8	–	0.4	0.8	0.4	0.6	1.1
CaO/SiO_2 ratio	3.08	1.12	1.03	0.95	1.11	1.02	0.97
$CaO/(SiO_2 + Al_2O_3)$ ratio	2.50	0.81	0.78	0.74	0.81	0.77	0.76

Results and discussion

Characterization of raw materials

The main constituents of FA and BA powder are SiO_2 and Al_2O_3 while more than 90 % of SiO_2 is presented in SF powder (as shown in Table 1). It is worthwhile to point out that more than 10 % of CaO is presented in FA and BA powder. Table 3 shows the percentage of insoluble and soluble phase of FA, BA, and SF powder after treated with 1 % HF solution. The insoluble residue of all samples refers to crystalline phase while the amorphous phase (soluble phase) was dissolved in HF solution. The main chemical compositions of soluble phase are SiO_2 and Al_2O_3. The results showed the amorphous phase of FA, BA, and SF powder of 63, 52.64, and 74.06 %, respectively. It is found that FA powder has more amorphous phase than BA powder. Thus, it can be expected that FA powder is more reactive than BA powder. X-ray diffraction was used to determine crystalline phase of powder sample. The crystalline phase of FA powder consists of anhydrite, magnetite, gehlenite, lime, quartz, and chabazite while BA powder contains of augite, magnetite, and anorthite as main crystalline compounds, with hematite, gehlenite, quartz, corundum, and chabazite as minor constituents (as shown in Fig. 1). BA powder can be seen to contain more crystalline phases than FA powder which relates to amorphous phase determination by the selective dissolution method.

X-ray diffraction analysis

The XRD analyses of 28 day hydration blended cement pastes are shown in Fig. 2. The XRD patterns of all specimens cured in water at 25 and 60 °C (Fig. 2a, b) indicated the main peaks of calcium hydroxide ($Ca(OH)_2$), ettringite ($Ca_6Al_2(SO_4)_3(OH)_{12}\cdot 26H_2O$), and C–S–H ($Ca_2SiO_4H_2O$) phase which is the main hydration product. In addition, small unhydrated peaks of Alite (Ca_3SiO_5:C_3S) and Belite (Ca_2SiO_4:C_2S) phases (originated from Portland cement) and calcite ($CaCO_3$) are also detected. The hydration process may be determined using XRD by determining the amount of $Ca(OH)_2$ or unreacted cement constituents [23]. However, some C–S–H crystalline phase can be detected by XRD which can also give an indication of the hydration process. From the results, it is found that the C–S–H phase of samples cured in water at 25 °C cannot be detected in XRD patterns. This is due to the C–S–H gel is mostly formed in the poorly crystalline form or amorphous

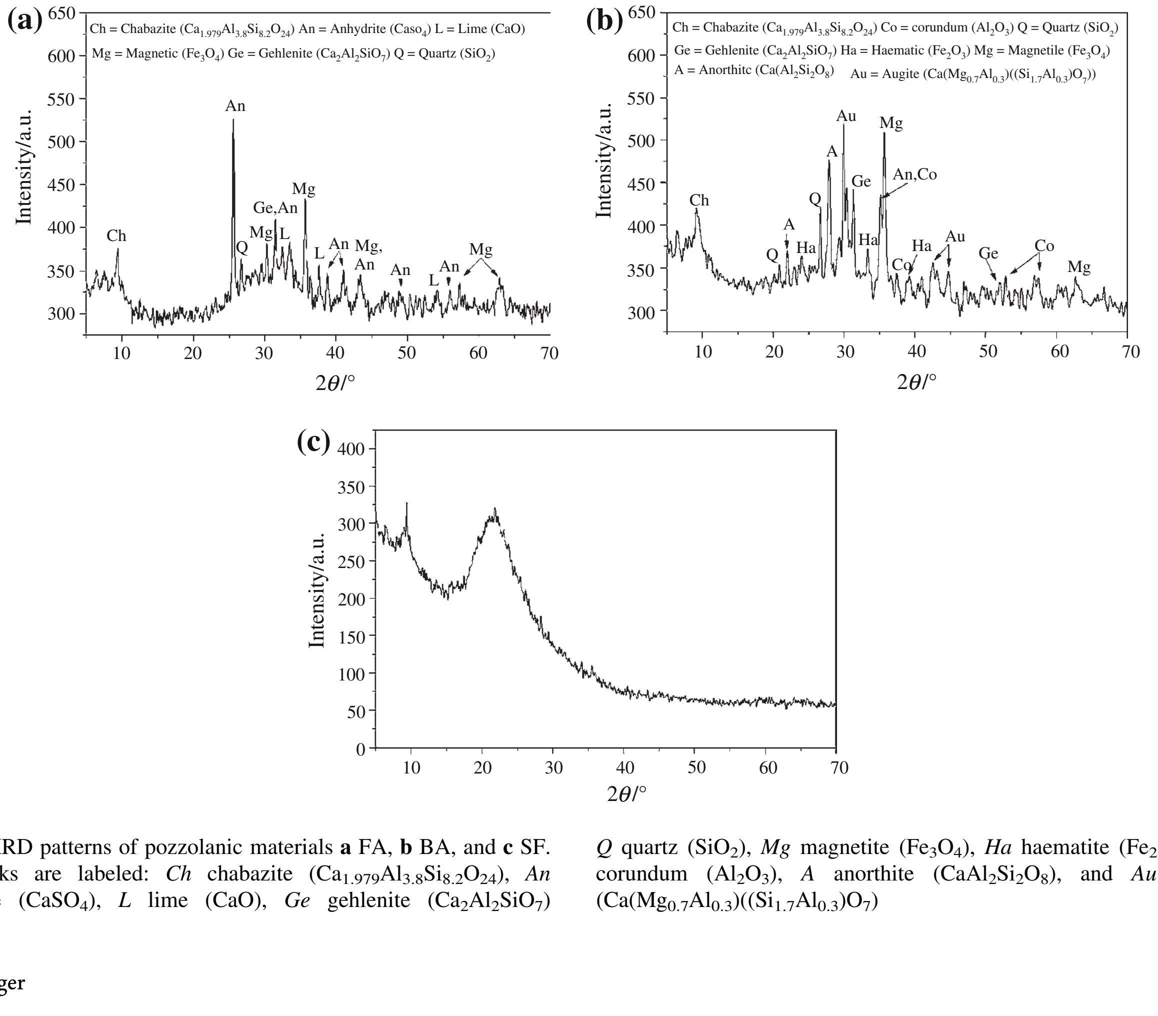

Fig. 1 XRD patterns of pozzolanic materials **a** FA, **b** BA, and **c** SF. The peaks are labeled: *Ch* chabazite ($Ca_{1.979}Al_{3.8}Si_{8.2}O_{24}$), *An* anhydrite ($CaSO_4$), *L* lime (CaO), *Ge* gehlenite ($Ca_2Al_2SiO_7$) *Q* quartz (SiO_2), *Mg* magnetite (Fe_3O_4), *Ha* haematite (Fe_2O_3), *Co* corundum (Al_2O_3), *A* anorthite ($CaAl_2Si_2O_8$), and *Au* augite ($Ca(Mg_{0.7}Al_{0.3})((Si_{1.7}Al_{0.3})O_7)$)

Fig. 2 XRD patterns of blended cement **a** water curing at 25 °C, **b** water curing at 60 °C, and **c** autoclaved curing for 6 h

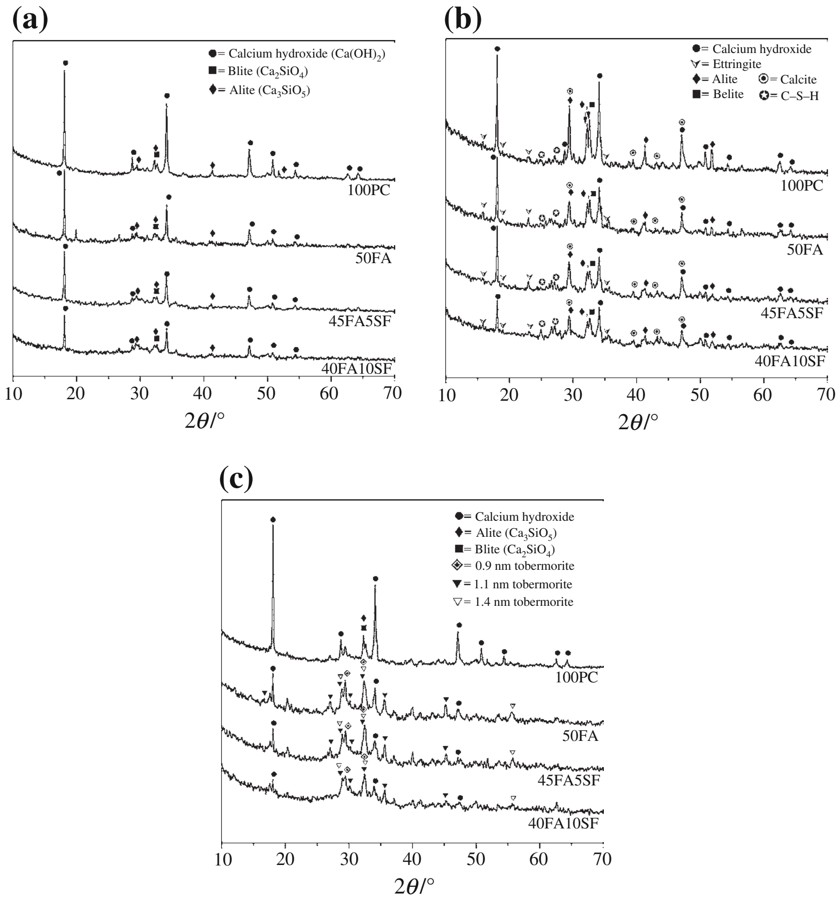

disordered structures at room temperature, but the stable and highly crystalline C–S–H gel will be formed when heated [24–26]. Thus, the C–S–H gel in samples cured at 25 °C is not detected in XRD, but can be detected in the samples cured at 60 °C. In this study, it is found that the intensity of $Ca(OH)_2$ peak of the mix containing pozzolanic materials (50FA, 45FA5SF, and 40FA10SF mixes) was lower than that of the PC control. Moreover, the intensity of $Ca(OH)_2$ peak can be seen to decrease with increased SF substitution. The unhydrated peaks of C_3S and C_2S phases also decreased due to the dilution effect. The reduction of intensity of $Ca(OH)_2$ peak is accompanied by an increase in intensity of C–S–H phase due to increasing pozzolanic reaction and C–S–H is seen to increase with increased SF substitution. The intensity of C–S–H phase of specimen cured in water at 60 °C is higher than that of specimen cured in water at 25 °C. This indicates that the pozzolanic reaction was improved with an increased in curing temperature, especially for mixes containing SF.

For specimen cured by autoclaved method for 6 h (Fig. 2c), the XRD patterns of all specimens show the main peaks of $Ca(OH)_2$ phase and peaks of C_3S and C_2S phases similar to the specimens cured in water at 25 and 60 °C. However, blended cement specimens showed the XRD patterns of 0.9 nm tobermorite ($Ca_5Si_6O_{16}(OH)_2$), 1.1 nm tobermorite ($Ca_5Si_6O_{16}(OH)_2{\cdot}4H_2O$), and 1.4 nm tobermorite ($Ca_5Si_6O_{16}(OH)_2{\cdot}8H_2O$) which exhibits the same basal spacing as the 1.1 nm tobermorite. Normally, tobermorite in autoclaved cement has only been found as the 1.1 nm tobermorite phase. Substitution of a part of the Si atoms in SiO_4 tetrahedral with Al is observed in synthetic 1.1 nm tobermorite. The 1.4 nm tobermorite shows only a minor degree of Al substitution [27]. This reason may lead to 0.9 nm tobermorite formation. Thus, the Al_2O_3 content which is the composition of pozzolanic material and $CaO/(Al_2O_3 + SiO_2)$ ratio has an effect on the formation of tobermorite. The consistency of tobermorite formation of 1.1 nm thus shows that pozzolanic reaction of blended cement is improved under autoclaved curing.

Thermogravimetry

Thermogravimetry (TG) of 28 day hydrated cement pastes are shown in Fig. 3. The results are plotted as derivative thermogravimetric (DTG) curves in order to identify the detected phases (Fig. 4). For normal hydration, the first major mass loss located below 200 °C is the result of dehydration reactions of several hydrates such as C–S–H,

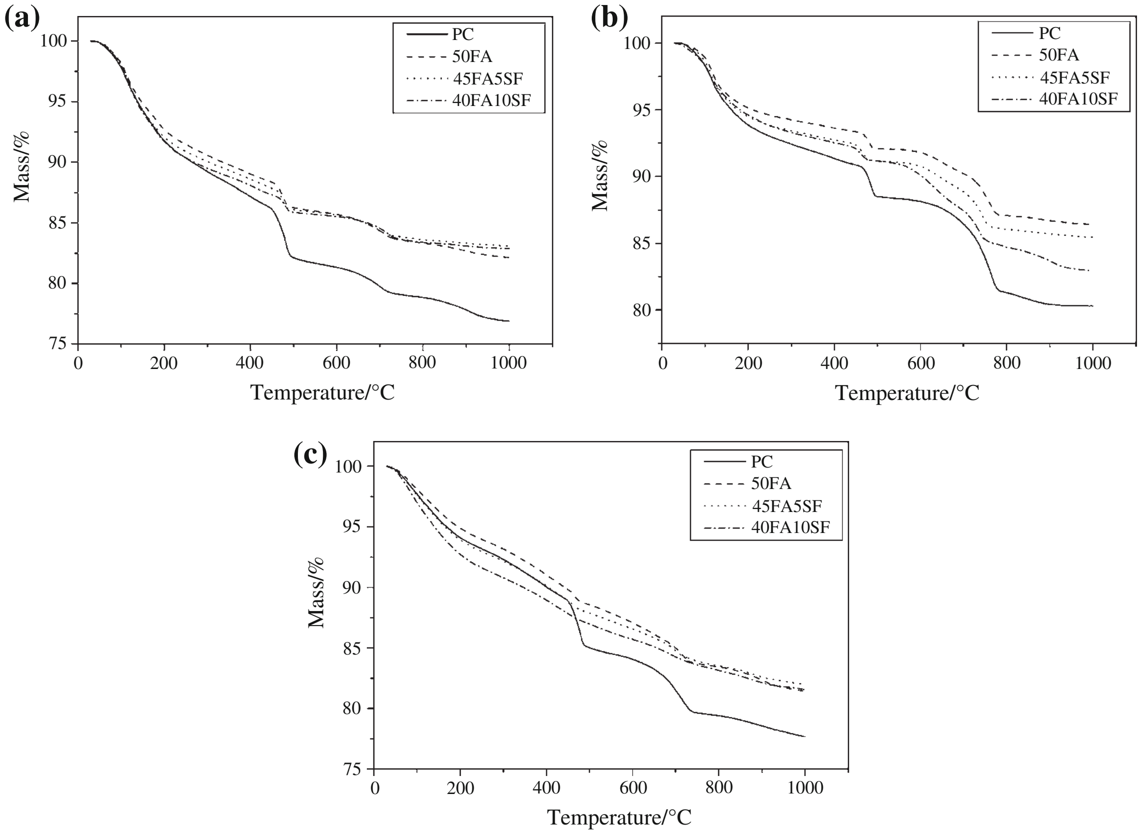

Fig. 3 TG curves of blended cement pastes **a** water curing at 25 °C, **b** water curing at 60 °C, and **c** autoclaved curing for 6 h

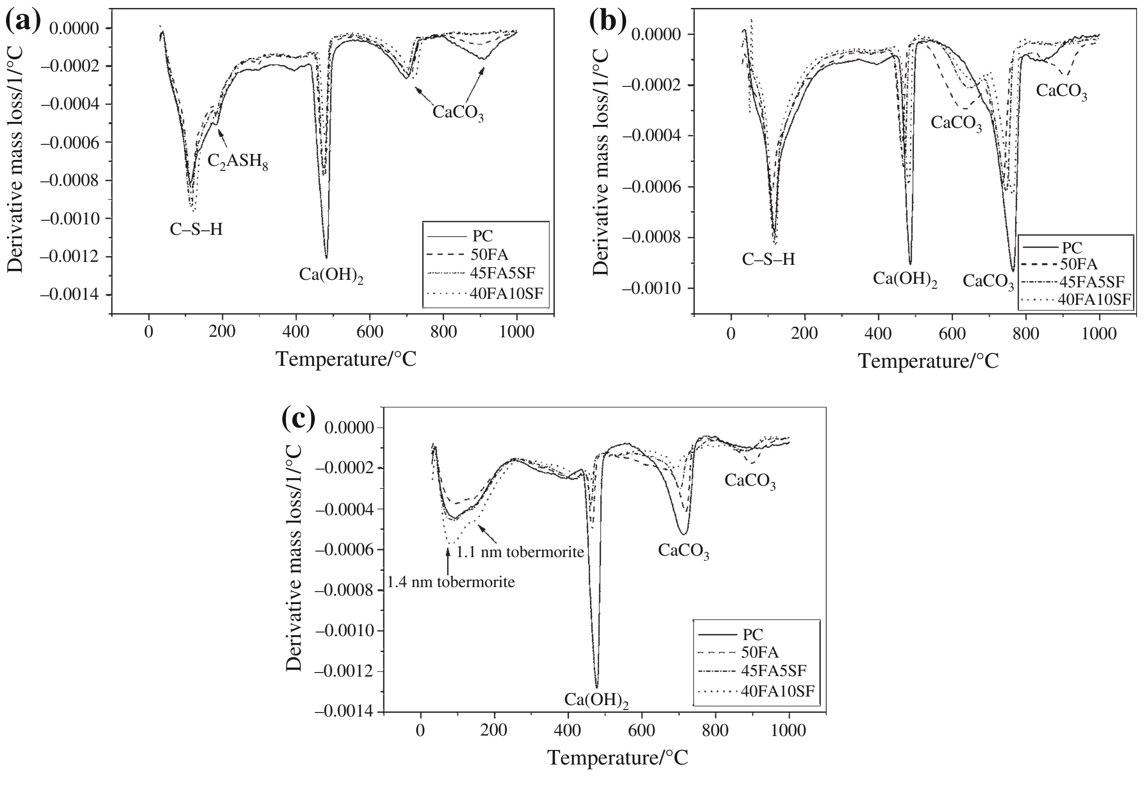

Fig. 4 DTG curves of blended cement pastes **a** water curing at 25 °C, **b** water curing at 60 °C, and **c** autoclaved curing for 6 h

ettringite (AFt) monosulfoaluminate (AFm), and gehlenite (C_2ASH_8) [28–30]. The second major mass loss, observed at 450–550 °C, corresponds to the dehydroxylation of portlandite ($Ca(OH)_2$). The third loss of mass appears at 750–900 °C and corresponds to the decarbonation of calcium carbonate [23]. In this study, the DTG curves of blended cement cured in water at 25 and 60 °C (Fig. 4a, b) show detection of C–S–H at ≈110–120 °C and $Ca(OH)_2$ at ≈460–480 °C, respectively. In addition, gehlenite hydrate (C_2ASH_8) was shown in specimen cured in water at 25 °C, but it disappeared in specimen cured in water at 60 °C. Moreover, the DTG curves of specimen cured in water at 25 °C show two strong endothermic peaks of $CaCO_3$ at about 700–720 and 890–905 °C. The first peak was decomposed of normal calcite in Portland cement. The second peak may be decomposed of another calcite due to decomposition of calcite is affected by surface area, particle size, partial pressure of CO_2, and impurities such as magnesium [31] or another formation such as carboaluminate ($Ca_4Al_2(OH)_{12}\cdot CO_3\cdot 5H_2O$) [32]. Furthermore, the DTG curves of specimen cured in water at 60 °C show three strong peaks of $CaCO_3$ at about 630–660 °C, 730–765 °C, and 890–905 °C, respectively, but these were observed in blended cement specimens only. From these results, it is found that the intensity of C–S–H curves of specimen containing SF (both cured in water at 25 and 60 °C) was higher than that of specimen containing only FA and it increased with increased SF content. This result was confirmed to the increasing of pozzolanic reaction with increased SF content.

For specimen cured by autoclaved method for 6 h (Fig. 4c), DTG curves show two peaks of C–S–H (tobermorite phase) at about 80–90 °C and 135–150 °C, $Ca(OH)_2$ peak at about 450–475 °C, and two peaks of $CaCO_3$ at about 680–715 °C and 870–900 °C, respectively. In the case of C–S–H peaks, the first peak is the result of dehydration of 1.4 nm tobermorite and the second peak corresponds to the dehydration of 1.1 nm tobermorite. The lower temperature dehydration of 1.4 nm tobermorite is attributed to a single-chain structure of silicate anion while 1.1 nm tobermorite has a double-chain structure of silicate anion [27].

Table 4 shows the percentages of mass loss to overall mass loss of binary and ternary blended cement pastes at 28 days hydration under water curing at 25, 60 °C and autoclaved curing for 6 h. To consider only first group of mass loss, the percentages of mass loss to overall mass loss of binary blended cement pastes under water curing at 25 and 60 °C were lower than PC control. However, the mass loss to overall mass loss of ternary blended cement pastes was higher than PC control and increased with increasing SF replacement. This indicates that the reaction (both of hydration and pozzolanic reaction) of blended cement paste was improved when containing SF replacement. Moreover, it was found that the percentages of mass loss to overall mass loss of all specimens cured with water 60 °C were higher than specimens cured with water 25 °C. This was due to the rate of reaction was increased with increasing temperature during moist curing. In addition, it can be observed that the percentages of mass loss to overall mass loss of $Ca(OH)_2$ group of binary and ternary blended cement decrease, compared to PC control. This was due to the $Ca(OH)_2$ was consumed by pozzolanic reaction of FA and SF which results to increasing C–S–H gel. However, the reduction of $Ca(OH)_2$ group not only decreased by pozzolanic reaction, but also effect by carbonation reaction to $CaCO_3$ formation [33]. For specimens cured with autoclaved, first group of mass loss was mostly the mass loss of C–S–H due to ettringite are not formed at higher temperature. Both the sulfate and alumina apparently enter into the C–S–H and tobermorite structure. The role of alumina is increasing the rate of crystallization of tobermorite [19]. It was found that the percentages of mass loss to overall mass loss of binary and ternary blended cement pastes were higher than PC control. This may be due to the different structure of α-C_2SH, obtained from PC control and tobermorite, which is the main product of binary and ternary blended cement pastes.

Table 4 Mass loss of blended cement pastes under water curing at 25, 60 °C and autoclaved curing for 6 h

Mix	Mass loss to overall mass loss/%								
	Free water + C–S–H + Ettringite + C_2ASH_8/AFm			$Ca(OH)_2$			$CaCO_3$		
	Water cured at 25 °C	Water cured at 60 °C	Autoclaved 6 h	Water cured at 25 °C	Water cured at 60 °C	Autoclaved 6 h	Water cured at 25 °C	Water cured at 60 °C	Autoclaved 6 h
PC	33.48	41.35	31.23	20.76	12.60	21.24	11.88	36.29	22.35
50FA	30.48	40.86	32.84	14.03	9.81	8.17	14.67	24.11	26.24
45FA5SF	40.85	44.48	39.90	11.36	9.86	5.55	11.71	20.83	18.60
40FA10SF	44.31	48.09	47.23	8.92	7.41	7.87	14.13	17.96	15.93

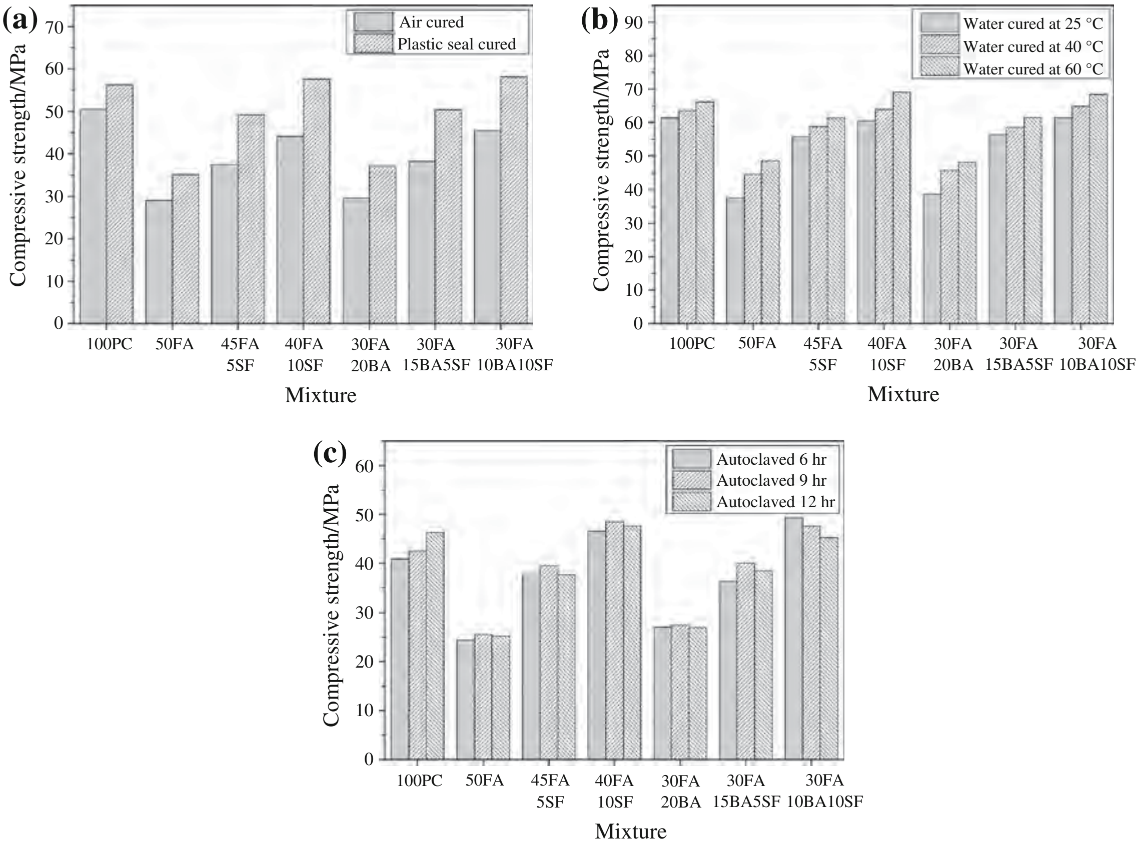

Fig. 5 Compressive strength of blended cement mortars **a** air and sealed curing, **b** water curing at 25, 40, and 60 °C, and **c** autoclaved curing

Compressive strength

The relationship between the compressive strength of 28 days blended (binary, ternary, and quaternary blended) cement under various curing method at ambient temperature and mix designs is presented in Fig. 5. Figure 5a shows the compressive strength of specimens cured in air and those sealed with plastic sheeting. It can be observed that the compressive strength of blended cement cured in air and sealed with plastic sheeting increased with increasing SF replacement. The compressive strength of all mixes cured with plastic sealed was higher than those cured in air. This is due to sealed curing method prevents loss of moisture of specimen and hence allows continued hydration. Therefore, specimen that was cured by sealed method preventing against moisture loss can improve strength more effectively than specimen cured in air. The compressive strength of all blended cements (binary, ternary, and quaternary systems) mixes cured in air was found to be lower than that of PC control. For specimen cured with plastic sealed, the compressive strength of 50FA, 45FA5SF, 30FA20BA, and 30FA15BA5SF mixes were also lower than that of PC control, while 40FA10SF and 30FA10BA10SF mix show the compressive strength similar to that of PC control. From these results, it was found that the compressive strength of the mixes containing only FA and BA cured in air decreased up to 42.45 % (at 50FA mix) and it decreased up to 37.43 % when sealed. While the compressive strength of the mixes containing SF decreased up to 12.69 % (at 40FA10SF mix) when cured in air. In addition, the compressive strength of 40FA10SF mix cured by sealed plastic method was similar to PC control. Therefore, the mix containing SF can improve the compressive strength of ternary and quaternary blended cement, particularly for high cement replacement levels. This is due to the high pozzolanic reaction and high amorphous SiO_2 content of SF. In addition, SF particles fill the micro and/or submicro pore size in paste that is known as a space filling effect [34].

Figure 5b shows the compressive strength of blended cement specimens cured in water at 25, 40, and 60 °C. It is found that the compressive strength of all mixes increased with increasing curing temperature. In addition, the compressive strength of 50FA mix cured at 60 °C decreased up to 26.56 % compared to the mix cured by sealed plastic sheet, but it was still lower than PC control. However, the mixes containing 10 % SF replacement had higher compressive strength than PC control. This is due to the increasing temperature increased the rate of reaction (both of hydration and pozzolanic reaction) of blended cement,

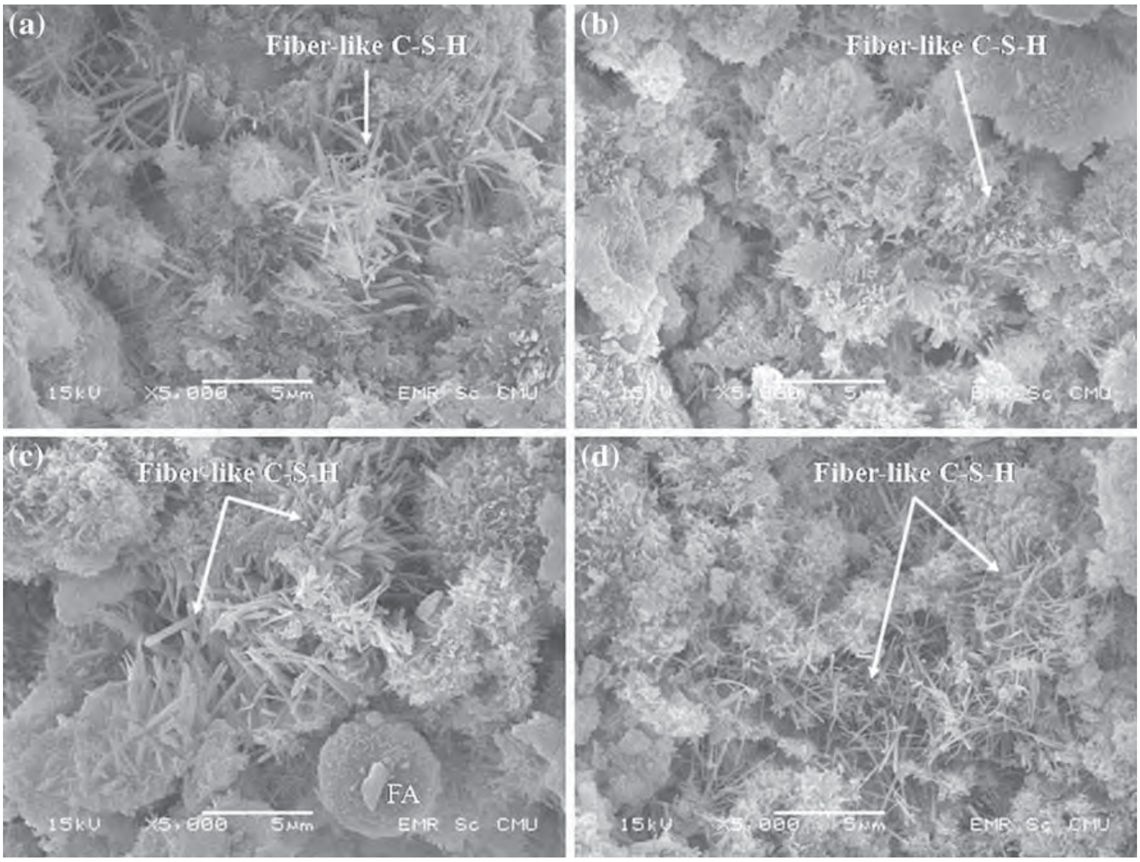

Fig. 6 SEM images of blended cement under water curing at 60 °C **a** PC control, **b** 50FA mix, **c** 45FA5SF mix, and **d** 40FA10SF mix

especially at lower degrees of reaction such as FA and BA. In these results, the compressive strength of all specimens cured in water at 25, 40, and 60 °C were higher than specimens cured in air and sealed with plastic sheeting.

The compressive strength of blended cement specimens under autoclaved curing is shown in Fig. 5c. It can be seen that the compressive strength of blended cement increased with increasing SF replacement at the same autoclaved period, especially at 10 % SF replacement where the compressive strength is higher than PC control. In addition, the compressive strength of PC control tends to increase with increasing autoclaving time while the compressive strength of blended cement increased with increasing autoclaving time up to 9 h and then begin to decrease when autoclaving time increase to 12 h. Under autoclaved method, the CaO/SiO_2 ratio has a significant effect on the compressive strength of blended cement due to the chemical of hydration is substantially altered under high temperature and pressure conditions. In the absence of an external SiO_2 source, α-dicalcium silicate hydrate (α-C_2SH) is formed instead of an amorphous calcium silicate hydrate (C–S–H). In the presence of SiO_2 source, crystalline 1.1 nm tobermorite ($C_5S_6H_5$) is formed [21]. Tobermorite phase has a larger volume of structure than α-C_2SH phase which causes a decrease in porosity and increase in the compressive strength.

Meller et al. [35] reported $CaO–SiO_2–H_2O$ phases from 50 to 1,000 °C. This phase diagram shows relationship between temperature and CaO/SiO_2 mol ratio. It is reported that tobermorite phase is formed at the CaO/SiO_2 ratio between about 0.5–1.5 and at temperature above 110 °C. In this study, it was found that blended cement specimen had a CaO/SiO_2 ratio between 0.95 and 1.12. The CaO/SiO_2 ratio decreased with increasing amount of SF replacement and thereby increased the compressive strength of blended cement. Therefore, FA, BA, and SF can be used as an alternative SiO_2 source in blended cement which results to tobermorite formation. The maximum compressive strength of 48.51 MPa was obtained from 40FA10SF mix using an autoclaved period of 9 h. The reduction of compressive strength of blended cement at 12-h autoclaved period may be due to tobermorite phase becoming unstable at long autoclaving time. Maeshima et al. [27] reported that stable tobermorite is normally treated at 170–210 °C in order to shorten the autoclaving time of approximately 5–8 h.

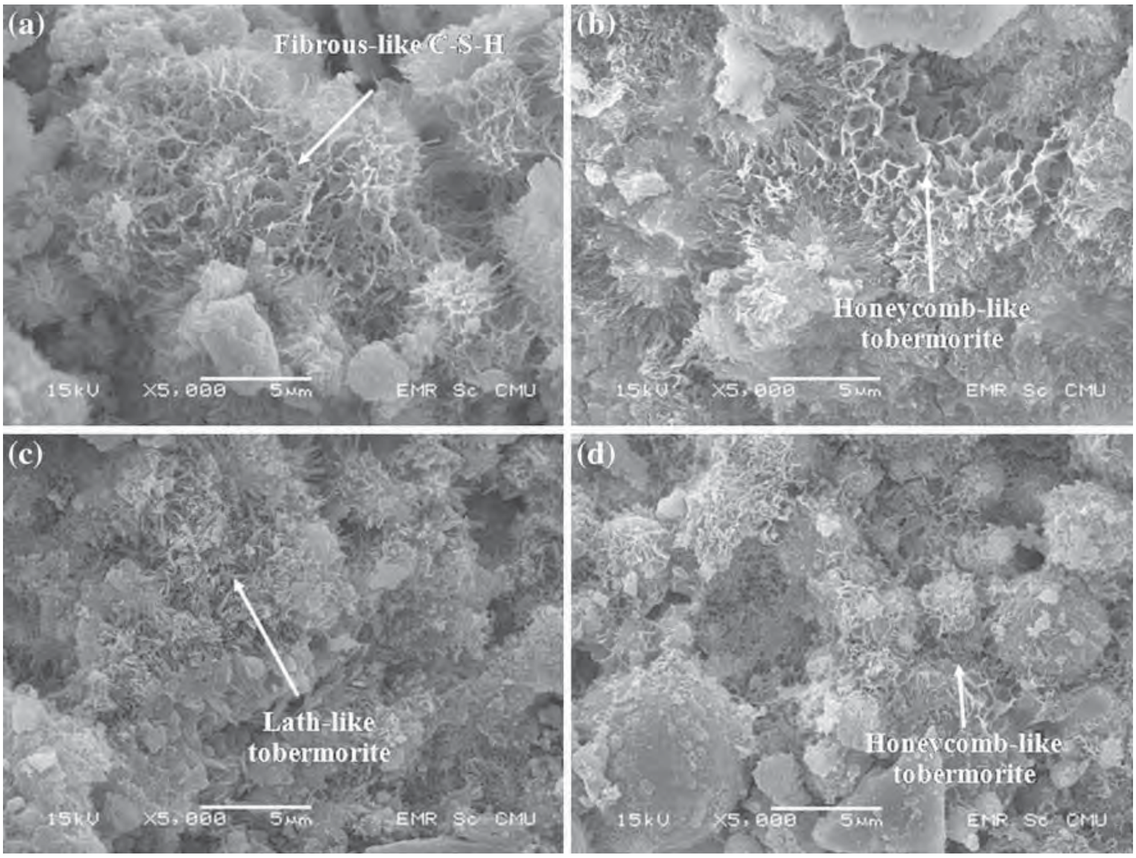

Fig. 7 SEM images of blended cement under autoclaved curing for 6 h. **a** PC control, **b** 50FA mix, **c** 45FA5SF mix, and **d** 40FA10SF mix

Microstructure

The microstructure of 28 day hydrated blended cement under various curing methods using scanning electron microscope (SEM) is shown in Figs. 6 and 7. The fracture specimens of paste were used to determine the microstructure and morphology of blended cement. Figure 6 represents SEM image of specimen under water curing at 60 °C. It can be seen that the fiber-like C–S–H was shown as the main C–S–H product of plain and blended cement. In addition, 50FA mix indicated the length of fiber-like C–S–H to be shorter than that of PC control. The length of fiber-like C–S–H tends to increase with increasing SF content. It can be observed that CaO/SiO_2 ratio decreased with increasing amount of SF which increased the length of fiber-like C–S–H. Therefore, the CaO/SiO_2 ratio has a significant effect on the shape of C–S–H cured in water at 60 °C.

Figure 7 shows SEM images of specimen under autoclaved curing at 130 °C under 20 psi pressure for 6 h. The fibrous-like C–S–H (α-C_2SH) phase can be seen presented in PC control. In addition, the honeycomb-like tobermorite phases were seen in specimens with pozzolanic materials. Moreover, the lath-like tobermorite can be found in the mixes containing SF replacement. Tobermorite phase has a significantly effect on the properties such as compressive strength of blended cement under high temperature and pressure conditions [19]. From SEM images (Fig. 7a–d), it can be seen that the tobermorite phases (both of honeycomb-like and lath-like formation) give denser microstructure than fibrous-like C–S–H phase. The α-C_2SH phase has smaller volume of the solid phase and as a consequence results in an increase in the porosity when compared to the tobermorite phase [19]. Therefore, a denser microstructure due to the presence of tobermorite structure would lead to higher compressive strength.

Conclusions

- To determine percentage of reactive phases, it is found that SF powder has more amorphous phase than FA and BA powder (74.06, 63, and 52.64 %, respectively). The compressive strength of blended cement containing FA and BA was lower than blended cement containing SF at the same curing method. The compressive strength of all mixes cured in air was lower than PC control while the compressive strength of blended cement containing SF 10 % by mass cured with plastic sealed and cured in water at 25 and 40 °C was equal to PC control. However, the compressive strength of blended cement containing SF 10 % by mass cured in water at 60 °C was higher than PC control. For autoclaved curing, the compressive strength of PC control tends to increase with increasing time of autoclaved while the compressive strength of blended cement increased with increasing time of autoclaved up to 9 h and tends to decrease with increasing time of autoclaved up to 12 h.

- XRD results show that the intensity of $Ca(OH)_2$ peak of blended cement was lower than that of PC control and it decreased with increased SF replacement and temperature curing. This indicates that the pozzolanic reaction was improved with the use of SF. XRD results showed the patterns of 0.9, 1.1, and 1.4 nm tobermorite in the blended cement specimens using autoclaved curing. TG results indicated the decomposition of C–S–H, C_2ASH_8, $Ca(OH)_2$, and $CaCO_3$ of specimen cured in water at 25 °C, while specimen cured in water at 60 °C show the decomposition of C–S–H, $Ca(OH)_2$, and $CaCO_3$. For autoclaved curing, the dehydration of 1.4 nm tobermorite and 1.1 nm tobermorite were showed at about 80–90 °C and 135–150 °C, respectively.
- SEM images of plain and blended cement under water curing at 60 °C indicated the fiber-like C–S–H. For autoclaved curing, SEM image showed fibrous-like C–S–H (α-C_2SH) phase as the main product of plain cement while blended cements exhibit honeycomb-like tobermorite and lath-like tobermorite phases which give denser microstructure than α-C_2SH phase.

Acknowledgments Mr. Watcharapong Wongkeo would like to thank the Office of the Higher Education Commission, Thailand for supporting by Grant fund under the program Strategic Scholarships for Frontier Research Network for the Ph.D. Program Thai Doctoral degree for this research. The Graduate School, Chiang Mai University is also acknowledged. The authors would like to express their gratitude for National Research University (NRU) awarded to Assistant Prof. Dr. Arnon Chaipanich by the Commission of Higher Education (Thailand). This work was also financially supported by the Thailand Research Fund (TRF) under the TRF Senior Research Scholar Contract No. RTA5480004.

References

1. Mehta PK. High-performance, high-volume fly ash concrete for sustainable development. In: Proceedings of the international workshop on sustainable development and concrete technology, Beijing, China, 2004. pp. 3–14.
2. Bouzoubaa N, Zhang MH, Malhotra VM. Mechanical properties and durability of concrete made with high-volume fly ash blended cements using a coarse fly ash. Cem Concr Res. 2001;31:1393–402.
3. Atis CD. Strength properties of high-volume fly ash roller compacted and workable concrete, and influence of curing condition. Cem Concr Res. 2005;35:1112–21.
4. Dinakar P, Babu KG, Santhanam M. Durability properties of high volume fly ash self compacting concretes. Cem Concr Comp. 2008;30:880–6.
5. Papayianni I, Anastasiou E. Production of high-strength concrete using high volume of industrial by-products. Constr Build Mater. 2010;24:1412–7.
6. Duran-Herrera A, Juarez CA, Valdez P, Bentz DP. Evaluation of sustainable high-volume fly ash concretes. Cem Concr Comp. 2011;33:39–45.
7. Shih JY, Chang TP, Hsiao TC. Effect of nanosilica on characterization of Portland cement composite. Mater Sci Eng A. 2006;424:266–74.
8. Li GY, Wang PM, Zhao X. Pressure-sensitive properties and microstructure of carbon nanotube reinforced cement composites. Cem Concr Comp. 2007;29:377–82.
9. Chaipanich A, Nochaiya T, Wongkeo W, Torkittikul P. Compressive strength and microstructure of carbon nanotubes–fly ash cement composites. Mater Sci Eng A. 2010;527:1063–7.
10. Konsta-Gdoutos MS, Metaxa ZS, Shah SP. Multi-scale mechanical and fracture characteristics and early-age strain capacity of high performance carbon nanotube/cement nanocomposites. Cem Concr Comp. 2010;32:110–5.
11. Mostafa NY, Mohsen Q, El-Hemaly SAS, El-Korashy SA, Brown PW. High replacements of reactive pozzolan in blended cements: microstructure and mechanical properties. Cem Concr Comp. 2010;32:386–91.
12. Nassif HH, Najm H, Suksawang N. Effect of pozzolanic materials and curing methods on the elastic modulus of HPC. Cem Concr Comp. 2005;27:661–70.
13. Guneyisi E, Gesoglu M, Ozbay E. Strength and drying shrinkage properties of self-compacting concretes incorporating multi-system blended mineral admixtures. Constr Build Mater. 2010;24: 1878–87.
14. Barbhuiya SA, Gbagbo JK, Russell MI, Basheer PAM. Properties of fly ash concrete modified with hydrated lime and silica fume. Constr Build Mater. 2009;23:3233–9.
15. Nochaiya T, Wongkeo W, Chaipanich A. Utilization of fly ash with silica fume and properties of portland cement–fly ash–silica fume concrete. Fuel. 2010;89:768–74.
16. Cheriaf M, Rocha JC, Pera J. Pozzolanic properties of pulverized coal combustion bottom ash. Cem Concr Res. 1999;29: 1387–91.
17. Wongkeo W, Chaipanich A. Compressive strength, microstructure and thermal analysis of autoclaved and air cured structural lightweight concrete made with coal bottom ash and silica fume. Mater Sci Eng A. 2010;527:3676–84.
18. Bentur A, Goldman A. A curing effects, strength and physical property of high strength silica fume concretes. J Mater Civ Eng ASCE. 1989;1(1):46–58.
19. Mindess S, Young JF, Darwin D. Concrete. 2nd ed. Upper Saddle River: Pearson Education; 2003. p. 287–300.
20. Hewlett PC. Lea's chemistry of cement and concrete. 4th ed. Oxford: Reed Education and Professional Publishing Ltd; 1998. p. 288.
21. Yazici H, Yardimci MY, Yigiter H, Aydin S, Turkel S. Mechanical properties of reactive powder concrete containing high volumes of ground granulated blast furnace slag. Cem Concr Comp. 2010;32:639–48.
22. Fernandez-Jimenez A, de la Torre AG, Palomo A, Lopez-Olmo G, Alonso MM, Aranda MAG. Quantitative determination of phases in the alkali activation of fly ash Part I. Potential ash reactivity. Fuel. 2006;85:625–34.
23. Ramachandran VS, Beaudoin JJ. Handbook of analytical techniques in concrete science and technology Principles techniques and applications. Norwich: William Andrew publishing/Noyes Publication; 2001. p. 130.

24. Houston JR, Maxwell RS, Carroll SA. Transformation of metastable calcium silicate hydrates to tobermorite: reaction kinetics and molecular structure from XRD and NMR spectroscopy. Geochem Trans. 2009;10:1–14.
25. Blanc Ph, Bourbon X, Lassin A, Gaucher EC. Chemical model for cement-based materials: temperature dependence of thermodynamic functions for nanocrystalline and crystalline C–S–H phases. Cem Concr Res. 2010;40:851–66.
26. Zhang Q, Guang Y. Dehydration kinetics of Portland cement paste at high temperature. J Therm Anal Calorim. 2012;110:153–8.
27. Maeshima T, Noma H, Sakiyama M, Mitsuda T. Natural 1.1 and 1.4 nm tobermorites from Fuka, Okayama, Japan: chemical analysis, cell dimension, ^{29}Si NMR and thermal behavior. Cem Concr Res. 2003;33:1515–23.
28. Neves A Jr, Toledo Filho RD, Fairbairn EMR, Dweck J. Early stages hydration of high initial strength Portland cement, Part I. thermogravimetric analysis on calcined mass basis. J Therm Anal Calorim. 2012;108:725–31.
29. Petkova V, Stoyanov V, Pelovski Y. TG–DTG–DTA in studying white self-compacting cement mortars. J Therm Anal Calorim. 2012;109:797–806.
30. Kuliffayova M, Krajci L, Janotka I, Smatko V. Thermal behaviour and characterization of cement composites with burnt kaolin sand. J Therm Anal Calorim. 2012;108:425–32.
31. Mitchell LD, Margeson JC. The effects of solvents on C–S–H as determined by thermal analysis. J Therm Anal Calorim. 2006; 86(3):591–4.
32. Ramachandran VS, Zhang CM. Thermal analysis of the $3CaO{\cdot}Al_2O_3$–$CaSO_4{\cdot}2H_2O$–$CaCO_3$–H_2O system. Thermo Acta. 1986;106:273–82.
33. Galan I, Andrade C, Castellote M. Thermogravimetrical analysis for monitoring carbonation of cementitious materials: uptake of CO_2 and deepening in C–S–H knowledge. J Therm Anal Calorim. 2012;110:309–19.
34. Yazıcı H, Yardımcı MY, Aydın S, Karabulut AS. Mechanical properties of reactive powder concrete containing mineral admixtures under different curing regimes. Constr Build Mater. 2009;23:1223–31.
35. Meller N, Kyritsis K, Hall C. The mineralogy of the CaO–Al_2O_3–SiO_2–H_2O (CASH) hydroceramic system from 200 to 350 °C. Cem Concr Res. 2009;39:5–45.

Int. J. Appl. Ceram. Technol., 10 [S1] E77–E87 (2013)
DOI:10.1111/ijac.12021

International Journal of
Applied
Ceramic
TECHNOLOGY
Ceramic Product Development and Commercialization

Reducing Loss Tangent by Controlling Microstructure and Electrical Responses in $CaCu_3Ti_4O_{12}$ Ceramics Prepared by a Simple Combustion Method

Prasit Thongbai,* Supree Pinitsoontorn, and Vittaya Amornkitbamrung

Department of Physics, Faculty of Science, Khon Kaen University, Khon Kaen 40002, Thailand

Teerapon Yamwong

National Metal and Materials Technology Center (MTEC), Thailand Science Park, Pathumthani 12120, Thailand

Santi Maensiri

School of Physics, Institute of Science, Suranaree University, Nakhon Ratchasima 30000, Thailand

Prinya Chindaprasirt

Sustainable Infrastructure Research and Development Center, Department of Civil Engineering, Faculty of Engineering, Khon Kaen University, Khon Kaen 40002, Thailand

The dielectric and electrical properties of $CaCu_3Ti_4O_{12}$ ceramics prepared by a simple combustion method were investigated. Fine-grained $CaCu_3Ti_4O_{12}$ ceramics exhibited good dielectric properties and temperature stability. Very low loss tangents of 0.020–0.016 and high dielectric constant of 5776–6406 (at 1 kHz and 20°C) with temperature coefficient less than ±15% in the temperature range of −70 to 90°C were observed. Dielectric relaxation processes were observed in large-grained $CaCu_3Ti_4O_{12}$ ceramics. The dielectric relaxation in the temperature range of 60–150°C may be associated with sample–electrode contact. The relaxation in temperatures below −40°C is related to the electrical response at grain boundaries.

---

*pthongbai@kku.ac.th

Introduction

Recently, the discovery of new materials showing a very high dielectric constant (ε') has stimulated significant research activity.[1] This is because materials with large dielectric constants are used to fabricate ceramic capacitors. The values of ε' and loss tangent (tanδ) are the primary parameters determining the performance of capacitors. Among new giant materials, $CaCu_3Ti_4O_{12}$ (CCTO) has gained considerable interest both scientifically and technologically.[2–13] CCTO ceramics can exhibit very high ε' of about 10^3–10^5 at room temperature, depending on the ceramic microstructures[14–16] and processing conditions.[8] Unfortunately, their tanδ values are still too large and tend to increase as ε' is increased.[14] Investigation to optimize the values of ε' and tanδ by controlling the microstructure of CCTO ceramics is therefore important.

Over the past few years, many investigations have been carried out to clarify and understand the physical mechanism(s) related to the apparent giant dielectric response in CCTO ceramics. Unfortunately, the origin of giant dielectric properties is still unclear. Both intrinsic and extrinsic effects have been proposed that describe the unusually high ε' values of CCTO ceramics and single crystals.[3–6,8,13,15] For the intrinsic effect, several models were proposed to describe the giant dielectric response. These include the mixed-valent structure model,[13,17,18] polaron relaxation model,[19] incipient ferroelectricity model,[20] nanoscale disorder model,[21–23] and dipolar effect related to disordered Ca/Cu sites.[24]

Based on the extrinsic effect, the origin of the giant dielectric response in the CCTO ceramics is widely accepted to be caused by interfacial polarization at grain boundaries (GBs).[3,4] The microstructure of CCTO ceramics consists of semiconducting grains and insulating GBs, that is, an electrical structure model or internal barrier layer capacitor (IBLC) model. Thus, GBs of CCTO ceramics play two significant roles in the overall dielectric properties. First, GBs trap the charge carriers producing electrical polarization. Second, GBs behave as insulating layers blocking the long-range motion of free charges that can cause an increase in tanδ, especially in a low-frequency range. Besides polarization at GBs, polarization can also be introduced at other places such as domain boundaries (DBs) and sample–electrode interfaces.[6,25]

According to the sample–electrode effect, the value of ε' can be enhanced due to the formation of Schottky barrier at the interface between CCTO surfaces and metal electrodes. In general, formation of the Schottky barrier is caused by the difference between the work functions of the metal electrode and semiconducting surface.[26] Ideally, it depends only on the different levels of work functions. However, for CCTO ceramics, it was found that the sample treatment and aging of electrode contact can also affect the low-frequency ε' value contributed by the electrode effect.[27] The time constant of the electrical response of a Schottky barrier is usually much longer than that occurring in bulk ceramics.[26] Therefore, such dielectric response appears in a relatively low-frequency range compared to that measured in bulk ceramics. Occasionally, the portion of the dielectric constant contributed by the sample–electrode effect cannot be observed in the measured frequency range. Fortunately, this response can be observed in the radio frequency range by increasing measurement temperature. This is due to the electrical response of Schottky barrier being a thermally activated mechanism. Thus, a strong increase in the value of ε' at a high temperature might be caused by the sample–electrode effect.

According to the IBLC model, tanδ can be reduced by increasing the total GB resistivity (R_{gb}). Enhancement of R_{gb} can be carried out in several ways such as (1) doping CCTO with suitable metal ions to modify defect equilibrium at GBs,[28] (2) changing Ca and Cu molar ratios to produce CCTO/$CaTiO_3$ composites,[29–31] (3) increasing the molar concentration of Ti in CCTO to produce CCTO/TiO_2 composites,[32] (4) incorporating oxygen at GBs,[33] (5) and reducing the grain size to increase the density of GB layers.[14] To obtain CCTO ceramics with a small grain size and high GB density, CCTO ceramics should be prepared from CCTO nanopowders or smaller submicrometer powders and sintered at a lower temperature and/or short time.

In this work, we prepared CCTO ceramics using a simple combustion method and sintered at low temperature and short reaction times (1040°C for 1 and 3 h). Fine-grained CCTO ceramics with good dielectric properties were obtained. The dielectric relaxations and electrical responses in large-grained CCTO ceramics were studied using an impedance spectroscopy. The possible mechanisms related to the relaxation processes and electrical responses are discussed.

Experimental Procedure

In this work, a simple combustion method was used to synthesize CCTO powder. $Ca(NO_3)_2$ $4H_2O$ (99%, Sigma-Aldrich Chemie, Steinheim, Germany), $Cu(NO_3)_2$ $4H_2O$ (99.5%, Carlo Erba, Milano, Italy), $C_{16}H_{28}O_6Ti$ (75 wt.% in isopropanol, Sigma-Aldrich), citric acid, ethanol, and aqueous ammonia (27%) were employed as starting raw materials. Stoichiometric amounts of $Ca(NO_3)_2$ $4H_2O$ and $Cu(NO_3)_2$ $4H_2O$ were dissolved in the solution of citric acid (5 wt%) in ethanol with constant stirring at room temperature. Then, $C_{16}H_{28}O_6Ti$ solution was mixed with the metal ion solution above under constant stirring at 150°C until a transparent gel was formed. Then, 1 mL of aqueous ammonia was added to the Ca^{2+}, Cu^{2+}, and Ti^{4+} mixture solution with constant stirring at 150°C. This mixed solution was dried at 350°C for 30 min. The resulting dried porous precursor was ground into powder and divided into two portions. One was calcined in air at 750°C for 2 h, and other was calcined at 750°C for 6 h. These two CCTO powders are referred to as P1 and P2 powders, respectively. P1 and P2 powders were ground and pressed into pellets having dimensions of 9.5-mm diameter and ~1–2 mm in thickness by uniaxial compression at 200 MPa. Finally, the green-body disks prepared from P1 powder were sintered in air at 1040°C for 1 and 3 h and referred to as CCTO-1 and CCTO-2 samples, respectively. The green-body disks prepared from P2 powder were sintered in air at 1040°C for 1 and 3 h and referred to as CCTO-3 and CCTO-4 samples, respectively.

The phase composition and microstructure of sintered CCTO powders and ceramics were characterized using X-ray diffraction (XRD) (PW3040, Philips, Eindhoven, The Netherlands) and scanning electron microscopy (SEM) with energy dispersive spectroscopy (EDS) (S-3400, Hitachi, Tokyo, Japan), respectively. Transmission electron microscopy (TEM) (Tecnai G^2, FEI, Eindhoven, The Netherlands) was used to characterize the CCTO powders. The dielectric response of the samples was measured using an Agilent E4980A (Agilent Technologies, Palo Alto, CA) Precision LCR Meter over the frequency and temperature ranges of 10^2–10^6 Hz and −70 to 150°C, respectively. An oscillation voltage of 1.0 V was used in each case. Each measured temperature was kept constant with an accuracy of ±1°C. Prior to making measurements, the ceramic samples were polished. Au was sputtered on each pellet surface at a current of 25 mA for 8 min using a Polaron SC500 (Sussex, U.K.) sputter coating unit.

Results and Discussion

The XRD patterns of dried precursor, CCTO powders, and the sintered CCTO ceramics are shown in Fig. 1. CuO phase was observed in the XRD patterns of the dried precursor. The XRD patterns of CCTO powders and the sintered ceramics confirm the formation of the $CaCu_3Ti_4O_{12}$ phase (JCPDS card no. 75-2188). The diffraction peaks corresponding to CCTO phase were detected. All XRD patterns are perfectly indexed based on the body-centered cubic structure with space group *Im*3. The XRD results indicate that CCTO phase can be successfully prepared by a very simple method using a relatively low calcination temperature and short reaction time, that is, 750°C for 2 h. A small amount of CuO and TiO_2 impurity phases still appeared in the XRD patterns of CCTO powders. Only pure phase of CCTO, that is, with no impurities, was detected in the XRD patterns of the sintered CCTO ceramics. The values of lattice parameters were calculated using Cohen's least mean square method and found to be 7.390, 7.390, 7.391, 7.392, 7.391, and 7.390 Å for the P1 powder, P2 powder, CCTO-1, CCTO-2, CCTO-3, and CCTO-4 samples,

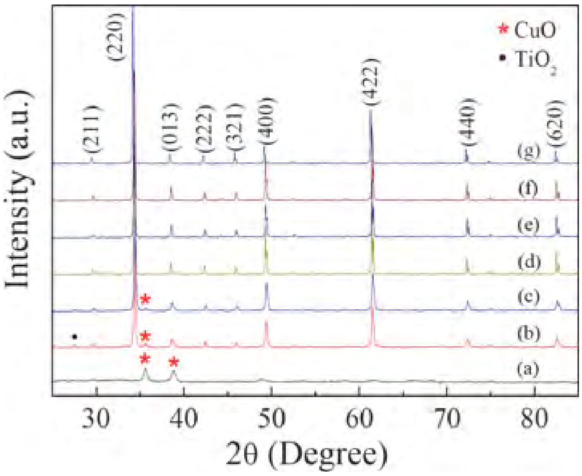

Fig. 1. X-ray diffraction patterns of (a) precursor, (b) CCTO powder calcined at 750°C for 2 h, (c) CCTO powder calcined at 750°C for 6 h, (d) CCTO-1, (e) CCTO-2, (f) CCTO-3, and (g) CCTO-4 samples.

respectively. These values are comparable to the values reported in literature[2] and JCPDS card no. 75-2188 for 7.391 Å. Figures 2a,b show TEM images of CCTO powders calcined at 750°C for 2 and 6 h, respectively. The particle size of CCTO tended to increase as the calcination time was increased. The particle sizes of the P1 and P2 powders were estimated to be 130–260 nm and 150–300 nm, respectively.

Figures 3a–d show SEM images of the surface morphologies of the CCTO samples. The CCTO-1 sample sintered at 1040°C for 1 h shows a fine-grained microstructure with grain sizes of about ~2–3 μm (Fig. 3a). As seen in Fig. 3c, the CCTO-3 sample sintered at same condition as the CCTO-1 sample exhibits its fine-grained microstructure as was observed in the CCTO-1 sample. However, small grains in some regions start to connect together. Increasing sintering time from 1 to 3 h results in abnormal grain growth. For the CCTO-2 and CCTO-4 samples (the samples that were prepared from P1 and P2 powders, respectively) sintered at 1040°C for 3 h, some grains grow rapidly to sizes of ~10–15 μm. This microstructural evolution in CCTO ceramics has been reported in the literature.[14] The microstructures of the CCTO-1 and CCTO-3 samples were observed to have small grain sizes with narrow distribution of these values. This microstructural feature is required for most applications. The dielectric properties of these two ceramic samples are therefore expected to be improved. Figure 3e shows the EDS spectrum of the CCTO-4 sample, confirming the presence of each chemical, that is, Ca, Cu, Ti, and O.

As shown in Fig. 4, sintering time has an effect on the dielectric properties of CCTO ceramics. ε' at 20°C of the fine-grained CCTO-1 and CCTO-3 samples is independent of frequency over the measured range, 10^2–10^6 Hz. In contrast with the fine-grained ceramic samples, the CCTO-2 and CCTO-4 samples exhibit a strong frequency dependence upon ε' especially in a low-frequency range. As demonstrated in the inset of Fig. 4, the low-frequency values of $\tan\delta$ of the fine-grained CCTO-1 and CCTO-3 ceramics are much lower than the values of $\tan\delta$ for the CCTO-2 and CCTO-4 samples. $\tan\delta$ values of these two fine-grained ceramics are lower than 0.1 in the frequency range from 10^2 to 10^5 Hz. The values of ε' and $\tan\delta$ at 1 kHz and 20°C for all CCTO samples are summarized in Table I. The dielectric properties of these two samples are comparable to those of 0.1 wt% ZrO_2-doped CCTO ceramic ($\varepsilon' \sim 5030$ and $\tan\delta \sim 0.016$ at 1 kHz).[28] It was also reported that 0.5% ZrO_2-doped CCTO ceramic exhibited $\tan\delta$ values below 0.05 over a wide frequency range. For the CCTO–1 and CCTO-3 samples, $\tan\delta$ was found to be lower than 0.05 over frequency ranges of 200 Hz–158 kHz and 100 Hz–50 kHz, respectively.

The exact origin of the giant dielectric response in CCTO ceramics is still unclear. However, it is usually found that the electrical and dielectric properties of CCTO ceramics are strongly related to their prepara-

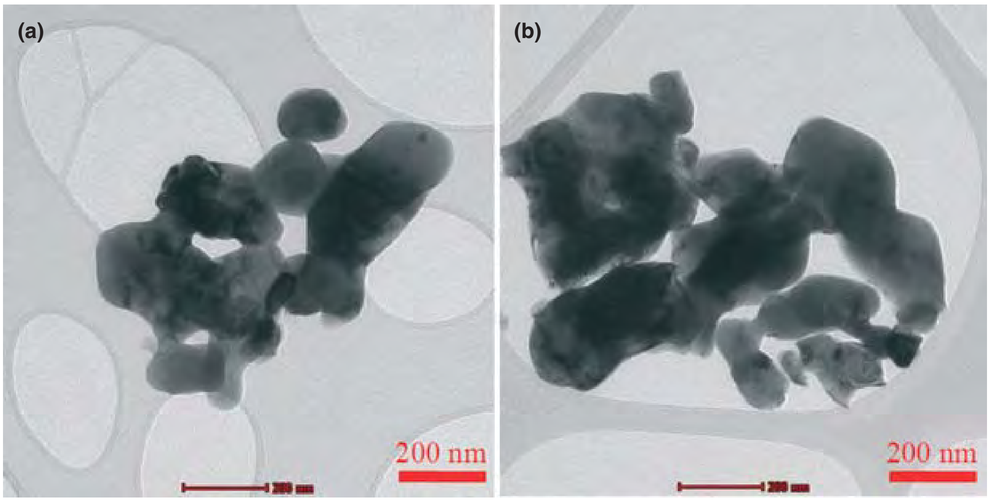

Fig. 2. Transmission electron microscopy images of CCTO powders calcined at 750°C for (a) 2 h and (b) 6 h.

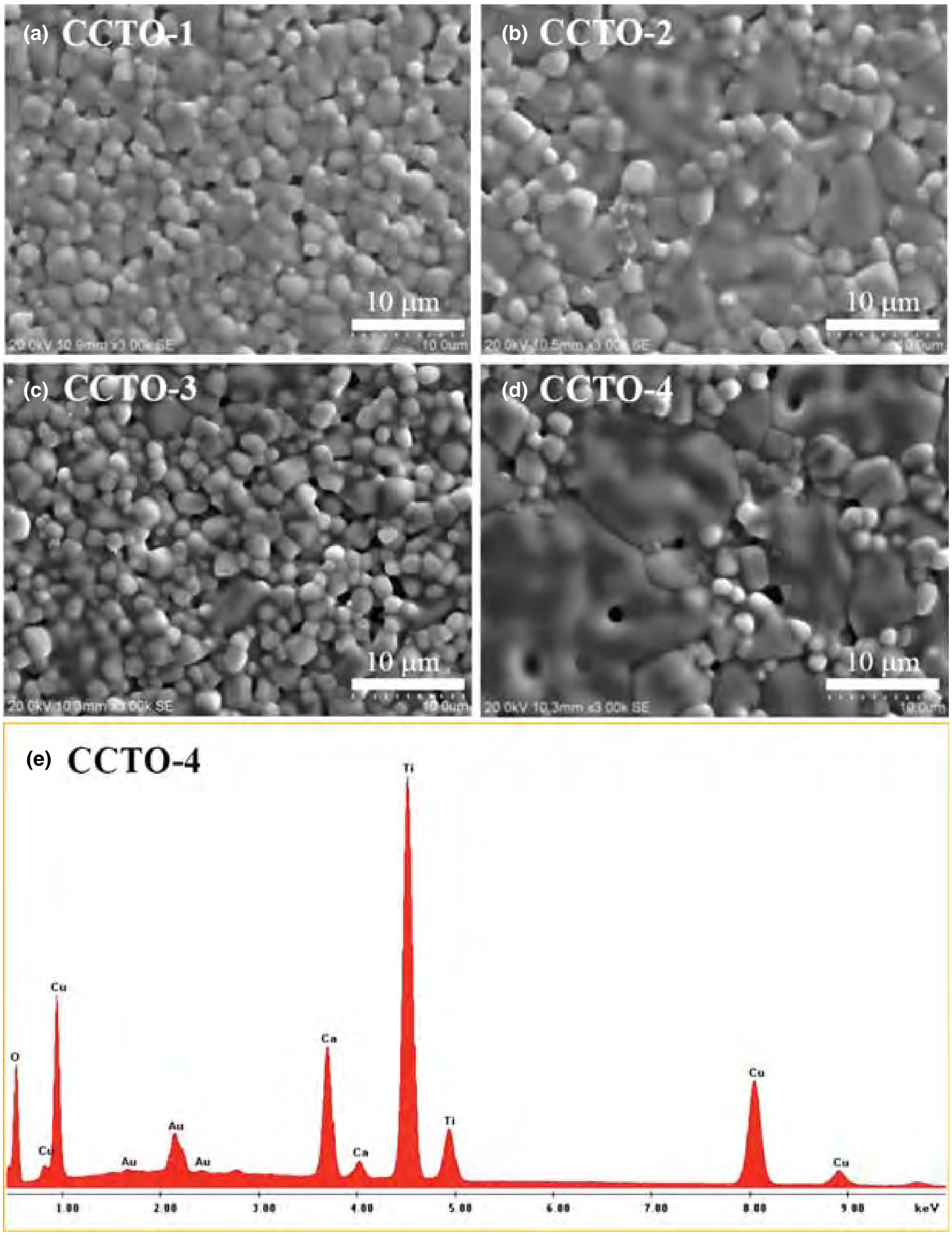

Fig. 3. *(a–d) SEM images of surface morphologies of CCTO-1, CCTO-2, CCTO-3, and CCTO-4 samples, respectively. (e) energy dispersive spectroscopy spectrum of CCTO-4 sample.*

tion conditions and resulting microstructure. Notably, it has been shown that CCTO ceramics are electrically heterogeneous, consisting of semiconducting grains and insulating GBs.[4] However, changes in microstructure (e.g., the increase in the grain size) may cause the changes in intrinsic factors in grains such as concentration of defects. Therefore, an increase in ε′ can be considered in two different ways: (1) an increase in the mean grain size and/or GBs capacitance and (2) changes in intrinsic factors. In this work, we hypothe-

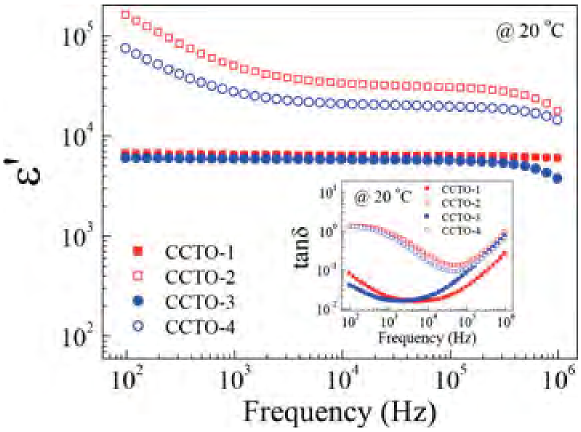

Fig. 4. Frequency dependence of ε' at 20°C for all CCTO samples; inset shows the frequency dependence of tanδ at 20°C.

sized that microstructural heterogeneity is the primary cause of the giant dielectric properties of CCTO ceramics. This work does not discredit other intrinsic models.[17–24] We just demonstrate that giant dielectric properties of CCTO ceramics can be effectively improved by controlling microstructure. All concepts and models used to describe the giant dielectric behavior of CCTO single crystal and polycrystalline ceramics require further experimental validation.

Based on the electrically heterogeneous microstructure found in insulating GBs and semiconducting grains,[2,3,6] the density of insulating GB layers was increased by controlling the microstructure of CCTO ceramics to obtain small grain sizes with narrow size distribution. The increase in insulating layers caused a decrease in dc conduction in the fine-grained CCTO ceramics. Therefore, the low-frequency tanδ of the CCTO-1 and CCTO-3 ceramics is therefore reduced.

To develop a high-permittivity ceramic that can be used for ceramic capacitor applications, variations in ε' must be investigated over the standard temperature range.[34] For example, variation in ε' for high-permittivity ceramics suitable to fabricate X5R and X7R capacitors should be less than ±15% over the temperature ranges of −55 to 85°C and −55 to 125°C, respectively. The variation in ε' [Δε'(%)] as a function of temperature in °C is defined as $(\varepsilon'_T - \varepsilon'_{20})/\varepsilon'_{20} \times 100$, where ε'_T and ε'_{20} are ε' at a specific experimental temperature and 20°C, respectively. As shown in Fig. 5, ε' of the CCTO-1 and CCTO-3 samples seems to be nearly independent on temperature over the range from −70 to 150°C. However, ε' of the CCTO-2 and CCTO-4 samples is found to be strongly dependent on measurement temperature. Investigation of ε' temperature variations using conditions of 20°C (at 10^3 Hz) as a basis reveals that the variations of ε' for the fine-grained CCTO-1 and CCTO-3 samples were less than ±15% over the temperature range of −70 to 90°C and −70 to 100°C, respectively. This result indicates that the CCTO-1 and CCTO-3 ceramics have the potential for capacitor applications, that is, X5R capacitors.

As shown in the inset of Fig. 4, the increase in tanδ for all samples in a high-frequency range (10^5–10^6 Hz) is attributed to the main dielectric relaxation process. This behavior of CCTO ceramics is well reported in the literature.[3,5,6,10,11,13–15] It is likely that the high tanδ values observed for the CCTO-2 and CCTO-4 samples in a low-frequency range may be attributed to the dielectric relaxation process. The CCTO-2 and CCTO-4 samples exhibited two sets of dielectric relaxation processes. To study these two relaxation processes, the frequency dependence of dielectric properties (i.e., ε', tanδ, and ε'' [ε'' = ε' × tanδ]) at various temperature was investigated. As shown in Fig. 6 and inset (1), two sets of relaxation peaks for the CCTO-4 sample are observed. These two sets are indicated by ε'' peaks for low-temperature relaxation and tanδ peaks for high-temperature relaxation. The observation of tanδ peaks corresponds to the step-like decrease in ε' at the same

Table I. ε' and tanδ Values (at 20°C and 1 kHz), Activation Energies for Low- and High-Temperature Relaxation Processes (E_{a1} and E_{a2}), Grain Boundary Conduction Activation Energy (E_{gb}), and Activation of Electrode Response (E_e) for $CaCu_3TiO_{12}$ Ceramics

Sample	ε'	tanδ	E_{a1} (eV)	E_{a2} (eV)	E_{gb} (eV)	E_e (eV)
CCTO-1	6406	0.020	-	-	0.672	-
CCTO-2	49,261	0.908	0.093	0.577	0.455	0.541
CCTO-3	5776	0.016	-	-	0.676	-
CCTO-4	27,062	0.720	0.108	0.588	0.495	0.582

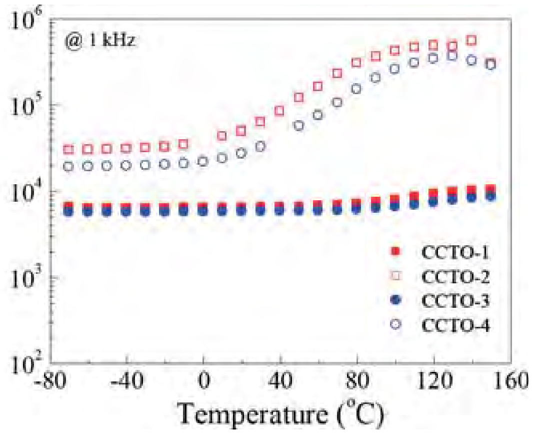

Fig. 5. Temperature dependence of ε' at 20° C for all CCTO samples.

temperature range, as shown in the inset (2) of Fig. 6. Over the measured ranges of temperature and frequency (−70 to 150°C and 10^2–10^6 Hz), both ε″ and tanδ peaks were observed in the CCTO-2 and CCTO-4 samples only, but were not observed in the fine-grained CCTO-1 and CCTO-3 samples. The ε″ and tanδ peaks shift to higher frequency as the temperature increased, indicating a thermally activated dielectric relaxation processes. The activation energies for the low-temperature relaxation process (E_{a1}) were found to be 0.093 and 0.112 eV for CCTO-2 and CCTO-4, respectively. These values are comparable to the values reported in the literature.[3,11,14] The activation energies for the high-temperature relaxation process (E_{a2}) were found to be 0.577 and 0.588 eV for CCTO-2 and CCTO-4, respectively. Higher E_{a2} values may be related to either the electrical response of GBs or sample–electrode effects.

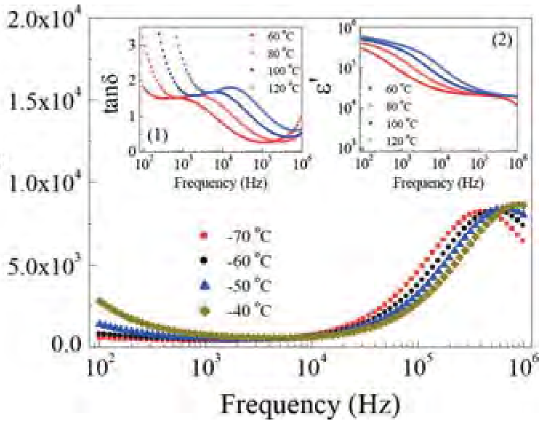

Fig. 6. Frequency dependence of ε″ at low temperatures for CCTO-4 sample showing low-temperature dielectric relaxation. Insets (1) and (2) show, respectively, the frequency dependence of tanδ and ε' over the temperature range of 60–120° C for CCTO-4 sample.

To study the effects of electrical responses of GBs and sample–electrode interfaces, impedance complex plane (Z*) plots for all samples were used to investigate possible mechanisms. Figures 7a–d show Z* plots at 100°C for all samples. Only one semicircle arc is observed in the fine-grained CCTO-1 and CCTO-3 samples. Two arcs in Z* plots are observed in the CCTO-2 and CCTO-4 samples. Grains, GBs, and sample–electrode effects in combination are possibly responsible for the two electrical responses observed in Figs. 7c and d. To clarify the mechanisms responsible for these two semicircle arcs, combined Z″ and M″ spectroscopic plots at 100°C were used to examine the electrical responses. As shown in Figs. 8a,b, Z″ and M″ of the CCTO-1 and CCTO-3 samples are located in nearly the same frequency range. The low-frequency peaks of Z″ for the CCTO-2 and CCTO-4 samples are observed at 1 kHz and 630 Hz, respectively (Figures 8c, d). The observation of a low-frequency peak in the Z″ spectrum is related to the electrical response of a large semicircle arc. In the high-frequency range, the shoulders of Z″ spectra for the CCTO-2 and CCTO-4 samples are observed at a frequency of about 10^5 Hz. The shoulders are located in nearly the same frequency range as their M″ peaks. This means that the high-frequency Z″ and M″ peaks originated from the same mechanism. At frequencies higher than the frequency of M″ peak, it is observed the values of M″ continue to increase. This increase in the M″ spectrum indicates the presence of another set of M″ peaks.[35] However, very low temperatures (<−70°C) are required to obtain data in the frequency measurement range.[36] The increase in the M″ spectrum suggests an electrical response of grains. Therefore, the high-frequency Z″ and M″ peaks (at $\sim 10^5$ Hz) likely originated from the electrical response of GBs. The low-frequency Z″ peak is therefore attributed to the effect of sample–electrode interfaces.[35,36]

To further study the electrical response of GBs, the frequency dependence of M″ at different temperatures was investigated. As shown in Figs. 9a,b, the M″ peak shifts to higher frequencies as the temperature

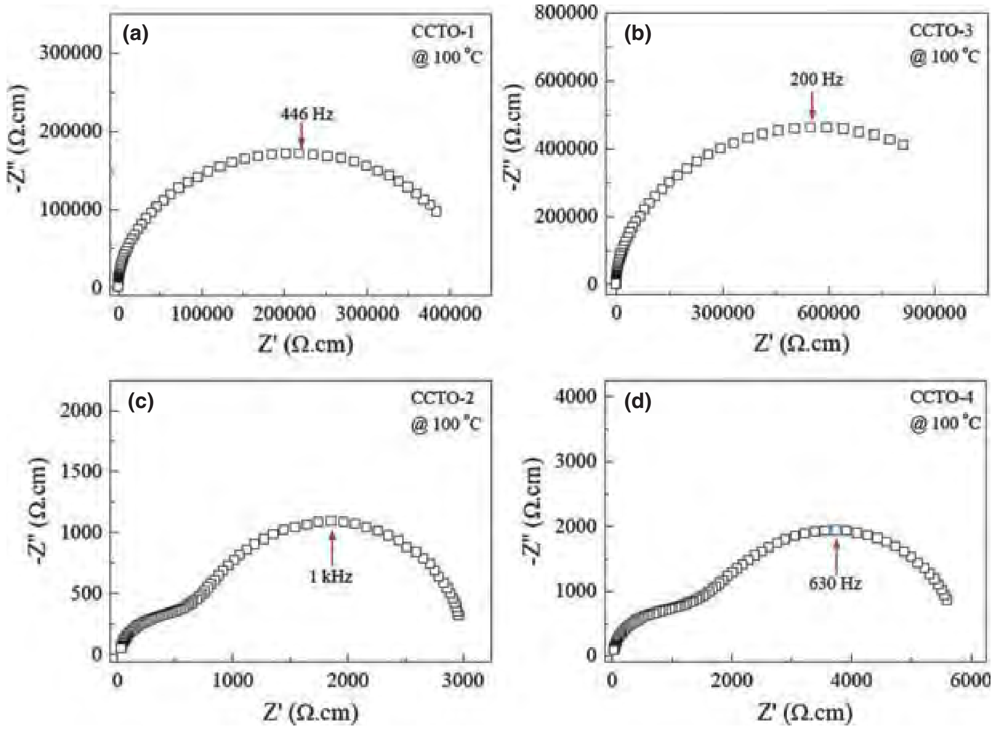

Fig. 7. Impedance complex plane plot (Z) at 100°C for (a) CCTO-1, (b) CCTO-3, (c) CCTO-2, and (d) CCTO-4 samples.*

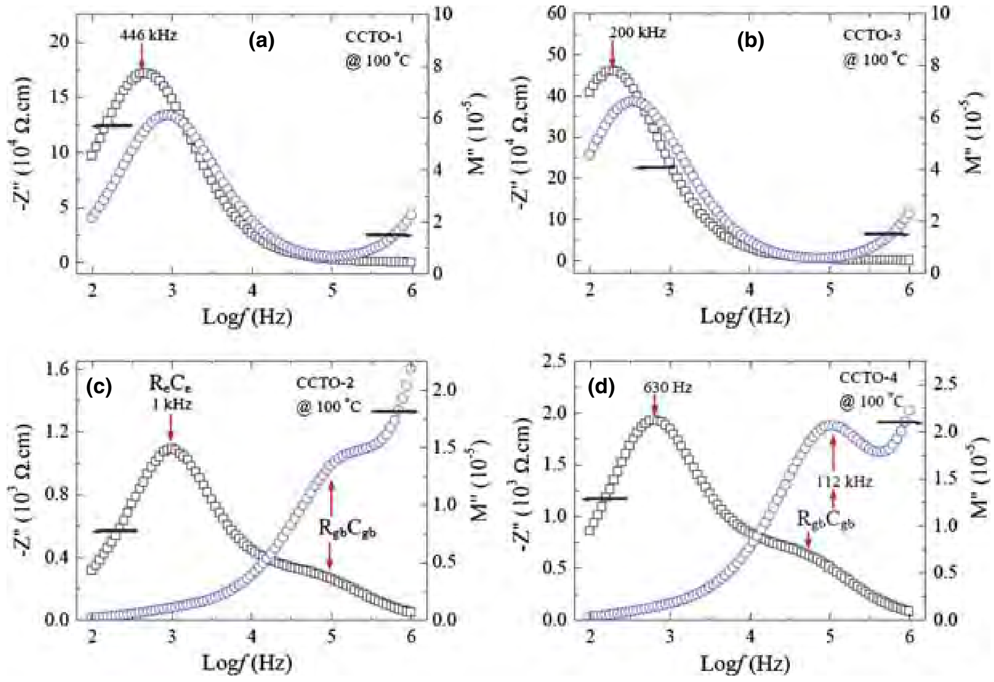

Fig. 8. (a–d) Combined Z'' and M'' spectroscopic plots at 100°C for (a) CCTO-1, (b) CCTO-3, (c) CCTO-2, and (d) CCTO-4 samples.

increases. Note that M″ peak of the CCTO-2 sample cannot be observed at temperature higher than 90°C, as shown in the inset of Fig. 9b. The GB conductivity ($\sigma_{gb} = 1/R_{gb}$) can be calculated from the peak maxima based on the relationships[35,36]:

$$M'' = \frac{C_0}{2C_{gb}}, \quad (1)$$

$$2\pi f_{\max} R_{gb} C_{gb} = 1, \quad (2)$$

where R_{gb} and C_{gb} are the resistance and capacitance of GBs, respectively. The electrode contact conductivity ($\sigma_e = 1/R_e$, where R_e is the resistance due to electrode contact) can be calculated from the plots of Z″ as a function of frequency in a high temperature range. At the peak of Z″ related to electrical response of electrode contact, R_e can be estimated from the relationship $Z'' = R_e/2$. σ_e values were calculated at various temperatures. It was found that the temperature dependence of σ_{gb} and σ_e follows the Arrhenius law for conduction processes as shown Fig. 10. This is given by

$$\sigma = \sigma_0 \exp\left(\frac{-E}{k_B T}\right) \quad (3)$$

where σ_0 is the prefactor term, E is the activation energy for conduction process, k_B is Boltzmann constant, and T is absolute temperature. According to the data fitted to Eq. (3), the GB conduction activation energy (E_{gb}) for all samples and the activation energy for electrode response (E_e) of the CCTO-2 and CCTO-4 samples can be calculated from the slopes of the plots. The calculated values are summarized in Table I. It was found that the high-temperature dielectric relaxation activation energy (E_{a2}) and E_e are nearly the same in value. It is likely that that dielectric relaxation behavior in the high-frequency range observed in the CCTO-2 and CCTO-4 samples is mainly related to the effect of sample–electrode contact.

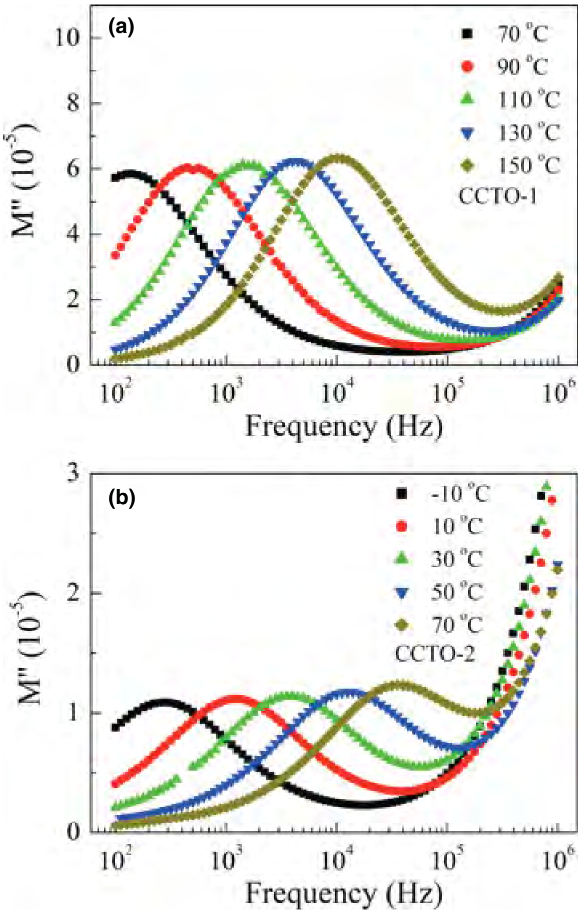

Fig. 9. Frequency dependence of M″ at different temperatures for (a) CCTO-1 and (b) CCTO-2 samples.

Conclusions

The dielectric properties and electrical responses in CCTO ceramics prepared by a simple combustion method were investigated. Fine-grained CCTO

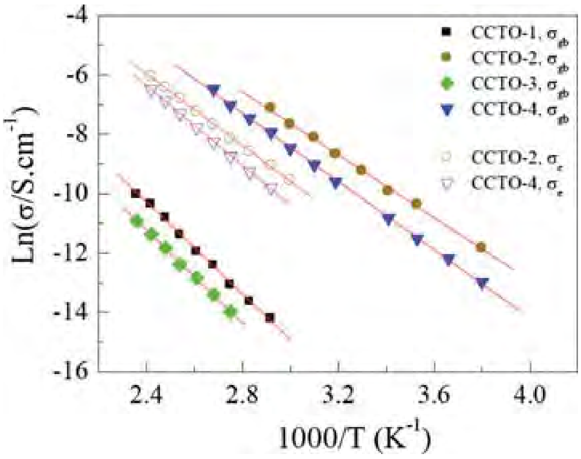

Fig. 10. Arrhenius plot of grain boundary conductivity (σ_{gb}) (extracted from M″ plots) and electrode contact conductivity (extracted from Z″ plots).

ceramics with good dielectric properties (tan$\delta \sim 0.020$ –0.0.16 and $\varepsilon' \sim 5776$–6406) and temperature stability in the range of −70 to 90°C were obtained by sintered at 1040°C for 1 h. Large-grained CCTO ceramics sintered at 1040°C for 3 h exhibited two sets of dielectric relaxations. Using an impedance spectroscopy analysis, the high-temperature dielectric relaxation was found to be likely caused by the effect of sample–electrode contact.

Acknowledgments

This work was financially supported by the Higher Education Research Promotion and National Research University Project of Thailand, Office of the Higher Education Commission, through the Advanced Functional Materials Cluster of Khon Kaen University and the Thailand Research Fund (TRF) under the TRF Senior Research Scholar Contract No. RTA5480004.

References

1. S. Krohns, *et al.*, “The Route to Resource-Efficient Novel Materials,” *Nat. Mater.*, 10 899–901 (2011).
2. M. A. Subramanian, D. Li, N. Duan, B. A. Reisner, and A. W. Sleight, “High Dielectric Constant in $ACu_3Ti_4O_{12}$ and $ACu_3Ti_3FeO_{12}$ Phases,” *J. Solid State Chem.*, 151 323–325 (2000).
3. D. C. Sinclair, T. B. Adams, F. D. Morrison, and A. R. West, “$CaCu_3Ti_4O_{12}$: One–Step Internal Barrier Layer Capacitor,” *Appl. Phys. Lett.*, 80 2153–2155 (2002).
4. S.-Y. Chung, I.-D. Kim, and S.-J. L. Kang, “Strong Nonlinear Current–Voltage Behaviour in Perovskite-Derivative Calcium Copper Titanate,” *Nat. Mater.*, 3 774–778 (2004).
5. P. Thongbai, J. Jumpatam, T. Yamwong, and S. Maensiri, “Effects of Ta^{5+} Doping on Microstructure Evolution, Dielectric Properties and Electrical Response in $CaCu_3Ti_4O_{12}$ Ceramics,” *J. Eur. Ceram. Soc.*, 32 2423–2430 (2012).
6. P. Lunkenheimer, S. Krohns, R. Fichtl, and S. G. Ebbinghaus, A Reller and A Loidl, “Colossal Dielectric Constants in Transition–Metal Oxides,”*Eur. Phys. J. Special Topics*, 180 61–89 (2010).
7. P. Leret, M. A. de la Rubia, F. Rubio-Marcos, J. J. Romero, and J. F. Fernandez, “Effect of Processing on the Sintering of High Dielectric Constant $CaCu_3Ti_4O_{12}$ Ceramics,” *Int. J. Appl. Ceram. Technol.*, 8 [5] 1201–1207 (2011).
8. R. Yu, H. Xue, Z. Cao, L. Chen, and Z. Xiong, “Effect of Oxygen Sintering Atmosphere on the Electrical Behavior of CCTO Ceramics,” *J. Eur. Ceram. Soc.*, 32 1245–1249 (2012).
9. L. Liu, H. Fan, P. Fang, and X. Chen, “Sol–Gel Derived $CaCu_3Ti_4O_{12}$ Ceramics: Synthesis, Characterization and Electrical Properties,” *Mater. Res. Bull.*, 43 800–1807 (2008).
10. B. S. Prskash and K. B. R. Varma, “Microstructural and Dielectric Properties of Donor Doped (La^{3+}) $CaCu_3Ti_4O_{12}$ Ceramics,” *J. Mater. Sci.: Mater. Electron.*, 17 899–907 (2006).
11. P. Thongbai, C. Masingboon, S. Maensiri, T. Yamwong, S. Wongsaenmai, and R. Yimnirun, “Giant Dielectric Behaviour of $CaCu_3Ti_4O_{12}$ Subjected to Post-Sintering Annealing and Uniaxial Stress,” *J. Phys.: Condens. Matter*, 19 236208 (2007).
12. J. Yuan, Y.-H. Lin, H. Lu, B. Cheng, and C.-W. Nan, “Dielectric and Varistor Behavior of $CaCu_3Ti_4O_{12}$–$MgTiO_3$ Composite Ceramics,” *J. Am. Ceram. Soc.*, 94 [7] 1966–1969 (2011).
13. Y. Wang, L. Ni, and X. M. Chen, “Effects of Nd-Substitution on Microstructures and Dielectric Characteristics of $CaCu_3Ti_4O_{12}$ Ceramics,” *J. Mater. Sci.: Mater. Electron.*, 22 345–350 (2011).
14. P. Thongbai, B. Putasaeng, T. Yamwong, and S. Maensiri, “Current–Voltage Nonlinear and Dielectric Properties of $CaCu_3Ti_4O_{12}$ Ceramics Prepared by a Simple Thermal Decomposition Method,” *J. Mater. Sci.: Mater. Electron.*, 23 795–801 (2012).
15. L. Ni, X. M. Chen, X. Q. Liu, and R. Z. Hou, “Microstructure-Dependent Giant Dielectric Response in $CaCu_3Ti_4O_{12}$ Ceramics,” *Solid State Commun.*, 139 45–50 (2006).
16. R. Kashyap, O. P. Thakur, and R. P. Tandon, “Study of Structural, Dielectric and Electrical Conduction Behavior of Gd Substituted $CaCu_3Ti_4O_{12}$ Ceramics,” *Ceram. Int.*, 38 3029–3037 (2012).
17. L. Ni and X. M. Chen, “Enhancement of Giant Dielectric Response in $CaCu_3Ti_4O_{12}$ Ceramics by Zn Substitution,” *J. Am. Ceram. Soc.*, 93 [1] 184–189 (2010).
18. L. Ni, X. M. Chen, and X. Q. Liu, “Structure and Modified Giant Dielectric Response in $CaCu_3(Ti_{1-x}Sn_x)_4O_{12}$ Ceramics,” *Mater. Chem. Phys.*, 124 982–986 (2010).
19. C. C. Wang and L. W. Zhang, “Polaron Relaxation Related to Localized Charge Carriers in $CaCu_3Ti_4O_{12}$,” *Appl. Phys. Lett.*, 90 142905 (2007).
20. C. P. L. Rubinger, *et al.*, “Intrinsic and Extrinsic Dielectric Responses of $CaCu_3Ti_4O_{12}$ Thin Films,” *J. Appl. Phys.*, 110 074102 (2011).
21. Y. Zhu, *et al.*, “Nanoscale Disorder in $CaCu_3Ti_4O_{12}$: A New Route to the Enhanced Dielectric Response,” *Phys. Rev. Lett.*, 99 037602 (2007).
22. J.-C. Zheng, *et al.*, “Nanoscale Disorder and Local Electronic Properties of $CaCu_3Ti_4O_{12}$: An Integrated Study of Electron, Neutron, and X-ray Diffraction, X-ray Absorption Fine Structure, and First-Principles Calculations,” *Phys. Rev. B*, 81 144203 (2010).
23. J. Kumar and A. M. Awasthi, “Fractional Power-Law Spectral Response of $CaCu_3Ti_4O_{12}$ Dielectric: Many-Body Effects,” *Appl. Phys. Lett.*, 101 062908 (2012).
24. C. H. Kim, *et al.*, “Effect of Mn Doping on the Temperature-Dependent Anomalous Giant Dielectric Behavior of $CaCu_3Ti_4O_{12}$,” *Phys. Rev. B*, 85 245210 (2012).
25. T.-T. Fang and C. P. Liu, “Evidence of the Internal Domains for Inducing the Anomalously High Dielectric Constant of $CaCu_3Ti_4O_{12}$,” *Chem. Mater.*, 17 5167–5171 (2005).
26. M. Li, A. Feteira, and D. C. Sinclair, “Relaxor Ferroelectric-Like High Effective Permittivity in Leaky Dielectrics/Oxide Semiconductors Induced by Electrode Effects: A Case Study of CuO Ceramics,” *J. Appl. Phys.*, 105 114109 (2009).
27. S. Krohns, P. Lunkenheimer, S. G. Ebbinghaus, and A. Loidl, “Colossal Dielectric Constants in Single-Crystalline and Ceramic $CaCu_3Ti_4O_{12}$ Investigated by Broadband Dielectric Spectroscopy,” *J. Appl. Phys.*, 103 084107 (2008).
28. E. A. Patterson, S. Kwon, C.-C. Huang, and D. P. Cann, “Effects of ZrO_2 Additions on the Dielectric Properties of $CaCu_3Ti_4O_{12}$,” *Appl. Phys. Lett.*, 87 182911 (2005).
29. W. Kobayashi and I. Terasaki, “$CaCu_3Ti_4O_{12}/CaTiO_3$ Composite Dielectrics: Ba/Pb–Free Dielectric Ceramics with High Dielectric Constants,” *Appl. Phys. Lett.*, 87 032902 (2005).
30. P. Thongbai, B. Putasaeng, T. Yamwong, and S. Maensiri, “Improved Dielectric and Non-Ohmic Properties of $Ca_2Cu_2Ti_4O_{12}$ Ceramics Prepared by a Polymer Pyrolysis Method,” *J. Alloys Compd.*, 509 7416–7420 (2011).
31. J. Jumpatam, P. Thongbai, B. Kongsook, T. Yamwong, and S. Maensiri, “High Permittivity, Low Dielectric Loss, and High Electrostatic Potential Barrier in $Ca_2Cu_2Ti_4O_{12}$ Ceramics,” *Mater. Lett.*, 76 40–42 (2012).
32. Y.-H. Lin, J. Cai, M. Li, C.-W. Nan, and J. He, “Grain Boundary Behavior in Varistor-Capacitor TiO_2-Rich $CaCu_3Ti_4O_{12}$ Ceramics,” *J. Appl. Phys.*, 103 074111 (2008).

33. Q. Zhang, T. Li, Z. Chen, R. Xue, and Y. Wang, "The Non-Ohmic and Dielectric Behavior Evolution of $CaCu_3Ti_4O_{12}$ After Heat Treatments in Oxygen-Rich Atmosphere," *Mater. Sci. Eng., B*, 177 168–172 (2012).
34. A. J. Moulson and J. M. Herbert, "*Electroceramics*," 2nd edition, Wiley, New York, 2003.
35. M. Li and D. C. Sinclair, "The Extrinsic Origins of High Permittivity and Its Temperature and Frequency Dependence in $Y_{0.5}Ca_{0.5}MnO_3$ and $La_{1.5}Sr_{0.5}NiO_4$ Ceramics," *J. Appl. Phys.*, 111 054106 (2012).
36. M. Li, D. C. Sinclair, and A. R. West, "Extrinsic Origins of the Apparent Relaxorlike Behavior in $CaCu_3Ti_4O_{12}$ Ceramics at High Temperatures: A Cautionary Tale," *J. Appl. Phys.*, 109 084106 (2011).

Construction and Building Materials 48 (2013) 585–591

Contents lists available at ScienceDirect

Construction and Building Materials

journal homepage: www.elsevier.com/locate/conbuildmat

Use of lightweight aggregates in pervious concrete

Yuwadee Zaetang, Ampol Wongsa, Vanchai Sata *, Prinya Chindaprasirt

Sustainable Infrastructure Research and Development Center, Department of Civil Engineering, Faculty of Engineering, Khon Kaen University, Khon Kaen 40002, Thailand

HIGHLIGHTS

- Three lightweight aggregates were used to make pervious concrete (LWPC).
- Mechanical properties, water permeability, and thermal conductivity were tested.
- LWPCs 558–775 kg/m^3 density and 2.47–5.99 MPa compressive strength were obtained.
- LWPCs density and thermal conductivity had 3–4 times lower than normal aggregate.

ARTICLE INFO

Article history:
Received 1 April 2013
Received in revised form 11 June 2013
Accepted 21 July 2013
Available online 15 August 2013

Keywords:
Lightweight aggregate
Porous concrete
Diatomite
Pumice
Autoclaved aerated concrete
Thermal conductivity

ABSTRACT

In this study, the use of lightweight aggregate (LWA) for making lightweight pervious concrete (LWPC) was presented. Diatomite (DA) and pumice (PA) were used as natural LWAs in pervious concretes. Three cement paste contents of 15%, 20%, and 25% by volume were used. The results were compared to those of LWPC containing recycled LWA from autoclaved aerated concrete (RA). The results indicated that the use of DA, PA, and RA as coarse aggregates in pervious concrete could reduce the density and thermal conductivity about 3–4 times compared with pervious concrete containing natural aggregate. The densities were 558–775 kg/m^3 which were lower than 800 kg/m^3 and suited for use as insulating concrete. The 28-day compressive strengths of LWPCs ranged from 2.47 to 5.99 MPa. The increase in cement paste content improved the mechanical properties of LWPCs. LWPC containing DA showed higher mechanical properties and a lower thermal conductivity than those of RA and PA. However PA exhibited higher water permeability.

1. Introduction

Lightweight aggregates (LWAs) can be used as aggregates to produce lightweight concretes (LWCs) in a wide range of densities and strengths with different applications. The low density LWCs with compressive strengths ranging from 0.69 to 6.89 MPa are usually employed as insulating concrete. Moderate strength LWCs with compressive strengths ranging from 6.89 to 17.24 MPa are as “fill” concrete. Structural LWCs with compressive in excess of 17.24 MPa with reduced dead load are used for reinforced concrete [1].

The primary benefit of using LWA is the reducing of dead load. LWAs are generally porous materials resulting in superior thermal, acoustic and fire insulations [2,3]. Diatomite is natural lightweight rock resulting from the siliceous fossilized remains of diatoms. It consists of rigid perforated shells called frustules and possesses low density and high porosity. Diatomite can be used as pozzolanic additive to improve plasticity and strengths of concrete [4,5] and can be used in producing lightweight concrete and insulation bricks [3,4]. Pumice is a natural lightweight aggregate with a sponge-like structure created by the release of gases during the solidification of lava. There are two types of pumice: basaltic pumice (scoria) and acidic pumice. The density of acidic pumice is rather less than basaltic pumice. Pumice aggregate can be used in the production of lightweight concrete with sufficient strength and density for use as structural lightweight concrete [6]. Generally, the effective insulating concrete is found in LWCs with high porosity or very low density. The LWCs containing natural LWAs viz., diatomite and pumice [3,7,8] are less effective than insulator materials due to the higher its density as specified in ASTM C332 [9].

Pervious concrete is the concrete with no fine aggregate. The connected void allows water and air to pass through. It can be used in environmental applications such as permeable concrete for pavement, water purifying concrete, noise absorbing concrete, air permeable concrete, and other civil engineering and architectural applications [10–13]. Moreover, pervious concrete contains a large amount of voids and thus its density and thermal conductivity are less than that of conventional concrete [14]. With these special features, the pervious concrete containing natural LWAs further reduces the weight and thermal conductivity of LWCs and therefore

---

* Corresponding author. Tel.: +66 4320 2846 (127); fax: +66 4320 2846 (102).
E-mail address: vancsa@kku.ac.th (V. Sata).

0950-0618/$ - see front matter © 2013 Elsevier Ltd. All rights reserved.
http://dx.doi.org/10.1016/j.conbuildmat.2013.07.077

they may be used as better acoustic and thermal insulating materials. In addition, there are few published studies on the properties of lightweight pervious concrete (LWPC) [15]. Therefore, this study focused on the use of LWA in previous concrete.

In this experiment, the effects of LWA types and cement paste contents on the properties of lightweight pervious concrete (LWPC) were studied. The diatomite and pumice were used as natural coarse LWAs. The cement paste contents of 15%, 20% and 25% by volume were used for each type of LWA. The total void ratio, water permeability coefficient, density, compressive strength, splitting tensile strength, surface abrasion resistance, and thermal conductivity coefficient of LWPCs were evaluated. In addition, the results were compared to those of LWPC containing recycled coarse LWA from autoclaved aerated concrete.

2. Material and sample preparation

2.1. Cement paste

Cement paste was prepared from ordinary Portland cement (OPC) with specific gravity of 3.15 and Blaine fineness of 3120 cm^2/g, type F superplasticizer (SP) at the dosage of 1.25% by weight of cement, and tab water. The constant water to cement ratio (W/C) of 0.24 was used for all mixes with the designed flow value of cement paste of 170–180 mm measured in accordance with JIS R 5201 [16].

2.2. Lightweight aggregates (LWAs)

Three types of LWAs viz., diatomite aggregate (DA), pumice aggregate (PA), and recycled aggregate from autoclaved aerated concrete (RA) were used as coarse aggregates. DA was taken from Lampang province in the north of Thailand. It was calcined at 800 °C for 4 h to reduce clay mineral [17,18]. Commercially variable acidic pumice was used as PA. RA was broken autoclaved aerated concrete blocks obtained from construction site. All types of aggregates were crushed and sieved into the same particle sizes of 4.8–9.5 mm. The coarse aggregates were prepared in saturated surface dry (SSD) condition before the mixing to maintain the same flow value of cement paste of 170–180 mm and to prevent cracking problems due to the water absorption of aggregate [19–21].

2.3. Mix proportions

In order to investigate the effects of different types of LWAs and cement paste contents on the physical and mechanical properties of LWPCs, the mixtures were made with three types of LWAs (DA, PA, and RA) and three cement paste contents of 15%, 20%, and 25% by volume. Nine mix proportions are summarized in Table 1. The names of concretes were given by aggregate type and paste content. For example, RA-15 denotes the LWPC containing RA and 15% of cement paste content by volume.

2.4. Mixing and casting

Cement paste was mixed in a pan-type of mixer for 3 min and then coarse aggregates was added to the mixture and mixed for 2 min. The mixture was placed into a mold and vibrated on vibrating table for 10 s. Two sizes of the samples were cast. The cylindrical samples of 100 mm in diameter and 200 mm in height were used to measure the compressive strength, splitting tensile strength, water permeability, density, total void ratio, and thermal conductivity. The 150 × 300 × 35 mm rectangular samples were used to measure the surface abrasion resistance. The cast samples were covered with damp cloth and plastic sheet to prevent moisture loss and were demolded after 1 day and stored in a moist room until testing age.

Table 1
Mix proportions of LWPCs.

Mix	LWA in SSD (kg/m^3)			OPC (kg/m^3)	Water (kg/m^3)	SP (kg/m^3)
	DA	PA	RA			
DA-15	740	–	–	269	64.6	3.35
DA-20	740	–	–	359	86.1	4.47
DA-25	740	–	–	448	107.6	5.59
PA-15	–	565	–	269	64.6	3.35
PA-20	–	565	–	359	86.1	4.47
PA-25	–	565	–	448	107.6	5.59
RA-15	–	–	630	269	64.6	3.35
RA-20	–	–	630	359	86.1	4.47
RA-25	–	–	630	448	107.6	5.59

3. Tests

3.1. Physical property tests of LWAs

Unit weight and bulk specific gravity with absorption were tested in according with ASTM C29 [22] and ASTM C127 [23], respectively. To determine the resistance to degradation of LWA, the procedure as specified in ASTM C131 [24] was adapted for this study using eight 46-mm diameter steel balls of approximately 400 g each. The volume of LWA for the test was the same as that of natural aggregate. This amounted to 1500 g of oven dry LWA for the Los Angeles test.

3.2. Mechanical property tests of LWPCs

Compressive strengths were tested at the ages of 7 and 28 days in according with ASTM C39 [25]. Before the testing, the samples were capped at both ends with sulfur capping compound to level the loading surface. The splitting tensile strength was tested at 28 days in according with ASTM C496 [26]. The reported results were the averages of 3 samples.

Surface abrasion resistance was tested at 28 days by the rotating-cutting method in accordance with ASTM C944 [27]. The samples were left to dry for 1 day before the test (air-dry condition). The sample was abraded with 98 N loads on the surface for 30 s after contact between the cutter and the surface. The abrasion resistances of each pervious concrete were done six times, three on each side of the concrete samples.

3.3. Total void ratio, density, and water permeability tests of LWPCs

Total void ratio and density of samples was tested in accordance with ASTM C1754 [28]. With the recommendation of ACI 522 [29], the water permeability coefficient of LWPC was measured using the constant head method. To prevent flow between sample and surface of measuring cylinder, the side of cylindrical sample was wrapped by rubber tube and tightened by circular clamps. The time required for a quantity of water to flow through was measured after a steady state flow. The coefficient of water permeability was calculated following Darcy's Law as shown in the following equation:

$$k = QL/HAt \tag{1}$$

where k is the water permeability coefficient (cm/s), Q is the quantity of water collected (cm^3) over time t (s), L is the length of specimen (cm), H is the water head (cm), and A is the cross sectional area of the specimen (cm^2).

3.4. Thermal conductivity test of LWPCs

The thermal conductivity coefficients were tested using a direct measuring instrument with surface probe (ISOMET2114, Applied Precision Ltd.). The measurement ranges of the device are 0.04–6.0 W/m K.

4. Results and discussion

4.1. Properties of LWAs

Visual observation of all LWAs as shown in Fig. 1 clearly showed that surface texture of RA was rougher and more porous than those of DA and PA. For particle shape, PA was rounded, while DA was slightly rounded and RA was angular. The crushed surfaces of LWAs were examined with Scanning Electron Microscope (SEM) and shown in Fig. 2. It could be clearly observed that RA consisted of large round pores of approximately 200 μm in size while PA consisted of very irregular pores ranging in size of smaller than 10 μm to slightly smaller than 200 μm. The surface texture of DA was different as it appeared denser with uniform pores of size mostly smaller than 10 μm.

The physical properties and chemical composition of all coarse aggregates are shown in Tables 2 and 3. The dry loose bulk densities of DA, PA, and RA were 346, 353, and 361 kg/m^3, respectively which were lower than 880 kg/m^3 of maximum density of LWA for structural concrete as specified in ASTM C330 [30]. The DA, PA, and RA had high water absorptions of 114.1%, 60.3%, and 74.5%, respectively, due to their highly porous surfaces. The values of specific gravity of DA, PA, and RA were 1.32, 1.14, and 1.16, respectively. The Los Angeles abrasion of LWA was presented in the percent weight loss. The weight losses of DA, PA and RA were 52.6%, 66.2%, and 89.9%, respectively. The results showed that DA had higher abrasion resistance than PA and RA and were consistent with the pore and surface texture results.

4.2. Compressive strengths, splitting tensile strengths, and surface abrasion resistances of LWCPs

Table 4 summarizes the compressive strengths, splitting tensile strengths, and weight losses by surface abrasion of LWPCs. When the cement paste content increased from 15% to 25%, the mechanical properties were enhanced. For example, for LWPC containing RA, the 28-day compressive strength increased from 2.62 to 4.45 MPa, the splitting tensile strength increased from 0.58 to 0.93 MPa, and the weight loss decreased from 17.0 to 9.7 g. With regards to the effect of LWA types, DA-25 showed the highest 28-day compressive strength of 5.99 MPa and the lowest weight loss of 8.2 g. The compressive strengths and surface abrasions of LWPC containing DA were higher than those of PA and RA due to its denser texture as also shown by the high resistance to Los Angeles abrasion. In addition, DA in this study was calcined to reduce clay mineral in order to enhance its pozzolanic property [17,18] and this improved the strength of DA concrete. However, the differences between splitting tensile strengths of these three LWAs were not significant.

The 7-day compressive strengths of all LWPCs were approximately 83% of the 28-day compressive strength which was slightly higher than the conventional concrete (70–80%). This may be due to porous and rough surface of LWAs allowed the infiltration of cement paste into aggregate resulting in the absence of wall effect at interfacial zone and the improvement of LWAs [31]. In addition, the strength of the low W/C cement paste developed quite rapidly [32]. The compressive strengths at 28 days of LWPCs were 2.47–5.99 MPa. Although the LWPCs had no fine aggregate and large pore, the compressive strengths were close to those of insulating concrete containing diatomite (3.5–5.8 MPa) [3] and aerated concrete (2.0–8.5 MPa) [33], and were higher than insulating concrete containing micro-sphere from pulverised fuel ash (0.6–2.9 MPa) [34]. The ratios of the splitting tensile strengths to the compressive strengths ranged from 15.2–22.9% with the average of 18.8%. They were higher than those of pervious concrete containing natural aggregate which ranged from 9–14% [35].

4.3. Densities, total void ratios, and water permeability coefficients of LWPCs

The results of densities, total void ratios, and water permeability coefficients of LWPCs are shown in Table 5. The increase in cement paste raised the density while the total void ratio and water permeability coefficient decreased. The densities of LWPCs of 558–775 kg/m^3 were lower than those of pervious concrete containing natural aggregate from crushed limestone (about 3 times) [14,36]. Besides, they were lower than 800 kg/m^3 and thus suited for insulating concrete in according with ASTM C495 [37]. The total void ratios of 15.6–31.8% were within the range recommended by ACI 522 [29] for the appropriate permeability of pervious concrete. When cement paste content of LWPCs increased from 15% to 20%, the water permeability coefficients reduced rapidly such as the reduction of 4.77–1.30 cm/s of PA concrete. This indicated that the connected voids of LWPCs were drastically decreased. The LWPC containing PA tended to have higher water permeability than those containing RA and DA. This may be attributed to the quite round shape of PA.

As the total void content decreased, the compressive strength increased. The increase of cement paste content increased the thickness of paste covering of aggregate and decreased total void ratio, consequently the compressive strength increased. Fig. 3 showed the state of paste covering and voids of LWPC cut surfaces. The total void area was obtained from the image analysis. Each image had a size of 6 × 6 cm^2 with resolution of 2000 × 2000 pixels. The obtained void ratios (V_{im}) were similar to the measured values. At 15% cement paste content, the thin layer of paste merely covered aggregate surface resulting in a large void and relatively small contact area. At 20% and 25% cement paste contents, not only the covering of paste was thicker but the excess paste filled the void resulting in a small void and relatively high contact area.

The relationship between the compressive strength and the total void ratio are plotted in Fig. 4. The graph of DA concrete lies on the top and shifts to the right side, while the graphs of RA and PA concretes lie below and are close together. It showed that at the same total void ratio, the compressive strength of LWPC containing DA was higher than those of PA and RA although it used lower cement paste content. The empirical equations relating compressive strengths (σ) and total void ratios (V) are obtained as:

$$\sigma = 13.25e^{-0.0500V},\ R^2 = 0.991 \text{ for LWPC with DA} \tag{2}$$

$$\sigma = 10.09e^{-0.0441V},\ R^2 = 0.995 \text{ for LWPC with PA} \tag{3}$$

$$\sigma = 11.95e^{-0.0515V},\ R^2 = 0.989 \text{ for LWPC with RA} \tag{4}$$


(a) DA (b) PA (c) RA

Fig. 1. Particle shapes of LWAs.

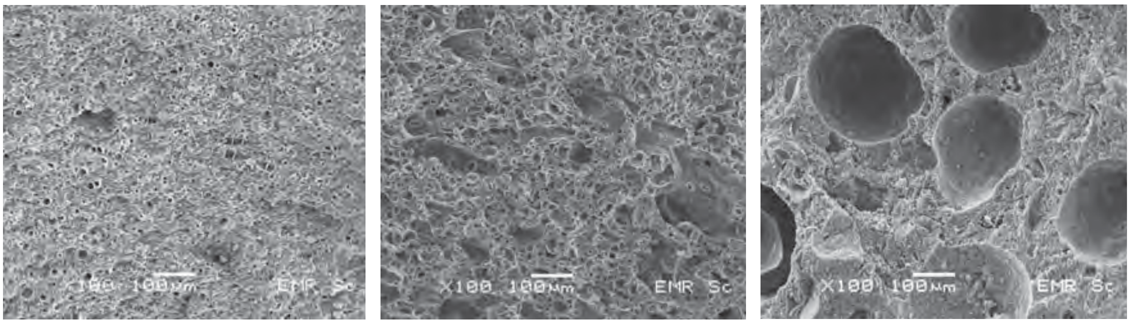

(a) DA (b) PA (c) RA

Fig. 2. SEM surfaces of LWAs (100×).

Table 2
Physical properties of LWAs.

Property	DA	PA	RA
Dry loose bulk density (kg/m^3)	346	353	361
Specific gravity	1.32	1.14	1.16
Water absorption (%)	114.1	60.3	74.5
Los Angeles abrasion weight loss (%)	52.6	66.2	89.9

Table 3
Chemical composition of LWAs.

Chemical composition (%)	DA	PA	RA
SiO_2	83.07	61.09	38.48
Al_2O_3	7.78	12.30	2.45
Fe_2O_3	4.60	5.29	1.83
CaO	0.52	3.68	36.33
MgO	0.45	1.11	0.71
Na_2O	0.14	6.11	0.26
K_2O	1.92	5.35	1.48
SO_3	–	0.09	5.71
TiO_2	0.51	0.74	0.11
LOI	0.80	3.30	12.40

Table 4
Mechanical properties of LWPCs.

Mix	7-Day compressive strength (MPa)	28-Day compressive strength (MPa)	28-Day splitting tensile strength (MPa)	Surface abrasion weight loss (g)
DA-15	2.65	3.20	0.57	13.2
DA-20	3.79	4.68	0.71	10.2
DA-25	5.10	5.99	0.93	8.2
PA-15	1.94	2.47	0.47	17.8
PA-20	2.14	3.50	0.75	12.3
PA-25	3.88	4.30	0.99	10.2
RA-15	2.26	2.62	0.58	17.0
RA-20	2.56	3.43	0.67	14.7
RA-25	4.58	4.45	0.93	9.7

In addition, these exponential equations with high correlation coefficient could predict the compressive strengths at zero total void ratios of 11.95, 13.25, and 10.09 MPa for LWPCs with RA, DA, and PA, respectively. The relatively strong relation between the compressive strength and void ratio of LWPC was similar to a porous brittle material and normal pervious concrete as suggested by Ryshkewitch [38] and Chindaprasirt et al. [39,40]. In addition, the relationship between the compressive strength and water permeability coefficient of LWPC with different types of LWAs are plotted in Fig. 5 and the equations could be expressed as:

Table 5
Physical properties of LWPCs.

Mix	Density (kg/m^3)	Total void ratio (%)	Water permeability coefficient (cm/s)
DA-15	558	28.1	2.43
DA-20	644	21.4	0.97
DA-25	740	15.5	0.42
PA-15	602	31.8	4.77
PA-20	690	24.5	1.30
PA-25	765	19.1	0.90
RA-15	602	29.7	2.93
RA-20	701	23.6	0.98
RA-25	775	19.6	0.30

$$\sigma = 6.56e^{-0.301k},\ R^2 = 0.983 \text{ for LWPC with DA} \tag{5}$$

$$\sigma = 4.48e^{-0.127k},\ R^2 = 0.922 \text{ for LWPC with PA} \tag{6}$$

$$\sigma = 4.45e^{-0.187k},\ R^2 = 0.932 \text{ for LWPC with RA} \tag{7}$$

where σ is compressive strength of LWPC (MPa) and k is water permeability coefficient (cm/s).

The linear relationship between the density and void ratio of LWPC with different types of LWAs are plotted in Fig. 6. The DA concrete showed lower density than the PA and RA concretes at the same void content. The correlation coefficient of the results was high with R^2 of 0.995–0.999. The densities and total void ratios could be expressed as:

$$D = 961 - 14.45V,\ R^2 = 0.995 \text{ for LWPC with DA} \tag{8}$$

$$D = 1047 - 14.69V,\ R^2 = 0.999 \text{ for LWPC with PA} \tag{9}$$

$$D = 1105 - 16.99V,\ R^2 = 0.999 \text{ for LWPC with RA} \tag{10}$$

where D is dry density of LWPC (kg/m^3) and V is total void ratio (%).

In this study, the graphs of water permeability coefficient and total void ratio are plotted in Fig. 7. It can be observed that the water permeability coefficients of LWPCs with higher cement paste content were clearly lower than those with low cement paste content because the connected pores reduced with the increase in cement paste content. The graph of PA lies on the top and shifts to the right. It indicated that the permeability and total void ratio of LWPC containing PA was higher than those of LWPC containing DA. Moreover, at the same total void ratio, the permeability of LWPC containing PA was higher than that of LWPC. This could be attributed to the more rounded shape of PA that resulted in higher pore connectivity. For the graph of RA, it lies on the bottom and presents the lowest water permeability. For the graph of RA, it lies

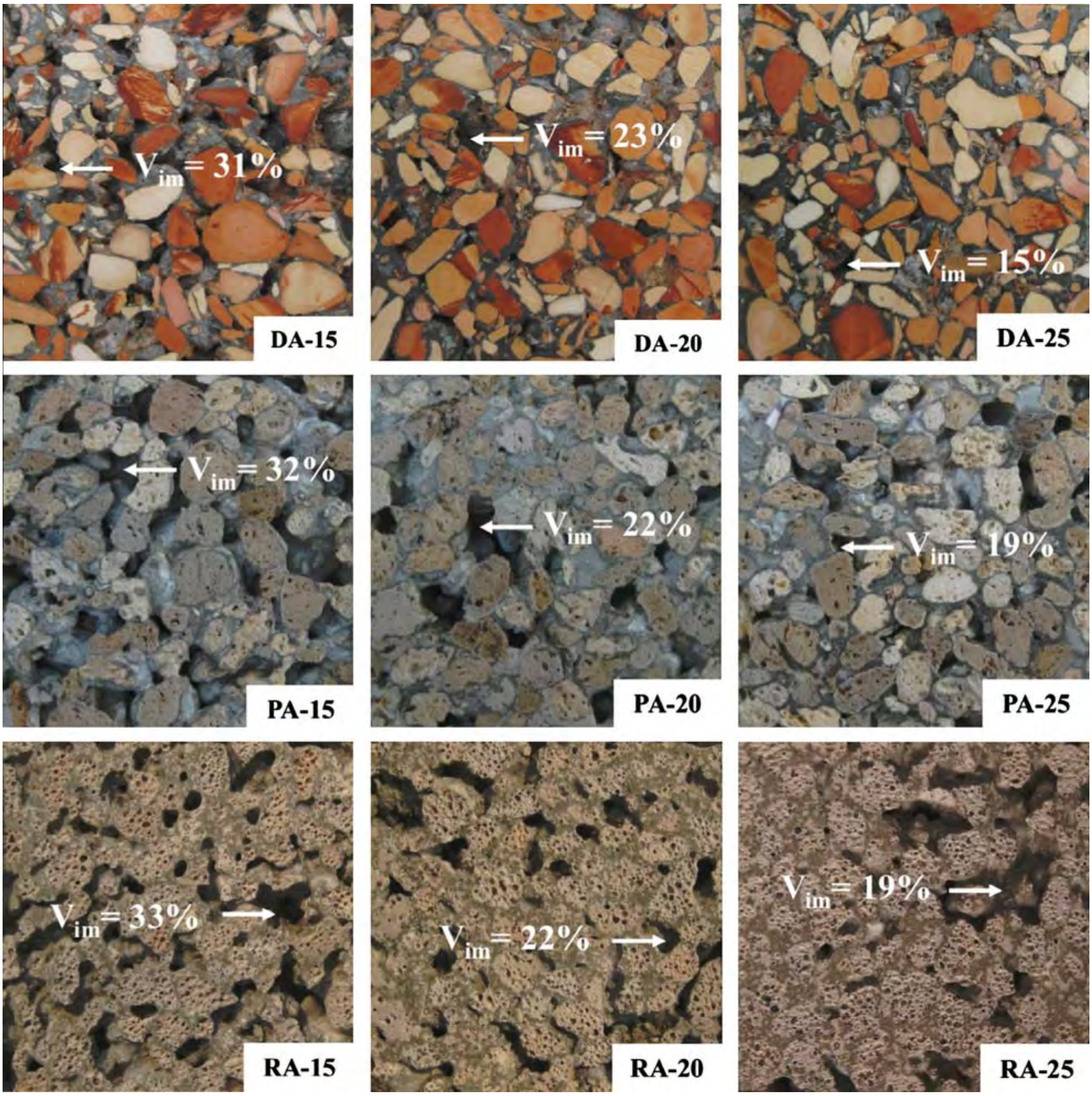

Fig. 3. State of the paste covering and total void content of LWPCs.

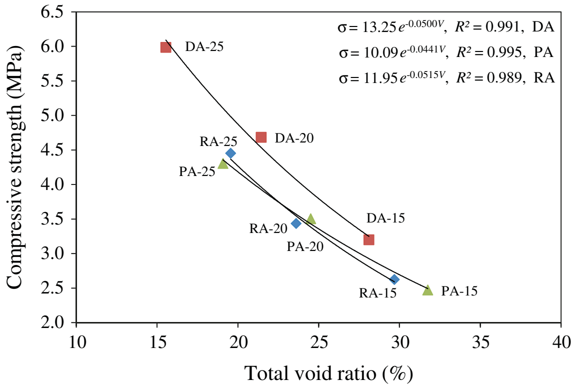

Fig. 4. Compressive strength and total void ratio of LWPCs.

at the bottom and presents the slightly lower water permeability than DA concrete. As already discussed, this may be due to the fact that the RA consisted of large round pores of approximately 200 μm, which are unconnected pores. The strong relationship between water permeability coefficient and total void ratio was an exponential equation as also reported by other researches [41,42]. The three equations could be expressed as:

$$k = 0.047e^{0.140V}, R^2 = 0.999 \text{ for LWPC with DA} \tag{11}$$

$$k = 0.061e^{0.134V}, R^2 = 0.948 \text{ for LWPC with PA} \tag{12}$$

$$k = 0.004e^{0.220V}, R^2 = 0.982 \text{ for LWPC with RA} \tag{13}$$

where k is water permeability coefficient (cm/s) and V is total void ratio (%).

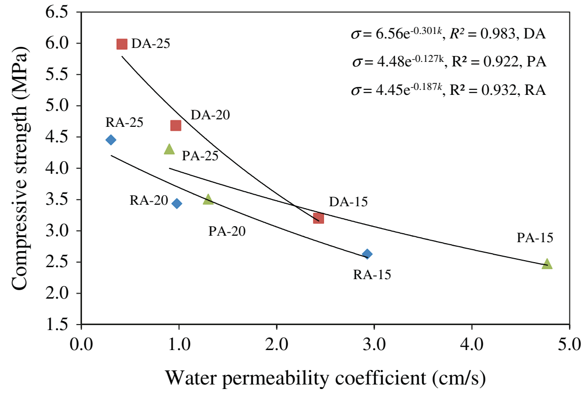

Fig. 5. Compressive strength and water permeability coefficient of LWPCs.

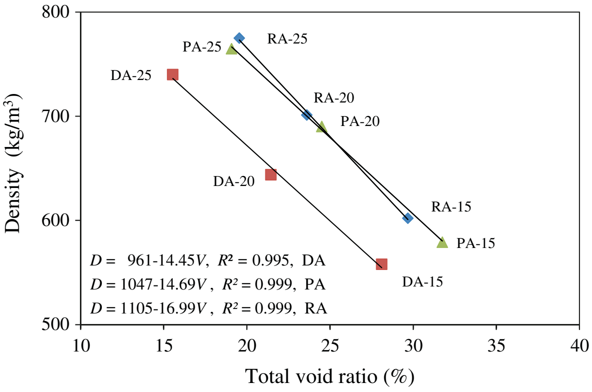

Fig. 6. Density and total void ratio of LWPCs.

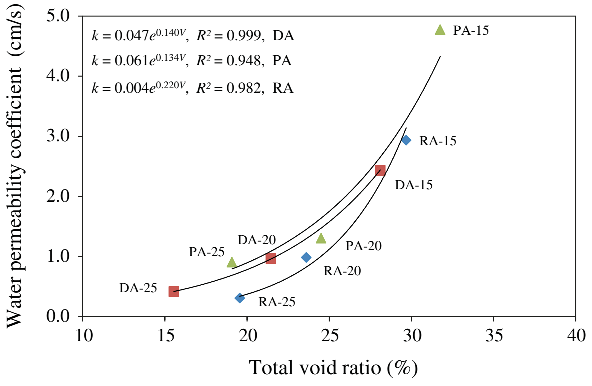

Fig. 7. Water permeability coefficient and total void ratio of LWPCs.

4.4. Thermal conductivity coefficients of LWPCs

The thermal conductivity coefficients are shown in Fig. 8. The results thermal conductivity coefficients depended on the cement paste contents and types of aggregates. When the cement paste content of LWPCs increased from 15% to 25%, the thermal conductivity coefficient increased from 0.16 to 0.23 W/m K for DA concrete, from 0.16 to 0.24 W/m K for PA concrete, and from 0.17 to 0.25 W/m K for RA concrete. The increase in cement paste content caused the filling of paste in voids and increased the density, consequently the thermal conductivity coefficient increased [43]. The thermal conductivity coefficients of LWPC containing DA were slightly lower than those of PA and RA due to its lower density.

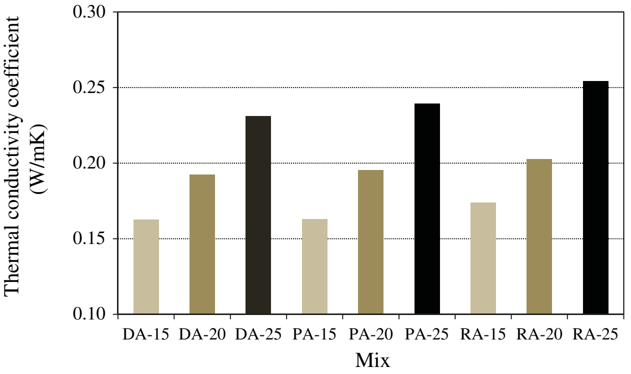

Fig. 8. Thermal conductivity coefficients of LWPCs.

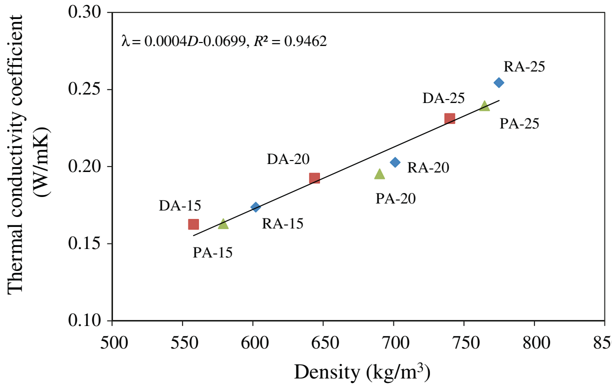

Fig. 9. Thermal conductivity coefficient and density of LWPCs.

The thermal conductivity coefficients of LWPCs (0.16–0.25 W/m K) were slightly higher than autoclaved aerated concrete (0.11–0.21 W/m K) with similar strength of 2.8–8.5 MPa and density of 600–700 kg/m^3 [33]. The LWPCs showed lower thermal conductivities and densities than those of natural LWC (thermal conductivities of 0.23–0.314 W/m K and densities of 900–1190 kg/m^3) [3]. In addition, the thermal conductivities of LWPCs was approximately 3–4 times lower than that of pervious concrete containing natural [13].

The linear relationships between the thermal conductivity coefficients and the densities of LWPCs containing different types of LWAs are plotted in Fig 9. The correlation coefficient of the results was high with R^2 ranging between 0.9462. The equation of results could be expressed as:

$$\lambda = 0.0004D - 0.0699, R^2 = 0.9462 \text{ for LWPCs} \tag{14}$$

where λ is thermal conductivity coefficient (W/m K) and D is dry density of LWPC (kg/m^3).

5. Conclusions

The use of RA, DA, and PA as coarse aggregates in pervious concrete reduced the density and thermal conductivity compared with that of pervious concrete containing natural aggregate (approximate 3–4 times). The densities of all LWPCs ranged from 558 to 775 kg/m^3 with the 28 days compressive strengths varied between 2.47 and 5.99 MPa and could be used for application in insulating material. The thermal conductivity coefficients of LWPCs were 0.16 and 0.25 W/m K which were slightly higher than that of autoclaved aerated concrete and similar to low density LWCs. The increase in cement paste content decreased total void ratio and water permeability, while mechanical properties and density were increased. The increasing of cement paste content from 15% to 20% could rapidly reduce water permeability. LWPC containing DA exhibited a higher quality of mechanical properties and a lower thermal conductivity than those of RA and PA. However, LWPC containing PA showed the highest water permeability.

Acknowledgements

This work was financial supported by the Thailand Research Fund (TRF) under the TRF Senior Research Scholar, Grant No. RTA5480004 and Kasetsart University Chalermphrakiat, Sakon Nakhon Province Campus. The authors also would like to acknowledge the support of the Higher Education Research Promotion and National Research University Project of Thailand, Office of the Higher Education Commission, through the Advanced Functional Materials Cluster of Khon Kaen University.

References

[1] ACI committee 213. Guide for structural lightweight aggregate concrete. Report No. 213R-87. Detroit, USA: American Concrete Institute; 1999. p. 27.
[2] Tay J, Yip W. Sludge ash as lightweight concrete material. J Environ Eng 1989;115(1):56–64.
[3] Ünal O, Uygunoğlu T, Yildiz A. Investigation of properties of low-strength lightweight concrete for thermal insulation. Build Environ 2007;42(2):584–90.
[4] Gökçe MV, Koç İ. Use of diatomite in the production of lightweight building elements with cement as binder. Sci Res Essays 2012;7(7):774–81.
[5] Fragoulis D, Stamatakis MG, Papageorgiou D, Chaniotakis E. The physical and mechanical properties of composite cements manufactured with calcareous and clayey Greek diatomite mixtures. Cem Concr Compos 2005;27(2):205–9.
[6] Anwar Hossain KM. Properties of volcanic pumice based cement and lightweight concrete. Cem Concr Res 2004;34(2):283–91.
[7] Topçu İB, Uygunoğlu T. Properties of autoclaved lightweight aggregate concrete. Build Environ 2007;42(12):4108–16.
[8] Uysal H, Demirboğa R, Şahin R, Gül R. The effects of different cement dosages, slumps, and pumice aggregate ratios on the thermal conductivity and density of concrete. Cem Concr Res 2004;34(5):845–8.
[9] American Society for Testing and Materials (ASTM) C332. Standard specification for lightweight aggregates for insulating concrete; 2009.
[10] Field R, Masters H, Singer M. An overview of porous pavement research. J Am Water Res Assoc 1982;18(2):265–70.
[11] Park S-B, Tia M. An experimental study on the water-purification properties of porous concrete. Cem Concr Res 2004;34(2):177–84.
[12] Park SB, Seo DS, Lee J. Studies on the sound absorption characteristics of porous concrete based on the content of recycled aggregate and target void ratio. Cem Concr Res 2005;35(9):1846–54.
[13] Wong JM, Glasser FP, Imbabi MS. Evaluation of thermal conductivity in air permeable concrete for dynamic breathing wall construction. Cem Concr Compos 2007;29(9):647–55.
[14] Sata V, Wongsa A, Chindaprasirt P. Properties of pervious geopolymer concrete using recycled aggregates. Constr Build Mater 2013;42:33–9.
[15] Kim HK, Lee HK. Influence of cement flow and aggregate type on the mechanical and acoustic characteristics of porous concrete. Appl Acoust 2010;71(7):607–15.
[16] Japanese Industrial Standard (JIS) R5201. Physical testing methods for cement; 1997.
[17] Pimraksa K, Chindaprasirt P. Lightweight bricks made of diatomaceous earth, lime and gypsum. Ceram Int 2009;35(1):471–8.
[18] Yılmaz B, Ediz N. The use of raw and calcined diatomite in cement production. Cem Concr Compos 2008;30(3):202–11.
[19] González-Corrochano B, Alonso-Azcárate J, Rodas M, Luque FJ, Barrenechea JF. Microstructure and mineralogy of lightweight aggregates produced from washing aggregate sludge, fly ash and used motor oil. Cem Concr Compos 2010;32(9):694–707.
[20] Lo Y, Gao XF, Jeary AP. Microstructure of pre-wetted aggregate on lightweight concrete. Build Environ 1999;34(6):759–64.
[21] Lo TY, Cui HZ, Tang WC, Leung WM. The effect of aggregate absorption on pore area at interfacial zone of lightweight concrete. Constr Build Mater 2008;22(4):623–8.
[22] American Society for Testing and Materials (ASTM) C29/C29M. Standard test method for bulk density (“unit weight”) and voids in aggregate; 2003.
[23] American Society for Testing and Materials (ASTM) C127. Standard test method for density, relative density (specific gravity), and absorption of coarse aggregate; 2001.
[24] American Society for Testing and Materials (ASTM) C131. Standard test method for resistance to degradation of small-size coarse aggregate by abrasion and impact in the Los Angeles machine; 2003.
[25] American Society for Testing and Materials (ASTM) C39. Standard test method for compressive strength of cylindrical concrete specimens; 2001.
[26] American Society for Testing and Materials (ASTM) C496. Standard test method for splitting tensile strength of cylindrical concrete specimens; 1996.
[27] American Society for Testing and Materials (ASTM) C944. Standard test method for abrasion resistance of concrete or mortar surfaces by the rotating-cutter method; 1999.
[28] American Society for Testing and Materials (ASTM) C1754. Standard test method for density and void content of hardened pervious concrete; 2012.
[29] ACI committee 522. Pervious Concrete, Report No. 522R-10. Detroit, USA: American Concrete Institute; 2010. p. 38.
[30] American Society for Testing and Materials (ASTM) C330. Standard specification for lightweight aggregates for structural concrete; 2003.
[31] Lo TY, Cui HZ. Effect of porous lightweight aggregate on strength of concrete. Mater Lett 2004;58(6):916–9.
[32] Neville AM, Brooks JJ. Concrete technology. Malaysia: Prentice Hall; 2010.
[33] Narayanan N, Ramamurthy K. Structure and properties of aerated concrete: a review. Cem Concr Compos 2000;22(5):321–9.
[34] Losiewicz M, Halsey DP, Dews SJ, Olomaiye P, Harris FC. An investigation into the properties of micro-sphere insulating concrete. Constr Build Mater 1996;10(8):583–8.
[35] Kevern JT, Wang K, Schaefer VR. Effect of coarse aggregate on the freeze-thaw durability of pervious concrete. J Mater Civil Eng 2010;22(5):469–75.
[36] Yang J, Jiang G. Experimental study on properties of pervious concrete pavement materials. Cem Concr Res 2003;33(3):381–6.
[37] American Society for Testing and Materials (ASTM) C495. Standard test method for compressive strength of lightweight insulating, concrete; 1999.
[38] Ryshkewitch E. Compression strength of porous sintered alumina and zirconia. J Am Ceram Soc 1953;36(2):65–8.
[39] Chindaprasirt P, Hatanaka S, Chareerat T, Mishima N, Yuasa Y. Cement paste characteristics and porous concrete properties. Constr Build Mater 2008;22(5):894–901.
[40] Chindaprasirt P, Hatanaka S, Mishima N, Yuasa Y, Chareerat T. Effects of binder strength and aggregate size on the compressive strength and void ratio of porous concrete. Int J Minerals Metall Mater 2009;16(6):714–9.
[41] Tho-in T, Sata V, Chindaprasirt P, Jaturapitakkul C. Pervious high-calcium fly ash geopolymer concrete. Constr Build Mater 2012;30:366–71.
[42] Neithalath N, Sumanasooriya MS, Deo O. Characterizing pore volume, sizes, and connectivity in pervious concretes for permeability prediction. Mater Charact 2010;61(8):802–13.
[43] Demirboğa R, Gül R. The effects of expanded perlite aggregate, silica fume and fly ash on the thermal conductivity of lightweight concrete. Cem Concr Res 2003;33(5):723–7.

Materials and Design 52 (2013) 580–586

Contents lists available at SciVerse ScienceDirect

Materials and Design

journal homepage: www.elsevier.com/locate/matdes

Lightweight geopolymer concrete containing aggregate from recycle lightweight block

Patcharapol Posi[a], Chaiyapong Teerachanwit[a], Chatchai Tanutong[a], Suttikait Limkamoltip[a], Surasit Lertnimoolchai[b], Vanchai Sata[a], Prinya Chindaprasirt[a,*]

[a] Sustainable Infrastructure Research and Development Center, Dept. of Civil Engineering, Faculty of Engineering, Khon Kaen University, Khon Kaen 40002, Thailand
[b] Concrete Precision Unit, Udornthani 41000, Thailand

ARTICLE INFO

Article history:
Received 10 April 2013
Accepted 2 June 2013
Available online 15 June 2013

Keywords:
Lightweight geopolymer concrete
Lightweight aggregate
Recycle block
Compressive strength
Density

ABSTRACT

In this research, the properties of lightweight geopolymer concrete containing aggregate from recycle lightweight block were studied. The recycle block was crushed and classified as fine, medium and coarse aggregates. The compressive strength and density with various liquid alkaline/ash ratios, sodium silicate/NaOH ratios, NaOH concentrations, aggregate/ash ratios and curing temperatures were tested. In addition, porosity, water absorption, and modulus of elasticity were determined. Results showed that the lightweight geopolymer blocks with satisfactory strength and density could be made. The 28-day compressive strength of 1.0–16.0 MPa, density of 860–1400 kg/m^3, water absorption of 10–31% and porosity of 12–34%, and modulus of elasticity of 2.9–9.9 GPa were obtained. It can be used as lightweight geopolymer concrete for wall and partition.

1. Introduction

The construction of building and structures in Thailand and many countries relies heavily on the Portland cement products. The structural members are usually made of reinforced concrete. The walls and panels are also Portland cement based products. The problems of the size and weight of reinforced concrete members and wall panels are of great concern [1]. In order to reduce the weight, lightweight structural concrete and normal lightweight concrete in the form of lightweight concrete block or wall using cast-in-place lightweight concrete have been developed. The purpose is to reduce the dead load of structure which also results in smaller and lighter structures and reduced cost of construction.

Lightweight concrete made with natural or artificial lightweight aggregates are available in many parts of the world. It can be used in producing concrete in a wide range of unit weights and suitable strengths for various applications including internal and external walls, inner leaves of roof decks and floors [2,3]. The production of lightweight aggregate concrete has been expanding, and now includes all types of no-fines concrete of low density of 300–1200 kg/m^3 for block production and of medium density of 1000–2000 kg/m^3 for structural concrete. The production of all types of concrete is normally based on the availability of lightweight aggregate, and cost dictates the use of lightweight aggregate concrete in place of normal-weight concrete [2].

The manufacturing of Portland cement results in the release of a large amount of carbondioxide into the Earth's atmosphere. Up to 13,500 tons per year or accounted to 7% of the green house gas produced annually [4]. Therefore, the other form of cementitious materials termed geopolymer was developed. It is made from starting materials containing silicon and aluminum which are activated in a high alkali solution. The starting material is usually based on class F fly ash and sometime called alkali-activated fly ash cement [5–9]. High calcium fly ash (class F) is also suitable for use as source materials [10,11].

The use of lightweight concrete block is increasing and its waste also increases from the damage of blocks from manufacturing, transportation and handling. The increased used especially for the housing industries also indicate the amount of lightweight block to be recycled.

This research aims to study the properties of lightweight geopolymer concrete made of lightweight aggregate from recycle block. The knowledge would be beneficial to future applications of the materials and construction industry.

2. Experimental program

2.1. Materials

Materials used in this research consisted of lignite fly ash from Mae Moh power station in the north of Thailand, sodium silicate with 15.32% Na_2O, 32.87% SiO_2, and 51.8% water, and sodium

---

[*] Corresponding author. Tel.: +66 8 1871 9588.
E-mail address: prinya@kku.ac.th (P. Chindaprasirt).

0261-3069/$ - see front matter
http://dx.doi.org/10.1016/j.matdes.2013.06.001

Fig. 1. Coarse, medium and fine recycle aggregates.

Table 1
Physical properties of materials.

Materials	Fly ash	FA	MA	CA
Specific gravity	2.52	2.61	1.96	1.42
Median particle size (μm)	18.6	–	–	–
Particle size (mm)	–	0.001–1.18	1.18–4.75	4.75–12.5
Fineness modulus	–	1.75	3.90	5.74
Density (kg/m^3)	–	720	390	360
Water absorption (%)	–	56	68	76

hydroxide (NaOH) of three concentrations of 5, 10, and 15 M and recycle lightweight block (RLB). RLBs were crushed and classified as fine aggregate (FA), medium aggregate (MA) and coarse aggregate (CA) with particle sizes ranging between 0.001 and 1.18, 1.18–4.75, 4.75–12.5 mm, respectively as shown in Fig 1. Chemical compositions of fly ash were determined using X-ray fluorescence (XRF) are shown in Table 2 and its X-ray diffraction (XRD) is shown in Fig. 2. The fly ash consisted of a high content of 45.23% SiO_2, 19.94% Al_2O_3, 13.15% Fe_2O_3, and 15.5% Ca0 with the loss on ignition (LOI) 0.87%. It was, therefore, a class F in accordance which ASTM:C618. The XRD analysis showed mainly amorphous phase with the peaks of crystals of magnetite, magnesioferrite, dachiardite, and calcium aluminum oxide. The physical properties of materials are shown in Table 1. The fly ash was 48% retained on sieve No. 325 (45 μm) with mean particle sized of 18.6 μm and Blaine finenesses of 2409 cm^2/g. It consists of mainly spherical particles with smooth surface as shown in Fig. 3.

2.2. Mix proportion

2.2.1. Aggregate gradation

To study the effect of aggregate gradation, the FA and MA portions were varied and the CA portion was kept constant at 30%. The effect of the change in the small aggregate portion is larger than that of the large portion [12]. A total of three aggregate gradations with FA:MA:CA ratios of 0:70:30 (0F), 30:40:30 (30F), and 70:0:30 (70F) were used.

2.2.2. Mix compositions

Five series of mixes were used to test the effects of liquid alkaline/ash ratios (series A), sodium silicate/NaOH ratios (series B), concentration of NaOH (series C), temperature of curing (series D), and aggregate/ash ratios (series E). The details of mixes are shown in Table 3.

2.3. Details of mixing

NaOH solution and fly ash were firstly mixed for 5 min in a pan mixer. Sodium silicate solution was then added and mixing was done for another 5 min until the mixture was uniform. The aggregate was added next and mixing was done for 1.5 min. The fresh lightweight geopolymer concretes were placed into 50 mm cube molds in accordance with ASTM:C109, into 100 mm cube molds, and 150 × 300 mm cylindrical molds in accordance with ASTM:C39. The specimens were covered damp cloth and plastic sheet to prevent moisture loss and placed in a 25 °C controlled room for 1 h [10]. The specimens were then transferred to oven curing for 48 h. Finally, the specimens were demolded and wrapped again with plastic sheet and stored in a 25 °C controlled room.

2.4. Details of test

2.4.1. Density and compressive strength

The density was determined at the ages of 28 days using the compressive strength specimens as described in ASTM:C138. The density was measured. After the density determination, the cube specimens were tested to determine the compressive strength in accordance with ASTM:C109. The reported density and compressive strengths were the average of three samples.

2.4.2. Water absorption and porosity

The cube specimens of series E were tested for porosity and water absorption at the age of 28 days in accordance with ASTM:C642. The porosity was calculated using Eq. (1) and the water absorption was calculated using Eq. (2).

$$\text{Porosity}(\%) = (C - A)/(C - D) \tag{1}$$

$$\text{Absorption}(\%) = [(B - A)/A] \times 100 \tag{2}$$

where A is the mass of oven – dry sample in air (g), B is mass of surface – dry sample in air after immersion (g), C is mass of surface – dry sample in air after immersion and boiling (g), and D is apparent mass of sample in water after immersion and boiling (g)

2.4.3. Modulus of elasticity

The cylinder specimens of series E were tested for the chord modulus at the age of 28 days in accordance with ASTM:C469. The reported results were the average of two samples.

3. Results and discussion

3.1. Compressive strength and density

3.1.1. Liquid alkaline/ash ratio

The results of compressive strength of lightweight geopolymer concrete series A with varies liquid alkaline/ash ratios are shown in Fig. 4a. The optimum compressive strength was at L/A ratio of 2.4. At low L/A ratios of 2.0 and 2.2, the mix was difficult to mix and compact due to the low liquid content [13]. The increase in the L/A ratio at this range increased the compressive strength of the geopolymer. However, when the L/A ratio increased from 2.4 to 2.8, the compressive strength decreased due to the excess liquid and bleeding in a similar manner to Portland cement concrete [14–

Table 2
Chemical composition of materials (by weight).

Chemical compositions (%)	SiO_2	Al_2O_3	Fe_2O_3	CaO	K_2O	TiO_2	Na_2O	P_2O_5	MgO	LOI
Fly ash	45.23	19.95	13.15	15.50	2.15	0.39	0.52	0.81	2.02	0.88

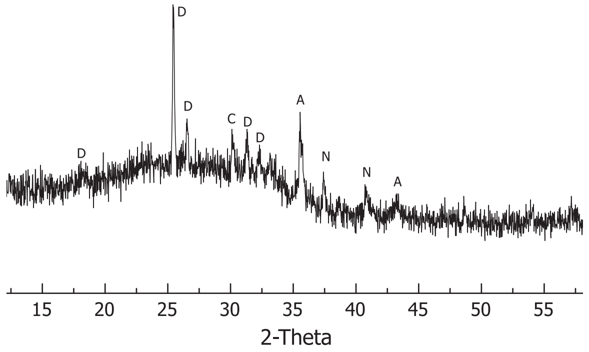

Fig. 2. XRD patterns of fly ash. A-magnetite: Fe_3O_4; C-magnesioferrite: Fe_2MgO_4; D-dachiardite: $Na_{1.1}K_{.7}Ca_{1.7}Al_{5.2}Si_{18.8}O_{48}$ $(H_2O)_{12.7}$; N-calcium aluminum oxide: $CaAl_2O_4$.

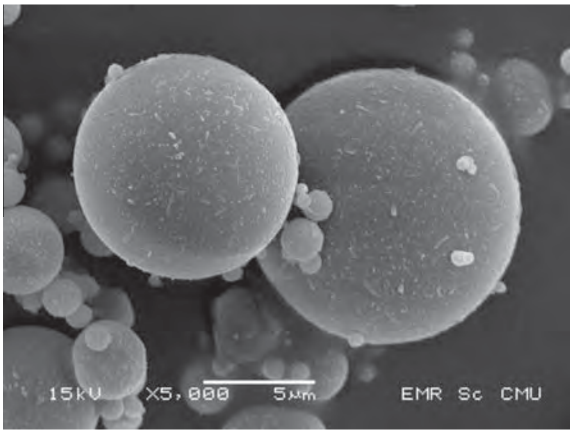

Fig. 3. SEM of fly ash.

Table 3
Weight ratios of geopolymer lightweight concrete mixes.

Series	L/A ratio	NS/NaOH ratio	NaOH (M)	Temp. of curing (°C)	Aggregate/ ash ratio
A	2.0, 2.2, 2.4, 2.6, 2.8	1.0	10	60	2.2
B	2.2	0.33, 0.67, 1.00, 1.50, 3.00	10	60	2.2
C	2.2	1.0	5, 10, 15	60	2.2
D	2.2	1.0	10	25, 40, 60	2.2
E	2.2	1.0	10	60	2.0, 2.2, 2.4, 2.6

16]. For example, the 28-day compressive strengths of 70F series A mixes with L/A ratios of 2.0, 2.2, 2.4, 2.6, and 2.8 were 7.0, 11.0, 12.7, 6.2, and 4.8 MPa, respectively.

With regards to aggregate sizes, the compressive strengths of mixes with the high amount of FA were higher than those with the low amount of FA. For example, the 28-day compressive strengths of L/A ratio of 2.2 mixes with 0F, 30F, and 70F aggregates were 2.0, 4.4, and 11.0 MPa, respectively. The use of FA aggregate with high surface area resulted in the better bonding of matrix and aggregate than that of CA and led to an increase in strength [17]. For the density, the results of lightweight geopolymer concrete with various L/A ratios are shown in Fig. 4b. The increased in L/A ratios resulted in lightweight geopolymer concrete with a slightly increase in density. For example, the density of lightweight geopolymer concretes with L/A ratios of 2.0, 2.2, 2.4, 2.6, and 2.8, and with 30F aggregate were 1099, 1131, 1252, 1237, and 1389 kg/m^3, respectively. The increase was due to the reduced ash which was low in density.

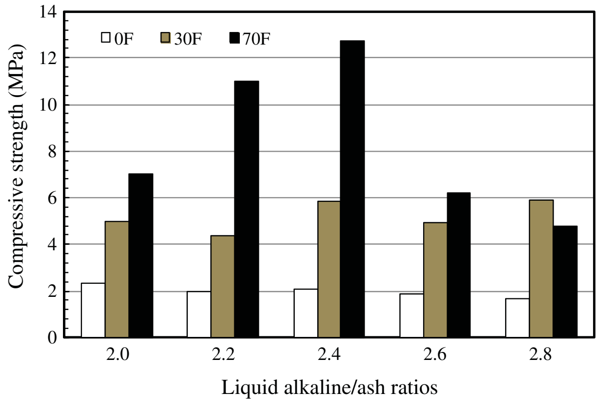

(a) Compressive strength

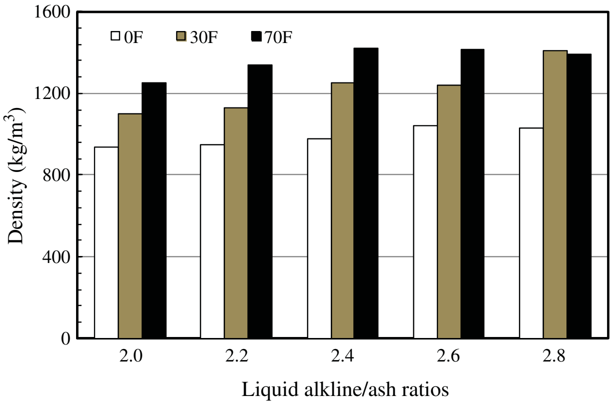

(b) Density

Fig. 4. Compressive strength and density at 28 days of lightweight geopolymer concrete series A at various L/A ratios.

Similarly, the density also increased with the increasing amount of FA. The densities of 0F, 30F, and 70F mixes with L/A ratio of 2.2 were 948, 1132, and 1336 kg/m^3, respectively. The density of FA was high at 720 kg/m^3 compared with the lower values of MA and CA of 390 and 360 kg/m^3, respectively (Table 1) and thus the use of a higher amount of FA resulted in geopolymer with higher density.

3.1.2. Sodium silicate/NaOH ratio

The effects of compressive strength of lightweight geopolymer concrete with varies NS/NaOH ratios are shown in Fig. 5a. The compressive strength increased with the increasing of NS/NaOH ratios. Similar increases in strength were reported with NS/NaOH ratio up to 1.50, however, the increased in NS/NaOH ratio beyond this value resulted in a reduction in strength due to difficulties in compaction of the mixes as the mix was too stiff with the low liquid/ash ratio of 0.6 [13]. For this study, the strength increased even with the NS/NaOH ratio of 3.0. The increase in strength at this NS/NaOH ratio was possible as a result of high liquid/ash ratio of 2.2 which made the mix workable and compactable. For example, the 28-day compressive strength of samples with NS/NaOH ratios of 0.33, 0.67, 1.00, 1.50, and 3.00 were 7.6, 9.7, 10.5, 12.9, and 15.4 MPa, respectively. The NS/NaOH ratios also affected the pH conditions and the strength development of geopolymer [10]. The densities of lightweight geopolymer concrete with various NS/NaOH ratios were

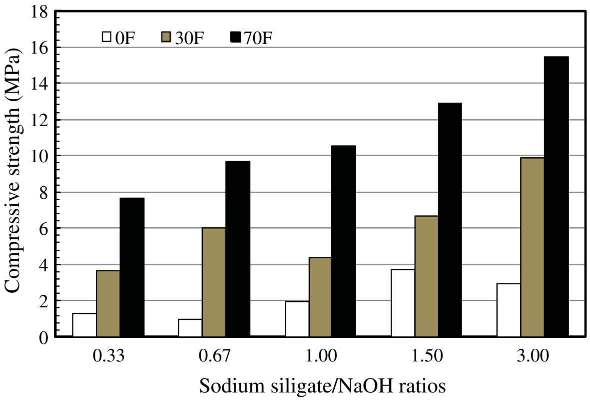

(a) Compressive strength

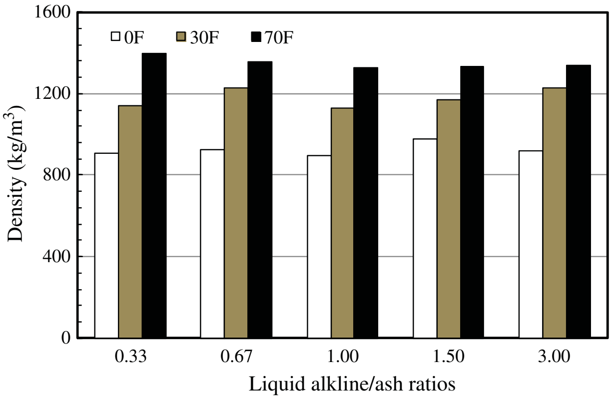

(b) Density

Fig. 5. Compressive strength and density at 28 days of lightweight geopolymer concrete series B at various NS/NaOH ratios.

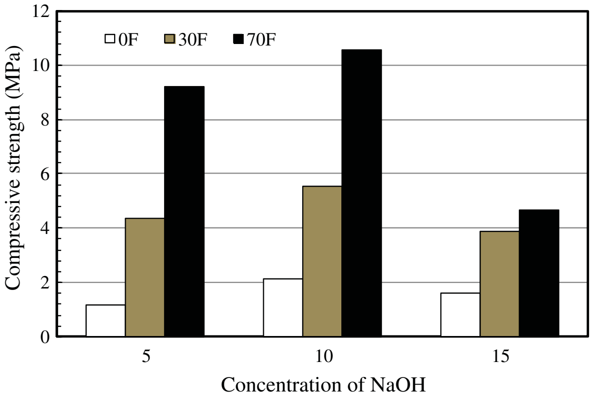

(a) Compressive strength

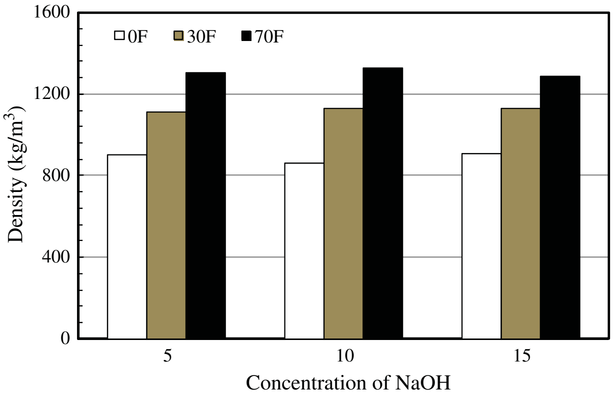

(b) Density

Fig. 6. Compressive strength and density at 28 days of lightweight geopolymer concrete series C at various concentrations of NaOH solution.

not very different as shown in Fig. 5b. This was due to the amount of liquid in the mixes was the same and the change in the liquid density was small.

3.1.3. Concentration of NaOH solution

The results of the compressive strength of lightweight geopolymer concrete with various concentrations of NaOH solution are shown in Fig. 6a. The optimum concentration of NaOH solution was 10 M and the maximum strength of 10.5 MPa was obtained. An increased the concentration of NaOH solution from 5 M to 10 M resulted in the increasing compressive strength. However, an increased the concentration of NaOH solution from 10 to 15 M resulted in a decrease in the compressive strength. At high concentration of NaOH, excessive hydroxide ions caused aluminosilicate gel precipitation at the very early stages. Consequently, compressive strength of geopolymer were lower [18–20]. For example, the 28-day compressive strength of 70F mixes with concentration of NaOH solution of 5, 10, and 15 M were 9.2, 10.5, and 4.7 MPa, respectively.

The densities of lightweight geopolymer concretes with various concentrations of NaOH solution were similar as shown in Fig. 6b. The densities were not affected by the concentrations of NaOH solution as the densities of the liquid in the mixes were similar with various concentrations of NaOH solution.

3.1.4. Temperature of curing

The results of compressive strength of lightweight geopolymer concrete with various temperatures of curing are shown in Fig. 7a. The compressive strength increased with the increasing temperature of curing. For example, the 28-day compressive strength of 70F mixes with temperature of curing of 25, 40, and 60 °C were 6.6, 9.4, and 10.5 MPa, respectively. The increase in temperature of curing to 60 °C enhanced the geopolymerization and increased the strength of geopolymer [10,21–23]. The results of densities of lightweight geopolymer concrete with various temperatures of curing are shown in Fig. 7b. The densities of lightweight concrete, however, decreased with the increase in temperature of curing due to the increased geopolymerization and the loss of moisture from the sample [8]. For example, the 28-day densities of 0F mixes with temperatures of curing of 25, 40, and 60 °C were 984, 975, and 861 kg/m^3, respectively.

3.1.5. Aggregate/ash ratio

The results of compressive strength of lightweight geopolymer concrete with various aggregate/ash ratios are shown in Fig. 8a. The compressive strength significantly decreased with the increasing aggregate/ash ratios. For example, the 28-day compressive strength of 70F mixes with aggregate/ash ratios of 2.0, 2.2, 2.4, and 2.6 were 13.5, 10.5, 7.5, and 4.9 MPa, respectively. The lightweight aggregate is normally weaker than the geopolymer matrix and its increased amount reduced the strength of lightweight concrete [24–26]. The results of densities of lightweight geopolymer concrete with various aggregate/ash ratios are shown in Fig. 8b. The increasing the amount of lightweight aggregate resulted in density reductions due to the lighter weight aggregate. When lightweight aggregate was inserted into the matrices, the porosities of concrete increased and densities decreased [27]. For example, the 28-day densities of 30F mix with aggregate/ash ratios of 2.0, 2.2, 2.4, and 2.6 were 1219, 1131, 1090, and 1037 kg/m^3, respectively.

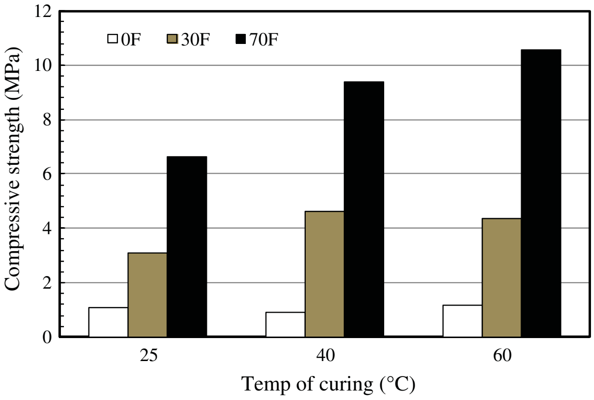

(a) Compressive strength

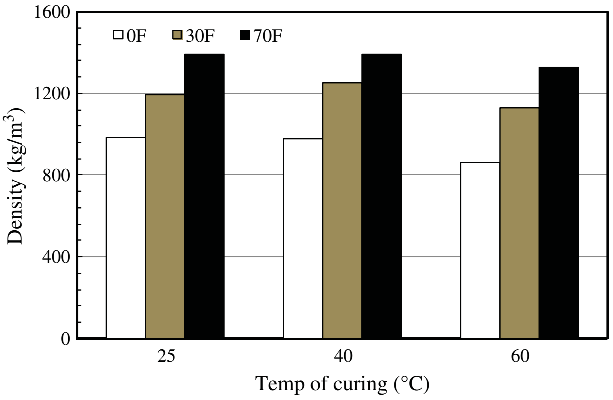

(b) Density

Fig. 7. Compressive strength and density at 28 days of lightweight geopolymer concrete series D at various temperatures of curing.

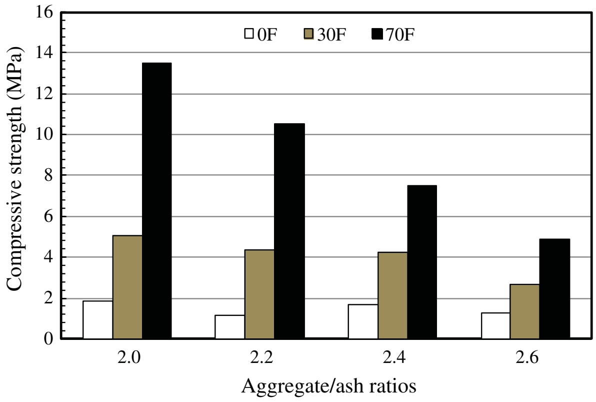

(a) Compressive strength

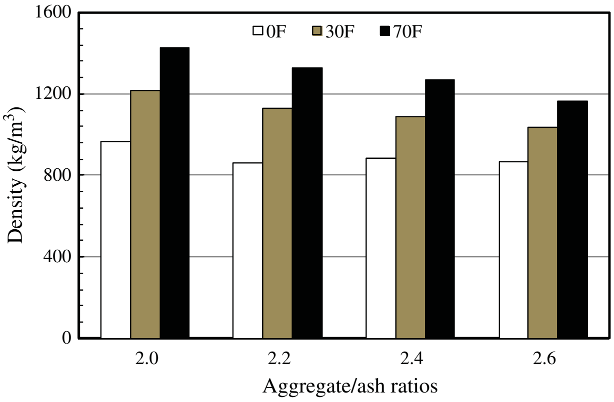

(b) Density

Fig. 8. Compressive strength and density at 28 days of lightweight geopolymer concrete series E at various aggregate/ash ratios.

3.2. Water absorption and porosity

The result of water absorption of lightweight geopolymer concrete with various aggregate/ash ratios are shown in Fig. 9. The water absorption slightly increased with the increase in the amount of aggregate/ash ratios. For example, the water absorption at 28 day of 0F mixes with aggregate/ash ratios of 2.0, 2.2, 2.4, and 2.6 were 30.13%, 30.70%, 31.40%, and 32.15%, respectively. The results of porosity were similar to those of water absorption as shown in Fig. 10. The porosity values increased with the increasing aggregate/ash ratios.

With regard to amount of fine aggregate, the water absorption decreased with the increasing amount of fine aggregate. This was due to the fine aggregate filled the voids in the matrices and thus reduced the porosity. This also resulted in a low water absorption concrete [12].

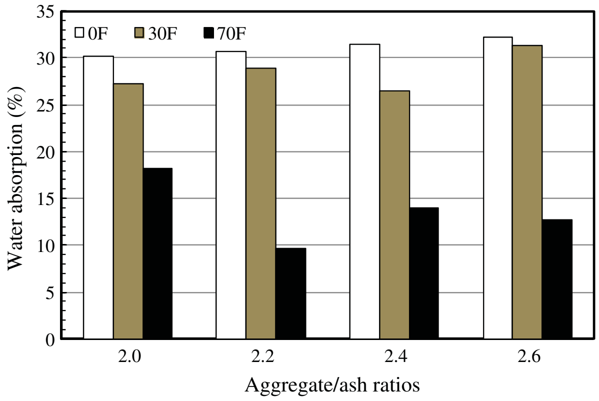

Fig. 9. Water absorption at 28 days of lightweight geopolymer concrete.

3.3. Modulus of elasticity

The results of modulus of elasticity of lightweight geopolymer concrete with various aggregate/ash ratios are shown in Fig. 11. The modulus of elasticity of lightweight concrete showed a similar pattern to those of strength with various aggregate/ash ratios. The optimum density was at aggregate/ash ratio of 2.2 whereas the optimum strength was at a slightly higher aggregate/ash ratio of 2.4. The initial increase in the volume of lightweight aggregate decreased the compressive strength and modulus of elasticity [12,25,28]. For example, the modulii of elasticity of 70F mixes of aggregate/ash ratios of 2.0, 2.2, 2.4, and 2.6 were 7.0, 9.9, 9.2, and 4.5 GPa, respectively. The increase in amount of fine aggregate also resulted in the increase in modulus of elasticity due to the small aggregates filled the pore in matrices which made the concrete more compact and stronger than that with large aggregate.

3.4. Relationship of compressive strength, density, and modulus of elasticity

The relationships between compressive strength and density of lightweight concrete with various aggregate/ash ratios were presented by Eq. (3) and shown Fig. 12. The compressive strength in-

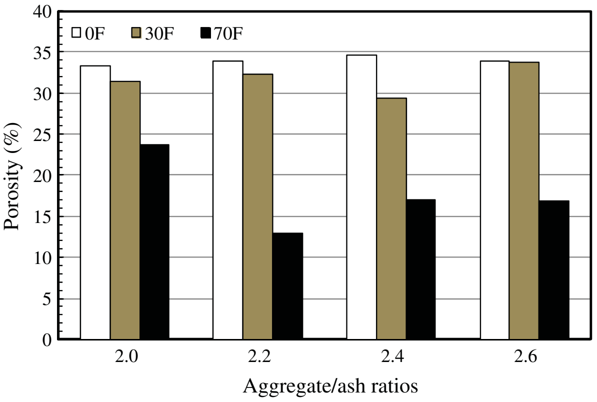

Fig. 10. Porosity at 28 days of lightweight geopolymer concrete.

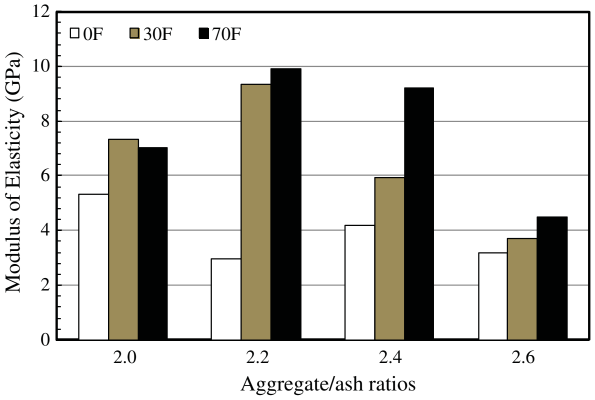

Fig. 11. Modulus of elasticity at 28 days of lightweight concrete.

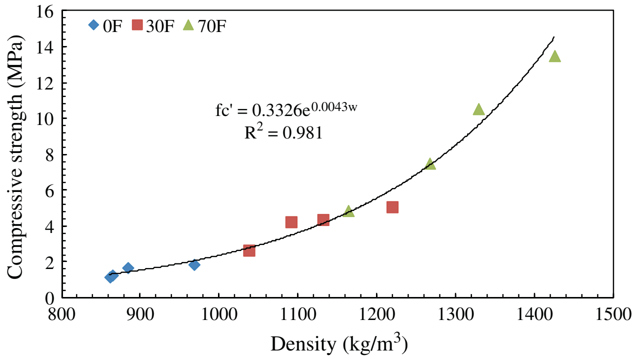

Fig. 12. Relationship of compressive strength and density of lightweight geopolymer concrete.

creased with the increasing density of lightweight geopolymer concrete [11].

$$f'_c = 0.3326e^{0.0043w} \tag{3}$$

where f'_c is compressive strength of lightweight geopolymer concrete (MPa) and w is density of lightweight geopolymer concrete (kg/m^3).

The relationship between modulus of elasticity and compressive strength of lightweight geopolymer concrete is shown in Fig. 13. The modulus of elasticity tended to increase linearly to the square root of compressive strength. The relationship could be predicted in the form shown in Eq. (4). The results indicated the modulus of elasticity between 2.9 and 9.9 GPa which is substantially lower than that of ACI 318 for normal concrete [12,16]. The trends of the relationship of the modulus of elasticity and the square root of compressive strength were similar. The results showed the same trend as that of other research [29].

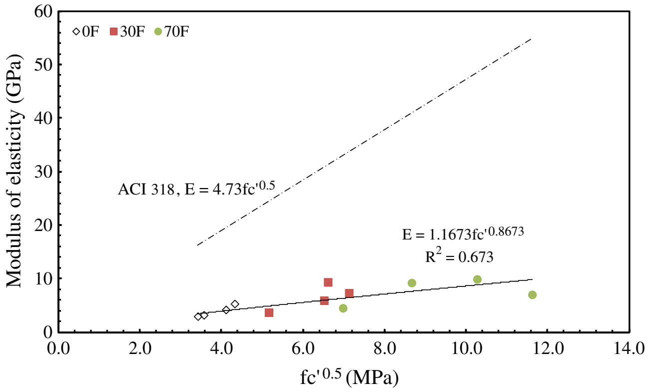

Fig. 13. Relationship of compressive strength and modulus of elasticity of lightweight geopolymer concrete.

$$E = 1.1673f'^{0.8673}_c \tag{4}$$

where E is modulus of elasticity (GPa) and f'_c is compressive strength (MPa).

4. Conclusion

Based on the obtained data, the following conclusion can be draw.

(1) The recycle lightweight block (RLC) could be used as lightweight aggregate for making lightweight geopolymer concrete. The compressive strength increased with the increasing NS/NaOH ratio and temperature of curing but decreased with the increasing aggregate/ash ratio. The optimum L/A ratio was 2.4 and NaOH concentration was 10 M for maximum compressive strength.

(2) The density of lightweight geopolymer concrete increased with the increasing L/A ratio and decreased with the increasing temperature of curing and aggregate/ash ratio. In addition, NS/NaOH ratio and concentration of NaOH did not have a significant effect on the density of lightweight geopolymer concrete.

(3) The aggregate/ash ratios had significant effect on the properties of lightweight geopolymer concrete. The increase in the aggregate portion increased the water adsorption capacity and the porosity of the geopolymer block. The increase in aggregate/ash ratio also increased with compressive strength, density, and modulus of elasticity of the geopolymers.

(4) The results showed that the lightweight geopolymer concrete with 28-day compressive strength of 1.0–16.0 MPa and density of 860–1400 kg/m^3 could be made. It can be used as lightweight geopolymer concrete for masonry wall and partitions.

Acknowledgement

This work was supported by the Higher Education Research Promotion and National Research University Project of Thailand, Office of the Higher Education Commission, through the Advanced Functional Materials Cluster of Khon Kaen University AFM-2553-

Ph.d-01, and the Thailand Research Fund (TRF) under the TRF Senior Research Scholar, Grant No. RTA5480004.

References

[1] Nadim Hassoum M. Structural concrete, theory and design. Upper Sandle River, New Jersey: Prentice-Hall Inc; 2002.

[2] Chandra SBL. Lightweight aggregate concrete: science, technology and application. Norwich, New York, USA: William Andrew Publishing; 2002.

[3] İlker Bekir T. Semi lightweight concretes produced by volcanic slags. Cem Concr Res 1997;27:15–21.

[4] Malhotra VM. Introduction: sustainable development and concrete technology. Concr Int 2002;24:22.

[5] Palomo A, Grutzeck MW, Blanco MT. Alkali-activated fly ashes: a cement for the future. Cem Concr Res 1999;29:1323–9.

[6] Hardjito D, Wallah SE, Sumajouw DMJ, Rangan BV. On the development of fly ash-based geopolymer concrete. ACI Mater J 2004;101:467–72.

[7] Swanepoel JC, Strydom CA. Utilisation of fly ash in a geopolymeric material. Appl Geochem 2002;17:1143–8.

[8] Bakharev T. Geopolymeric materials prepared using class F fly ash and elevated temperature curing. Cem Concr Res 2005;35:1224–32.

[9] Fernández-Jiménez A, Palomo A, Criado M. Microstructure development of alkali-activated fly ash cement: a descriptive model. Cem Concr Res 2005;35:1204–9.

[10] Chindaprasirt P, Chareerat T, Sirivivatnanon V. Workability and strength of coarse high calcium fly ash geopolymer. Cem Concr Compos 2007;29:224–9.

[11] Tho-in T, Sata V, Chindaprasirt P, Jaturapitakkul C. Previous high-calcium fly ash geopolymer concrete. Constr Build Mater 2012;30:366–71.

[12] Ünal O, Uygunoğlu T, Yildiz A. Investigation of properties of low-strength lightweight concrete for thermal insulation. Build Environ 2007;42:584–90.

[13] Sathonsaowaphak A, Chindaprasirt P, Pimraksa K. Workability and strength of lignite bottom ash geopolymer mortar. J Hazard Mater 2009;168:44–50.

[14] Rols S, Ambroise J, Péra J. Effects of different viscosity agents on the properties of self-leveling concrete. Cem Concr Res 1999;29:261–6.

[15] Kharita MH, Yousef S, AlNassar M. The effect of the initial water to cement ratio on shielding properties of ordinary concrete. Prog Nucl Energy 2010;52:491–3.

[16] Wongpa J, Kiattikomol K, Jaturapitakkul C, Chindaprasirt P. Compressive strength, modulus of elasticity, and water permeability of inorganic polymer concrete. Mater Des 2010;31:4748–54.

[17] Husem M. The effects of bond strengths between lightweight and ordinary aggregate–mortar, aggregate–cement paste on the mechanical properties of concrete. Mater Sci Eng, A 2003;363:152–8.

[18] Somna K, Jaturapitakkul C, Kajitvichyanukul P, Chindaprasirt P. NaOH-activated ground fly ash geopolymer cured at ambient temperature. Fuel 2011;90:2118–24.

[19] Lee WKW, van Deventer JSJ. The effects of inorganic salt contamination on the strength and durability of geopolymers. Colloids Surface A 2002;211:115–26.

[20] Pimraksa K, Chindaprasirt P, Rungchet A, Sagoe-Crentsil K, Sato T. Lightweight geopolymer made of highly porous siliceous materials with various Na_2O/Al_2O_3 and SiO_2/Al_2O_3 ratios. Mater Sci Eng, A 2011;528:6616–23.

[21] Lee S, Seo M-D, Kim Y-J, Park H-H, Kim T-N, Hwang Y, et al. Unburned carbon removal effect on compressive strength development in a honeycomb briquette ash-based geopolymer. Int J Miner Process 2010;97:20–5.

[22] Joseph B, Mathew G. Influence of aggregate content on the behavior of fly ash based geopolymer concrete. Scien Iranica 2012;19:1188–94.

[23] Olivia M, Nikraz H. Properties of fly ash geopolymer concrete designed by Taguchi method. Mater Des 2012;36:191–8.

[24] Xu Y, Jiang L, Xu J, Li Y. Mechanical properties of expanded polystyrene lightweight aggregate concrete and brick. Constr Build Mater 2012;27:32–8.

[25] Yang C-C, Huang R. Approximate strength of lightweight aggregate using micromechanics method. Adv Cem Mater 1998;7:133–8.

[26] Kockal NU, Ozturan T. Strength and elastic properties of structural lightweight concretes. Mater Des 2011;32:2396–403.

[27] Al-Jabri KS, Hago AW, Al-Nuaimi AS, Al-Saidy AH. Concrete blocks for thermal insulation in hot climate. Cem Concr Res 2005;35:1472–9.

[28] Cui HZ, Lo TY, Memon SA, Xing F, Shi X. Analytical model for compressive strength, elastic modulus and peak strain of structural lightweight aggregate concrete. Constr Build Mater 2012;36:1036–43.

[29] Chindaprasirt P. Influence of load history on the properties of concrete. PhD thesis, The University of New South Wales; 1980.

Integrated Ferroelectrics, 149:89–94, 2013

ISSN: 1058-4587 print / 1607-8489 online
DOI: 10.1080/10584587.2013.853574

Dielectric and Piezoelectric Properties of 2–2 PZT-Portland Cement Composites

ARNON CHAIPANICH,[1,*] RATTIYAKORN RIANYOI,[1]
RUAMPORN POTONG,[1] PRITSANA PENPOKAI,[1]
AND PRINYA CHINDAPRASIRT[2]

[1]Department of Physics and Materials Science, Faculty of Science, Chiang Mai University, Chiang Mai 50200, Thailand
[2]Sustainable Infrastructure Research and Development Center, Department of Civil Engineering, Faculty of Engineering, Khon Kaen University, Khon Kaen 40002, Thailand

Piezoelectric composites made from lead zirconate titanate (PZT) and cement are developed as sensors in smart concrete structures due to its compatibility to the host structure concrete. In this work, PZT ceramic-Portland cement composites of 2–2 connectivity were produced using a dice and fill method and their dielectric and piezoelectric properties are reported. The piezoelectric coefficients, d_{33}*, value of the 2–2 PZT-cement composite at PZT volume content of 60% and 70% are 99 pC/N and 113 pC/N respectively which are noticeably higher than that of previously tested 0–3 PZT-cement composites. The dielectric values in 2–2 composites are also higher than that of previously tested 0–3 composites.*

Keywords Composites; PZT ceramic; Portland cement; dielectric properties; piezoelectric properties

1. Introduction

A number of cement-based piezoelectric composites consisting of piezoelectric ceramic has been developed recently [1–9]. Piezoelectric ceramic material such as lead zirconate titanate ($Pb(Zr_{0.52}Ti_{0.48})O_3$ or PZT) ceramic exhibits high dielectric constant and high piezoelectric coupling coefficient and is recognised as a smart material [10–11]. Applications of smart PZT ceramics are found in ultrasonic transducers, sensors, actuators and control systems in the automotive, medical, military and consumer electronic industries [11]. For civil engineering applications, piezoelectric PZT-cement based composites have been developed for use as sensors in smart structures [12–23]. This is due to its better compatibility to concrete, the main structural material used in civil engineering, over other piezoelectric materials such as piezoelectric ceramics, piezoelectric polymer and polymer-based pieozoelectric composites [3]. The use of such composite would provide an advantage in the matching of structural concrete. Thus the ideal cement-based piezoelectric composites should have good piezoelectric properties as well as good compatibility to concrete. Piezoelectric-cement

---

Received December 9, 2012; in final form August 25, 2013.
*Corresponding author. E-mail: arnonchaipanich@gmail.com